

SYNTHESIS AND CHARACTERIZATION OF LANTHANIDE IONS DOPED NANOMATERIALS

By

**SANYASINAIDU BODDU
BHABHA ATOMIC RESEARCH CENTRE**

*A thesis submitted to the
Board of Studies in Chemical Sciences*

*In partial fulfillment of requirements
For the degree of*

DOCTOR OF PHILOSOPHY
of
HOMI BHABHA NATIONAL INSTITUTE



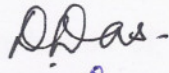
July 2011

Homi Bhabha National Institute

Recommendations of the Viva Voce Board

As members of the Viva Voce board, we certify that we have read the dissertation prepared by **Mr. SANYASINAIDU BODDU** entitled “**Synthesis and Characterization of Lanthanide Ions Doped Nanomaterials**” and recommend that it may be accepted as fulfilling the dissertation requirement for the Degree of Doctor of Philosophy.

Chairman – Prof. D. Das



Date: 23/2/12

External Examiner – Prof. M. L. P. Reddy



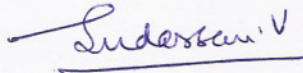
Date: 23/2/2012

Guide – Prof. V. K. Jain



Date: 23/2/2012

Co-Guide – Prof. V. Sudarsan



Date: 23/2/2012

Member 1 – Prof. P. N. Bajaj



Date: 23.02.2012

Member 2 – Prof. S. Kannan



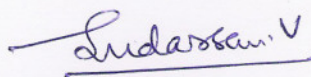
Date: 23.2.2012

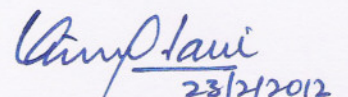
Final approval and acceptance of this dissertation is contingent upon the candidate's submission of the final copies of the dissertation to HBNI.

We hereby certify that we have read this dissertation prepared under our direction and recommend that it may be accepted as fulfilling the dissertation requirement.

Date: 23/2/2012

Place: Mumbai


Prof. V. Sudarsan


Prof. V. K. Jain
23/2/2012

STATEMENT BY AUTHOR

This dissertation has been submitted in partial fulfillment of requirements for an advanced degree at Homi Bhabha National Institute (HBNI) and is deposited in the Library to be made available to borrowers under rules of the HBNI.

Brief quotations from this dissertation are allowable without special permission, provided that accurate acknowledgement of source is made. Requests for permission for extended quotation from or reproduction of this manuscript in whole or in part may be granted by the Competent Authority of HBNI when in his or her judgment the proposed use of the material is in the interests of scholarship. In all other instances, however, permission must be obtained from the author.

Sanyasinaidu Boddu

DECLARATION

I, hereby declare that the investigation presented in the thesis has been carried out by me. The work is original and has not been submitted earlier as a whole or in part for a degree / diploma at this or any other Institution / University.

Sanyasinaidu Boddu

Dedicated to

My beloved brother

.....Ramu Naidu

ACKNOWLEDGEMENTS

I express my deep and sincere gratitude to my guide, Prof. (Dr.) V. K. Jain for his invaluable guidance, constant encouragement, keen interest and good wishes. I am also grateful to him for being patient while critically reviewing this thesis.

This thesis would not have been possible without the guidance, help, support, critical analysis and valuable suggestions from my co-guide Dr. V. Sudarsan. His enthusiasm, deep engagement in research and critical analysis of experimental data has made a deep impression on me. For his invaluable support both on academic and personal fronts, I am extremely grateful to him.

It gives me pleasure to place on record my sincere thanks to Dr. T. Mukherjee, Director, Chemistry Group, Dr. D. Das, Head, Chemistry Division and Dr. R. K. Vatsa, Head, Structural Chemistry Section for giving me an opportunity to work with a dedicated and learned team of scientists and for constant encouragement during the course of present investigation.

I am thankful to Dr. S. K. Ghosh, Dean of Academics, Chemical Sciences, HBNI for his help, support and constant encouragement right from the beginning of the Training School, BARC. I am grateful to HBNI for giving me this opportunity, providing funding and fellowship during this course of work.

I take this opportunity to thank Mr. B. Vishwanadh, Dr. R. Tewari, of Material Science Division, BARC, Prof. P. V. Satyam, Institute of Physics, Bhubaneswar for their help in providing TEM data. Thanks are due to Mr. Jitendra Nuvad and Dr. C.G.S.Pillai, for SEM measurements and Dr. M. Pandey for Raman measurements. I would like to acknowledge Drs. R. S. Ningthoujam, Sandeep Nigam, O. D. Jayakumar and R. Sashikala, Anshu Singhal who helped me in various ways and their cooperation during the course of this work. I am

also thankful to all the members of Structural Chemistry Section for their help and cooperation.

My special thanks to my classmate, my dear friend K. Srinivasu for his moral support, diversified help and continuous encouragement. I wish to thank my friends Vishwanadh, Siddharth, Dinesh, Bhanu, Vijay, Jerina Farheen, Sunil, Shyam, Murthy, Vishnu, Srinu, Naresh, Raghavendra and Prabhat for their help, close companionship and constant inspiration.

Finally, I convey my heartfelt gratitude to my family and beloved elder brother Ramu Naidu who have always encouraged me to follow my heart and inspired my inquisitive mind throughout my childhood and study career. Their inspiration, encouragement, blessings and support have helped me to achieve what I am today.

Sanyasinaidu Boddu

Mumbai

July 2011

CONTENTS

	Page No.
SYNOPSIS	xii - xxiii
LIST OF FIGURES	xxiv - xxxvi
LIST OF TABLES	xxxvii - xxxviii
CHAPTER 1: Introduction	1 - 29
1.1 History of Nanomaterials	1
1.2 Classification of nanomaterials	2
1.3 Synthesis of nanomaterials	3
1.3.1 Co-precipitation method	4
1.3.2 Sol-gel Method	7
1.3.3 Hydro-/ solvo-thermal method	8
1.3.4 Combustion method	8
1.4 Properties of nanomaterials	9
1.4.1 Electronic properties	9
1.4.2 Optical properties	10
1.5 Lanthanides and their Luminescence	13
1.5.1 Lanthanide Energy levels	14
1.5.2 Selection rules	17
1.5.3 Luminescence quenching	18
1.6 Recent work on luminescent nanomaterials	21
1.7 Scope of present work	28
CHAPTER 2: Experimental	30 - 53
2.1 Materials and reagents	30
2.2 General synthesis of undoped and lanthanide doped nanomaterials	30

2.3 Synthesis of binary oxide nanomaterials	31
2.4 Synthesis of phosphate nanomaterials	33
2.5 Synthesis of gallate nanomaterials	35
2.6 Synthesis of tungstate nanomaterials	36
2.7 Characterization Techniques	36
2.7.1 X-Ray Diffraction	36
2.7.2 Electron Microscopy	38
2.7.3 Atomic Force Microscope (AFM)	43
2.7.4 Vibrational spectroscopy	45
2.7.5 Nuclear magnetic resonance (NMR) Spectroscopy	47
2.7.6 Photoluminescence spectroscopy	50
2.7.7 Thermal analysis	53
CHAPTER 3: Binary Oxides	54 - 101
3.1 Introduction	54
3.2 Effect of urea concentration on size of GaOOH nanorods	58
3.3 Effect of lanthanide ion concentration on morphology and crystal structure of GaOOH	59
3.4 Effect of heat treatment on crystal phase and morphology of Ga ₂ O ₃ and Ga ₂ O ₃ :Ln ³⁺ nanomaterials	75
3.5 Effect of heat treatment on luminescence of Ga ₂ O ₃ :Ln ³⁺ nanomaterials	80
3.6 Structural and luminescence studies on antimony oxide nanomaterials	86
3.7 Effect of nanorods orientation on luminescence of Sb ₂ O ₃	88
3.8 Interaction of Eu ³⁺ ions with Sb ₂ O ₃ nanorods	93
CHAPTER 4: Phosphates	102 - 148
4.1 Introduction	102

4.2 Studies on GaPO ₄ and lanthanide ions containing GaPO ₄ nanomaterials	104
4.2.1 XRD, FT-IR and TEM study	104
4.2.2 Luminescence studies	106
4.2.3 ³¹ P MAS NMR studies	109
4.3 Studies on Antimony phosphate nanomaterials	113
4.3.1 Effect of ethylene glycol to glycerol ratio on size and shape of SbPO ₄ :Ln nanomaterials	113
4.3.2 Luminescence studies on SbPO ₄ :Ln nanoparticles/nanoribbons	117
4.3.3 Studies on Ce ³⁺ co-doped SbPO ₄ :Tb ³⁺ nanomaterials and their dispersion in silica	122
4.3.4 Proof for the incorporation of lanthanide ions into SbPO ₄ lattice	123
4.3.5 Luminescence studies on SbPO ₄ :Ce, Tb and effect of incorporation of nanomaterials in silica	126
4.4 Bismuth phosphate nanomaterials	133
4.4.1 Effect of reaction temperature on the particle size, shape and crystal structure	133
4.4.2 Effect of particle size and crystal structure on Eu ³⁺ emission from BiPO ₄ :Eu ³⁺ nanomaterials	137
4.4.3 Solid solution formation between bismuth and lanthanide phosphates	138
4.4.4 Luminescence studies on Eu ³⁺ doped BiPO ₄ nanomaterials	142
4.4.5 Luminescence studies on Tb ³⁺ doped BiPO ₄ nanorods	143
4.4.6 Energy transfer from Tb ³⁺ ions to Eu ³⁺ ions in Tb ³⁺ co-doped BiPO ₄ :Eu ³⁺ nanorods	144
4.4.7 Luminescence studies on Dy ³⁺ doped BiPO ₄ nanorods	145
4.4.8 Luminescence studies on Sm ³⁺ doped BiPO ₄ nanorods	147

CHAPTER 5: Zinc Gallate	149 - 164
5.1 Introduction	149
5.2 Effect of ethylene glycol (EG) - H ₂ O solvent ratio on particle size and photoluminescence of ZnGa ₂ O ₄ nanoparticles	150
5.3 Effect of precursor concentration on particle size	154
5.4 Effect of Indium doping on crystallinity and photoluminescence of ZnGa ₂ O ₄	158
5.5 Photoluminescence from lanthanide doped ZnGa ₂ O ₄ nanoparticles	161
5.5.1 Ce ³⁺ doped ZnGa ₂ O ₄ nanoparticles	161
5.5.2 Eu ³⁺ doped ZnGa _{1.5} In _{0.5} O ₄ nanoparticles	163
5.5.3 Tb ³⁺ doped ZnGa _{1.5} In _{0.5} O ₄ nanoparticles	164
CHAPTER 6: Tungstates	165 - 179
6.1 Introduction	165
6.2 Effect of nature of metal ion on the particle size	166
6.3 Effect of metal ion on luminescence of MWO ₄ :Eu ³⁺ nanoparticles	168
6.4 Luminescence studies on un-doped CaWO ₄ nanoparticles	170
6.5 Effect of heat treatment on particle size	171
6.6 Effect of particle size on photoluminescence of CaWO ₄ nanoparticles	172
6.7 Luminescence studies on Tb ³⁺ doped CaWO ₄ nanoparticles	174
6.8 Luminescence studies on Dy ³⁺ doped CaWO ₄ nanoparticles	175
6.9 Luminescence studies on Sm ³⁺ doped CaWO ₄ nanoparticles	176
6.10 Luminescence studies on Er ³⁺ doped CaWO ₄ nanoparticles	178
CHAPTER 7: Summary and Conclusions	180 - 184
References	185 - 201
List of Publications	202 - 205

Synthesis and Characterization of Lanthanide Ions Doped Nanomaterials

Synopsis

Nanomaterials or nanostructured materials are the materials with structural features in between those of atoms/ molecules and bulk materials, with at least one dimension in the range of 1 to 100 nm ($1 \text{ nm} = 10^{-9} \text{ m}$). The exponential growth of nanomaterials stems from their unique physical and chemical properties and functionalities that often differ significantly from the corresponding bulk counterparts [1]. It has been realized over the last two decades that the size and shape of materials play a major role in deciding their properties [1-3]. Many of the unique properties of nanomaterials are extremely promising for emerging technological applications, including nanoelectronics, nanophotonics, biomedicine, information storage, communication, energy conversion, catalysis, environmental protection, and space exploration [4]. One of the most fascinating and useful aspects of nanomaterials is their optical properties, including linear and non-linear absorption, photoluminescence, electroluminescence, and light scattering. The optical or luminescence properties of the nanomaterials can arise either due to their inherent property or due to doping of luminescent species like lanthanide ions. In the present study, nanomaterials with both types of luminescent properties have been investigated.

Lanthanide ions (Ln^{3+}) are important constituents in many optical materials [5-6]. Lanthanides are a group of fourteen elements appearing in the periodic table after lanthanum with atomic number ranging from 57 to 71 and electronic configuration $[\text{Xe}] 4f^{1-14} 5d^{0-1} 6s^2$. The 4f electrons of lanthanide ions are strongly shielded by filled outer shell orbitals. The sharp emission lines and long excited state lifetime values from lanthanide ions have been attributed to the shielding of 4f electron from the surrounding environment by 5d and 6s electrons. They have got wide variety of applications, including phosphors for fluorescent lighting, amplifiers for fiber-optic communication, materials for display monitors, X-ray

imaging, scintillators, lasers, etc. [7-9]. Lanthanide based luminescent materials are prepared either by complexing Ln^{3+} ions with suitable organic ligands or by doping Ln^{3+} in an appropriate inorganic lattices having different dimensions. The reduced optical scattering of nanometer-sized particles facilitates its use as active materials in polymer or glass based lasers and amplifiers. Such nanoparticles can be stabilized with suitable ligands during the synthesis and can be incorporated in different type of matrices. Composites consisting of luminescent nanoparticles dispersed in a polymer matrix are interesting materials. Such materials have certain advantages as the polymer lattice offers good processability and desirable mechanical properties while the inorganic luminescent material provides high luminescence efficiency and long-term chemical stability.

During the present investigation, a variety of inorganic matrices varying from oxides (Ga_2O_3 , Sb_2O_3), phosphates (SbPO_4 , BiPO_4 , GaPO_4), gallate (ZnGa_2O_4) to tungstates (CaWO_4 , SrWO_4 , BaWO_4) have been doped by lanthanide ions. Choice of the materials has been made by considering the environment around the cation which would be substituted by incoming lanthanide ion, phonon energy of the lattice and luminescent character of the host. Some of the materials have been incorporated into sol-gel and polymer films with a view to make luminescent films for different applications. The thesis is divided into 7 chapters each of which is briefly discussed below.

General and basic aspects of nanomaterials are discussed in **Chapter 1**. It contains brief introduction about the history of nanomaterials, different types of nanomaterials, their properties and applications. Emphasis is given to luminescent properties of different types of nanomaterials. Various methods used for the synthesis of nanomaterials are discussed briefly. As the present study mainly deals with the lanthanide ions doped nanomaterials, an overview of lanthanide ions luminescence in solids and its dependence on concentration in the host, particle size of the host, etc. has been given.

Chapter 2 deals with the experimental methods and characterization techniques employed in the present study. The generalized co-precipitation method used for the synthesis of various nanomaterials has been discussed. A brief description regarding various instrumental methods, such as powder X-ray diffraction (XRD), transmission electron microscopy (TEM), scanning electron microscopy (SEM), atomic force microscopy (AFM), nuclear magnetic resonance (NMR) spectroscopy, Fourier transmission infrared spectroscopy (FT-IR), spectro-fluorimetry, thermo-gravimetry (TG) and differential thermal analysis (DTA) used for the characterization has been given. The results of the present investigation are given and described in chapters 3-6.

Chapter 3 describes the synthesis and characterization of nanosized metal oxides Ga_2O_3 and Sb_2O_3 and is divided into two sections. In the first section results on lanthanide ions doped gallium oxide nanocrystals are presented. GaOOH nanorods, used as a precursor materials for Ga_2O_3 , were prepared by hydrolysis of $\text{Ga}(\text{NO}_3)_3 \cdot x\text{H}_2\text{O}$ using urea at 100°C in the presence of different amounts of lanthanide ions like Eu^{3+} , Tb^{3+} and Dy^{3+} . Based on X-ray diffraction (shown in Fig.1) and vibrational studies, it has been inferred that the layered structure of GaOOH collapsed even when a small amounts of lanthanide ions (1 atom % and more) were present in the reaction medium during the synthesis of GaOOH nanorods. Destruction of hydrogen bonding present between the layers of edge-sharing GaO_6 octahedra in GaOOH phase, brought about by the interaction of OH groups of GaOOH phase with Ln^{3+} ions is responsible for the collapse of the layered structure followed by its amorphisation. This process results in to finely mixed hydroxides of lanthanide and gallium.

The results were further supported by the steady state luminescence and excited state lifetime measurements of Ln^{3+} ions. It has been observed that the aspect ratio (ratio of length to width) of GaOOH nanorods can be tuned by varying the urea concentration in the reaction medium. These nanorods have been converted into α - and β - Ga_2O_3 phases with same

morphology by heating at 500 and 900°C, respectively. On heat treatment at 900°C, amorphous GaOOH containing more than 2 atom % lanthanide ions lead to the formation of β -Ga₂O₃ nanoparticles instead of nanorods. During the heat treatment, the fine dispersion of lanthanide with gallium hydroxides helped in diffusion of lanthanide ions into the Ga₂O₃ phase as revealed by the existence of strong energy transfer with efficiency more than 90% between the host Ga₂O₃ and lanthanide ions. Strong blue, red and green emissions have been observed from undoped, Eu³⁺ and Tb³⁺ doped β -Ga₂O₃, respectively whereas Er³⁺ doped β -Ga₂O₃ nanomaterials showed strong near infrared (NIR) emission (~1535 nm) on host excitation.

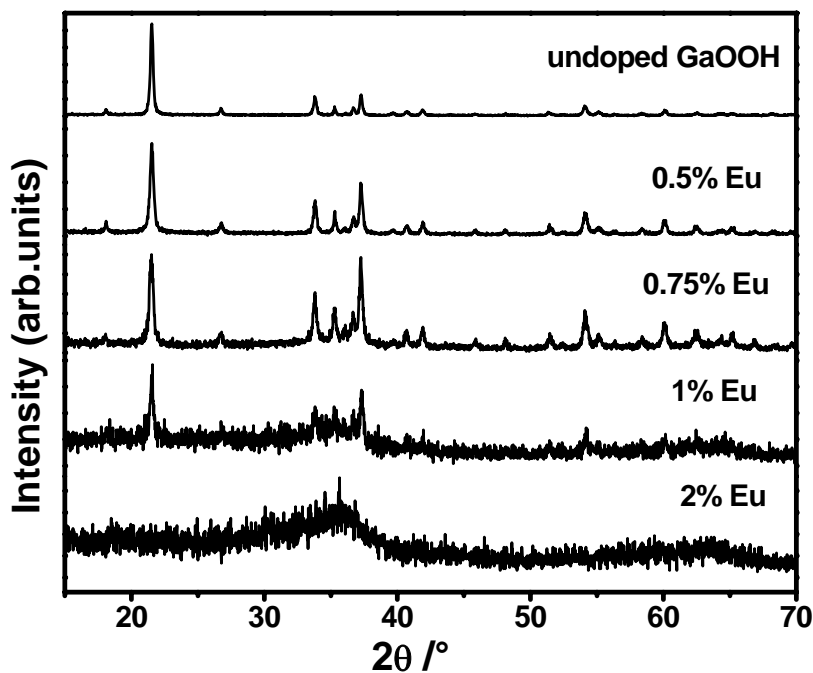


Figure 1. XRD patterns of GaOOH: Eu³⁺ nanorods

The second section of this chapter deals with the synthesis, characterization of undoped, and lanthanide containing Sb₂O₃ nanomaterials. Both undoped and lanthanide ions containing Sb₂O₃ nanorods were prepared at room temperature by hydrolysis of SbCl₃ in isopropanol medium and characterized for their structural and luminescent properties. These

nanorods have orthorhombic structure with length around 3-4 μm and width around 100-200 nm, as revealed by TEM (Fig.2). Luminescence around 390 nm has been observed from these samples. Morphology induced changes in photoluminescence properties of Sb_2O_3 nanorods both as prepared and the ones annealed at different temperatures have been investigated. A distinct photoluminescence band compared to bulk Sb_2O_3 has been observed over a region of 500-600 nm from the nanorods and is arising due to the morphology of Sb_2O_3 nanorods. Changes in the Raman spectrum at ~ 260 and 445 cm^{-1} , corresponding to the Sb-O-Sb stretching and bending modes, respectively. Temperature dependence of these bands further confirmed their shape / morphology selective nature. Attempts have been made to dope Ln^{3+} ions in these luminescent nanorods. Based on the detailed XRD, luminescence, Raman and infrared studies it has been established that the Eu^{3+} ions were not incorporated in the lattice of Sb_2O_3 instead interacted with Sb^{3+} ions in the presence of hydroxyl ions (present in the medium) to form an amorphous antimony-europium hydroxide compound. The amorphous compound on heating at high temperatures leads to formation of hydrated Sb(V) oxide and Eu_2O_3 as major phases.

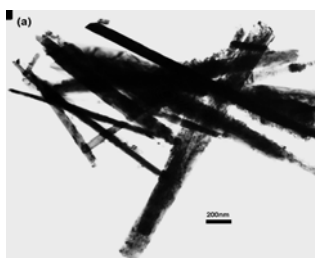


Figure 2. TEM image of Sb_2O_3 nanorods

Chapter 4 describes the synthesis and characterization of luminescent phosphate nanomaterials and is divided into three sections dealing with GaPO_4 , SbPO_4 and BiPO_4 nanomaterials. In the first section, synthesis, structural and luminescence properties of GaPO_4

nanoparticles having hexagonal structure with different amounts of Eu^{3+} doping is discussed. Synthesis has been carried out at 130°C in glycerol medium. The interaction between GaPO_4 nanoparticles and Eu^{3+} ions has been investigated using Eu^{3+} luminescence and ^{31}P magic angle spinning nuclear magnetic resonance (MAS NMR) techniques. Based on the studies it has been established that Eu^{3+} ions up to 2.5 atom % replaces the protons of the hydroxyl groups attached on Ga^{3+} ions present at the surface of the nanoparticles and above this concentration, separation of EuPO_4 phase has been observed. The anisotropy parameters derived from the side band intensities of the ^{31}P MAS NMR patterns from these samples confirmed the surface ion exchange at low Eu^{3+} concentration (2.5 atom % or less) and separation of EuPO_4 at high Eu^{3+} concentration (5 atom % and more). The increase in anisotropy at high Eu^{3+} contents has been attributed to the presence of paramagnetic europium species in the sample.

In the second section, synthesis and characterization of both undoped and lanthanide ions doped SbPO_4 nanomaterial are discussed. Nanoparticles and nanoribbons of SbPO_4 doped with lanthanide ions like Ce^{3+} , Eu^{3+} and Tb^{3+} were prepared at 140°C by co-precipitation method in a solvent mixture of ethylene glycol and glycerol. Nature and relative concentration of the solvents used for the synthesis had a pronounced influence on particle size, crystallinity and morphology of the nanoparticles/ nanoribbons. TEM studies have revealed that the sample prepared in a 2:3 mixture of ethylene glycol-glycerol solvent comprised of predominantly nanoribbons together with a small quantity of nanoparticles having average size less than 10 nm. The length of nanoribbons was in the range of 500-700 nm while the width was around 100 nm (Fig. 3). Solvent molecules (ethylene glycol and glycerol) assisted in stabilizing these nanomaterials, which was confirmed from IR studies on the samples. The SbPO_4 host was characterized by absorption at 220 nm and excitation of SbPO_4 : Ln^{3+} samples at this wavelength resulted in energy transfer from host to lanthanide

ions. $\text{SbPO}_4: \text{Eu}^{3+}$ and $\text{SbPO}_4: \text{Tb}^{3+}$ nanoribbons/ nanoparticles showed bright red and green emissions, respectively after excitation at 220 nm due to energy transfer from host to $\text{Eu}^{3+}/\text{Tb}^{3+}$ ions. Detailed vibrational and luminescence studies on these samples established that these lanthanide ions were incorporated at Sb^{3+} site of the SbPO_4 lattice. Co-doping of $\text{SbPO}_4: \text{Tb}^{3+}$ nanoparticles/nanoribbons with Ce^{3+} , resulted in improved luminescence due to energy transfer from Ce^{3+} to Tb^{3+} ions. The excitation spectrum corresponding to the Tb^{3+} emission and the excited state lifetime of the $^5\text{D}_4$ level of Tb^{3+} ions in the sample further confirmed energy transfer from Ce^{3+} to Tb^{3+} ions in the SbPO_4 host. Dispersion of these nanomaterials in silica matrix effectively shields the lanthanide ions at the surface of the nanoribbons/nanoparticles from vibrations of stabilizing ligands resulting in the reduction in extent of vibronic quenching of the excited state. The results showed significant reduction in surface contribution to the decay curve corresponding to the $^5\text{D}_4$ level of the Tb^{3+} ions after incorporating the nanoribbons/ nanoparticles in silica matrix.

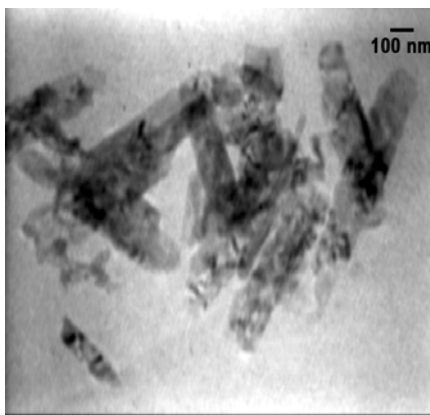


Figure 3. TEM image SbPO_4 nanoparticles and nanoribbons.

In the third section deals with the synthesis, characterization and luminescence properties of nanocrystalline lanthanide ions doped hexagonal $\text{BiPO}_4 \cdot x\text{H}_2\text{O}$, hexagonal BiPO_4 and monoclinic BiPO_4 . All the three forms of BiPO_4 were prepared at room temperature,

100°C and 185°C, respectively in ethylene glycol medium. XRD patterns of as synthesized samples confirmed the existence of different phases (Fig. 4). Hydrated BiPO₄ phase exists as nanoparticles having size ~50-80 nm. Unlike this, anhydrous hexagonal and monoclinic phases of BiPO₄ exist in the form of nanorods.

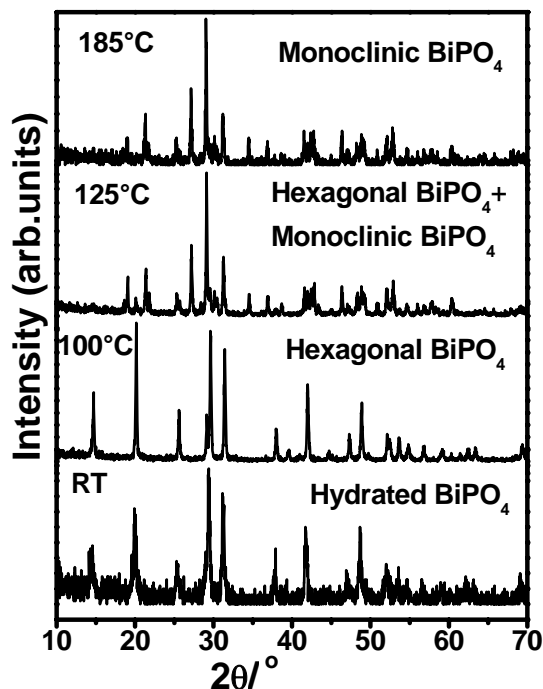


Figure 4. XRD patterns of BiPO₄ sample prepared at different temperatures

Nanorods of hexagonal BiPO₄ and monoclinic BiPO₄ were isolated having length / width in the ranges of 80-110/ ~ 20-30 nm and ~ 500-2000/ ~ 30-80 nm, respectively. BiPO₄ nanorods showed host absorption ~250 nm and energy transfer from host to lanthanide ions was observed in both Eu³⁺ and Tb³⁺ doped BiPO₄ nanorods. The optimum emission characteristics have been observed for 2.5 at % lanthanide ions doped BiPO₄. The emission intensity systematically increases starting from hydrated hexagonal BiPO₄ to anhydrous hexagonal BiPO₄ and then to monoclinic BiPO₄. Strong multi colour emissions have been observed from nanorods after doping with Dy³⁺ (blue, yellow), Tb³⁺ (green), Sm³⁺ (orange) and Eu³⁺ (red) ions. Based on the shift in the XRD peak maxima and line shape changes in

^{31}P magic angle spinning nuclear magnetic resonance (MAS NMR) patterns, the formation of solid solution between BiPO_4 and LnPO_4 phases has been inferred. Co-doping Eu^{3+} ions with $\text{BiPO}_4:\text{Tb}^{3+}$ nanorods resulted in strong energy transfer from Tb^{3+} to Eu^{3+} ions, as confirmed by both steady state and lifetime measurements corresponding to the excited states of Eu^{3+} and Tb^{3+} ions.

In **Chapter 5**, synthesis, characterization of undoped, and lanthanide ions doped gallate nanoparticles and their incorporation into polymer matrix is discussed. Bulk ZnGa_2O_4 is known to be a weak blue light emitting material with an emission maximum around 427 nm. Thus, it is of interest to prepare nanoparticles of these materials with true blue emission (emission maximum ~ 450 nm), as no bright blue light emitters based on processable nanoparticles are available at present, thereby hindering the development of polymer based pure white light displays. ZnGa_2O_4 nanoparticles with different sizes have been prepared by co-precipitation method at 120°C in ethylene glycol-water mixture. The emission characteristics of these nanoparticles have been studied. It was observed that the emission maximum can be tuned from 385 to 455 nm by increasing particle size. However, the emission intensity reduces with increasing the particle size. The emission in the visible region from ZnGa_2O_4 has been attributed to the excitation of GaO_6 octahedra upon UV excitation followed by de-excitation. Hence, it is expected that when Ga-O-Ga linkages are replaced Ga-O-In linkages, the energy levels of GaO_6 will decrease consequently shifting the emission to higher wavelength. In fact, the wavelength corresponding to the emission maximum shifted from 430 nm to 465 nm with increasing in In^{3+} content in ZnGa_2O_4 nanoparticles as is evident from Fig. 5(a). The $\text{ZnGa}_{1.5}\text{In}_{0.5}\text{O}_4$ nanoparticles gave maximum quantum yield of blue light emission with a value of $\sim 10\%$. This value is significantly higher than that reported for organic luminescent materials (pyrene-based materials) which are conventionally used polymer based blue light emitting materials. These nanoparticles have been incorporated

into poly methyl methacrylate (PMMA) polymer by a thermal polymerization reaction using AIBN as an initiator at 70°C. The viscous polymer solution was then coated on quartz plate by spin coating technique. Such films showed bright blue emission on UV excitation (Fig. 5(b)).

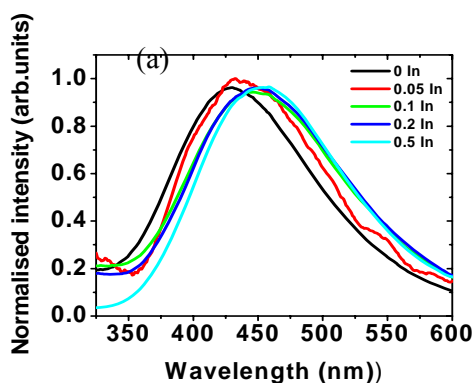


Figure 5.
(a)
Emission
spectrum

from $\text{ZnGa}_{2-x}\text{In}_x\text{O}_4$ ($0.0 \leq x \leq 0.5$) nanoparticles

(excitation

wavelength was 285 nm) and (b) The blue light emission up on UV excitation from PMMA film containing the nanoparticles.

Chapter 6 deals with the synthesis and characterization of lanthanide ions doped and undoped MWO_4 ($\text{M} = \text{Ca}, \text{Sr}, \text{Ba}$) nanoparticles. These nanoparticles have been synthesized at room temperature in ethylene glycol medium. Under identical experimental conditions, the particle size increases with increasing ionic size of the cations (Fig. 6 (a)). The undoped tungstate nanomaterials show strong absorption around 250 nm due to charge transfer in the WO_4^{2-} group and exhibit emission in the visible region. For example, CaWO_4 nanoparticles showed strong blue emission on UV excitation and the emission intensity increases with increase in the particle size. In the lanthanide doped CaWO_4 nanoparticles, strong energy transfer takes place from host to lanthanide ions. Thus when CaWO_4 nanoparticles are doped with Dy^{3+} , Tb^{3+} , Sm^{3+} and Eu^{3+} ions, yellow, green, orange and red emissions, respectively

(Fig.6 (b)) have been observed on excitation at 253 nm. Strong near infrared (NIR) emission (1535 nm) has also been observed from the Er^{3+} doped CaWO_4 nanoparticles.

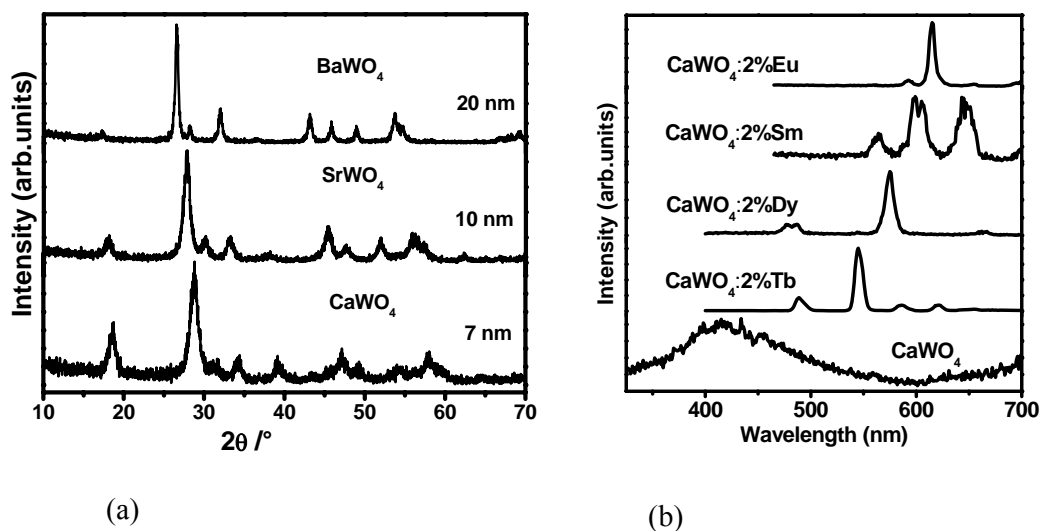


Figure 6. (a) XRD patterns of different tungstate nanoparticles and (b) Emission spectrum from lanthanide ions doped CaWO_4 nanoparticles. Samples were excited at 250 nm.

Chapter 7 gives the summary of the results on the luminescence and structural aspects of nanomaterials of the present study together with the future scope of this work. Possible reasons for the tunability of emission observed from different type of nanomaterials has been discussed mainly based on the different experimental parameters involved in their synthesis and in their structural aspects. Future scope and main interest involved in the development of such materials lies with their applications as active materials in display and electro-luminescent devices. Factors that are relevant for employing the above materials for such applications have also been discussed in this chapter.

References:

1. C. Burda, X. Chen, R. Narayanan, M. A. El-Sayed, Chem. Rev., 105 (2005) 1025.
2. T. Vossmeier, L. Katsikas, M. Giersig, I. G. Popovic, K. Diesner, A. Chemseddine, A. Eychmuller, H. Weller, J. Phys. Chem., 98 (1994) 7665.

3. N. M. Dimitrijevic, Z. V. Saponjic, B. M. Rabatic, O. G. Poluektov, T. Rajh, *J. Phys. Chem. C*, 111 (2007) 14597.
4. C. N. R. Rao, P.J. Thomas, G.U. Kulkarni, *Nanocrystals: Synthesis, Properties and Applications*, Springer-Verlag Berlin, Heidelberg, 2007
5. V. Sudarsan, S. Sivakumar, F. C. J. M. van Veggel, *Chem. Mater.*, 17 (2005) 4736.
6. T. Justel, H. Nikol, C. Ronda, *Angew. Chem., Int. Ed.*, 37 (1998) 3085.
7. D. B. Barber, C. R. Pollock, L. L. Beecroft, C. K. Ober, *Opt. Lett.*, 22 (1997) 1247.
8. V. I. Klimov, A. A. Mikhailovsky, S. Xu, A. Malko, J. A. Hollingsworth, C. A. Leatherdale, H. J. Eisler, M. G. Bawendi, *Science*, 290 (2000) 314.
9. G. A. Hebbink, J. W. Stouwdam, D. N. Reinhoudt, F. C. J. M. van Veggel, *Adv. Mater.*, 14 (2002) 1147.

List of figures:

- Fig.1: The Lycurgus cup appears (a) green in reflected light, (b) red in transmitted light and this cup is preserved in the British museum in London, (c) Colloidal dispersion of gold preserved in the Royal Institution, London
- Fig.2: Nanomaterials having different dimensions
- Fig.3: Schematic representation of variation of free-energy change as a function of nuclei radius during nucleation and growth
- Fig.4: Schematic representation of nanoparticles stabilization by (a) electrostatic repulsion (b) steric repulsion/ interaction
- Fig.5: Examples of metal complexes [$\text{Alq}_3(^1\pi-\pi^*)$, $\text{Eu}(\text{tta})_3\text{phen}(\text{f-f})$, $\text{PtOEP}(^3\pi-\pi^*)$, $\text{Ir}(\text{ppy})_3(^3\text{MLCT})$] which shows intense photoluminescence
- Fig.6: Splitting of $4f^n$ electronic energy levels due to coulomb repulsions, spin-orbit coupling and crystal field effect.
- Fig.7: Energy levels diagram for the lanthanide aquo ions. The main luminescent levels are drawn in red, while the ground state level is indicated in blue
- Fig.8: Energies for $4f \rightarrow 5d$ and CT transitions of trivalent lanthanide ions
- Fig.9: Schemes of possible mechanisms for luminescence concentration quenching: (a) energy migration of among donors (circles) in a chain followed by its migration to a killer site (black circle) which act as non-radiative sink; (b) cross relaxation between pairs of centers. (Sinusoidal arrows indicate nonradiative decay)
- Fig.10: Representative emission spectrum from ZnO nanocrystals obtained after excitation at 325 nm
- Fig.11: X-Ray diagram of a typical reflection mode diffractometer
- Fig.12: Schematic representation of SEM microscope

- Fig.13: (a) Simplified ray diagram of TEM, (b) Mass-thickness contrast
- Fig.14: Electron diffraction patterns from (a) single crystal, (b) polycrystalline materials and (c) nanocrystalline materials
- Fig.15: (a) Principle of AFM imaging, (b) Variation of interaction force versus distance between the AFM tip and substrate
- Fig.16: Principle of MAS NMR experiment
- Fig.17: Schematic representation of spectrofluorimeter
- Fig.18: XRD patterns of GaOOH nanomaterials prepared with different amounts of urea.
- Fig.19: SEM images of GaOOH nanorods prepared with (a) 15 mmol, (b) 80 mmol, (c) 115 mmol and (d) 180 mmol of urea
- Fig.20: XRD patterns of GaOOH sample prepared in presence of (a) 0 at % (b) 0.5 at % (c) 0.75 at % (d) 1 at % and (e) 2 at % of Eu^{3+} ions.
- Fig. 21: XRD patterns of GaOOH samples prepared in presence of (a) 2 at % Tb^{3+} and (b) 2 at % Dy^{3+} .
- Fig.22: SEM images of GaOOH nanorods prepared in presence of (a) 0 at % Eu^{3+} (b) 0.5 at % Eu^{3+} (c) 1 at % Eu^{3+} and (d) 2 at % Eu^{3+} .
- Fig.23: FT-IR patterns (A and B) of GaOOH sample prepared in presence of (a) 0 at % (b) 0.5 at % (c) 0.75 at % (d) 1 at % (e) 2 at % of Eu^{3+} ions and (f) amorphous $\text{Ga}(\text{OH})_3$. The Raman spectrum from the representative samples are shown in Fig.23 (C).
- Fig.24: GaOOH structure obtained using the software MOLDRAW, depicting the interaction of Eu^{3+} ions with GaOOH lattice and collapse of its layered structure to form amorphous gallium and europium hydroxide. Colour code: Green spheres represent Gallium, red spheres represent oxygen and white spheres represent hydrogen. Dotted red lines represent hydrogen bonding.

- Fig.25: XRD patterns corresponding to GaOOH nanorods treated with aqueous solution of Eu^{3+} ion in presence of urea $\sim 100^\circ\text{C}$ for (a) 0 minutes (b) 30 minutes (c) 2 hours. The corresponding pattern obtained only with Eu^{3+} ions in the absence of GaOOH is shown in Fig.25 (d).
- Fig.26: Emission spectrum obtained after 280 nm excitation and excitation spectrum corresponding to 435 nm emission from GaOOH nanorods prepared in the absence of any Eu^{3+} ions.
- Fig.27: Emission spectrum (left) obtained at 350 nm excitation and excitation spectrum (right) corresponding to 615 nm emission from GaOOH nanorods prepared in presence of (a and d) 0.5 at % Eu^{3+} , (b and e) 0.75 at % Eu^{3+} , (c and f) 2 at % Eu^{3+} .
- Fig.28: (a) Emission spectrum obtained by exciting the samples at 280 nm and (b) excitation spectrum for the emission at 575 nm from GaOOH nanorods prepared in presence of 1 at % Dy^{3+} ions.
- Fig.29: Decay curves corresponding to (a) $^5\text{D}_0$ level of Eu^{3+} ions (b) $^5\text{D}_4$ level of Tb^{3+} ions from GaOOH samples prepared with different amounts of Eu^{3+} , Tb^{3+} ions, respectively. ($\lambda_{\text{exc}} = 270, 255 \text{ nm}$ and $\lambda_{\text{em}} = 615, 545 \text{ nm}$ for Eu^{3+} and Tb^{3+} doped GaOOH, respectively)
- Fig.30: TG-DTA patterns of GaOOH nanorods prepared in presence of (a) 0 at % (b) 0.5 at % (c) 0.75 at % and (d) 1 at % Eu^{3+} ions.
- Fig.31: XRD patterns of as prepared, 500 and 900°C heated GaOOH nanorods
- Fig.32: SEM images of GaOOH nanorods heated at (a) 500°C and (b) 900°C
- Fig.33: XRD patterns of GaOOH samples containing 0, 0.5, 0.75, 1 and 2 at% of Eu^{3+} ions after heat treatment at 500°C .
- Fig.34: FT-IR spectra of GaOOH samples containing 0, 0.5, 0.75, 1, 2, 3 and 5 at % of

Eu³⁺ ions after heat treatment at 500°C.

Fig.35: XRD patterns of β -Ga₂O₃ doped with 0, 0.75, 1, 3 and 5 at % of Eu³⁺ (peak marked * correspond to Eu₂O₃). Values in brackets show average crystallite size

Fig.36: TEM images of (a) 0, (b) 0.75, (c) 3 and (d) 5 at % Eu doped β - Ga₂O₃

Fig.37: (a) Emission spectra, (b) decay curve corresponding to ⁵D₄ level of Tb³⁺ in Tb³⁺ doped GaOOH, α -Ga₂O₃ and β -Ga₂O₃ nanomaterials. ($\lambda_{exc} = 255$ nm and $\lambda_{em} = 544$ nm).

Fig.38: (a) Emission spectra of β -Ga₂O₃ nanomaterials doped with 0, 0.5, 1 and 2 at % Tb³⁺ ions. The corresponding excitation spectra for 1 at % Tb³⁺ doped sample, monitored at 460 and 544 nm emission, are shown in Fig. 38 (b).

Fig. 39: Decay curves corresponding to excited state of the host emission of β -Ga₂O₃ nanomaterials doped with 0, 0.5, 1 and 2 at % Tb³⁺ ions.

Fig.40: Emission spectrum (a) obtained after 260 nm excitation and excitation spectrum (b) corresponding to 575 nm emission from β -Ga₂O₃:Dy³⁺ nanomaterials. Corresponding emission ($\lambda_{exc} = 280$ nm) and excitation ($\lambda_{em} = 613$ nm) spectrum from Ga₂O₃:Eu nanorods are shown in Fig.40 (c and d).

Fig.41: (a) Emission spectrum and (b) excitation spectrum from Ga₂O₃:Er³⁺ nanorods. The excitation and emission wavelengths are 380 and 1535 nm, respectively.

Fig. 42: XRD pattern of (a) Sb₂O₃ sample prepared at room temperature in isopropanol medium. Corresponding patterns from the samples heated at 100, 200 and 400°C along with bulk Sb₂O₃ are shown in (b)–(e), respectively.

Fig.43: (a and b) AFM images showing the nanorods of Sb₂O₃ at two representative regions of the sample. TEM and SAED images for the nanorods along with that of bulk sample are shown in (c)–(f), respectively

Fig. 44: Emission spectra of (a) Sb₂O₃ nanorods and (b) bulk Sb₂O₃ as a function of

temperature. Room temperature emission spectra of as prepared Sb_2O_3 nanorods annealed at different temperatures are shown in (c). Excitation wavelength was 220 nm. Peaks marked * are artifacts.

Fig. 45: Raman spectrum of (a) as prepared Sb_2O_3 nanorods. The changes related to morphology/annealing are shown by arrows at $\sim 260\text{ cm}^{-1}$ and $\sim 445\text{ cm}^{-1}$. Enlarged view of the Raman spectrum corresponding to Sb–O–Sb stretching (b, d) and bending (c) modes of Sb_2O_3 nanorods annealed at various temperatures along with that of bulk sample are also shown. Fig.45 (b) shows peaks ‘A1’ and ‘A2’ for the 260 cm^{-1} peak and Fig.45 (c) shows ‘B1’, ‘B2’ and ‘B3’ for the 445 cm^{-1} peak. Encircled region in Fig.45 (d) shows the changes in the Sb–O–Sb stretching vibrations at various annealing temperatures.

Fig.46: XRD patterns of Sb_2O_3 nanorods prepared in presence of (a) 0 at % Eu^{3+} and (b) 5 at % Eu^{3+} .

Fig.47: Emission spectrum from Sb_2O_3 nanorods prepared in presence of 5 at % Eu^{3+} and obtained after (a) 220 nm excitation and (b) 395 nm excitation. The corresponding pattern from bulk Sb_2O_3 prepared in presence of 5 at % Eu^{3+} obtained after 395 nm excitation is shown in Fig.47 (c). The inset of Fig.47 (b) shows the excitation spectrum monitored at 615 nm emission.

Fig.48: Emission spectrum obtained after excitation at 395 nm from europium hydroxide sample prepared by the same procedure as adopted for antimony oxide nanorods. The excitation spectrum corresponding to 615 nm emission is shown in the inset.

Fig.49: Decay curves corresponding to $^5\text{D}_0$ level of Eu^{3+} in (a) Sb_2O_3 nanorods prepared in presence of Eu^{3+} (b) Europium hydroxide sample prepared by the identical procedure as adopted for Sb_2O_3 nanorods and (c) bulk Sb_2O_3 prepared in presence of Eu^{3+} . Samples were excited at 395 nm and emission monitored at

615 nm

- Fig.50: FT-IR patterns (a) and Raman Spectra (b) of Sb_2O_3 nanorods prepared in presence of different Eu^{3+} concentrations
- Fig.51: FT-IR patterns for the region corresponding to the OH stretching vibrations from (a) Sb_2O_3 nanorods (b) Sb_2O_3 nanorods with 10 at % Eu^{3+} .
- Fig.52: XRD patterns for the product obtained by the reaction between Sb^{3+} and Eu^{3+} ions taken in stoichiometric amounts and heated at different temperatures: (a) as prepared (b) 500°C and (c) 900°C .
- Fig.53: Emission spectra (a) and decay curves corresponding to the $^5\text{D}_0$ level of Eu^{3+} (b) for the product obtained by the reaction between Sb^{3+} and Eu^{3+} ions taken in the stoichiometric ratio. Samples were excited at 395 nm and emission monitored at 612nm.
- Fig.54: XRD patterns for (a) hexagonal GaPO_4 standard corresponding to JCPDS file no. 080497 (b) GaPO_4 nanoparticles, (c and d) GaPO_4 nanoparticles with 2.5 and 5 at % Eu^{3+} , respectively.
- Fig.55: TEM images of (a) GaPO_4 nanoparticles. The selected area electron diffraction pattern from nanoparticles is shown in Fig.55 (b).
- Fig.56: Emission spectrum from GaPO_4 nanoparticles containing (a) 2.5 at % and (b) 5 at % Eu^{3+} ions. The corresponding pattern from EuPO_4 nanoparticles is shown in Fig.56 (c). All samples were excited at 260 nm.
- Fig.57: Emission spectrum of europium hydroxide sample prepared in glycerol medium by the identical method as that employed for GaPO_4 and EuPO_4 nanoparticles, except that urea rather than ammonium dihydrogen phosphate was used to create the alkaline environment and to prevent the formation of EuPO_4 phase.
- Fig. 58: ^{31}P MAS NMR patterns of GaPO_4 nanoparticles containing (a) 0 at % (b) 2.5 at

% (c) 5 at % and (d) 10 at % Eu^{3+} ions. Samples were spun at 10000Hz.

Fig.59: Schematic diagram of Eu^{3+} species present on the surface of the GaPO_4 nanoparticles.

Fig.60: FT-IR spectrum of GaPO_4 nanoparticles containing 0 % and 2.5 at % Eu^{3+}

Fig.61: XRD Patterns of $\text{SbPO}_4:\text{Tb}^{3+}$ nanomaterials synthesized from (a) 20 ml glycerol, (b) 10 ml ethylene glycol and 10 ml glycerol, (c) 12 ml ethylene glycol and 8 ml glycerol and (d) 20 ml ethylene glycol.

Fig.62: FT-IR Spectra of $\text{SbPO}_4:\text{Tb}^{3+}$ samples obtained in (a) ethylene glycol medium, (b) glycerol medium and (c) mixture of ethylene glycol and glycerol medium (10 ml each).

Fig.63: TEM images of (a) $\text{SbPO}_4:\text{Tb}^{3+}$ nanoribbons and (b) $\text{SbPO}_4:\text{Tb}^{3+}$ nanoparticles. The selected area electron diffraction pattern from the sample and the high resolution TEM image of a nanoribbon are shown in Fig.63 (c and d) respectively.

Fig.64: Emission spectrum of (a) $\text{SbPO}_4:\text{Eu}^{3+}$, (b) $\text{SbPO}_4:\text{Tb}^{3+}$ nanoparticles/nanoribbons obtained after 220 nm excitation. Insets show corresponding excitation spectrum monitored at 616 and 545 nm emission.

Fig.65: Emission spectrum of EuPO_4 sample obtained after 250 nm excitation.

Fig.66: Emission spectrum of (a) $\text{SbPO}_4:\text{Eu}^{3+}$ and (b) $\text{SbPO}_4:\text{Tb}^{3+}$ bulk materials prepared by solid state reaction (excitation wavelength was 220 nm). Insets show corresponding excitation spectrum monitored at 616 and 545 nm emission.

Fig.67: Emission spectra of SbPO_4 nanoparticles/ nanoribbons doped with 1, 2, 2.5, 5, 10, 20 and 25 at % Tb^{3+} ions. Samples were excited at 250 nm.

Fig.68: TEM images of (a) $\text{SbPO}_4:\text{Ce}^{3+}(2.5\%),\text{Tb}^{3+}(5\%)$ nanoribbons in silica and (b) $\text{SbPO}_4:\text{Ce}^{3+}(2.5\%),\text{Tb}^{3+}(5\%)$ nanoparticles in silica. A representative selected

area electron diffraction pattern and a high resolution TEM image the nanoribbon are shown in Fig. 68 (c and d) respectively.

Fig.69: Raman spectrum over the entire region (a) corresponding to un-doped SbPO_4 , $\text{SbPO}_4:\text{Ce}^{3+}(2.5\%),\text{Tb}^{3+}(5\%)$ and $\text{SbPO}_4:\text{Ce}^{3+}(2.5\%),\text{Tb}^{3+}(5\%)$ samples dispersed in silica. The peak corresponding to the asymmetric stretching vibrations of PO_4 tetrahedra in these samples observed over the region of $1000\text{-}1080\text{ cm}^{-1}$ is shown in Fig.69 (b).

Fig.70: FT-IR pattern corresponding to SbPO_4 nanoribbons/nanoparticles containing different concentrations of Tb^{3+} ions. The peak corresponding to the Sb-O stretching vibration in these samples observed over the region of $600\text{-}700\text{ cm}^{-1}$ is shown in Fig.70 (b).

Fig.71: Raman spectrum corresponding to symmetric PO_4 stretching mode of (a) un-doped SbPO_4 (b) $\text{SbPO}_4:\text{Ce}^{3+}(2.5\%),\text{Tb}^{3+}(5\%)$ and (c) $\text{SbPO}_4:\text{Ce}^{3+}(2.5\%),\text{Tb}^{3+}(5\%)$ samples dispersed in silica.

Fig.72: Emission spectrum from nanoribbons/ nanoparticle of (a) $\text{SbPO}_4:\text{Tb}^{3+}(5\%)$, (b) $\text{SbPO}_4:\text{Ce}^{3+}(2.5\%),\text{Tb}^{3+}(5\%)$, and (c) $\text{SbPO}_4:\text{Ce}^{3+}(2.5\%),\text{Tb}^{3+}(5\%)$ dispersed in silica. Samples were excited at 250 nm. Inset at the left side shows the emission spectrum of TbPO_4 samples prepared by the identical method as that adopted for other samples and the inset at the right side shows the Ce^{3+} emission from $\text{SbPO}_4:\text{Ce}^{3+}(2.5\%),\text{Tb}^{3+}(5\%)$ sample obtained after 278 nm excitation. The peak marked “*” in the left inset is an artifact.

Fig.73: Decay curves corresponding to the $^5\text{D}_4$ level of Tb^{3+} ions from nanoribbons/nanoparticles of (a) $\text{SbPO}_4:\text{Tb}^{3+}(5\%)$, (b) $\text{SbPO}_4:\text{Ce}^{3+}(2.5\%),\text{Tb}^{3+}(5\%)$, and (c) $\text{SbPO}_4:\text{Ce}^{3+}(2.5\%),\text{Tb}^{3+}(5\%)$ dispersed in silica. The samples were excited at 250 nm and emission monitored at 544 nm.

- Fig.74: Schematic representation showing the effect of incorporating the nanoparticles in silica matrix.
- Fig.75: Excitation spectrum corresponding to the $^5D_4 \rightarrow ^7F_5$ transition of Tb^{3+} ions (544 nm) from nanoribbons/ nanoparticles of (a) $SbPO_4:Tb^{3+}(5\%)$, (b) $SbPO_4:Ce^{3+}(2.5\%), Tb^{3+}(5\%)$, and (c) $SbPO_4:Ce^{3+}(2.5\%), Tb^{3+}(5\%)$ dispersed in silica.
- Fig.76: XRD patterns of 2.5 at % Eu^{3+} doped $BiPO_4$ samples prepared at room temperature, 100, 125 and 185°C.
- Fig.77: TG-DTA pattern of $BiPO_4$ sample prepared at room temperature.
- Fig.78: FT-IR spectra of $BiPO_4$ samples prepared at room temperature, 100, 125 and 185°C
- Fig.79: TEM images of $BiPO_4$ samples prepared at (a) room temperature, (b) 100, (c) 125 and (d) 185°C. Inset shows the SEAD patterns of corresponding samples.
- Fig.80: (a) Emission spectra of $BiPO_4$ samples prepared at room temperature, 75 and 185°C after excitation at 270 nm and (b) corresponding excitation spectra monitored at 615 nm emission.
- Fig.81: XRD patterns of $Bi_{1-x}La_xPO_4$ ($x = 0, 0.3, 0.5, 0.7, 1$) nanomaterials prepared at 185°C
- Fig.82: FT-IR patterns of $Bi_{1-x}La_xPO_4$ ($x = 0, 0.3, 0.5, 0.7, 1$) nanomaterials prepared at 185°C showing the regions (a) $480 - 680\text{ cm}^{-1}$ and (b) $750 - 1300\text{ cm}^{-1}$.
- Fig.83: ^{31}P MAS-NMR patterns of $Bi_{1-x}La_xPO_4$ ($x = 0, 0.3, 0.5, 0.7, 1$) nanomaterials prepared at 185°C.
- Fig.84: XRD patterns of $Bi_{1-x}Tb_xPO_4$ ($x = 0, 0.1, 0.25, 0.5, 1$) nanomaterials prepared at 185°C
- Fig.85: (a) Emission spectra obtained after excitation at 275 nm, (b) decay curves corresponding to 5D_0 level of Eu^{3+} from $BiPO_4:Eu^{3+}$ nanoparticles containing

different amounts of Eu^{3+} .

- Fig.86: (a) Emission spectra obtained after excitation at 255 nm, (b) decay curves corresponding to $^5\text{D}_4$ level of Tb^{3+} ion from $\text{BiPO}_4:\text{Tb}^{3+}$ nanorods prepared at 185°C
- Fig.87: (a) Emission spectra from $\text{BiPO}_4:\text{Tb}^{3+}$ (5 at%) and $\text{BiPO}_4:\text{Eu}^{3+}$ (5 at%), Tb^{3+} (5 at%) nanomaterials after excitation at 255 nm. The corresponding excitation spectrum is shown in Fig.87 (b) Decay curve corresponding to $^5\text{D}_4$ level of Tb^{3+} from these samples are shown in Fig.87 (c).
- Fig.88: (a) Emission spectrum obtained after excitation at 350 nm (b) excitation spectra monitored at 573 nm emission (c) decay curve corresponding to $^4\text{F}_{9/2}$ level of Dy^{3+} ion in $\text{BiPO}_4:\text{Dy}^{3+}$ nanorods.
- Fig.89: (a) Emission spectrum obtained after 402 nm excitation, (b) excitation spectra monitored at 597 nm emission and (c) decay curve corresponds to $^4\text{G}_{5/2}$ level of Sm^{3+} in $\text{BiPO}_4:\text{Sm}^{3+}$ nanorods.
- Fig.90: XRD patterns of ZnGa_2O_4 nanoparticles prepared in solvents containing different values of EG- H_2O ratios.
- Fig.91: FT-IR spectra of ZnGa_2O_4 nanoparticles prepared in solvents containing different amounts of EG and water.
- Fig.92: (a) Emission spectra of ZnGa_2O_4 nanoparticles prepared in solvents containing different ratios of EG and H_2O . Corresponding excitation spectra are shown in Fig.92 (b).
- Fig.93: Schematic representation of possible energy transitions in ZnGa_2O_4 nanoparticles.
- Fig.94: XRD patterns of ZnGa_2O_4 nanoparticles prepared with different concentration of Ga^{3+} ions.

- Fig.95: FT-IR spectra of ZnGa₂O₄ nanoparticles prepared with different amounts of starting material.
- Fig.96: TEM images (a, d), HREM images (b, e), SAED patterns (c, f) of ZnGa₂O₄ nanoparticles prepared with 1.44 and 22.96 mmol Ga, respectively.
- Fig.97: (a) Emission spectra of ZnGa₂O₄ nanoparticles prepared by using different concentrations Ga³⁺ after exciting the samples in the range of 250-290 nm and (b) corresponding excitation spectra.
- Fig.98: XRD patterns of ZnGa_{2-x}In_xO₄ (x = 0, 0.05, 0.1, 0.2, 0.3, 0.5) nanoparticles.
- Fig.99: (a) TEM image, (b) HRTEM image of ZnGa_{1.5}In_{0.5}O₄ nanoparticles. SAED pattern from these nanoparticles is shown in the inset of Fig.99 (a)
- Fig.100: (a) Emission spectra of ZnGa_{2-x}In_xO₄ (x = 0, 0.05, 0.2, 0.5) nanoparticles after exciting samples in the UV region (260 to 280 nm). (b) Decay profile corresponding to blue emission from ZnGa_{1.5}In_{0.5}O₄ nanoparticles
- Fig.101: Photograph of blue light emission from thin film of PMMA containing ZnGa_{1.5}In_{0.5}O₄ nanoparticles, on a quartz substrate. The excitation wavelength was 270 nm.
- Fig.102: XRD patterns of undoped ZnGa₂O₄ and 5 at % Ce³⁺ doped ZnGa₂O₄ nanoparticles
- Fig.103: (a) Emission and excitation spectra of 5 at % Ce³⁺ doped ZnGa₂O₄ nanoparticle and (b) excited state decay profile of Ce³⁺ (λ_{exc} =265 nm, λ_{em} =350 nm)
- Fig.104: (a) Emission spectra obtained after 280 nm excitation and (b) excitation spectra obtained after monitoring 615 nm and 460 nm emission along with (c) the decay curve corresponding to ⁵D₀ level of Eu³⁺ in ZnGa_{1.5}In_{0.5}O₄ nanoparticles
- Fig.105: (a) Emission spectrum and (b) ⁵D₄ decay profile of Tb³⁺, from Tb³⁺ doped ZnGa_{1.5}In_{0.5}O₄ nanoparticles. The excitation and emission wavelengths are 280

and 545 nm, respectively.

Fig.106: XRD patterns of MWO_4 ($M = Ca, Sr, Ba$) nanoparticles.

Fig.107: TEM image of (a and b) $CaWO_4$, (c) $SrWO_4$ and (d) $BaWO_4$ nanomaterials and inset of the images shows corresponding SAED pattern.

Fig.108: (a) Emission spectra and (b) excitation spectra from $CaWO_4: Eu^{3+}$, $SrWO_4: Eu^{3+}$, $BaWO_4: Eu^{3+}$ nanoparticles. ($\lambda_{exc} = 270$ nm and $\lambda_{em} = 615$ nm)

Fig.109: Emission spectrum (a) and photograph of emission (b) obtained from $CaWO_4:Eu$ nanoparticles after excitation at 253 nm. The corresponding excitation spectrum and decay curve, both monitored at 425 nm emission, is shown in Fig.109 (c) and (d) respectively.

Fig.110: XRD patterns of as prepared, 300, 500, 700 and 900°C heated $CaWO_4$ nanoparticles.

Fig.111: Emission spectra (a) and excited state decay curves (b) of $CaWO_4$ nanoparticles as a function of heat treatment (particle size). ($\lambda_{exc} = 253$ nm and $\lambda_{em} = 425$ nm)

Fig.112: Emission spectra (a) and photograph of emission (b) obtained after excitation at 253 nm from $CaWO_3:Tb^{3+}$ nanoparticles. The corresponding excitation spectrum and decay curve monitored at 545 nm emission is shown in Fig.112 (c and d) respectively.

Fig.113: Emission spectrum (a) and photograph of emission (b) obtained after excitation at 253 nm from $CaWO_4:Dy^{3+}$ nanoparticles. Corresponding excitation spectrum and decay curve monitored at 574 nm emission is shown in Fig.113 (c and d).

Fig.114: Emission spectrum (a) and photograph of emission (b) obtained after excitation at 253 nm from $CaWO_4:Sm^{3+}$ nanoparticles. Corresponding excitation spectrum and decay curve monitored at 602 nm emission is shown in Fig.114 (c and d).

Fig.115: CIE diagram. A, B, C, D and E in the diagram represent the color coordinates of that phosphor.

Fig.116: (a) Emission spectrum and (b) excitation spectrum of Er^{3+} doped CaWO_4 nanoparticles.

Fig.117: Schematic representation of an optical amplifier.

Fig.118: Schematic diagram of an electro-luminescent device.

List of Tables:

- Table 1: Variation in the lattice parameters of GaOOH samples prepared in presence of different amounts of Eu^{3+} ions
- Table 2: Summary of important modes of vibrations in GaOOH nanorods containing different amounts of Eu^{3+} ions along with that of $\text{Ga}(\text{OH})_3$.
- Table 3: Variation in the lattice parameters of $\beta\text{-Ga}_2\text{O}_3$ samples prepared in presence of different amounts of Eu^{3+} ions
- Table 4: Lifetime values corresponding to $^5\text{D}_4$ level of Tb^{3+} from GaOOH: Tb^{3+} heated at different temperatures.
- Table 5: Excited state lifetime values of host emission after doping with different amounts of Tb^{3+} ions.
- Table 6: The anisotropy parameter ($\Delta\delta$) obtained from the components of the chemical shift tensor (δ_{11} , δ_{22} and δ_{33}) which are calculated from the side band intensities observed from the ^{31}P MAS NMR patterns of GaPO_4 sample containing different amounts of Eu^{3+} ions. The line width of the peak (Γ) is also given in the table. Error in the chemical shift values is ± 1 ppm.
- Table 7: Effect of variation volume of solvents on the average crystallite size of SbPO_4 nanomaterials. Errors in the average crystallite size are ± 3 nm and obtained from duplicate measurements.
- Table 8: The lifetime values corresponding to the $^5\text{D}_4$ level of Tb^{3+} ions in $\text{SbPO}_4:\text{Ce}^{3+}$, Tb^{3+} nanoribbons/ nanoparticles along with the χ^2 values obtained from fitting. The numbers in brackets give the relative concentration of each lifetime components. Error in the lifetime values are within 5% as revealed by the duplicate measurements

- Table 9: Lifetime values corresponding to 5D_0 level of Eu^{3+} in BiPO_4 nanorods doped with different amounts of Eu^{3+} ions.
- Table 10: Lifetime values of 5D_4 level of Tb^{3+} from BiPO_4 nanorods doped with different amounts of Tb^{3+} ion.
- Table 11: Lifetime values of excited states of Tb^{3+} and Eu^{3+} ions in presence and in absence of other ion in BiPO_4 nanorods.
- Table 12: Calculated crystallite size of ZnGa_2O_4 nanoparticles as a function of the EG- H_2O ratio.
- Table 13: Calculated crystallite size of ZnGa_2O_4 nanoparticles as a function of increasing the reactants concentration.
- Table 14: Average crystal size of CaWO_4 nanoparticles as a function of heat treatment temperatures
- Table 15: Excited state lifetime values of CaWO_4 nanoparticles as a function of heat treatment temperature and particle size.

CHAPTER 1: Introduction

1.1 Historical Background of Nanomaterials: Nanomaterials are the materials with structural features in between those of atoms/ molecules and bulk materials, with at least one dimension in the range of 1 to 100 nm ($1 \text{ nm} = 10^{-9} \text{ m}$) and are known to mankind for a long time starting from the Roman period. In earlier days, nanomaterials of metals (also known as the colloidal metal particles) were used to dye glass articles and fabrics. For example the age old popular dye, “The Purple of Cassius”, is formed on reacting stannic acid with chloroauric acid, and made up of tin oxide and Au nanocrystals [1]. The Romans were adept at impregnating glass with metal particles to achieve dramatic colour effects. The Lycurgus cup, a glass cup of 4th century AD, appears green in reflected light and red in transmitted light (Fig.1). This effect is due to the presence of Au and Ag nanocrystals in the walls of the cup. Maya blue, a blue dye used by the Mayas around 7th century AD is found to consist of silica, metal and oxide nanocrystals [2]. Systematic studies on nanoparticles began to appear as early as seventeenth century. In 1612, Antonio Neri, a Florentine glassmaker and priest of Italy, described the synthesis of colloidal gold in his treatise *L’Arte Vetraria*.

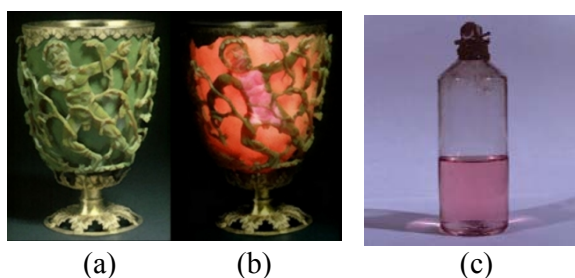


Fig.1. The Lycurgus cup appears (a) green in reflected light, (b) red in transmitted light and this cup is preserved in the British museum in London, (c) Colloidal dispersion of gold preserved in the Royal Institution, London [3, 4].

John Knuckel of Germany discovered that addition of small gold particles in glass leads to appearance of red colour. Michael Faraday in 1857 [5] carried out groundbreaking work on colloidal metals. He called them as divided metals and observed that colloidal metal

sols were thermodynamically unstable and they must be stabilized kinetically against aggregation. He observed that gold nanoparticles of different colours could be stabilised in solvents. Some of the nanoparticles dispersed in solvents are still preserved in the Royal Institution, London [Fig. 1(c)].

Ostwald also carried out extensive work on colloidal particles. His observations, results and conclusions were published in a book entitled “The world of neglected dimensions” in 1915. During this time, many methods were also discovered to make colloidal particles of metals like gold. For example, Bredig [6] prepared gold sols by striking an arc between Au electrodes immersed in dilute alkali. Donau [7] suggested that passing CO through a solution of chloroauric acid can provide colloidal gold particles. Zsigmondy [8] discovered that formaldehyde can be used to make gold sols from the corresponding salts under mild alkaline conditions. Zsigmondy has been awarded Nobel Prize in 1925, partly for his work on colloidal gold particles. The renewed interest in nanomaterials research started after the well known lecture by the Nobel laureate Richard. P. Feynman in 1959 at the California Institute of Technology where he stated, “there is a plenty of room at the bottom” [9] and indicated the vast potential of materials having small dimensions. In subsequent years, number of technological applications were envisaged/ demonstrated for nanomaterials leading to development of an area referred as “nanoscience and nanotechnology” [10]. Nanotechnology has become a very active area of research encompassing almost all disciplines of science and engineering. In the following section, a brief description is given regarding the different types of nanomaterials commonly encountered.

1.2 Classification of nanomaterials: Nanomaterials can be classified based on dimensionality namely 0D, 1D, 2D and 3D (Fig.2). Highly symmetric isotropic spheres, cubes, decahedra and tetrahedra can be classified as zero-dimensional (0D) nanostructures and are the most familiar shapes encountered in the field of nanoscience and nanotechnology.

Rods, cylinders, wires and tubes are examples of one-dimensional (1D) nanostructures. One-dimensional nanostructures of semiconductors and metal oxides exhibit unique optical properties due to anisotropic shape [11]. Discs, ribbons and plates with polygon shapes belong to two-dimensional (2D) nanostructures, [12].

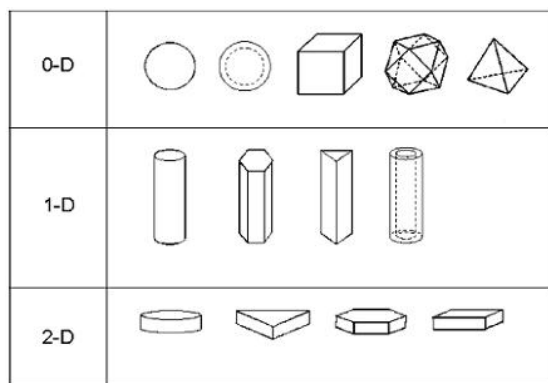


Fig.2. Nanomaterials having different dimensions [12].

To explain the formation of nanomaterials with different shapes and dimensions, one requires prior understanding of the mechanism involved in their formation. However, for generalisation, there are no kinetic and mechanistic studies available regarding the formation pathways of compositionally and geometrically well defined nanocrystals. Recent studies revealed that factors like the reaction temperature and duration of reaction, surfactants/ ligands used for capping and precursor concentrations play a major role in deciding the shape and dimensions.

1.3 Synthesis of nanomaterials: During the past two decades, synthesis of nanostructured materials by tailoring the atomic and/ or chemical structures on a nanometer scale has become one of the most rapidly growing areas of material science. Synthesis of a desired shaped material with the right length scale is as important as understanding its structure and composition. Chemistry has played a pivotal role in developing synthetic strategies to prepare controlled size and shaped materials required for different applications.

There are two approaches generally followed for the synthesis of nanoparticles. They are namely the top-down and bottom-up approaches. In top-down approach (physical methods), synthesis is accomplished by size reduction of bulk material by different physical techniques, whereas in the bottom-up approach (chemical methods), synthesis is carried out from atoms or molecules which are added one by one to form bigger particles of desired size. Lithography, ball milling, laser ablation, etc. belong to top-down approach, whereas sol-gel synthesis, co-precipitation method, micro-emulsion method, hydro-/ solvo-thermal method, etc. fall into bottom-up approach. In the present study, bottom-up approach is used for the synthesis of nanomaterials of different sizes and shapes. Commonly used methods based on the bottom up approach are briefly described below.

1.3.1 Co-precipitation method: Co-precipitation method involves simultaneous precipitation of more than one type of ions from a solution. This synthetic strategy has following advantages.

- Low temperature synthesis,
- High homogeneity of particles,
- Composition can be tuned very easily,
- Does not require expensive equipment,
- Dispersability of the particles can be tuned

All the co-precipitation techniques involve two steps, namely the nucleation and growth. Nucleation involves the formation of nuclei, which is defined as the smallest solid phase formed by combination/ aggregation of minimum number of atoms/ ions/ molecules. The nuclei are susceptible for spontaneous growth to bigger particles. Thermodynamic processes involved in the nucleation and growth are briefly discussed below.

In a particular solvent, there is a certain solubility limit for a solute, whereby addition of any excess solute will cause precipitation. Thus, for nucleation to take place, the solution

must be supersaturated either by directly dissolving the solute at higher temperature and then cooling to low temperature or by adding the required amounts of reactants to the solution during the reaction. Once the solution reaches a critical supersaturation of the particle forming species, nucleation occurs. The overall free energy change ΔG for the nucleation process is the sum of the free energy due to the formation of a new volume and the free energy due to the new surface created (Fig.3) [13].

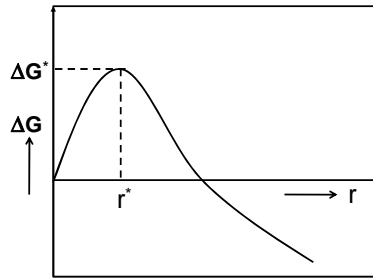


Fig.3. Schematic representation of variation of free-energy change as a function of nuclei radius during nucleation and growth [13].

For spherical particles, free energy change involved in nucleation can be expressed by equation 1 [13]

$$\Delta G = -\frac{4}{V} \pi r^3 k_B T \ln(S) + 4\pi r^2 \gamma \dots\dots\dots (1)$$

Where V is the molecular volume of precipitated species, r is the radius of the nuclei, k_B is the Boltzmann constant, S is the saturation ratio and γ is the surface free energy per unit surface area. Saturation ratio S is defined as C/C_0 , where C and C_0 are solute concentration at saturation and equilibrium respectively.

When saturation ratio $S > 1$, ΔG has a positive maximum at a critical size, r^* . This maximum free energy corresponds to the minimum activation energy required for the formation of nuclei with critical radius r^* . Nuclei larger than the critical size will further decrease their free energy by growth to form particles and nuclei smaller than critical size

will get dissolved in the reaction medium. The critical nuclear size, r^* , can be obtained from equation (1) by applying the condition, $\frac{d(\Delta G)}{dr} = 0$, and is given by equation 2.

$$r^* = \frac{2V\gamma}{3k_B T \ln(S)} \dots\dots\dots (2)$$

When concentration of species comes down to the critical supersaturation level, nucleation comes to an end. Continuous diffusion of solutes onto the existing nuclei leads to growth of particle until the concentration of the solute is just lowered below the solubility level [14].

Particles grow by diffusion of monomer towards the surface followed by its reaction on the surface. The particle growth will be controlled either by diffusion of the monomer if the diffusion coefficient is much smaller than the rate of reaction or by monomer reaction on the surface of the particle if the diffusion coefficient is much higher than the rate of the reaction. The smaller particles (particles with size just above the critical size) grow more rapidly than the larger ones because the driving force for minimum free energy is higher for smaller particles than that of the bigger particles. Nearly mono-disperse size distribution can be obtained at this stage either by stopping the reaction (nucleation and growth) quickly or by supplying reactant source to keep a saturated condition during the reaction period. When the reactants are depleted, Ostwald ripening occurs, where the larger particles continue to grow at the expense of smaller ones. Because the saturation ratio (S) decreases and corresponding critical nuclei size (r^*) increases (from equation 2), the particles smaller than this new critical size will dissolve in the reaction medium/ solvent. Stopping the reaction at this stage, leads to the formation of particles with a broad size distribution.

Nanoparticles are thermodynamically unstable because of large surface free energy. To get stable nanoparticles, they have to be stabilized kinetically during the reaction by adding stabilizing agents such as organic/ inorganic ligands or capping agents. Nanocrystals dispersed in liquids are either charge-stabilized or sterically stabilized [15]. In the case of

charge stabilized nanoparticles, an electric double layer is formed on the surface of the particle. This double layer acts as stabiliser due to electrostatic repulsion between layers of different particles. In the case of sterically stabilized nanoparticles, capping agent is adsorbed on the surface of the particles either by forming chemical bonds or by weak interactions. These capping agents act as stabilisers due to repulsion between their tail groups. Both types of stabilisation are schematically shown in Fig.4.

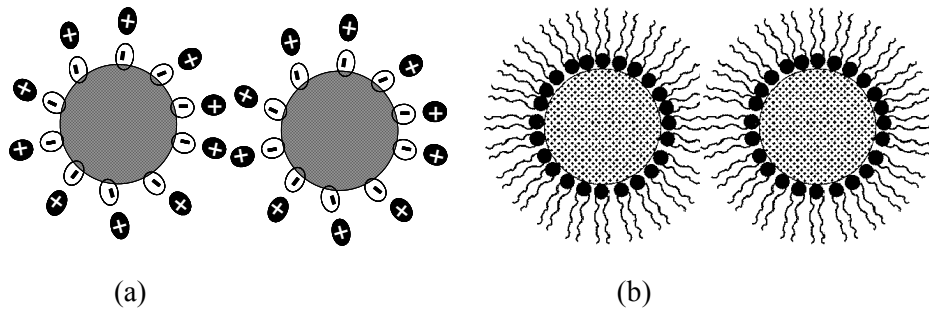
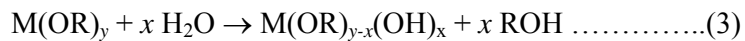


Fig.4. Schematic representation of nanoparticles stabilization by (a) electrostatic repulsion (b) steric repulsion/ interaction [15].

1.3.2 Sol-gel Method: Sol-gel technique is one of the most popular solution processing methods for producing metal oxide nanoparticles. In sol-gel processing, a reactive metal precursor, such as metal alkoxide is hydrolyzed by water, and the hydrolyzed species are allowed to condense with each other to form precipitates of metal hydroxide/ oxide nanoparticles. The precipitate is subsequently washed and dried and then calcined at an elevated temperature to form crystalline metal oxide nanoparticles [16]. Hydrolysis of metal alkoxides involves nucleophilic reaction with water (equation 3).



Condensation occurs when either hydrolyzed species react with each other and release a water molecule, or a hydrolyzed species reacts with an unhydrolyzed species and releases an alcohol molecule. The rates at which hydrolysis and condensation reactions take place are important parameters that affect the properties of the final product. For example, slower and

more controlled hydrolysis typically leads to smaller particles and base-catalyzed hydrolysis/condensation reactions leads to denser particles. The size of the sol particles depends on the solution composition, pH, and temperature. The advantage of this method is that the uniform size distribution can be easily obtained. The major disadvantage is that many metal alkoxides are highly reactive and susceptible to hydrolysis thus causing problem of their handling.

1.3.3 Hydro-/ solvo-thermal method: The solvo-thermal method provides a means of using solvents at temperatures well above their boiling points, by carrying out the reaction in a sealed vessel. The pressure generated in the vessel due to solvent vapours elevates the boiling point of the solvent. Typically, solvothermal methods make use of solvents such as ethanol, toluene, water, etc. During the synthesis of nanocrystals, parameters such as water pressure, temperature, reaction time, precursors, etc. can be modified to maintain a high nucleation rate leading to the formation particles with uniform size distribution [16]. The main advantage of this method is that high quality nano/ micro crystal can be obtained and main disadvantages are the high temperature, high pressure developed during the reaction and lack of flexibility for controlling the nucleation and growth processes.

1.3.4 Combustion method: Combustion synthesis is an important powder processing technique generally used to produce complex oxide ceramics. The method is generally employed to prepare oxide materials, although the preparation of metal chalcogenides has also been reported in the literature. The process involves the exothermic reaction between an oxidizer such as metal nitrates and organic fuel, like urea (H_2NCONH_2), carbonylhydrazide ($\text{CO}(\text{NHNH}_2)_2$), or glycine ($\text{C}_2\text{H}_5\text{NO}_2$) [17]. The combustion reaction is initiated in a muffle furnace or on a hot plate at temperatures of the order of 500°C or less. In a typical reaction, the precursor (mixture of water, metal nitrates and fuel) on heating decomposes, dehydrates and ruptures into a flame. The resultant product is a voluminous, foamy powder, which occupies the entire volume of the reaction vessel. The chemical energy released from the

exothermic reaction between the metal nitrates and fuel can rapidly heat the system to high temperatures without an external heat source. Nanomaterials synthesized by combustion route are generally homogeneous, contain fewer impurities, and have higher surface areas than powders prepared by conventional solid-state methods. The parameters that influence the reaction are the nature of fuel, fuel to oxidizer ratio, ignition temperature and water content of the precursor mixture. The major advantage of this method is that large-scale production can be made at relatively low temperatures and disadvantage is that the particles obtained are highly agglomerated and can not be dispersed in solvents.

1.4 Properties of nanomaterials: A number of physical phenomena become noticeably pronounced as the size of the material decreases. The electronic properties of solids are significantly altered with reduction in particle size. This effect becomes dominant when the nanometer size range is reached. Additionally, a number of physical (mechanical, electrical, optical, etc.) properties change when compared to macroscopic systems. In the following section, electronic and optical properties of materials with nanosize dimensions are discussed.

1.4.1 Electronic properties: In atoms or molecules, the electronic energy levels are discrete and the electronic wave functions of many such atoms/ molecules overlap and give band structure in bulk materials. As the particle size decreases the energy level corresponding to the charge carriers increases. Further, the energy gap between valance band and conduction band also increases when bands become discrete energy levels with decrease in the crystal/ particle size. Reduction in particles size not only causes an increase of the energy gap (blue shift of the absorption edge) but also changes the density of states (DOS). Density of states is defined as the number of energy states available in a unit energy interval in unit volume to be occupied. Electronic and optical properties observed for the bulk materials and their corresponding low dimensional system can be explained based on their differences in the density of states.

1.4.2 Optical properties: Existence of vast differences in the optical properties like optical absorption, emission, scattering, etc. of bulk and corresponding nanomaterials, prompted detailed investigation on the optical properties of nanomaterials during the last few years. As materials are generally classified as metals, semiconductors and insulators, materials in nanosize dimensions can also be classified similarly. It is expected that their optical properties will also be quite different compared to bulk materials.

Metal nanoparticles are characterised by a phenomenon known as surface plasmon resonance. In this process, absorption of light due to coherent oscillations of conduction band electrons created by the periodically varying electric field of incident light takes place. This phenomenon is observed when the size of the nanoparticle is much smaller than the wavelength of the incident light. Surface plasmon frequency of metal particles depends on its size, shape and dielectric constant. It also depends on the dielectric constant of the surrounding medium [18]. The surface plasmon resonance absorption by noble metal nanoparticles, like Ag and Au, is observed in the visible region. As the size of the nanoparticle decreases there is a blue shift in the wavelength maximum (λ_{\max}) corresponding to surface plasmon absorption.

Semiconductors and insulators are characterised by a gap between their energy levels corresponding to valence and conduction bands. The band gap energy for insulators is much higher as compared to semiconductors. Many optical properties of semiconductors can be explained based on the concept of exciton formation and recombination. Electrons at the bottom of the conduction band or a level just below it can have columbic interaction with positive charged holes in the valence band leading to the formation of an electron-hole pair, which is electrically neutral and are known as excitons. Radiative recombination of exciton is known as excitonic emission or band edge emission. Excitons can be considered as hydrogen atom and their radius (Bohr radius) can be expressed by equation 4. Where ϵ is dielectric

constant, \hbar is $h/2\pi$, e is the electron charge, m_e and m_h are effective mass of electron and hole, respectively.

$$a = \frac{\epsilon \hbar^2}{e^2} \left[\frac{1}{m_e} + \frac{1}{m_h} \right] \dots\dots\dots(4)$$

When the particle size is smaller than the Bohr radius, quantum confinement plays an important role in the optical properties of semiconductors. Their absorption spectra show a consistent blue shift as the size of the particle decreases. In some cases, up to 10 discrete optical transitions between different discrete energy levels of the QDs have been observed in the absorption spectrum.

In insulators, luminescence can arise through different mechanisms. The localised centres provided by defects and dopants offer a major contribution to the luminescence in this type of materials. The dopants are also known as activators and they can create states within the forbidden zone of the band gap of a material and in the valance and conduction bands [19]. Generally, two types of activator ions can be distinguished. In the first case, energy levels of the activator ion involved in the emission process show only weak interactions with the host lattice. Typical examples are lanthanide ions (Ln^{3+}), where the optical transitions take place solely within 4f levels which are well shielded from chemical environment by outer electrons. Therefore, characteristic line like emission spectra can be observed from such materials. The second type of activator ions strongly interact with the host lattice. This is the case when d electrons or ion with s^2 configurations are involved. Examples include Mn^{2+} , Eu^{2+} , Ce^{3+} , Pb^{2+} , Sb^{3+} , etc. Similar situation is also observed for ions like WO_4^{2-} , MoO_4^{2-} , NbO_4^{3-} , VO_4^{3-} , etc. The strong coupling of the electronic states of emitting ion with vibrational modes of the lattice leads to broad bands in the emission and absorption/excitation spectra.

Organic compounds are one of the important classes of luminescent materials and their luminescence is essentially based on localized π -electron systems within individual organic molecules. Emission from such materials can be classified into two categories namely luminescence from electronically excited singlet (S_1) state to the ground state and the other from the triplet (T_1) excited state to the ground state. Emission from singlet-excited states is called as fluorescence, whereas the emission from triplet-excited states is known as phosphorescence. Naphthalene, anthracene, pyrene, perylene, *p*-terphenyl, and *p*-quarterphenyl are commonly encountered organic light emitting compounds. Pyrene based derivatives are commercially used as blue emitting materials [20].

In addition to the organic compounds, metal complexes with organic ligands are important class of fluorescent compounds. Some of these compounds exhibit rather broad fluorescence spectra similar to those of organic ligands. One such compound is tris(8-hydroxyquinolino)aluminium(III) (Alq_3), which has been used in organic thin-film electroluminescent devices. Complexes of heavy metal ion such as Ir, Pt, Ru and Au with ligands such as 2-(imidazol-2-yl)pyridine, metalated 2-phenyl pyridine, 1,3-dipyridylbenzene and 2,6-diphenylpyridine, etc. are shown to have intense phosphorescence due to transition between the triplet state of the complex (brought about by metal to ligand charge transfer (MLCT)) and its ground state. Since MLCT process involves the mixing of singlet and triplet excited states, radiative decays are allowed between triplet excited state and singlet ground state, leading to intense phosphorescence. In particular, Ir complexes have been extensively investigated in recent years for developing bright luminescent materials. For example metalated 2-phenyl pyridine complex of iridium, $[Ir(NC_5H_4-C_6H_4)_3]$ show nearly 100% phosphorescence efficiency [21]. Platinum complexes with ligands like 2,3,7,8,12,13,17,18-octaethyl-21H,23H-porphine (OEP), 2,6-diphenylpyridine has also been used as potential candidates for organic light emitting display devices. Photo- and electro-luminescence from

these platinum complexes have been reported [22, 23]. Europium and terbium complexes with ligands like 2-thenoyltrifluoroacetone (tta), bis(ferrocenyl-ethynyl)-1,10-phenanthroline (Fc_2phen), 6,6,7,7,8,8,8-heptafluoro-2,2-dimethyloctane-3,5-dione (fod) are well known narrow band luminescent materials. In these materials, ligands act as sensitizers and absorb light energy which is transferred to the metal ion. The latter, on de-excitation gives a narrow band emission. Ligands based on β -diketones are well known sensitizers which can transfer energy to lanthanide ions in β -diketone-lanthanide complexes. Several such complexes and their luminescence properties have been reviewed recently [24-28]. More than 80% quantum yield has been reported for some of these complexes after incorporation in polymers [29, 30]. A few representative examples of luminescent metal complexes are given in Fig.5 [31].

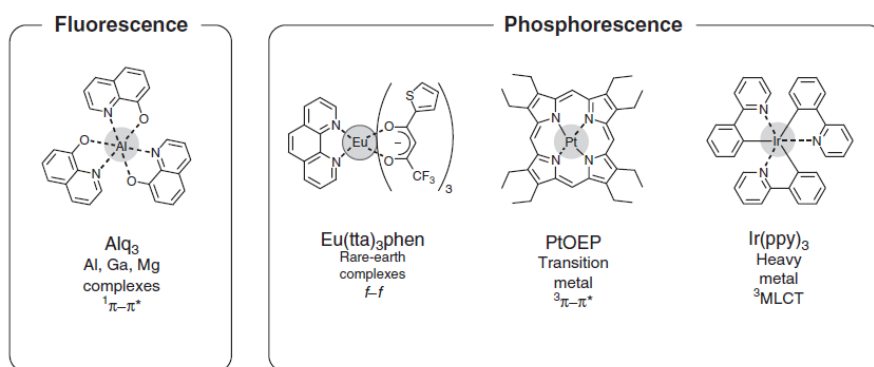


Fig.5.Examples of metal complexes [$\text{Alq}_3(^1\pi-\pi^*)$, $\text{Eu}(\text{tta})_3\text{phen}(f-f)$, $\text{PtOEP}(^3\pi-\pi^*)$, $\text{Ir}(\text{ppy})_3(^3\text{MLCT})$] which shows intense photoluminescence [31].

1.5 Lanthanides and their Luminescence: Lanthanides are silvery-white, relatively soft, reactive metals. It took more than 160 years until all of them were discovered, starting from 1787 when C.A. Arrhenius found a black stone near Ytterby (Sweden) from which several lanthanides could be isolated [32]. It became apparent that the dominant oxidation state of the lanthanides is +3 and the electronic configuration of a trivalent lanthanide ion can be represented as $[\text{Xe}]4f^n$ [33]. Their popularity in modern technology is due to their exceptional luminescence and magnetic properties. The 4f electrons are shielded by the 5s and 5p outer

orbitals with filled electronic configuration. As a result, the 4f electrons are only weakly affected by the ions surrounding lanthanide ions (ligands) in the crystal. Because of this, all trivalent lanthanide ions, except cerium, show atomic-like sharp absorption and emission spectra.

1.5.1 Lanthanide Energy levels: The perturbation of the 4f levels of lanthanide ions caused by the crystal field is rather weak as compared to the Coulomb interaction between the electrons and spin-orbit coupling [34]. The Coulomb interaction between the electrons within the 4f shell has the largest contribution to the energy level splitting and this leads to separated energy levels with energy difference of the order of 10^4 cm^{-1} . Each of these levels split further into several levels by the spin-orbit interaction with an energy difference of the order of 10^3 cm^{-1} . All these levels form the 4f configuration of the free lanthanide ions and each level can be characterized with the symbol $^{2S+1}\mathbf{L}_J$, where \mathbf{S} is the total spin, \mathbf{L} the total orbital angular momentum, and \mathbf{J} the total angular momentum of the 4f electrons. When the Ln^{3+} ions are put into a host material, the crystal field not only affects the strength of the intra-configurational f-f transitions but also brings about an additional splitting of the 4f states that depends on the site symmetry of the lanthanide ions [34]. Although the 4f electrons are well shielded, when lanthanide ion occupies a site with certain symmetry, the crystal field effects can lead to splitting of levels which may range up to several tenths of electron volts [35]. A schematic diagram of 4f energy level splitting is given in the Fig.6. Unlike the 4f levels of lanthanide ions, their 5d energy levels (like 5d levels of Ce, Tb, etc.) are largely perturbed by the crystal field. The magnitude of the splitting of the 5d levels depends strongly on the shape and size of the anion polyhedron coordinating the lanthanide ion [36]. The dependence of shape of the coordinating polyhedron on the crystal field splitting can be explained qualitatively within the point charge electrostatic model. The first energy level diagram displaying the 4f levels of the trivalent free Ln^{3+} ions in aqueous medium in the infra-red

(IR), visible and ultra-violet (UV) region of the spectrum was presented by Dieke and Crosswhite in 1963 (Fig.7) [37, 38]. Most of the emitting levels are separated from the next lower level by an energy value of $\sim 2 \times 10^3 \text{ cm}^{-1}$ or more.

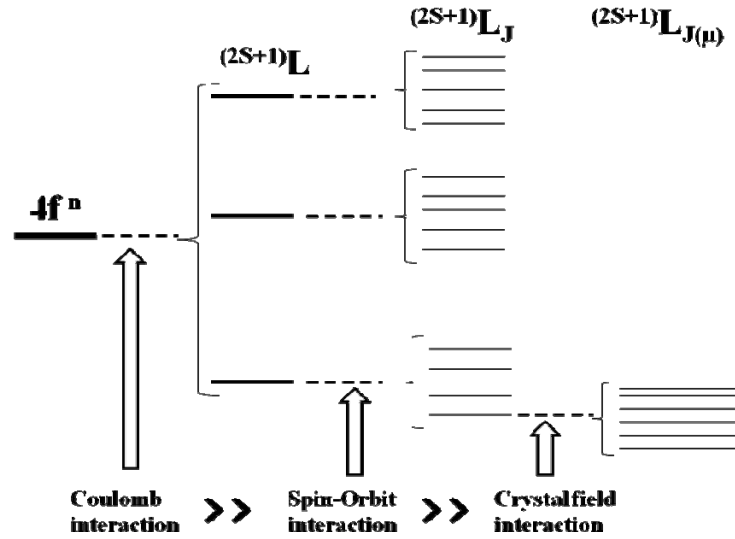


Fig.6. Splitting of $4f^n$ electronic energy levels due to coulomb repulsions, spin-orbit coupling and crystal field effect.

The excited states of lanthanide ions relax via two competitive pathways namely by light emission and phonon emission processes. The rate of phonon emission, ω , depends on the number of phonons emitted simultaneously to bridge the energy gap and is expressed by equation 5.

$$\omega \propto \exp\left(-\frac{k\Delta E}{h\nu_{\max}}\right) \dots\dots\dots (5)$$

Where, ΔE is the energy gap to the nearest lower level and $h\nu_{\max}$ is the maximum energy of phonons coupled to the emitting states. The phonon emission rate, ω , decreases rapidly with an increase in ΔE , so that the competitive light emission or radiative process becomes dominant [39]. Thus, the well-known high luminescence efficiencies for 5D_0 of Eu^{3+} and 5D_4 of Tb^{3+} are based on the large energy gap of more than 10^4 cm^{-1} that needs to be bridged to

the next lower level of these ions. The above formula implies that large values of $h\nu_{\max}$ also quench light emission. This is demonstrated by the fact that luminescence of Eu^{3+} in aqueous solution is almost quenched, but begins to appear if H_2O is replaced by D_2O [40].

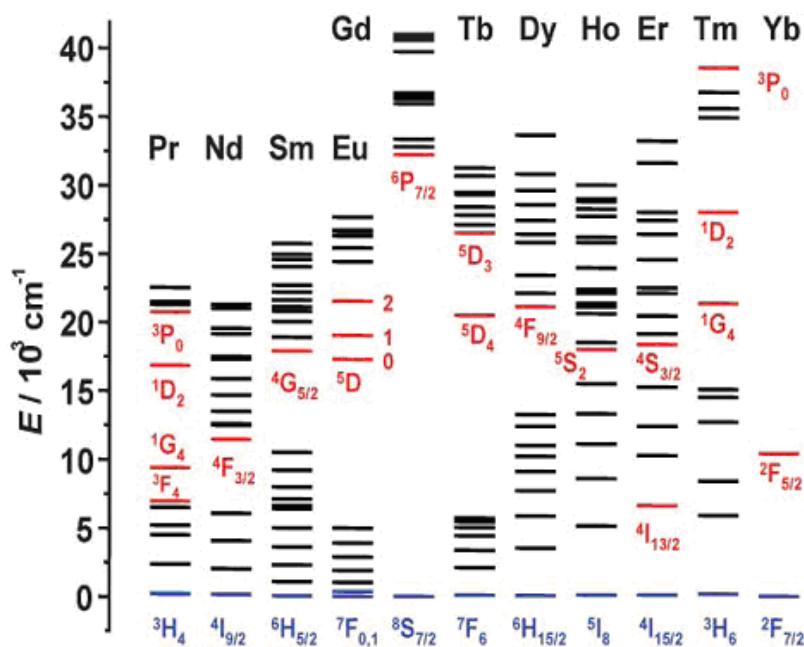


Fig.7. Energy levels diagram for the lanthanide aquo ions. The main luminescent levels are drawn in red, while the ground state level is indicated in blue [38].

In the energy region spanned by 4f levels, two additional electronic states (transitions) with different characteristics from those of intra 4f levels are also observed for lanthanide ions. They are the transition between $4f^{n-1} \rightarrow 5d^1$ states and the charge transfer transitions (CT). In the former, one of the 4f electrons is transferred to a 5d orbital while in the latter case, electrons in the neighboring anions are transferred to a 4f orbital. Both these processes are allowed and result in strong optical absorptions. Unlike intra 4f transitions, transition energies involved in the $4f^{n-1} \rightarrow 5d^1$ and CT transitions are strongly dependent on their environments. The transition energies corresponding to $4f \rightarrow 5d$ and CT transitions for different lanthanide ions are shown in Fig.8 [31]. These energies are obtained based on the absorption spectra of trivalent lanthanide oxides. As shown in the figure, $4f \rightarrow 5d$ transitions

in Ce^{3+} , Pr^{3+} , Tb^{3+} and CT absorptions in Eu^{3+} and Yb^{3+} have energies less than $ca. 40 \times 10^3 \text{ cm}^{-1}$. Therefore, they can interact with 4f levels leading to emissions corresponding to intra 4f transitions. In case, the energy levels of these states are lower than those of 4f levels, direct luminescence transitions from these levels are found, such as $5d \rightarrow 4f$ transitions in Ce^{3+} , Pr^{3+} and Eu^{2+} . Luminescence due to charge transfer transitions has also been reported for Yb^{3+} [41].

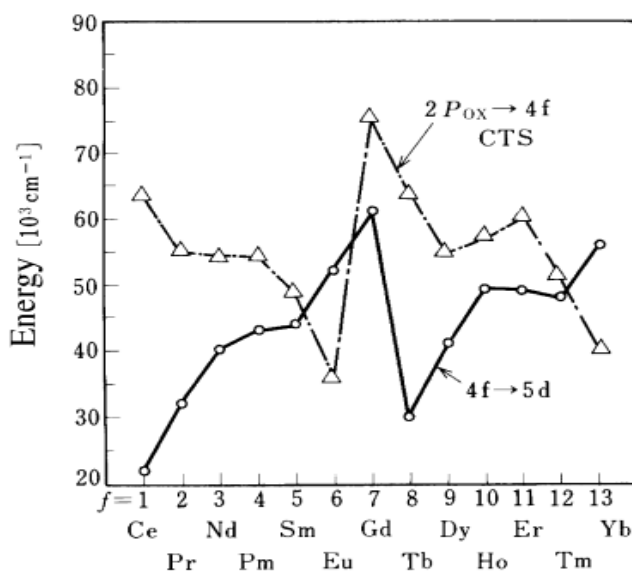


Fig.8. Energies for $4f \rightarrow 5d$ and CT transitions of trivalent lanthanide ions [31].

It can be concluded from the above discussion that those ions that are easily oxidized to the tetravalent state have lower $4f \rightarrow 5d$ transition energies, while those that are easily reduced to the divalent state have lower CT transition energies. So far the absorption or excitation characteristic of Ln^{3+} ions is discussed. In the following section, factors affecting the emission/ luminescence properties of lanthanide ions are discussed.

1.5.2 Selection rules: Luminescence originating from electronic transitions between 4f levels is predominantly due to electric dipole or magnetic dipole interactions. Electric dipole f-f transitions in free 4f ions are parity-forbidden, but become partially allowed by mixing with orbitals having different parity. Typical examples of this mechanism are demonstrated by the

luminescence from the 5D_J states of Eu^{3+} . The intensity of these transitions depends strongly on the site symmetry in a host crystal. Magnetic dipole allowed f-f transitions are not affected much by the site symmetry. The J selection rule in this case is $\Delta J = 0, \pm 1$ (except for $0 \rightarrow 0$). For electric dipole transition, the difference in the J values (ΔJ) is ± 2 . Oscillator strengths are of the order of 10^{-5} to 10^{-8} for electric dipole transitions, and 10^{-8} for magnetic dipole transitions [31].

1.5.3 Luminescence quenching: Luminescence can be quenched due to the non-radiative decay of the excited state. This non-radiative decay is brought about by different mechanisms involving energy transfer from the excited state of the donor to different types of acceptors like host lattice, organic molecules on the surface, defect levels or nearby ions which may or may not act as activator. In the following section different types of non-radiative path ways of the excited state is given.

Multiphonon emission: As discussed in the previous section (equation 5) it is clear that the extent of quenching due to phonons depends on the energy gap between the emitting states and value of phonon energy. General observation is that if the energy difference is more than 5 times the phonon energy, then luminescence is the main de-excitation process than the multi-phonon quenching [42]. This also explains the quenching of lanthanide ions excited state by organic molecules containing functional groups with high phonon energy. Hence, efforts for the development of new efficient luminescent materials based on Ln^{3+} ions are directed towards the search for low effective phonon energy host materials. The general order of phonon energy of hosts are fluorides < sulfides < oxides < phosphates.

Energy transfer: An excited state can also relax to the ground state by non-radiative energy transfer to a second nearby state/ center. For energy transfer to take place the energy levels of the donor and acceptor should match. However, when there is a mismatch between the energy levels/ transitions of the donor and acceptor ions, the energy transfer process needs to be

assisted by lattice phonons of appropriate energy, $\hbar\Omega$, and this is usually known as phonon-assisted energy transfer process. The interaction Hamiltonian for the energy transfer process involves different types of interactions; namely, multipolar (electric and/ or magnetic) interactions and/ or quantum mechanical exchange interaction. The dominant interaction is strongly dependent on the separation between the donor and acceptor ions and on the nature of their wave functions. Exchange interactions only occur if the donor and acceptor ions are close enough for direct overlap of their electronic wave functions. Consequently, energy transfer due to quantum mechanical exchange interactions between the D and A ions is only important at very short distances (nearest neighbor positions). Irrespective of the mechanism of energy transfer, the fluorescence lifetime of the donor center, τ_D , is affected as a result of any energy transfer process to an acceptor [42]. Therefore, the lifetime of the donor ions (τ_D) can be expressed by equation 6.

$$\frac{1}{\tau_D} = \frac{1}{(\tau_D)_0} + A_{nr} + P_t \dots\dots\dots (6)$$

where $(\tau_D)_0$ is the radiative lifetime of the donor ion, A_{nr} is the non-radiative rate due to multi-phonon relaxation, and P_t is the transfer rate due to energy transfer. Hence the observed lifetime of the donor is a measure of extent of energy transfer. In addition to this, variation of the emission intensity as a function of time can also give information regarding the distribution of donor and acceptor centres in the system.

Concentration Quenching: In principle, an increase in the concentration of a luminescent center in a given material should be accompanied by an increase in the emitted light intensity, this being due to the corresponding increase in the absorption efficiency. However, such behavior only occurs up to a certain critical concentration of the luminescent centres. Above this concentration, the luminescence intensity starts to decrease. This process is known as concentration quenching of luminescence. In general, the origin of luminescence

concentration quenching lies in very efficient energy transfer among the luminescent centers. Two mechanisms are generally invoked to explain the concentration quenching of luminescence.

(i) Due to very efficient energy transfer, the excitation energy can migrate about a large number of centers before being emitted. However, even for the purest crystals, always a certain concentration of defects or trace ions can act as acceptors, so that the excitation energy can finally be transferred to them. These centres can relax to their ground state by multiphonon emission or by infrared emission. Thus, they act as an energy sink within the transfer chain and so the luminescence becomes quenched, as illustrated in Fig.9 (a) [42]. These kinds of centers are called killers or quenching traps.

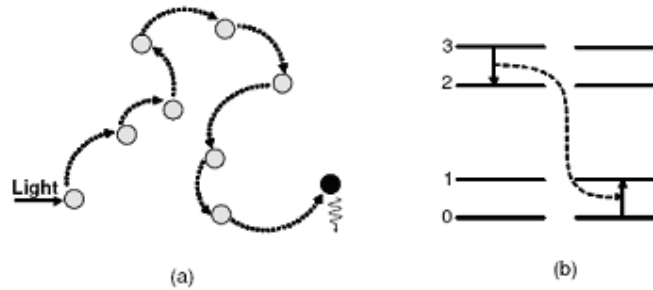


Fig.9. Schemes of possible mechanisms for luminescence concentration quenching: (a) energy migration among donors (circles) in a chain followed by its migration to a killer site (black circle) which acts as non-radiative sink; (b) cross relaxation between pairs of centers. (Sinusoidal arrows indicate nonradiative decay) [42].

(ii) Concentration quenching can also take place without actual migration of the excitation energy among the luminescent centers. This occurs when the excitation energy is lost from the emitting state via a cross relaxation mechanism. This kind of relaxation mechanism occurs by resonant energy transfer between two identical adjacent centers, brought about by the particular energy-level structure of these centers (Fig.9 (b)).

As the concentration quenching results from energy transfer processes, the decay time of the emitting ions is reduced along with the luminescence quantum yield. In general, this

decay-time reduction is much easier to measure than the reduction in the quantum efficiency. The critical concentration is that for which the lifetime starts to be reduced.

For employing lanthanide luminescence for various applications, two approaches, are followed. They are (i) in the form of lanthanide doped bulk inorganic materials and (ii) in the form of lanthanide complexes. In the former case, their luminescence efficiency is very high, they are chemically stable but their processability is very poor. In the latter case, their processability is very good but their luminescence efficiency and chemical stability is poor. If one dopes lanthanide ions in processable inorganic nanoparticles then they can have advantages of both inorganic bulk materials and complex compounds. Because lanthanide ions will be inside the robust inorganic particle which will give the good luminescence efficiency and the surface of the nanoparticles will be functionalised with ligand molecules which will give good processability. As a result, they can be dispersible in polar/ nonpolar solvents and they can be incorporated in inorganic polymers like silica, alumina or organic polymers like PMMA, PVA, etc. Reduced scattering and homogeneous composite formation capability with polymers make the nanoparticles as better candidates for luminescence applications.

1.6 Recent work on luminescent nanomaterials: The luminescent nanomaterials can be broadly classified into two categories. In the first category of nanomaterials luminescence is arising due to the inherent nature of the material or the type of structural units present in the material, whereas in the second category, luminescence is attributed to the dopant ion present in the non-luminescent host having nano size dimensions. Oxides like ZrO_2 , Ga_2O_3 , SnO_2 , ZnO , Sb_2O_3 , $ZnGa_2O_4$, $BaSnO_3$, etc. are examples of the first category of materials. Systems like $Y_2O_3:Ln$, $Y_3Al_5O_{12}:Ln$, $YPO_4:Ln$, $CePO_4:Ln$, $LaF_3:Ln$, $GdF_3:Ln$, etc. (where Ln stands for the lanthanide ion) are few examples of second category of materials. Some of the transition metal ions also act as luminescent centers in different inorganic hosts. In the

following section, luminescent properties of some of the above-mentioned materials are discussed.

A number of studies have been reported on the luminescence aspects of oxides like ZrO_2 , Ga_2O_3 , SnO_2 , ZnO , Sb_2O_3 , ZnGa_2O_4 , BaSnO_3 etc. ZrO_2 nanomaterials are known to have host emission in the visible region [43, 44] and emission maximum can be tuned by varying the particle size. Zhang, et al. [44] have prepared ZrO_2 nanoparticles having narrow size distribution by the controlled hydrolysis of zirconium butoxide, followed by annealing over the temperature range of 300-500°C. These authors have observed that by changing the annealing temperature the emission maximum from ZrO_2 nanoparticles can be tuned. Joy et al. also observed emission around 390 nm from nanocrystalline ZrO_2 films on UV excitation and they have attributed this to the defects present in ZrO_2 host [45]. Other investigations explained luminescence from ZrO_2 nanomaterials as a combined effect of the presence of impurities as well as defects in the lattice [46, 47].

Similar to ZrO_2 , β and γ forms of Ga_2O_3 nanomaterials are also known to give strong emission in the visible region upon UV excitation. β - Ga_2O_3 is an important wide band gap (band gap value is 4.9 eV) transparent semiconductor [48, 49] and is a potential candidate for optoelectronic applications [50, 51]. A number of reports are available on the luminescence properties of nanoparticles and thin films of β - Ga_2O_3 . [52-56]. Generally GaOOH is used as the precursor material for the preparation of different forms of Ga_2O_3 nanomaterials. Li, et al. [56] have prepared β - Ga_2O_3 nanorods from GaOOH nanorods and observed emission around 438 nm upon ultraviolet and low voltage electron beam excitations. The blue emission from these nanomaterials has been attributed to GaO_6 octahedra present in β - Ga_2O_3 lattice.

ZnO is a direct band gap semiconductor and has emission in both near UV and visible region. Many groups have investigated in detail the different types of luminescence centres present in ZnO nanomaterials [57, 58]. A representative emission spectrum from ZnO

nanocrystals is shown in Fig.10 [58]. The spectrum is characterised by mainly two peaks, one sharp peak around 382 nm and other broad peak around 500 nm. The sharp peak has been attributed to the band edge emission and the broad peak to the recombination of electrons trapped at the oxygen defect levels and holes in the valance band of ZnO. It is observed that the emission maximum is shifted in the visible regions depending on the synthesis conditions and annealing temperatures [57].

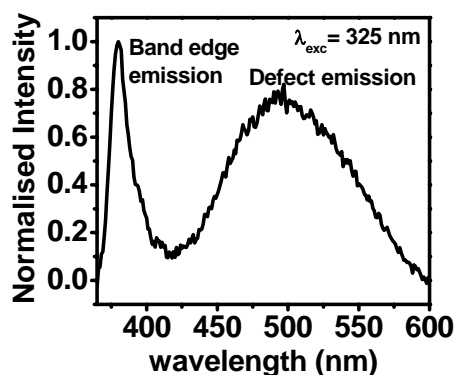


Fig.10. Representative emission spectrum from ZnO nanocrystals obtained after excitation at 325 nm [58].

BaSnO₃ belongs to the family of cubic perovskite structure and exhibit interesting optical and electrical properties. Mizoguchi, et al. [59] observed emission around 590 nm from BaSnO₃ powder samples at low temperatures with corresponding excited state lifetime of ~ 10μs. These authors have also observed emission in the near-infrared region from these samples. SnO₂ is a direct band gap n-type semiconductor ($E_g = 3.6$ eV). It is extensively used for making sensors and optical devices [60-62]. Many authors have reported synthesis of luminescent SnO₂ nanoparticles. For example, Gu, et al. [63] have reported the preparation of SnO₂ nanoparticles by sol-gel method using SnCl₄·5H₂O and NH₄OH followed by heating over the temperature range of 400 - 600°C. These particles showed luminescence around 400 nm characteristic of oxygen vacancies present in the nanoparticles and its intensity decreased on increasing heat treatment temperature.

Unlike SnO_2 , Sb_2O_3 is an indirect band gap semiconducting material with a band gap of ~ 3.3 eV. It exists mainly in two crystalline forms, namely, the cubic senarmonite form and the orthorhombic valentinite form. Deng, et al. [64, 65] have carried out luminescence studies on self-assembled structures of Sb_2O_3 nanorods and nanowires. They observed broad emission peak over the region of 390 to 500 nm, in addition to the band edge emission centered around 374 nm. Broad emission over the region of 390 to 500 nm has been attributed to the emission from oxygen vacancies related defect centers present in the lattice of Sb_2O_3 .

ZnGa_2O_4 is also a transparent semiconducting oxide having spinel structure. It is a potential candidate for Field emission and vacuum fluorescent display applications because of its high thermal stability. Bae, et al. [66] prepared vertically aligned ZnGa_2O_4 nanowires by chemical vapor deposition method and observed strong photoluminescence and cathodoluminescence in the blue wavelength region. Different types of soft chemical methods [67, 68] have been reported for the preparation of ultra fine particles of ZnGa_2O_4 , which show photoluminescence in the blue region. Their particle size and luminescence properties can be tuned by modifying the experimental conditions during its synthesis.

Lanthanide ions doped luminescent nanomaterials: Lanthanide ions doped in different inorganic hosts are extensively used in various display applications. Extensive literature is available regarding the luminescence properties of lanthanide doped inorganic nanoparticles. In the following section, brief description regarding the previous studies on representative lanthanide ions doped inorganic nanoparticles (for example $\text{Y}_2\text{O}_3:\text{Ln}$, $\text{Y}_3\text{Al}_5\text{O}_{12}:\text{Ln}$, $\text{YPO}_4:\text{Ln}$ and $\text{CePO}_4:\text{Ln}$) is given.

Y_2O_3 is widely used as a host for various lanthanide ions and such phosphor materials are used in various display devices [69]. Number of studies has been reported on the luminescent properties of $\text{Y}_2\text{O}_3:\text{Ln}^{3+}$ (Ln^{3+} = lanthanide ions) nanoparticles. Luminescence

depends strongly on the nature of the synthesis method and conditions employed [70-73]. For example, Sharma, et al. [73] synthesised $Y_2O_3:Eu$ nanoparticles having size in the range of micrometers to nanometers with the help of organic surface modifiers like Tween-80 and Emulsogen-OG. The authors observed a five fold enhancement in emission intensity from the nanoparticles when 10 wt. % of surface modifier was added during the synthesis of $Y_2O_3:Eu$ nanoparticles. Taner and Wang [74] investigated the luminescence properties of $Y_2O_3:Eu$ nanoparticles prepared by flame spray pyrolysis method and compared it with that of conventional pyrolysis method. The intensity of 5D_1 emission of Eu^{3+} ions from the C_{3i} site (S_6) in Y_2O_3 is significantly less compared to the emission from Eu^{3+} ions in the C_2 site for these samples. Igarashi, et al. [75] compared luminescence properties of bulk and nanoparticles of $Y_2O_3:Eu$ prepared using yttrium hydroxy carbonate precursor method and established that the increase in ionicity of Eu-O bond due to decrease in particles size is responsible for observed blue shift of excitation peak with decrease in particle size. Song and co-workers [76, 77] have observed that the radiative and non-radiative transition rates of Eu^{3+} ions in $Y_2O_3:Eu$ nanoparticles increased with decrease in particle size and this is attributed to the crystal lattice degeneration and surface effects. Further, ultraviolet (UV) light irradiation on $Y_2O_3:Eu$ nanoparticles has been found to reduce the intensity of Eu-O charge transfer peak [78,89]. Temperature and particle size effect on photoluminescence properties of $Y_2O_3:Tb$ nanoparticles have also been investigated by the same authors. Based on the studies it has been established that relative intensity of $^5D_4 \rightarrow ^7F_J$ transitions and oxygen defect emission ~ 620 nm characteristic of Y_2O_3 host are related to extent of thermal quenching process [80]. Tb^{3+} concentration dependence on photoluminescence intensity of $Y_2O_3:Tb$ nanoparticles is investigated by Park, et al. [81]. These authors have observed that for $Y_2O_3:Tb$ nanoparticles, prepared by solution route followed by annealing at $400^\circ C$ and containing 8 wt. % Tb^{3+} , gave optimum intensity for green emission. Mukherjee, et al. [82] have observed a variation

in the relative intensity of excitation transitions between 7F_6 ground state and low spin and high spin $4f^75d^1$ excited states of Tb^{3+} in $Y_2O_3:Eu, Tb$ nanoparticles annealed at 600 and 1200°C. This is explained due to the combined effect of distortion around Y^{3+}/Tb^{3+} in YO_6/TbO_6 polyhedra and size of the nanoparticles.

Yttrium aluminum garnet (YAG) doped with lanthanide ions is an efficient phosphor material and has got potential application as an active material in cathode ray tubes (CRTs), field emission and vacuum fluorescent displays (FEDs and VFDs) [83-85]. Ce^{3+} doped YAG is a yellow light emitting phosphor with absorption in the blue region [86]. Hence mixing YAG:Ce phosphor with blue light emitting materials such as GaN or ZnS:Ag, Cl [87, 88] can give rise to white light emitting materials. Yellow light emission from YAG:Ce phosphor arises due to $5d \rightarrow 4f$ transition of Ce^{3+} . This transition is very sensitive to the presence of other lanthanide ions in the host and conditions employed for their synthesis [89-92]. For example co-doping bulk YAG:Ce with Eu^{3+} and Mn^{2+} ions results in a significant decrease in luminescence intensity of $5d \rightarrow 4f$ transition of Ce^{3+} ions [90]. Energy transfer from the excited state of Ce^{3+} ions to Mn^{2+} or Eu^{3+} levels is the reason for observed decrease in intensity of Ce^{3+} emission from these samples. Unlike this, increase in concentration of Tb^{3+} ions in the bulk YAG:Ce host increases the luminescence intensity corresponding to $5d \rightarrow 4f$ transition of Ce^{3+} . This has been attributed to energy transfer from Tb^{3+} to Ce^{3+} levels in the sample [91]. There are also reports regarding the change in peak position corresponding to $5d \rightarrow 4f$ transition of Ce^{3+} brought about by Tb^{3+} co-doping in YAG:Ce phosphor. Jang, et al. [93] have observed that partial replacement of Ce^{3+} by Tb^{3+} in bulk YAG:Ce phosphor results in shifting of $5d \rightarrow 4f$ transition of Ce^{3+} to longer wavelengths. This has been attributed to the distortion of dodecahedral symmetry around Ce^{3+} ions brought about by Tb^{3+} substitution and subsequent lowering of 5d energy level due to the large crystal field splitting. This results in the lowering of energy gap between 5d and 4f levels, thereby leading to red shift of the

corresponding emission and excitation peaks [93]. Mukherjee, et al. [94] investigated the energy transfer between Ce^{3+} and ions like Tb^{3+} , Eu^{3+} and Dy^{3+} , when doped in nanoparticles of YAG host. It is observed that the energy transfer has been found to take place only from Tb^{3+} to Ce^{3+} ions, leading strong yellow emission along with emission characteristic of Tb^{3+} ions.

Lanthanide phosphates ($LnPO_4$) are robust materials for various technological applications involving lasers due to their high thermal and chemical stability, extremely low solubility in water and improved solubility for rare earth ions like Nd^{3+} [94-101]. YPO_4 based phosphors are used in plasma display panels due to their high ultra violet absorption cross-section and high vacuum ultraviolet radiation stability [102, 103]. Synthesis and luminescence properties of YPO_4 nanoparticles doped with lanthanide ions have been reported [104-107]. For example, He, et al.[105] observed that co-doping Bi^{3+} in $YPO_4:Dy$ nanoparticles leads to improvement in Dy^{3+} emission from the nanoparticles upon UV excitation This has been attributed to the improved UV light absorption properties of the nanomaterial brought about by Bi^{3+} doping. Srinivasu, et al. [106] observed a reduction in both Eu^{3+} and Dy^{3+} luminescence when Dy^{3+} ions are co-doped in $YPO_4:Eu$ nanoparticles followed by annealing them at high temperature (900°C). This has been attributed to the clustering effect of the lanthanide ions. The authors also observed that the nature and extent of strain associated with the YPO_4 lattice change with incorporation of Eu^{3+}/Dy^{3+} ion in the nanoparticles as well as the heat treatment temperature. Based on the detailed structural and luminescence studies, Luwang, et al. [107] inferred that the association of water molecules with the hexagonal phase of Bi^{3+} co-doped $YPO_4:Eu$, is the reason for the significant decrease in Eu^{3+} luminescence intensity when compared with $YPO_4:Eu$ nanomaterials. $CePO_4$ belongs to lanthanide phosphate category and exists mainly in two forms. One has the hexagonal structure with molecular formula $CePO_4 \cdot xH_2O$ ($x = 0.3-0.5$) (also known as

Rhabdophane) and the other is monoclinic CePO_4 [108, 109]. $\text{CePO}_4/\text{LaPO}_4$ nanorods as well as $\text{CePO}_4:\text{Tb}^{3+}-\text{LaPO}_4$ core-shell nanorods were synthesised and characterised by Cao, et al. [110] and Zhu, et al. [111] under hydrothermal condition in presence of surfactants and ultra-sonication respectively. Li and Yam [112] have prepared $\text{CePO}_4:\text{Tb}^{3+}$ nanowires in aqueous medium at room temperature by the reaction between $\text{Ce}^{3+}/\text{Tb}^{3+}$ ions and $\text{NH}_4\text{H}_2\text{PO}_4$ in presence of cyclodextrin. Kompe, et al.[113] employing co-precipitation in presence of coordinating ligands like tributyl phosphate (TBP) and trihexyl amine, prepared $\text{CePO}_4:\text{Tb}^{3+}$ core and $\text{CePO}_4:\text{Tb}^{3+}-\text{LaPO}_4$ core – shell nanoparticles in water free environments at 200°C . These studies revealed that luminescence property of $\text{CePO}_4:\text{Tb}^{3+}$ nanorods/ nanoparticles get significantly improved when covered by a shell of LaPO_4 . Improved dispersability of nanoparticles/ wires in alcohols and water is extremely important for making good quality silica sols and xero-gels incorporated with nanoparticles. Such sols and xero-gels, when immobilized with proteins and enzymes, combines the advantages of biological inertness, biodegradability and compatibility with bio-molecules at the same time, can also act as efficient luminescence based biosensors for monitoring the protein and enzyme activities in biological systems. Gulnar, et al. [114] have prepared crystalline CePO_4 , $\text{CePO}_4:\text{Tb}^{3+}$ and $\text{CePO}_4:\text{Dy}^{3+}$ nanoleaves with monoclinic structure. These nanomaterials are dispersible in solvents like water and methanol and can be incorporated in silica sols based on sol-gel method. Such nanoleaves incorporated silica sols have improved luminescence properties compared to silica sols directly doped with lanthanide ions.

1.7 Scope of present work: In the present investigation, a variety of inorganic matrices varying from oxides (Ga_2O_3 , Sb_2O_3), phosphates (SbPO_4 , BiPO_4 , GaPO_4), gallate (ZnGa_2O_4) to tungstates (CaWO_4 , SrWO_4 , BaWO_4) both undoped and doped with lanthanide ions have been synthesised and their luminescent properties are investigated. Even though number of reports are available on the luminescence properties of both undoped and lanthanide ions

doped nanomaterials of the above mentioned systems, very few studies have been reported on the variation of synthesis conditions and the nature of precursor on the luminescence properties of the above nanomaterials. For example, GaOOH is a precursor material for Ga₂O₃ nanomaterials. Understanding the morphology and luminescence properties of GaOOH prepared under different experimental conditions is essential for adapting the right synthesis procedure for making Ga₂O₃ nanomaterials with required optical properties. This aspect is not properly addressed in previous studies. Similarly, in the case of Sb₂O₃ nanomaterials, effect of morphology on its luminescence properties is not known so far. This aspect is investigated in detail in the present work. Luminescence properties of hosts like SbPO₄, BiPO₄ and GaPO₄ both undoped and doped with lanthanide ions are investigated for the first time with a view to develop new and robust phosphor materials having multi functional applications. Off late, considerable attention is paid to develop efficient blue light emitting nanomaterials for incorporating them in polymers and sol-gel films. Such polymers/sol-gel films are suitable candidates for the fabrication of economic and cheap white light display devices. Compounds like ZnGa₂O₄, CaWO₄, etc. have host emission in the visible region over the range of 400-550 nm. Hence, it is expected that suitable modification in the synthesis procedure as well doping them with lanthanide ions can give efficient luminescent materials which can have multi colour emission. With this in mind, the luminescence properties of these nanomaterials have been investigated during the course of the present investigation.

CHAPTER 2: Experimental

2.1. Materials and reagents: All the solvents, viz. iso-propanol, ethylene glycol, glycerol, methanol and acetone, were of AR grade and these were used as received without further purification. Starting materials, gallium metal (99.99%), Ga(NO₃)₃.xH₂O (99.999%), Zn(OOCCH₃)₂.2H₂O (99.9%), InCl₃ (99.999%), SbCl₃ (99.9%), Bi(NO₃)₃.5H₂O (99.9%), La(NO₃)₃.6H₂O (99.9%), Ca(NO₃)₂.H₂O (99.9%), SrCl₂.6H₂O (99.995%), Ba(NO₃)₂ (99%), Tb(NO₃)₃.xH₂O (99.99%), Tb₄O₇ (99.99%), Eu(NO₃)₃.5H₂O(99.99%), Eu₂O₃ (99.99%), Dy₂(CO₃)₃.xH₂O (99.9%), Dy(NO₃)₃.5H₂O (99.9%), Ce(NO₃)₃.6H₂O (99.9%), Sm(NO₃)₃.xH₂O (99.9%), Sm₂O₃ (99.99%), Dy(NO₃)₃.xH₂O (99.9%), and Er(OOCCH₃)₃.xH₂O (99.9%) were obtained from commercial sources. The reagents urea (99.5%), ammonium dihydrogen phosphate (99.9%) and Na₂WO₄.2H₂O (99.5%), were used as obtained for precipitation.

2.2. General synthesis of undoped and lanthanide doped nanomaterials: The nanomaterials were synthesized by co-precipitation method in different organic solvents. A typical synthesis procedure is given below.

Starting materials, chlorides or nitrates, were dissolved in solvents like ethylene glycol, glycerol, water or their mixture. Some solvents like ethylene glycol and glycerol can act both as a solvent as well as a stabilizing agent. These solvents were chosen as they are stable up to a temperature of 180°C and most of the inorganic metal salts (acetates, chlorides, nitrates, etc.) are soluble in them. Further, they are cheaply available, quite stable under ambient conditions and are non-toxic in nature. Precipitating agents depends on the type of the nanomaterial, which is being prepared. For preparing the metal oxide nanoparticles/nanomaterials, urea was used as a precipitating agent. It is superior over other bases like ammonia, NaOH, etc. as it decomposes at above 85°C and generates OH⁻ ions uniformly throughout the solution leading to homogeneous precipitation. Initially a hydroxide phase

will be formed and subsequently it is converted into oxide by increasing the reaction temperature or by heating the product in a furnace at high temperatures. For the synthesis of phosphate materials, ammonium dihydrogen phosphate was used as a precipitating agent. Ammonium dihydrogen phosphate on heating generates ammonia and phosphate ion, the former creates an alkaline environment, and the latter reacts with metal ions to form the phosphate phase. Alkaline environment facilitates precipitation of metal phosphate. For preparing metal tungstate nanomaterials, sodium tungstate was used as a precipitating agent.

Procedure: In a general, soluble metal salt was dissolved in an appropriate solvent and the solution was heated in a silicon oil bath under stirring upto-desired temperature. The precipitating agent was added to the reaction medium at high temperatures depending on the actual material to be synthesized. Temperature of the reaction medium was raised to a value close to reaction temperature so that the nanomaterial/ precursor for nanomaterials start precipitating. The solvent molecules also act as stabilising ligands to prevent aggregation of small particles. The precipitate was separated by centrifugation, washed with ethanol and acetone to remove unreacted species, and dried under ambient conditions. For the synthesis of doped nanoparticles, dopant metal ions were also added to starting chloride or nitrate solution of metal ions. Detailed procedures for the synthesis of individual compound are described below

2.3 Synthesis of binary oxide nanomaterials:

Preparation of GaOOH, α -Ga₂O₃ and β -Ga₂O₃ nanorods: Ga(NO₃)₃.xH₂O, Tb(NO₃)₃.xH₂O, Eu(NO₃)₃.5H₂O and Dy(NO₃)₃.5H₂O were used as starting materials for preparation of un doped GaOOH and lanthanide ions (Eu³⁺, Tb³⁺ and Dy³⁺) doped GaOOH nanorods. In a typical procedure for making GaOOH sample, Ga(NO₃)₃.xH₂O (1.0 g) was dissolved in 20 ml water in a 100 ml round bottom flask. The solution was slowly heated upto 70°C in a silicon oil bath while stirring followed by addition of urea (5.0 g). Temperature was

raised to 100°C and refluxed until a slightly turbid solution was obtained. At this temperature, sufficiently high concentration of OH⁻ is generated in the medium leading to high concentration of GaOOH nuclei, which facilitates growth of the nuclei into nanorod morphology. The temperature was maintained at this value for 2 hours. After the reaction, the precipitate was collected by centrifugation and was then washed two times with ethyl alcohol and three times with acetone followed by drying under ambient conditions. For Eu³⁺, Tb³⁺ and Dy³⁺ doped samples same procedure was used except that, Eu(NO₃)₃.5H₂O, Tb(NO₃)₃.xH₂O and Dy(NO₃)₃.5H₂O were used respectively along with Ga(NO₃)₃.xH₂O (1.0 g) and urea (5.0 g) as the starting materials. As prepared samples were heated in a furnace at 500 and 900°C for 10 hours to convert GaOOH and GaOOH:Ln³⁺ to α and β forms of Ga₂O₃ and Ga₂O₃:Ln³⁺.

Preparation of Sb₂O₃ nanorods with and without Eu³⁺ ions: For the synthesis of nanorods without Eu³⁺, SbCl₃ (0.5 g) was dissolved in conc. HCl and evaporated repeatedly by adding water drop wise while stirring. Repeated evaporation was done to remove excess HCl and drop wise addition of water was necessary for preventing the rapid hydrolysis of SbCl₃ leading to the formation of Sb(OH)₃ precipitate. Around 2 ml solution of SbCl₃ left over after the repeated evaporation was mixed with 20 ml of iso-propanol followed by the addition of 20% ammonium hydroxide solution drop wise while stirring until precipitation. This precipitate was centrifuged and washed several times with ethanol and acetone to remove free solvent and unreacted species. For samples containing different amounts of Eu³⁺ ions (2, 5 and 10 atom % Eu³⁺ with respect to Sb³⁺), same procedure was used except that Eu₂O₃ was dissolved in concentrated HCl and added to the acidic solution of SbCl₃ prior to the reaction. Bulk Sb₂O₃ sample with Eu³⁺ (5 atom % with respect to Sb³⁺) ions was obtained by hydrolysis of SbCl₃ and EuCl₃ in water at room temperature. For the purpose of comparison,

Eu^{3+} ions were also subjected to same reaction conditions as that used for the preparation of Sb_2O_3 nanorods and the resulting precipitate was, centrifuged, washed and dried.

2.4 Synthesis of phosphate nanomaterials:

Preparation of undoped GaPO_4 and Eu^{3+} ions containing GaPO_4 nanoparticles: For preparation of GaPO_4 and Eu^{3+} ions containing GaPO_4 nanoparticles, Ga metal and Eu_2O_3 were used as starting materials. For the synthesis of 5 at % Eu^{3+} (95 at % Ga^{3+} and 5 at % Eu^{3+}) containing GaPO_4 nanoparticles, gallium metal (0.21 g) and Eu_2O_3 (0.0265 g) (5 atom % Eu^{3+} with respect to Ga^{3+}) were dissolved in concentrated HCl in a beaker by heating and the excess acid was evaporated out repeatedly. To this solution, glycerol (20 ml) was added and transferred into a two-necked RB flask. The solution was slowly heated upto 70°C followed by addition of ammonium dihydrogen phosphate (0.35 g). Temperature was then raised to 130°C and maintained at this value for 2 hours. After the reaction, the precipitate was collected by centrifugation and then washed three times with ethyl alcohol and two times with acetone followed by drying under ambient conditions. A similar procedure was followed for the synthesis of undoped, 2.5 and 10 at % Eu^{3+} containing GaPO_4 nanoparticles.

Preparation of undoped and lanthanide doped SbPO_4 nanomaterials: For preparation of SbPO_4 and lanthanide ions (Tb^{3+} and Ce^{3+} - Tb^{3+}) doped SbPO_4 nanomaterials, SbCl_3 , Tb_4O_7 , Eu_2O_3 , $\text{Ce}(\text{NO}_3)_3 \cdot 6\text{H}_2\text{O}$ were used as starting materials. In a typical procedure for making $\text{SbPO}_4 \cdot \text{Tb}^{3+}$ (5%) sample (SbPO_4 sample doped with 5 at % Tb^{3+} ions), SbCl_3 (0.5 g) and Tb_4O_7 (0.01 g) (5 at %) were dissolved in concentrated HCl in a beaker and the excess acid was repeatedly evaporated. To this solution, ethylene glycol (12 ml) and glycerol (8 ml) were added and it was transferred into a two-necked 100 ml round bottom flask. The solution was slowly heated upto 70°C followed by addition of ammonium dihydrogen phosphate (0.75g). Temperature was raised to 90°C and maintained till slightly turbid solution was obtained. Finally, temperature was raised to 120°C and maintained at this value for 2 hours. After the

reaction, the precipitate was collected by centrifugation and then washed two times with acetone and three times with ethyl alcohol followed by drying under ambient conditions. Samples obtained by above method were dispersible in water and methanol. Same procedure was also employed for making SbPO_4 samples containing 1 and 2.5 at % Tb^{3+} ions (denoted as $\text{SbPO}_4:\text{Tb}^{3+}(1\%)$ and $\text{SbPO}_4:\text{Tb}^{3+}(2.5\%)$). For preparing Tb^{3+} , Ce^{3+} co-doped samples same procedure was used except that, 0.01 g of Tb_4O_7 (5 at %) and 0.012 g (2.5 at %) of $\text{Ce}(\text{NO}_3)_3 \cdot 6\text{H}_2\text{O}$ were used respectively along with 0.5 g of SbCl_3 (sample is denoted as $\text{SbPO}_4:\text{Ce}^{3+}(2.5 \text{ at } \%), \text{Tb}^{3+}(5 \text{ at } \%)$).

Preparation of $\text{SbPO}_4:\text{Ce}^{3+}(2.5 \text{ at } \%), \text{Tb}^{3+}(5 \text{ at } \%)$ nanomaterials dispersed in silica:

For the preparation of $\text{SbPO}_4:\text{Ce}^{3+}(2.5 \text{ at } \%), \text{Tb}^{3+}(5 \text{ at } \%)$ nanomaterials dispersed in silica (represented as $\text{SbPO}_4:\text{Ce}^{3+}(2.5 \text{ at } \%), \text{Tb}^{3+}(5 \text{ at } \%)-\text{SiO}_2$), SbCl_3 (0.5 g), Tb_4O_7 (0.01 g) and $\text{Ce}(\text{NO}_3)_3 \cdot 6\text{H}_2\text{O}$ (0.012 g) were dissolved in con. HCl and excess acid was evaporated by adding distilled water drop wise. To this solution, ethylene glycol (12 ml) and glycerol (8 ml) were added and it was transferred into a two-necked 100 ml RB flask. The solution was slowly heated upto 70°C while stirring followed by addition of ammonium dihydrogen phosphate (0.75 g). Temperature was raised to 120°C resulting in the formation of a turbid solution. After 10 min, 0.7 ml of tetraethyl orthosilicate (TEOS) was added to this. It was then refluxed for 2 hours at 120°C . The precipitate was centrifuged, washed with ethanol and acetone.

Synthesis of undoped and lanthanide doped BiPO_4 nanomaterials: For preparation of undoped BiPO_4 and lanthanide ions (Tb^{3+} , Eu^{3+} , Dy^{3+} , Sm^{3+}) doped BiPO_4 nanomaterials, $\text{Bi}(\text{NO}_3)_3 \cdot 5\text{H}_2\text{O}$, Tb_4O_7 , Eu_2O_3 , $\text{Dy}_2(\text{CO}_3)_3 \cdot x\text{H}_2\text{O}$, Sm_2O_3 were used as starting materials. For the synthesis of Eu^{3+} doped BiPO_4 , $\text{Bi}(\text{NO}_3)_3 \cdot 5\text{H}_2\text{O}$ (1.0 g) and Eu_2O_3 (0.011 g)(2.5 at %) were dissolved in concentrated HCl in a beaker and the excess acid was evaporated out repeatedly by adding water. To this solution, 20 ml of ethylene glycol was added and it was

transferred into a two-necked RB flask. An aqueous solution (3 ml) of ammonium dihydrogen phosphate (0.3 g) was added with stirring. The solution was heated at different temperatures viz. 75, 100, 125 and 185°C for two hours. The precipitate obtained was washed with methanol and acetone to remove unreacted species and dried under ambient conditions. The same procedure was followed for the synthesis of other lanthanide ions doped samples.

2.5 Synthesis of gallate nanomaterials:

Synthesis of undoped, In³⁺ and Ln³⁺ doped ZnGa₂O₄ nanoparticles: For the preparation of ZnGa₂O₄ nanoparticles gallium metal and Zinc acetate were used as starting materials. Gallium metal (0.2 g) was dissolved in concentrated HCl containing few drops of HNO₃ in a beaker and the excess acid was removed by repeated evaporation by adding water. This solution was transferred into a two-necked RB flask, containing appropriate amount of zinc acetate. Ethylene glycol (25 ml) and distilled water (10 ml) were added to this mixture. The solution was slowly heated up to 100°C followed by the addition of urea (3.0 g). It was heated at 120°C whereupon turbidity appeared. Temperature of the reaction was maintained for 2 hours to complete the reaction. The precipitate was collected by centrifugation and then washed three times with ethyl alcohol and two times with acetone followed by drying under ambient conditions. This process was repeated for different ratios of solvent to precursor concentration as well as ethylene glycol to water. For In³⁺, Eu³⁺ and Tb³⁺ doped samples same procedure was followed except addition of appropriate amounts of InCl₃, Eu₂O₃ and Tb₄O₇ was carried out while dissolving gallium metal in concentrated HCl.

Preparation of In³⁺ doped ZnGa₂O₄ nanoparticles incorporated PMMA matrix: For incorporating nanoparticles in polymer, the procedure reported by Gonsalves, et al. [115] was employed. The method is described below. Around 50 mg of ZnGa₂O₄ nanoparticles was dispersed in one ml of methyl methacrylate (MMA) by sonicating for one hour under argon atmosphere. Around 5 mg of azobisisobutyronitrile (AIBN) was added to this mixture and

heated for 2 hrs at 70°C under argon atmosphere. White solid was obtained and this solid was dissolved in CHCl₃ and re-precipitated with methanol. The precipitate was separated by centrifugation and dried under ambient conditions. For preparing thin polymer films containing the nanoparticles, the white solid obtained was dissolved in CHCl₃ and spin coated on a quartz substrate at a spinning rate of 2500 rpm.

2.6. Synthesis of un-doped and lanthanide doped MWO₄ (M = Ca, Sr, Ba)

nanomaterials: Starting materials used for the synthesis of undoped and lanthanide doped metal tungstates were Ca(NO₃)₂.H₂O, SrCl₂.6H₂O, Ba(NO₃)₂, Eu(NO₃)₃.5H₂O, Tb(NO₃)₃.xH₂O, Dy(NO₃)₃.xH₂O, Sm(NO₃)₃.xH₂O and Er(OOCCH₃)₃.xH₂O. For the synthesis of undoped metal tungstates, 2.12 mmol of metal salt was dissolved in 20 ml of ethylene glycol while stirring. Around 2.12 mmol of Na₂WO₄.2H₂O was added to this solution and stirring was continued for two hours. The precipitate formed was separated by centrifugation and washed with methanol and acetone to remove unreacted species. For the synthesis of lanthanide doped metal tungstates, same procedure was followed except that the addition of 2 atom % lanthanide salts to metal salt solution was done prior to the addition of Na₂WO₄.2H₂O.

2.7. Characterization Techniques: During the present investigation, various characterization techniques were employed and they are briefly discussed below.

2.7.1. X-Ray Diffraction: X-rays are invisible, electrically neutral, electromagnetic radiations. Their frequencies are intermediate between the ultra-violet (UV) and gamma radiations with wavelength (λ) ranging from approximately 0.04 Å to 1000 Å. When the X-rays are incident on a solid material (grating), they are either elastically/in-elastically scattered or absorbed. The elastic scattering of X-rays is known as Bragg scattering and follows the Bragg equation (equation 7)

$$n\lambda = 2d \sin \theta \dots\dots\dots (7)$$

Where λ is the wavelength of X-rays, θ is glancing angle, d is inter planar distance and n is order of diffraction. Depending on the interplanar distance and angle of diffraction, the diffracted/ scattered beam will interfere with each other giving bright (constructive interference) and dark (destructive interference) fringes.

Powder X-ray diffraction: X-ray diffraction experimental setup requires an X-ray source, sample under investigation and a detector to pick up the diffracted X-rays. A block sketch of the typical powder diffractometer is shown in the Fig.11. The X-ray beam passes through the soller and divergence slits and then fall on the sample which is spread uniformly over a rectangular area of a glass slide. The X-rays scattered (diffracted) from the sample pass through the soller and receiving slits and then fall on a monochromator before detection. The monochromator separates out the stray wavelength radiation as well as any fluorescent radiation emitted by the sample. The details of the X-ray production and the typical X-ray spectra are explained in several monographs [116, 117].

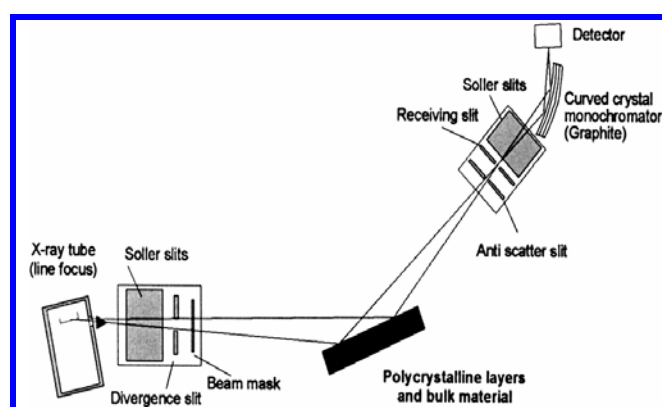


Fig.11 X-Ray diagram of a typical reflection mode diffractometer.

Data collection and Analysis: The output of the diffraction measurement is obtained as plot of intensity of diffracted X-rays versus Bragg angle. The data collection protocols often depend on the specific purpose for which the diffraction experiment is being carried out. In general a short time scan in the 2θ range of 10 to 70° is sufficient for the identification of phase of a well crystalline inorganic material. The scan time can be optimized for getting

good intensity peaks. In the present study, the observed diffraction patterns were compared with JCPDS (Joint Committee on Powder Diffraction Standards, 1974) files available for reported crystalline samples. The unit cell parameters were refined by a least squares method using the computer software “Powderx”. The average crystallite size of the nano powders was estimated from the full width at half maximum (FWHM) of the intense peak in the XRD pattern using the Scherrer’s formula, which is given by equation 8

$$D = \frac{0.9\lambda}{\beta \cos \theta} \dots\dots\dots (8)$$

Where D is the thickness of the crystal (in angstroms), λ the X-ray wavelength and θ the Bragg angle. The line broadening, β , is measured from the extra peak width at half the peak height and is obtained from the Warren formula (equation 9):

$$\beta^2 = \beta_M^2 - \beta_S^2 \dots\dots\dots (9)$$

Where β_M is the measured peak width in radians at half maxima and β_S is the measured peak width in radians at half maxima of the peak corresponding to standard material (silicon).

In the present study, Philips 1710 diffractometer based on the Bragg-Brentano reflection geometry, was used for the characterization of all the samples. The Cu-K α from sealed tube was used as the incident beam. A Ni foil was used as a filter and the diffracted beam was monochromatised with a curved graphite single crystal. The Philips (PW-1710) diffractometer is attached with a proportional counter (Argon filled) for the detection of X-rays. The X-ray tube rating was maintained at 30 kV and 20mA. The goniometer was calibrated for correct zero position using silicon standard. Samples are well grounded and made in the form of a slide. As all the micro crystals are randomly oriented, at any point on the sample different planes from crystals will be exposed to X-rays.

2.7.2. Electron Microscopy: Micro-structural characterization has become important for all types of materials as it gives substantial information about the structure-property correlation.

Micro-structural characterization broadly means ascertaining the morphology, identification of crystallographic defects and composition of phases, estimating the particle size, etc. Electron microscopic techniques are extensively used for this purpose. Electron microscopy is based on the interaction between electrons (matter wave) and the sample. In the present study, Scanning Electron Microscopy (SEM) and Transmission Electron Microscopy (TEM) have been used to characterize the nano powders. The principle and experimental details of these two techniques are given below.

Scanning Electron Microscopy (SEM): In a typical scanning electron microscope, a well-focused electron beam is incident and scanned over the sample surface by two pairs of electro-magnetic deflection coils. The signals generated from the surface by secondary electrons are detected and fed to a synchronously scanned cathode ray tube (CRT) as intensity modulating signals [118, 119]. Thus, the specimen image is displayed on the CRT screen. Changes in the brightness represent changes of a particular property within the scanned area of the specimen. Schematic representation of SEM is shown in Fig.12.

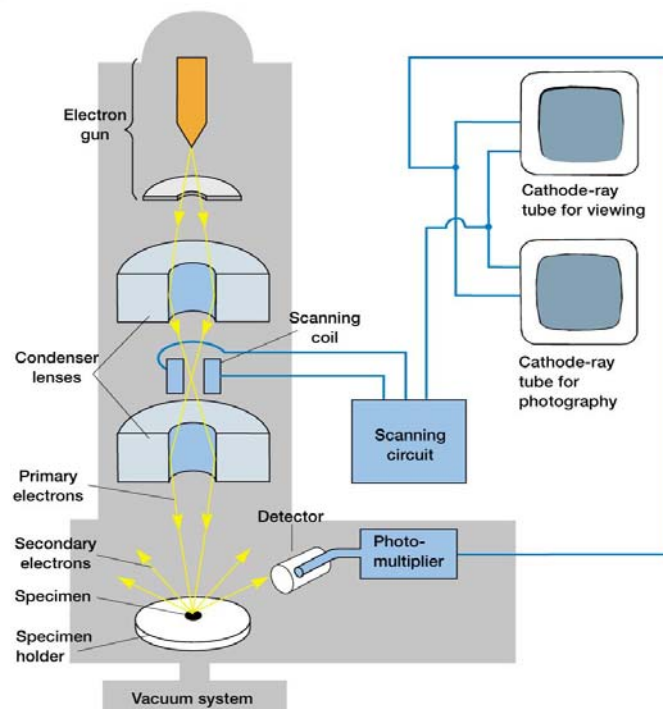


Fig.12. Schematic representation of SEM microscope.

For carrying out SEM analysis, the sample must be vacuum compatible ($\sim 10^{-6}$ Torr or more) and electrically conducting. The surfaces of non-conductive materials are made conductive by coating with a thin film of gold or platinum or carbon. In this study, the SEM technique was used to study the microstructure evolution of nanocrystalline powders and EDS (energy dispersive X-ray spectroscopy) is used for the compositional analysis.

In the present study, SEM instrument used was from Seron Inc. (Model AIS 2100) having standard tungsten filament. An accelerating voltage of 20 kV and magnification of 10kx was used for recording the micrographs. The samples were made in the form of slurry with isopropyl alcohol and spread over mirror polished single crystal of Si substrate prior to its mounting on the stub.

Transmission Electron Microscopy (TEM): In TEM, a beam of focused high-energy electrons is transmitted through the sample to form an image, which reveals information about its morphology, crystallography and particle size distribution at a spatial resolution of ~ 1 nm. TEM is unique as it can focus on a single nanoparticle and can determine its crystallite size. This technique is applicable to a variety of materials such as metals, ceramics, semiconductors, minerals, polymers, etc. [120, 121]. TEM setup consists of an electron gun, voltage generator, vacuum system, electromagnetic lenses and recording devices and the schematic diagram of TEM is shown in Fig.13 (a). Usually thermionic gun (tungsten filament, LaB₆ crystal, etc.) or field emission gun is used as an electron source to illuminate the sample. The electrons thus produced are accelerated at chosen voltages by a voltage generator. The electron beam after passing through the condenser lens system is directed towards a thin sample. Typically TEM specimen thickness is in the range of 50 to 100 nm and should be transparent to the electron beam. The microscope column is maintained at high vacuum levels to prevent scattering of electrons by the atmosphere inside the microscope. Information is obtained from both transmitted electrons (i.e. image mode) and diffracted

electrons (i.e. diffraction mode). In TEM, contrast formation depends greatly on the mode of operation. In conventional TEM, contrast is obtained by two modes namely the mass-thickness contrast and the diffraction contrast and both are based on amplitude contrast. In high resolution transmission electron microscopy (HRTEM), image contrast is due to phase contrast. Mechanism of all these types of contrasts is briefly discussed below.

Mass-thickness contrast: This is the common mode of operation in TEM and it is called as bright field imaging. In this mode, the contrast formation is obtained directly by occlusion and absorption of electrons in the sample. Thicker regions of the sample or regions with a higher atomic number will appear dark, while the regions with no sample in the beam path will appear bright – hence the term "bright field". The image is in effect assumed to be a simple two-dimensional projection of the sample. The effect of thickness and mass number of the sample on the brightness of the image can be seen in the Fig.13 (b).

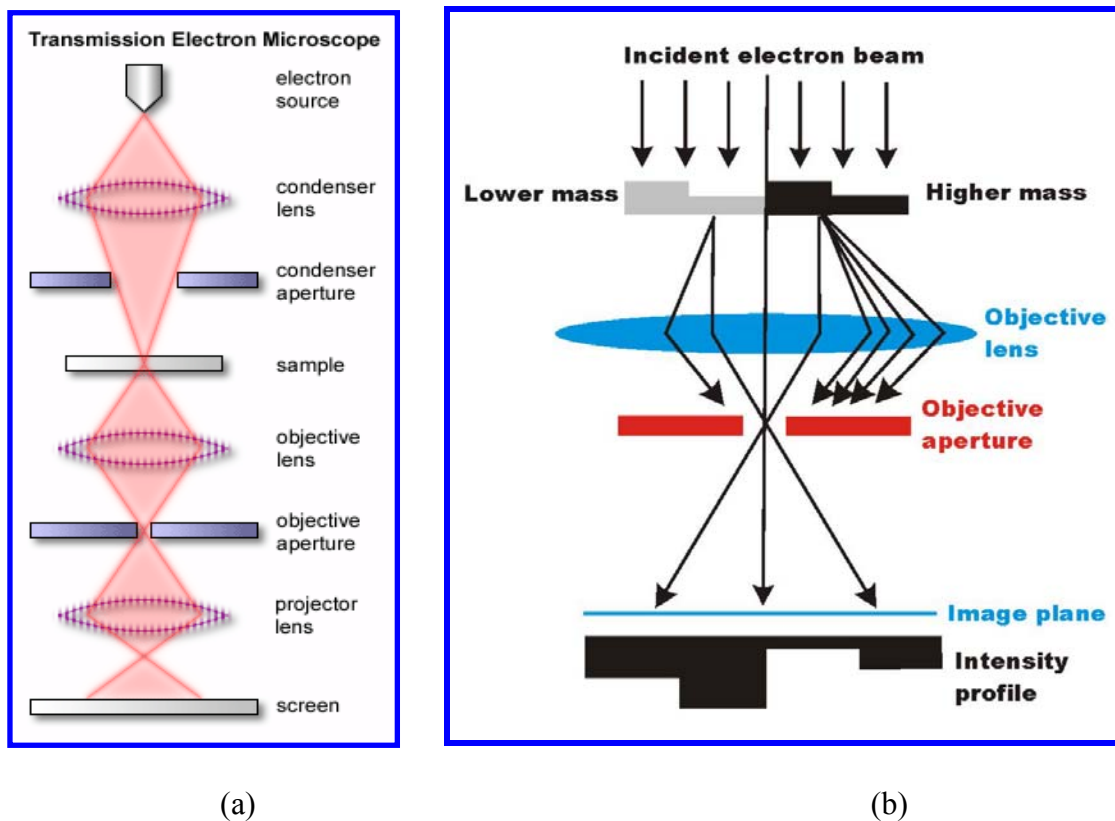


Fig.13. (a) Simplified ray diagram of TEM, (b) Mass-thickness contrast.

Diffraction contrast: This mode of operation is also known as dark field imaging. In the case of a crystalline sample, the electron beam undergoes Bragg scattering and it disperses electrons into discrete locations. By the placement of apertures in these locations, i.e. the objective aperture, the desired Bragg reflections can be selected (or excluded), thus only parts of the sample that are causing the electrons to scatter to the selected reflections will end up projected onto the imaging apparatus. A region without a specimen will appear dark if there are no reflections from that region. This is known as a dark-field image. This method can be used to identify lattice defects in crystals. By carefully selecting the orientation of the sample, it is possible not only to determine the position of defects but also to determine the type of defect present.

Phase contrast: Among all the techniques used to obtain structural information of materials, high resolution electron microscopy (HREM) has the great advantage that it yields information about the bulk structure, projected along the direction of electron incidence at a resolution comparable to the inter atomic distances. This enables the study of complicated structures, crystal defects, precipitates and so forth, down to the atomic level. In HRTEM, phase contrast is used for the imaging. High resolution images are formed by the interference of elastically scattered electrons, leading to a distribution of intensities that depends on the orientation of the lattice planes in the crystal relative to the electron beam. Therefore, at certain angles the electron beam is diffracted strongly from the axis of the incoming beam, whilst at other angles the beam is completely transmitted. In the case of high-resolution imaging, this allows the arrangement of atoms within the crystal lattice to be deduced. For HREM measurements, sample should be very thin.

Selected area electron diffraction (SAED): An aperture in the image plane is used to select the diffracted region of the specimen, giving site-selective diffraction analysis. SAED patterns are a projection of the reciprocal lattice, with lattice reflections showing as sharp

diffraction spots. By tilting a crystalline sample to low-index zone axes, SAED patterns can be used to identify crystal structures and measure lattice parameters. Figure 14 shows electron diffraction in (a) single crystal,(b) polycrystalline and (c) nanocrystalline materials. Electron diffraction pattern of polycrystalline or nanocrystalline materials can be indexed by using equation 10

$$Rd = \lambda L \dots\dots\dots (10)$$

Where R is the radius of diffraction ring, L is camera length, λ is the electron wavelength, and d is the spacing corresponding to planes.

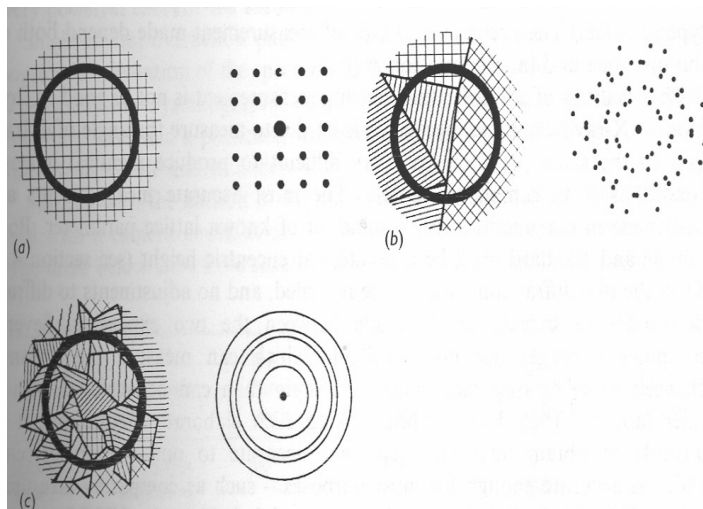


Fig.14. Electron diffraction patterns from (a) single crystal, (b) polycrystalline materials and (c) nanocrystalline materials [120].

In the present study, Transmission electron microscopic (TEM) measurements (bright field low magnification and lattice imaging) were performed using 200 keV electrons in JEOL 2010 UHR TEM microscope. Samples were dispersed in methanol and a drop of this solution was added on a carbon coated copper grid. These samples were dried properly prior to load in TEM.

2.7.3. Atomic Force Microscope (AFM): AFM measures the topography of conductors, semiconductors, and insulators with a force probe located within a few Å of the sample surface [122]. AFM images are recorded by moving fine tip attached to a cantilever across

the surface of the sample while the tip movements normal to the surface are measured. The deflections occurred in the tip, due to the interaction forces between the tip and sample surface, can be measured by focussing a laser beam onto cantilever and detecting the reflected light from the cantilever using a position sensitive detector. Schematic diagram of atomic force imaging is shown in Fig 15 (a). As the tip is rastered over the surface, a feedback mechanism is employed to ensure that the piezo-electric motors maintain a constant tip force or height above the sample surface. The tip movements normal to the surface are digitally recorded and can be processed and displayed in three-dimensions by a computer. This technique has a lateral resolution of 1 to 5 nm. AFM is typically used to obtain a three-dimensional surface image or to determine the surface roughness of thin films and crystal grains. There are mainly two types of AFM modes, namely the contact mode and the semi contact/tapping mode, which are used for imaging the samples. The schematic representation of the different types forces acting between tip and sample in the two methods of imaging is shown in Fig.15 (b) and are described below.

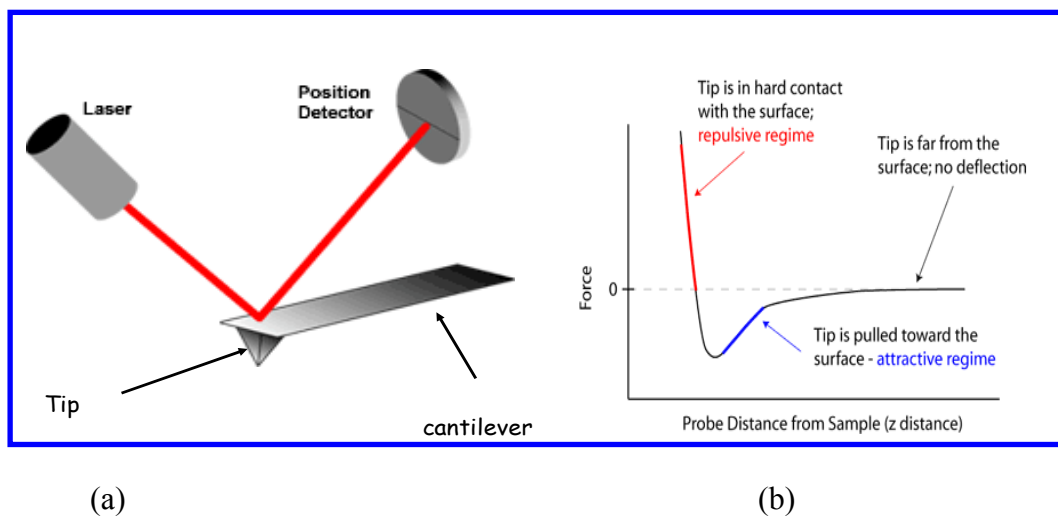


Fig.15. (a) Principle of AFM imaging, (b) variation of interaction force versus distance between the AFM tip and substrate.

(1) Contact mode: Here, the force between the probe tip and substrate is repulsive, and it is within the range of 10^{-8} to 10^{-7} N. The force is set by pushing a cantilever against the sample

surface. The contact mode can obtain a higher atomic resolution than the other modes, but it may damage a soft material due to excessive tracking forces applied from the probe on the sample. Unlike the other modes, frictional and adhesive forces will affect the image.

(2) Non-contact/tapping mode: Here, the main interaction force between the probe tip and the substrate is attractive due to van der Waals force and it is in the range of 10^{-10} to 10^{-12} N. In this mode, cantilever oscillates in the attractive region and its oscillation frequency gets modulated depending on the sample surface features. The tip is 5 to 150 nm above the sample surface. The resolution in this mode is limited by the interactions with the surrounding environment.

In the present study, Atomic force microscopic (AFM) measurements were performed in contact mode using an AFM instrument from Ms. NT-MDT (solver model) with a 50 μm scanner head. Samples were dispersed in methanol and a drop of this solution was added on highly oriented pyrolytic graphite (HOPG)/ mica sheets. These samples are dried properly before loading in AFM.

2.7.4. Vibrational spectroscopy: Vibrational spectroscopic techniques are extensively used to identify the nature of different linkages present in a material. These methods also give valuable information regarding the symmetry of different vibrational units. Two types of vibrational techniques, namely IR and Raman spectroscopy are used in the present study and the principle is briefly described below.

IR spectroscopy: Vibrations of bonds and groups which involve a change in the dipole moment results in the absorption of infrared radiation which forms the basis of IR spectroscopy. Modern IR instruments are based on Fourier transformation method to improve the signal to noise ratio. Unlike conventional IR instrument, in FTIR instrument, all the frequencies are used simultaneously to excite all the vibrational modes of different types of bonds/linkages present in the sample. This reduces the experimental time considerably.

In the present study, all infrared experiments were carried out using a Bomem MB102 FTIR machine having a range of 200-4000 cm^{-1} and with resolution of 4 cm^{-1} . IR radiation was generated from globar source (silicon carbide rod). The instrument used CsI single crystal, as the beam splitter and deuterated triglycine sulphate (DTGS) as a detector. Prior to IR measurements, the samples were ground thoroughly by mixing with dry KBr powder, made in the form of a thin pellet and introduced into the sample chamber of the instrument.

Raman spectroscopy: Raman spectroscopy is a very convenient technique for identification of crystalline or molecular phases, for obtaining structural information. Backscattering geometries allow films, coatings and surfaces to be easily analyzed. Ambient atmosphere can be used and no special sample preparation is needed for analyzing samples by this technique. The principle is briefly described below. When an intense beam of monochromatic light is passed through a substance, a small fraction of light is scattered by the molecules in the system. The electron cloud in a molecule can be polarized (deformed) by the electric field of the incident radiation. If we apply an oscillating electric field (the electric field vector of the light wave) to the molecule, the deformation of the electron cloud will also oscillate with the same frequency (ν_0) of the incident light beam. This oscillation of the electron cloud produces an oscillating dipole that radiates at the same frequency as the incident light. This process is called Rayleigh scattering. The Rayleigh-scattered radiation is emitted in all directions. Since only about 0.1 % of the light is scattered, we must use as intense a source as possible and a laser fulfills this requirement admirably. There is a small but finite probability that the incident radiation will transfer part of its energy to one of the vibrational or rotational modes of the molecule. As a result, the scattered radiation will have a frequency $\nu_0 - \nu_m$, where ν_m is the absorbed frequency. Similarly, there is a slight chance that molecules in excited vibrational or rotational states will give up energy to the light beam. In this case the scattered radiation will have a higher frequency ($\nu_0 + \nu_m$). Thus, it is possible to observe

three types lines in the scattered radiation: One line at ν_0 corresponding to the Rayleigh scattering and two Raman lines, one at $\nu_0 + \nu_m$ known as the anti-Stokes line, and the other at $\nu_0 - \nu_m$, known as the Stokes line. Since there are fewer molecules in the upper vibrational state than in the lower vibrational state, the intensity of the anti-Stokes line is much less than that of the Stokes line. The two Raman lines are extremely weak compared to the intensity of the Rayleigh scattered light and is less than 10^{-7} of the intensity of the incident light [123].

In the present study, Raman spectra were recorded on a home-made Raman spectrometer using 488 nm line from an air cooled Argon ion laser. The spectra were collected using a grating with 1200 groves/mm with a slit width of ~50 micron (yielding a resolution of $\sim 1 \text{ cm}^{-1}$), along with Peltier cooled CCD and a Razor edge filter.

2.7.5. Nuclear magnetic resonance (NMR) Spectroscopy: Nuclear magnetic resonance spectroscopy is a technique that exploits the nuclear magnetic properties of atomic nuclei and can give valuable information about the structure, dynamics and chemical environment of around a particular nucleus in a molecule/ lattice.

Chemical shift: The chemical shift of any nucleus is defined as the difference between its resonance frequency and the resonance frequency of the same nuclei in a reference sample and can be expressed by the equation 11

$$\delta = \frac{\omega - \omega_0}{\omega_0} * 10^6 \dots\dots\dots (11)$$

where ω , ω_0 represent resonance frequencies of nuclei in the sample and in the reference, respectively.

Chemical shielding interaction: Chemical shift arises because of the effective magnetic field felt by nuclei is brought about by the polarization effect of electron cloud around the nuclei created by the applied magnetic field. Since this is particularly sensitive to the

configuration of valance electrons, which is governed by the nature of chemical bonding, this aspect has been labeled as chemical shielding interaction. The Hamiltonian for this interaction can be given by the equation 12 [124, 125].

$$H_{cs} = \gamma I_z \sigma B_0 \dots\dots\dots (12)$$

where σ is a second rank (3x3) tensor known as chemical shielding tensor. This tensor can be diagonalised for a specific principal axis system and σ_{11} , σ_{22} , σ_{33} are the corresponding diagonal components. The isotropic component of the chemical shift tensor can be expressed by the relation (equation 13):

$$\sigma_{iso} = \frac{1}{3}(\sigma_{11} + \sigma_{22} + \sigma_{33}) \dots\dots\dots (13)$$

The symmetry parameter is defined by equation 14:

$$\eta = \frac{\sigma_{22} - \sigma_{11}}{\sigma_{33} - \sigma_{iso}} \dots\dots\dots (14)$$

Due to the presence of chemical shielding anisotropy, the nuclear precessional frequency depends on the orientation of principal axis system with respect to the external applied magnetic field and can be expressed by the relation (equation 15) [125]

$$\omega_p(\theta, \phi) = \gamma B_0 \left\{ (1 - \sigma_{11})^2 \cos^2 \phi \sin^2 \theta + (1 - \sigma_{22})^2 \sin^2 \phi \sin^2 \theta + (1 - \sigma_{33})^2 \cos^2 \theta \right\}^{1/2} \dots\dots(15)$$

where θ and Φ represent the orientation of principal axis system with applied magnetic field direction. For axial symmetry $\eta = 0$ and the precession frequency can be expressed by the relation (equation 16)

$$\omega_p(\theta) = \gamma B_0 \left[1 - \sigma_{iso} - \Delta\sigma \cdot (3 \cos^2 \theta - 1) / 3 \right] \dots\dots\dots (16)$$

For values of $\theta = 54.7^\circ$ the term $3 \cos^2 \theta - 1$ becomes zero and the dependence of chemical shielding anisotropy term on Larmor frequency gets averaged out to a very small value.

In solution NMR spectroscopy, the molecular motion averages out dipolar interactions and anisotropic effects. This is not so in the solid state and the NMR spectra of

solids tend to be broadened because of (a) magnetic interactions of nuclei with the surrounding electron cloud (chemical shielding interaction), (b) magnetic dipole – dipole interactions among nuclei and (c) interactions between electric quadrupole moment and surrounding electric field gradient. Hence, it is difficult to get any meaningful information from such patterns. However, by using suitable experimental strategies, such interactions can be averaged out, thereby improving the information obtained from solid-state NMR patterns. One such technique used to get high-resolution solid-state NMR pattern in solids is the magic angle spinning nuclear magnetic resonance (MAS NMR) technique. In the following section brief account of the MAS NMR technique has been given.

Magic Angle Spinning Nuclear Magnetic Resonance (MAS NMR): MAS NMR technique involves rotating the powder samples at high speeds, at an angle of 54.7° (magic angle) with respect to the applied magnetic field direction. When $\theta=54.7^\circ$, the term $3\cos^2\theta$ becomes unity. Since Hamiltonian for different anisotropic interactions have $3\cos^2\theta - 1$ term, these anisotropic interactions get averaged out in time during fast spinning. This is schematically shown in Fig.16 and explained below.

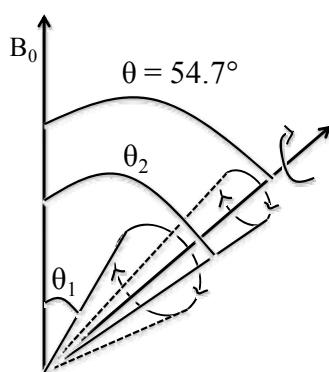


Fig.16. Principle of MAS NMR experiment

At sufficiently fast spinning speeds, the NMR interaction tensor orientations with initial angles of θ_1 and θ_2 relative to B_0 have orientational averages of 54.7° , resulting in the conversion of $3\cos^2\theta - 1$ term in expressions corresponding to various interactions to a very

small value, thereby giving rise to sharp NMR peaks. Thus, the MAS NMR technique simplifies the solid-state NMR patterns and individual chemical environments can be correlated with corresponding chemical shift values obtained from these samples [125, 126].

Although, MAS is an efficient technique employed for getting high resolution NMR patterns from solid samples, in many cases, due to spinning, side bands, which are mirror images of the isotropic peak and spread from the isotropic peak by integer multiples of the spinning frequency, appear along with the central isotropic peak for nuclei having wide range of chemical shift values. For nuclei having a nuclear spin value $\frac{1}{2}$, sideband pattern is a measure of the chemical shift anisotropy and valuable information regarding the symmetry of the electronic environment around a probe nuclei can be obtained from the intensity distribution of sidebands. However, in the presence of large number of isotropic peaks, the number of sidebands also increases, and there can be overlap between the sidebands and isotropic peaks, which makes the MAS NMR pattern complicated.

In the present study, ^{31}P MAS NMR patterns were recorded using a 500 MHz Bruker Avance machine with a ^{31}P basic frequency of 202.4 MHz. The samples were packed inside 2.5 mm rotors and subjected to various spinning speeds ranging between 5000 to 10000 Hz. The chemical shift values are expressed with respect to 85% H_3PO_4 solution. The typical 90° pulse duration and relaxation delay are 4 μs and 5s, respectively.

2.7.6. Photoluminescence spectroscopy: Photoluminescence (PL) is a process, in which a substance absorbs photons (electromagnetic radiation) and then re-radiates photons. Quantum mechanically, this can be described as an excitation to a higher energy state by absorption of photon and then a return to a lower energy state accompanied by the emission of a photon.

The schematic representation of spectrofluorimeter can be seen in Fig.17. The light from an excitation source passes through a monochromator, and strikes the sample. A proportion of the incident light is absorbed by the sample, and some of the molecules in the

sample fluoresce. The fluorescent light is emitted in all directions. Some of this fluorescent light passes through a second monochromator and reaches a detector, which is usually placed at 90° to the incident light beam to minimize the risk of transmitted or reflected incident light reaching the detector. Various light sources may be used as excitation sources, including lasers, photodiodes and lamps (xenon arcs and mercury-vapor lamps).

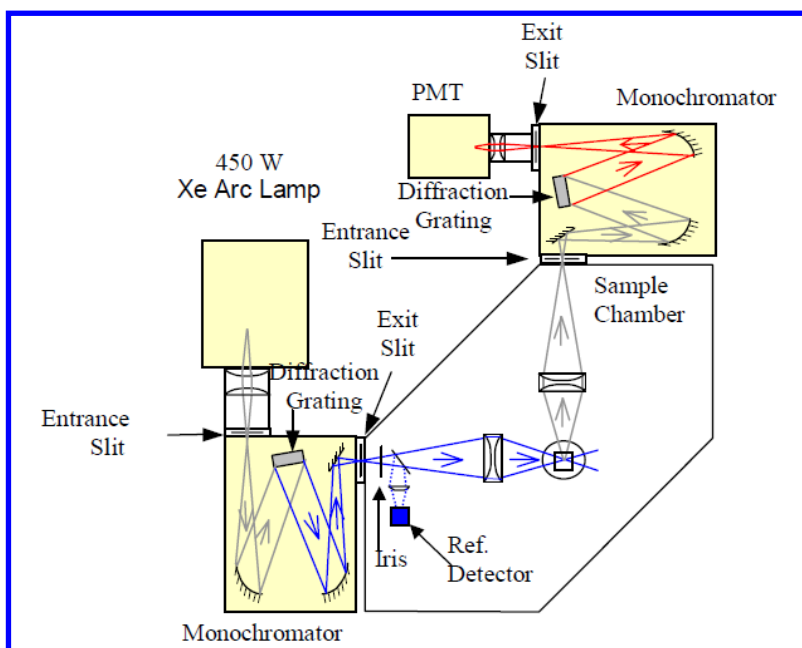


Fig.17. Schematic representation of spectrofluorimeter.

Xenon arc lamp has a continuous emission spectrum with nearly constant intensity in the range from 300-800 nm and a sufficient irradiance for measurements down to 200 nm. A monochromator transmits light of an adjustable wavelength with an adjustable tolerance. The most common type of monochromator utilizes a diffraction grating wherein a collimated light illuminates a grating and exits with a different angle depending on the wavelength. The monochromator can then be adjusted to select which wavelengths to transmit. The most commonly used detector is photomultiplier tube (PMT).

Excitation and Emission spectra: The spectrofluorometer with dual monochromators and a continuous excitation light source can record both excitation spectrum and emission

spectrum. When measuring emission spectra, the wavelength of the excitation light is kept constant, preferably at a wavelength of high absorption, and the emission monochromator scans the spectrum. For measuring excitation spectra, the wavelength passing through the emission monochromator is kept constant and the excitation monochromator is subjected to scanning. The excitation spectrum generally is identical to the absorption spectrum as the emission intensity is proportional to the absorption. Lifetime and quantum yields are two important properties of a phosphor and they can tell us about the quality of a phosphor.

Lifetime: The lifetime of the excited state is defined by the average time the molecule spends in the excited state prior to return to the ground state and is expressed by the equation 17 [127].

$$\tau = \frac{1}{k_r + k_{nr}} \dots\dots\dots (17)$$

Where k_r is the radiative decay rate, k_{nr} is the non-radiative decay rate. The radiative lifetime τ_0 is defined as the inverse of the radiative emission rate i.e, $\tau_0 = k_r^{-1}$. Lifetime measurements were performed using both time correlated single photon counting (TCSPC) and multi channel scaling (MCS) modes.

Quantum yield: It is defined as the ratio of the emitted to the absorbed photons. The quantum efficiency η can also be expressed in terms of the radiative lifetime (τ_0) and luminescence lifetimes (τ) by the equation 18 [127].

$$\eta = \frac{k_r}{k_r + k_{nr}} = \frac{\tau}{\tau_0} \dots\dots\dots (18).$$

In the present study all luminescence measurements were carried out by using an Edinburgh Instruments' FLSP 920 system, having a 450W Xe lamp, 60 W microsecond flash lamp and hydrogen filled nanosecond flash lamp (operated with 6.8 kV voltage and 40 kHz

pulse frequency) as excitation sources for steady state and for lifetime measurements. Red sensitive PMT was used as the detector. Quantum yield was measured by using integrating sphere which is coated inside with BaSO₄ as a reflector.

2.7.7. Thermal analysis: Thermal analysis methods are essential for understanding the compositional and heat changes involved during reaction. They are useful for investigating phase changes, decomposition, and loss of water or oxygen and for constructing phase diagrams.

Thermo gravimetric analysis (TGA): In TGA, the weight of a sample is monitored as a function of time as the temperature is increased at a controlled uniform rate. Loss of water of crystallization or volatiles (such as oxygen, CO₂, etc.) is revealed by a weight loss. Oxidation or adsorption of gas shows up as a weight gain.

Differential thermal analysis (DTA): A phase change is generally associated with either absorption or evolution of heat. In DTA experiments, the sample is placed in one cup, and a standard sample (like Al₂O₃) in the other cup. Both cups are heated at a controlled uniform rate in a furnace, and the difference in temperature (ΔT) between the two is monitored and recorded against time or temperature. Any reaction involving heat change in the sample will be represented as a peak in the plot of ΔT vs T. Exothermic reactions give an increase in temperature, and endothermic reaction leads to a decrease in temperature and the corresponding peaks appear in opposite directions.

In the present study, thermo-gravimetric-differential thermal analysis (TG-DTA) of samples was carried out in platinum crucibles using a Setaram, 92-16.18 make TG-DTA instrument. The sample was heated under argon environment up to 1100°C at a heating rate of 10°C/min.

CHAPTER 3: Binary oxides

3.1. Introduction: Oxides like Ga_2O_3 and Sb_2O_3 belong to class of materials known as transparent semiconducting oxides and find extensive applications in electro-luminescent devices, sensor materials for absorption of molecules like CO and CO_2 , catalysts, fire retardants, anode material for the Li-ion batteries, etc. [48-51, 128-137]. Ga_2O_3 exists in a variety phases, namely α , β , γ and ε modifications [138, 139], whereas Sb_2O_3 exists in two crystalline forms, cubic (senarmonite form) and orthorhombic (valentinite form). Depending on the nature of crystallographic modifications, they have different properties. For example, cubic Sb_2O_3 is used as an additive to improve the flame retardency of polymer resins whereas valentinite form of Sb_2O_3 is an essential component in Sb_2O_3 - B_2O_3 glasses showing enhanced non-linear optical properties [140]. Similarly β - Ga_2O_3 is a preferred material in optoelectronics for field emission applications. Different phases of gallium oxides are generally prepared by decomposition of a suitable precursor, like GaOOH whereas Sb_2O_3 is generally prepared either by the oxidation of antimony metal or by the hydrolysis of SbCl_3 . Several reports are available [141-149] on the synthesis of GaOOH in different shapes and sizes. These include methods like, hydrothermal treatment, sono-chemical reactions and precipitation in aqueous medium by addition of urea. It is also observed that the shape is retained when GaOOH is thermally decomposed to Ga_2O_3 [56, 150]. A number of reports are also available on the preparation of Sb_2O_3 in variety of forms such as nanoparticles [151-158], hollow nanospheres [159], nanowires, nanobelts and nanorods [64, 65, 160-163]. Doping GaOOH/ Ga_2O_3 and Sb_2O_3 nanomaterials with lanthanide ions (Ln^{3+}) is an attractive option to prepare efficient luminescent materials. In the following section a brief description on the optical and luminescence properties of both lanthanides, doped and undoped GaOOH and Sb_2O_3 have been discussed.

Lanthanide ions doped Ga₂O₃ nanomaterials [164-171] have been investigated by several workers. However, the effect of lanthanide doping on structural aspects of GaOOH nanomaterials, which is a precursor for Ga₂O₃, is not known. As the ionic radii of Ln³⁺ and Ga³⁺ are significantly different, it is quite interesting to know where the lanthanide ions are incorporated and what structural modification it makes with the GaOOH lattice during doping. Luminescence from different lanthanide ions can be used as a probe to understand the structural changes taking place with GaOOH brought about by lanthanide ions incorporation. Such studies are essential for understanding the mechanism of lanthanide ion incorporation in different structural modifications of Ga₂O₃ host which are obtained by the decomposition of lanthanide ions containing GaOOH phase. The main reason, behind lack of such studies on GaOOH:Ln³⁺ (Ln³⁺ for lanthanide ions) nanomaterials, is the significant quenching of the lanthanide ion excited state brought about by vibrations of OH groups present in GaOOH samples. For example Li, et al. [56] have carried out luminescence studies on GaOOH:Dy³⁺ nanorods and observed that Dy³⁺ emission from the sample is completely quenched. These authors also reported that thermal decomposition of GaOOH:Dy³⁺(3%) nanorods leads to the formation of Ga₂O₃:Dy nanorods along with small amounts of Dy₃Ga₅O₁₂. The secondary phase might have formed from the Dy³⁺ ions which are not incorporated in the GaOOH lattice. Also considering the ionic radii of Dy³⁺ and Ga³⁺ ions under a coordination number of six (0.91 and 0.62 Å) [172] it is difficult to visualise that all the Dy³⁺ ions have replaced Ga³⁺ in the GaOOH/ Ga₂O₃ lattice.

Very few reports are available [64, 65, 163] regarding the optical properties of Sb₂O₃ either in the nanocrystalline form or in the bulk form. Zhang, et al. [163] have investigated optical properties of Sb₂O₃ nanoparticles, obtained by the oxidation of antimony metal, over the visible and near infrared regions and observed that the reflectivity in this region depends on the metal contents in Sb₂O₃ nanoparticles. Deng, et al. [64, 65] have carried out

luminescence studies on self-assembled structures of Sb_2O_3 nanorods and nanowires. They observed broad emission peak in the region of 390 to 500 nm, in addition to the band edge emission centered around 374 nm. Broad emission over the region of 390 to 500 nm has been attributed to the emission from oxygen vacancies related defect centers present in the lattice of Sb_2O_3 . In a related study Deng, et al. [65] observed blue emission around 433 nm from Sb_2O_3 nanobelts, which has also been attributed to the oxygen related defect emission. Chen, et al. [173] has also observed broad emission in the region $\sim 400\text{-}700$ nm from orthorhombic Sb_2O_3 . However, no proper explanation was given for the observed broad emission. Sb^{3+} is known to be a good luminescent species when doped into different inorganic host lattices [174-176]. Oomen, et al. [174] have observed two emission bands, one in the UV and the other in the visible region from Sb^{3+} doped LnPO_4 samples (where Ln = Sc, Lu and Y). These emission bands arise from transitions between $^3\text{P}_1$ and $^3\text{P}_0$ (excited states) to $^1\text{S}_0$ (ground state) of Sb^{3+} ions and are strongly temperature dependent due to dynamic Jahn-Teller effect. Antimony doping improves green emission from PbWO_4 single crystals due to creation of O_i sites in the lattice [175]. However, in all these studies, luminescence properties of the Sb_2O_3 with different morphologies have been given only limited attention, particularly when luminescent species like lanthanide ions are associated with them. The difficulty in incorporation of lanthanide ions in the Sb_2O_3 lattice may possibly a reason for limited investigation on such materials. The factors responsible for this difficulty are (i) significant difference in the ionic radius between Eu^{3+} ions (0.95\AA under 6 coordination) and Sb^{3+} ions (0.76\AA under four coordination) [177] and (ii) difference in the stable coordination numbers of Eu^{3+} and Sb^{3+} ions. There is also a vast difference in their electro-negativity values. Generally Eu^{3+} ions prefer higher coordination number like 6, 8 and 9, whereas in orthorhombic Sb_2O_3 , antimony has a slightly distorted tetrahedral geometry with oxygen

atoms at three corners and the lone pair of electrons of antimony at the fourth corner with all the O - Sb - O bond angles different [178].

In spite of significant difference in terms of ionic radius, electro-negativity, coordination numbers between Sb^{3+} and Eu^{3+} ions, it is of interest to understand the chemical interaction taking place between them, particularly in aqueous/organic solvents under alkaline conditions. This is because many technologically important luminescent oxide nanoparticles doped with lanthanide ions and Sb^{3+} are prepared under these conditions. For example Wen, et al. [179] have demonstrated that by suitably modifying $\text{Eu}^{3+}/\text{Sb}^{3+}$ ratio in YBO_3 crystal, nearly white light emission can be obtained. Their interaction under high temperature heat treatment is also important as lanthanide ions are co-doped with Sb^{3+} ions in several oxide-based glasses, which are prepared at high temperatures [180, 181]. It is reported that presence of Sb_2O_3 in silicate glass doped with Er^{3+} , has significant effect on spontaneous emission rates of $^4\text{I}_{13/2}$ level of Er^{3+} in the glass [180]. Hence, it is of interest to understand the optical properties of the Sb_2O_3 synthesised in both the presence and absence of lanthanide ions in detail.

In the first section of this chapter, effect of lanthanide ion (Eu^{3+} , Tb^{3+} and Dy^{3+}) incorporation on the structural and morphological aspects of GaOOH nanorods has been presented. As the luminescence properties of Eu^{3+} ions with respect to its environment are well understood, it has been used as a probe to monitor the structural changes taking place with GaOOH lattice brought about by lanthanide ion incorporation. In the second section of this chapter, the photoluminescence and structural properties of Sb_2O_3 nanorods oriented along a particular direction and their interaction with lanthanide ions are discussed. The shape selective modifications in the structure and luminescence properties of the nanorods as well as the interaction of nanorods with lanthanide ions have been investigated using X-ray

diffraction, photoluminescence, Fourier transform infrared (FT-IR) and Raman spectroscopic techniques.

3.2 Effect of urea concentration on size of GaOOH nanorods: GaOOH nanomaterials were prepared by hydrolysis of gallium nitrate by urea. In order to find out the effect of hydroxyl ion concentration on size and shape of GaOOH nanomaterials, different concentrations of urea was used. Figure 18 shows the XRD patterns of as prepared samples with different concentrations of urea. The patterns match very well with the orthorhombic structure of GaOOH. Average crystal size was calculated using Deby-Scherrer formula and found that the particle size increases with increasing concentration of urea from 28 nm (15 mmol) to 50 nm (180 mmol). This could be attributed to an increase in the rate of hydrolysis by increasing concentration of urea. In order check whether the increase in extent of hydrolysis is associated with change in the morphology, SEM measurements were carried out on the samples prepared with different concentrations of urea.

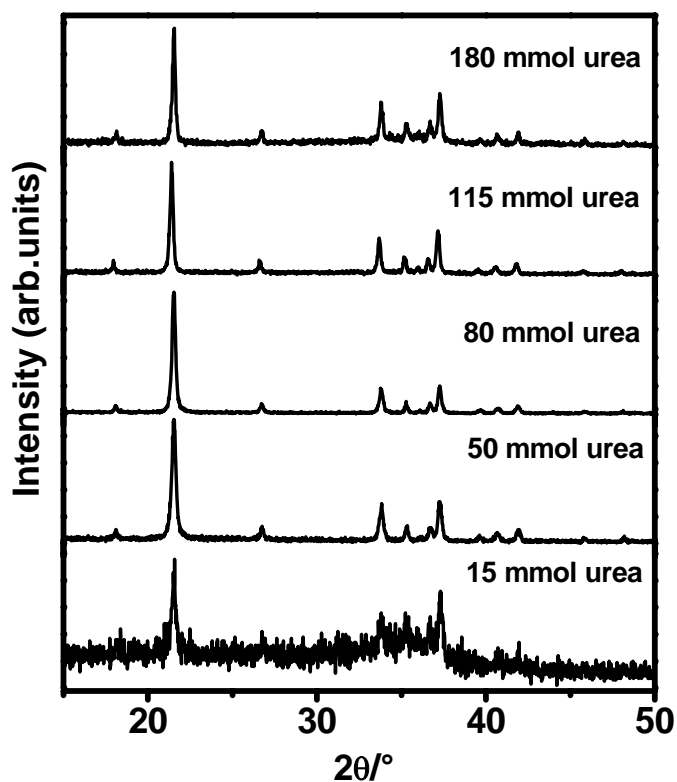


Fig.18. XRD patterns of GaOOH nanomaterials prepared with different amounts of urea.

Figure 19 (a-d) shows SEM images of GaOOH samples prepared with different concentration of urea. All the samples are having rod shaped morphology. With increase in the concentration of urea up to 80 mmol, the length and width of the nanorods increases from 0.6-0.8 and 0.1-0.15 μm to 2.4-3.0 and 1.5-2.5 μm , respectively. For further addition of urea, irregular shaped particle aggregates start forming along with nanorods. This can be explained based on nucleation and growth process which are controlled by number of hydroxyl ions generated in the reaction medium. Initially, upto 80 mmol of urea, nanorods growth take place in a particular direction due to the presence of hydroxyl ions whereas above that number of hydroxyl ions increases and growth takes place in all directions. As a result, irregular shaped particles start forming.

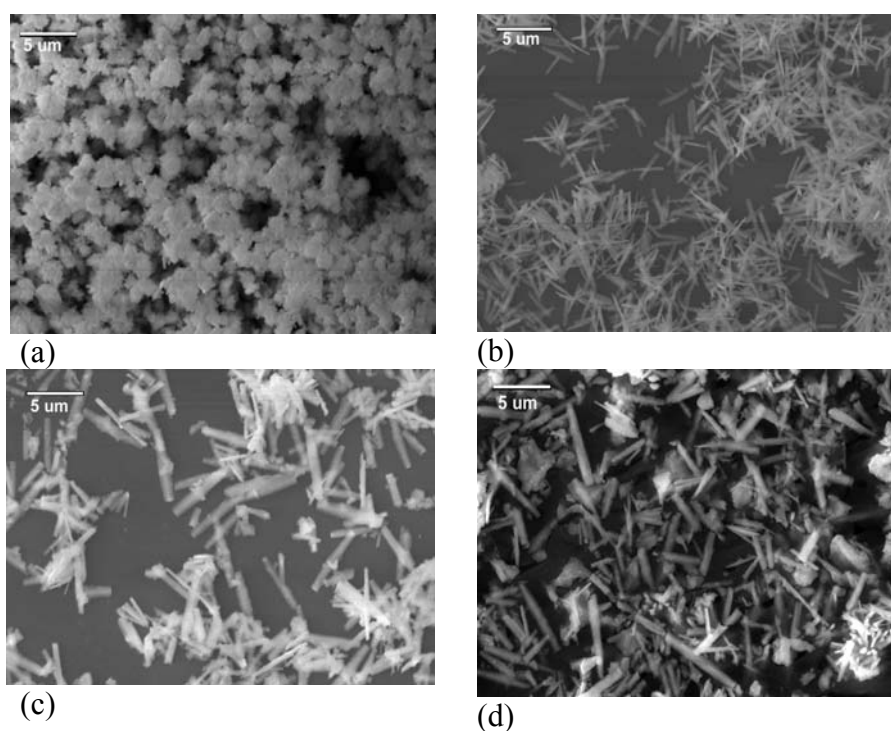


Fig.19. SEM images of GaOOH nanorods prepared with (a) 15 mmol, (b) 80 mmol, (c) 115 mmol and (d) 180 mmol of urea

3.3. Effect of lanthanide ion concentration on morphology and crystal structure of

GaOOH: The lanthanide doped GaOOH nanomaterials were prepared by co-precipitation method using hydrolysis of $\text{Ga}(\text{NO}_3)_3$ and $\text{Ln}(\text{NO}_3)_3 \cdot x\text{H}_2\text{O}$ by urea. In all preparations

gallium to urea ratio (1:20) remained unchanged while concentration of lanthanide ions were varied. Figure 20 (a-e) shows the XRD patterns of as prepared samples containing different amounts of Eu^{3+} ions. As prepared GaOOH sample without any Eu^{3+} ions is crystalline with orthorhombic crystal structure (JCPDS No. 06-0180). With increase in Eu^{3+} concentration, there is a slight increase in line width of diffraction peaks and for samples prepared in the presence of more than 1 at % Eu^{3+} , no sharp peak characteristic of the crystalline materials is observed instead a broad hump characteristic of the amorphous nature appeared. The lattice parameters have been calculated for the crystalline samples based on least square fitting of the diffraction peaks and are same within experimental errors for all the samples prepared in the presence of different amounts of Eu^{3+} ions (Table 1).

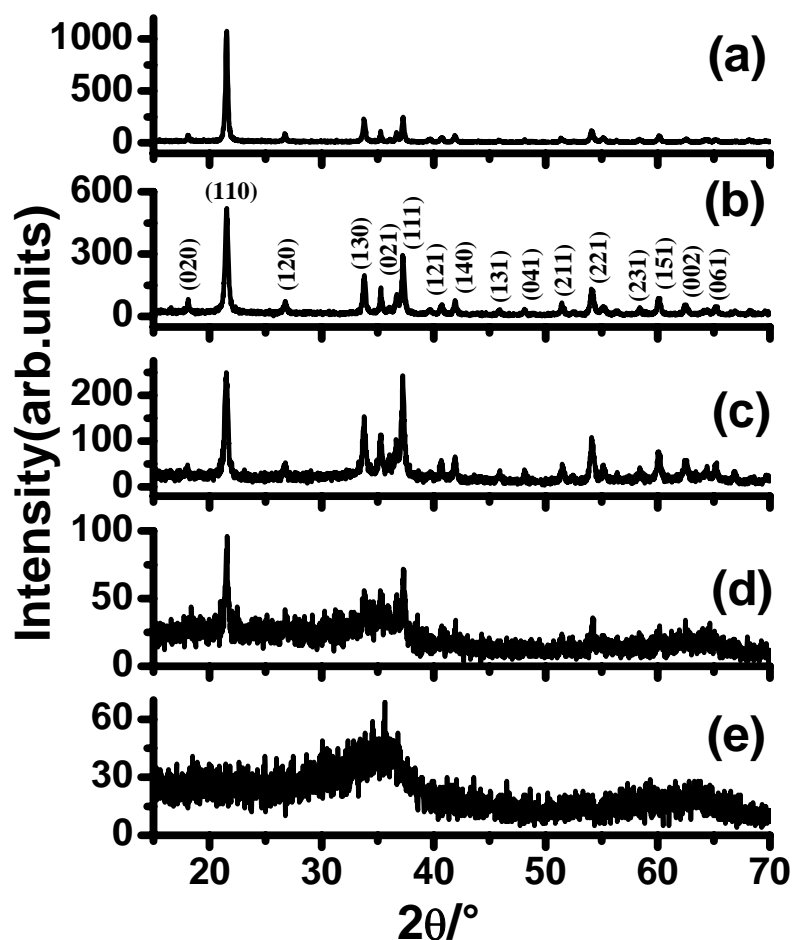


Fig.20 XRD patterns of GaOOH sample prepared in presence of (a) 0 at % (b) 0.5 at % (c) 0.75 at % (d) 1 at % and (e) 2 at % of Eu^{3+} ions.

Based on these results, it can be inferred that the Eu^{3+} ions are not replacing Ga^{3+} ions in the lattice of GaOOH . It is also in accordance with the significantly different ionic radii of Ga^{3+} and Eu^{3+} ions (0.62\AA and 0.95\AA respectively) [172] under a coordination number of six. However, broadening of the peaks and conversion of crystalline GaOOH to an amorphous phase with increase in Eu^{3+} concentration suggest that the GaOOH lattice is influenced by the presence of Eu^{3+} in the reaction medium. Similar results are also observed with Dy^{3+} and Tb^{3+} doped samples and corresponding XRD patterns are shown in Fig.21.

Table 1. Variation in the lattice parameters of GaOOH samples prepared in the presence of Eu^{3+} ions.

Eu^{3+} concentration (at %)	GaOOH			
	a (\AA)	b (\AA)	c (\AA)	Cell volume (\AA^3)
0	4.546(2)	9.797(2)	2.972(3)	132.35(2)
0.5	4.544(3)	9.786(2)	2.976(3)	132.32(2)
0.75	4.541(3)	9.787(3)	2.975(2)	132.23(3)
1	4.527(4)	9.805(3)	2.975(2)	132.05(4)

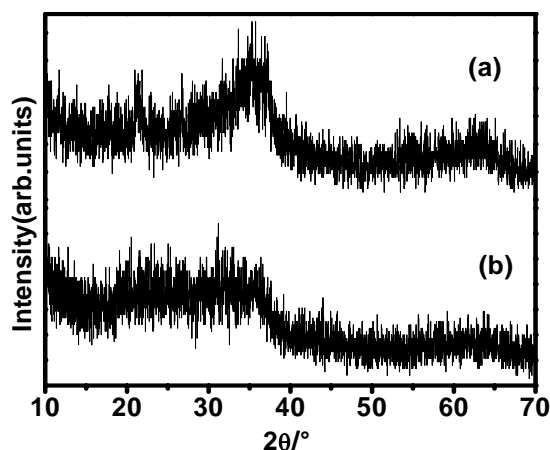


Fig.21. XRD patterns of GaOOH samples prepared in presence of (a) 2 at % Tb^{3+} and (b) 2 at % Dy^{3+} .

From the above studies, it is inferred that even the presence of around 2 at % Eu^{3+} / Tb^{3+} / Dy^{3+} during the precipitation process of GaOOH can significantly affect its

crystallinity. Thus, it was considered worthwhile to investigate the role played by lanthanide ions on the structural changes and associated stability of GaOOH nanorods. Hence, detailed structural and morphological investigations have been carried out on the samples and the results are described below.

Figure 22 shows SEM images of GaOOH samples prepared in the presence of different concentrations of Eu^{3+} ions. GaOOH sample prepared in the absence of Eu^{3+} ions showed rod like morphology (Fig.22 (a)). The rods have length around 2.5-3 μm and width around 300-400 nm. Similar rod like morphology has also been reported earlier for GaOOH samples prepared either by urea hydrolysis or by hydrothermal synthesis [56, 171, 182]. For GaOOH sample prepared in the presence of 0.5 at % Eu^{3+} ions, the nanorods have length around 1.5 to 2 μm and width around 200-300 nm (Fig.22 (b)). However when the GaOOH sample is prepared in the presence of 1.0 at % Eu^{3+} ions, along with nanorods a significantly aggregated/ agglomerated phase (with irregular shape) is also formed as is evident from the SEM image (Fig.22 (c)). The nanorods have size in the range of 0.5-2 μm and width around 200 nm. No nanorod formation is observed for samples containing more than 1 at % Eu^{3+} ions, instead an aggregated bulk phase is observed in the representative SEM image, (Fig.22 (d)). Based on XRD and SEM results, it can be inferred that the presence of Eu^{3+} ions prevents the formation of GaOOH nanorods or destroys the layered structure of GaOOH. In order to understand thoroughly the role of Eu^{3+} ions in the formation of GaOOH phase or on the structural changes of GaOOH lattice, it is necessary to know structural features of GaOOH and linkages between the basic building units constituting GaOOH lattice. Accordingly, in GaOOH structure, six oxygen atoms forming an irregular octahedron surround each Ga atom. Each octahedron shares edges with four neighbouring GaO_6 octahedra to form double chains along the c-axis. This structure consists of two non-equivalent axial oxygen atoms namely O_a and O_b . One of the octahedral axes, i.e. GaO_a is

almost normal to the equatorial plane with Ga at the centre, while the other octahedral axis formed with GaO_b is slightly tilted from the normal. The inequivalent oxygen atoms (O_a and O_b) form two different kinds of OH linkages in the GaOOH structure, with one of the axial oxygen atom (O_b) bonded directly to hydrogen, while another oxygen atoms (O_a) is hydrogen bonded with hydrogen of the neighboring octahedron.

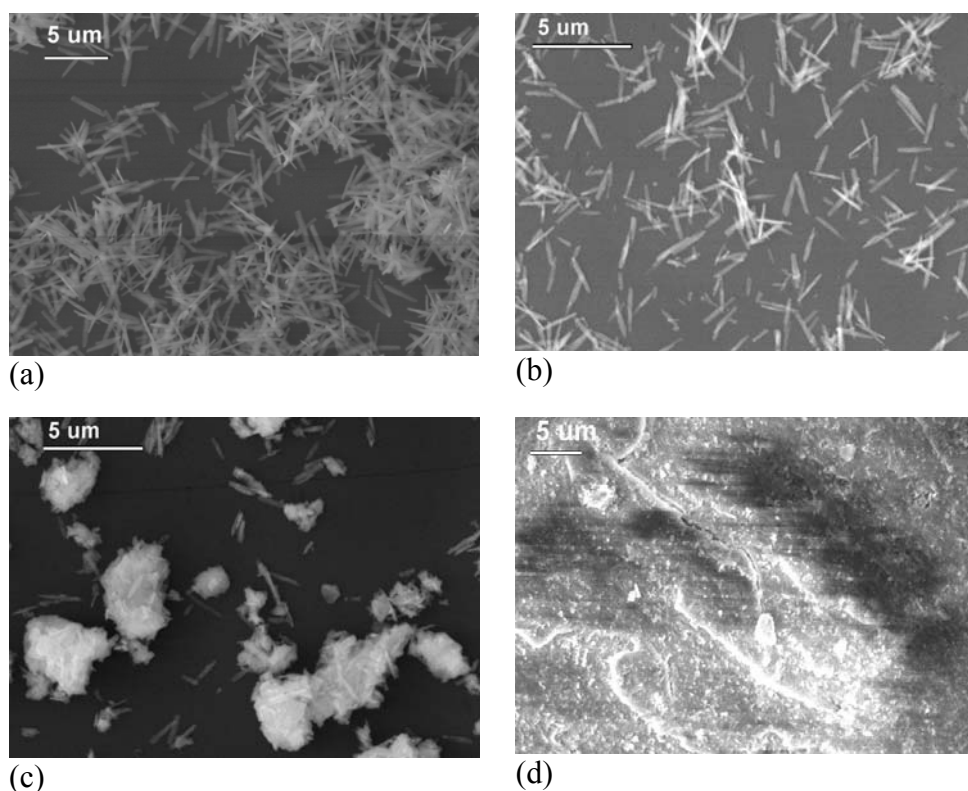


Fig.22. SEM images of GaOOH nanorods prepared in presence of (a) 0 at % Eu^{3+} (b) 0.5 at % Eu^{3+} (c) 1 at % Eu^{3+} and (d) 2 at % Eu^{3+} .

GaOOH phase has a structure similar to the mineral diasporite ($\alpha\text{-AlO}(\text{OH})$) [183]. Detailed vibrational studies were carried out using infrared (IR) and Raman spectroscopic techniques for understanding the effect of Eu^{3+} incorporation on the structure of GaOOH lattice. IR patterns corresponding to GaOOH samples prepared in presence of different concentrations of Eu^{3+} ions is shown in Fig.23 (A and B). For the purpose of direct comparison the IR pattern of $\text{Ga}(\text{OH})_3$ prepared by adding ammonium hydroxide to Ga^{3+} solution is also shown in the same figure (Fig.23 A(f)). GaOOH nanorods prepared without

any Eu^{3+} ions is characterised by sharp peaks at 1016, 947, 658, 526, 474, and 385 cm^{-1} (Fig.23A) along with a broad peak in the region 3670-2640 cm^{-1} (Fig.23 (B)). As is evident from Fig.23 (A) the peaks at 385 and 526 cm^{-1} disappear with Eu^{3+} incorporation, while the peaks at ~ 474 , 658, 947 and 1016 cm^{-1} are broadened. Furthermore, new modes starts appearing at 1490 and 1635 cm^{-1} , which are absent in pure GaOOH sample. Similar changes are also observed in the Raman spectra (Fig.23 (C)). The signal to noise ratio of Raman spectrum degraded significantly when Eu^{3+} content increased beyond 1 at %. The Raman spectrum of sample without Eu^{3+} incorporation shows well-defined peaks at ~ 276 , 433, 525, 612 and 696 cm^{-1} . With Eu^{3+} incorporation, width of the Raman peaks at ~ 525 cm^{-1} and 612 cm^{-1} increase, due to the development of additional shoulder peaks at ~ 550 and ~ 650 cm^{-1} and is attributed to GaOOH lattice distortions. A Summary of peaks observed with different samples with possible assignments, together with that observed in $\text{Ga}(\text{OH})_3$ is given in Table 2. As the peaks are significantly overlapping, de-convolution of individual peaks from the IR patterns could not be performed for estimating the line width. Even though there is broadening of peaks with increase in Eu^{3+} content, the peak positions corresponding to different vibrational modes in these samples remained same within experimental errors.

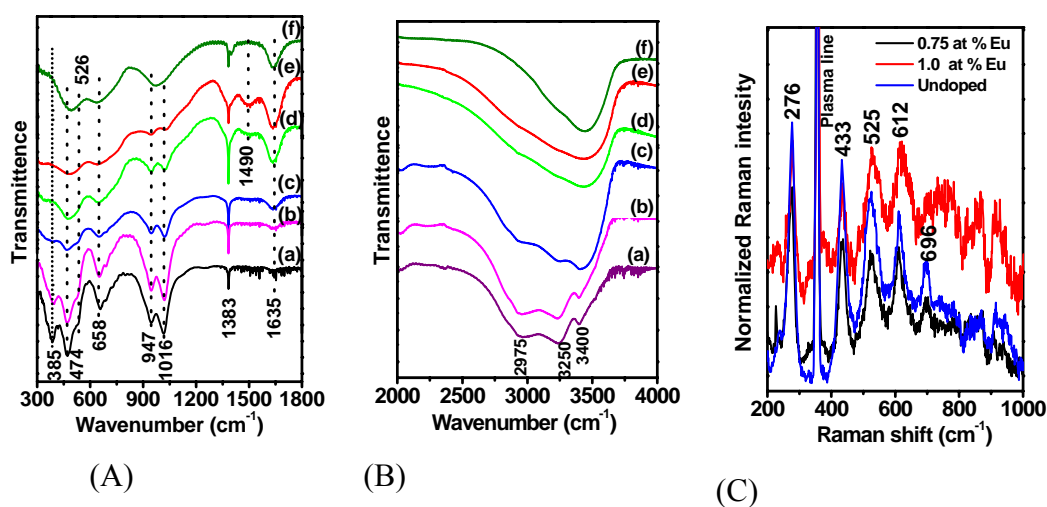


Fig.23. FT-IR patterns (A and B) of GaOOH sample prepared in presence of (a) 0 at % (b) 0.5 at % (c) 0.75 at % (d) 1 at % (e) 2 at % of Eu^{3+} ions and (f) amorphous $\text{Ga}(\text{OH})_3$. The Raman spectrum from the representative samples are shown in Fig.23 (C).

Table 2. Summary of important modes of vibrations in GaOOH nanorods containing different amounts of Eu³⁺ ions along with that of Ga(OH)₃.

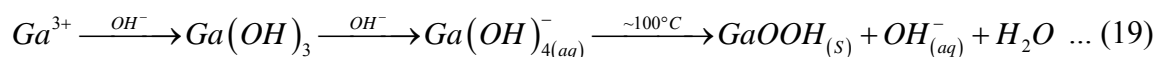
Frequencies in GaOOH (0% Eu)	GaOOH:0.75 %Eu	GaOOH:1%Eu	Ga(OH) ₃	Assignment
3400 (IR)	3410	3430	3440	OH-stretching (physisorbed H ₂ O)
3250 (IR)	3254 (w, br)			OH-stretching (non hydrogen bonded)
2975 (IR)	2940 (w, br)			OH-stretching (hydrogen bonded)
1635 (IR)	1638	1641	1634	OH bending modes
1016 (IR)	1016	1014	973 (br)	δ (OH) deformation modes
947 (IR)	944	941		
658 (IR)	646	640	633	Ga-O vibrations
612 (R)	611	608	-	Lattice modes
525 (R)	525	522	-	Stretching modes of GaO ₆ octahedra
474 (IR)	464	470	490	Stretching vibrations of GaO ₂ chains
433 (R)	430	425	-	-
385 (IR)	387	-	-	Deformation mode of GaO ₆ octahedron
276 (R)	274	-	-	-

The regular GaO₆ octahedron has an O_h symmetry and in principle should have 15 modes having the symmetry, $\Gamma_{\text{vib}} = A_{1g}(\text{R}) + E_g(\text{R}) + 2T_{1g}(\text{IR}) + T_{2g}(\text{R}) + T_{2u}$ [184]. The prominent Raman modes in such a regular octahedron are observed at 526 (A_{1g}), 430 (E_g) and 328 cm⁻¹ (T_{2g}). The only mode observed in IR is found at around 510 cm⁻¹. However, in GaOOH, the GaO₆ octahedron is distorted and hence many more modes become active in IR. According to Zhao and Frost [185] the peaks at 276, 433 and 525 cm⁻¹ are due to the associated Ga-OH units of α - GaOOH phase. The 474 cm⁻¹ peak in IR has been assigned to the stretching mode of GaO₂ chains. The peak at 385 cm⁻¹ is attributed to deformation mode corresponding to GaO₆ and is reported both in GaOOH and in β -Ga₂O₃ [186, 187]. This is because both GaOOH and Ga₂O₃ are made up of GaO₆ octahedra as basic building units. Peaks around 1016 and 947 cm⁻¹ are arising due to the δ (OH) deformation vibrations [141]. The peaks at ~612 and 696 cm⁻¹ observed in Raman spectra are however not clearly

understood, but these peaks have also been observed in the GaOOH nanorods [185]. The disappearance of peaks at 385 and 525 cm^{-1} , together with reduced intensity of other peaks, clearly indicate that Eu^{3+} incorporation results in the disruption of basic building blocks of GaOOH phase. When the later is compared with amorphous $\text{Ga}(\text{OH})_3$ sample, similar features are observed in $\text{Ga}(\text{OH})_3$ sample too, indicating that the crystal structure is being disrupted with Eu^{3+} addition and finally with more than 1 at. % Eu^{3+} it is completely disrupted. This is further evident by new peaks appearing at ~ 1490 and 1635 cm^{-1} for GaOOH containing higher Eu^{3+} concentrations (Fig.23 (A)). Based on the previous IR studies of rare earth hydroxides like $\text{La}(\text{OH})_3$ [188] and the pattern corresponding to $\text{Ga}(\text{OH})_3$ shown in Fig.23A(f), the peaks at 1490 and 1635 cm^{-1} have been attributed to the bending vibrations of the OH groups associated with $\text{Eu}(\text{OH})_3$ and $\text{Ga}(\text{OH})_3$ phases respectively. Another peak at 1383 cm^{-1} which is present in the FT-IR patterns of all the samples is arising due to adsorbed carbonate species [56, 189] formed during sample preparation. The structure of GaOOH being affected by Eu^{3+} incorporation is also seen in the high frequency region $\sim 3500\text{-}2600 \text{ cm}^{-1}$. This may be considered as the overlapping of peaks around 3400 , 3250 and 2975 cm^{-1} (Fig.23B). From the previous vibrational studies [56, 182, 190-194] on GaOOH and AlOOH (which has the structure similar to GaOOH), the peak around 3400 cm^{-1} can be attributed to the OH stretching vibrations of physisorbed H_2O molecules, while that 2975 and 3250 cm^{-1} may be attributed to the two different kinds of OH bonds associated with its structure. As discussed earlier, in the basic building unit of GaOOH, the two non-equivalent oxygen atoms in the GaO_6 octahedron are bound differently to the adjacent hydrogen atoms. One of the oxygen atoms is bound directly to hydrogen, while the other one is bound via the hydrogen bonding, making differences in their bond strengths. The peak at $\sim 2975 \text{ cm}^{-1}$ is attributed to the stretching vibrations of the OH groups which are hydrogen bonded to GaO_6 octahedra, while the peak at $\sim 3250 \text{ cm}^{-1}$ is due to non-hydrogen bonded OH linkages. The

systematic disappearance of these two absorptions in the Eu^{3+} containing GaOOH sample, indicate that Eu^{3+} is in fact affecting the lattice structure through the OH linkages.

An attempt was made to understand structural changes taking place in the GaOOH lattice with Eu^{3+} incorporation. At this stage, it is necessary to understand how the GaOOH phase is being formed and how interactions with lanthanide ions affect different types of linkages in GaOOH lattice. Under alkaline conditions GaOOH is thought to be formed from $\text{Ga}(\text{OH})_4^-$ species generated in solution (equation 19) [143]. This $\text{Ga}(\text{OH})_4^-$ on thermal decomposition at $\sim 100^\circ\text{C}$ leads to the formation of GaOOH.



A schematic representation of a fragment of GaOOH lattice, depicting GaO_6 octahedra, O tetrahedra and H atoms attached with oxygen atoms, obtained by the simulation program MOLDRAW [195] is shown in Fig.24. The unit cell is shown within the rectangle drawn with light black line. Hydrogen bonds existing between the layers stabilize the layered structure of GaOOH. When lanthanide ions like Eu^{3+} are present in the reaction medium, due to the higher solubility product of lanthanide hydroxides ($\text{Ln}(\text{OH})_3$) compared to $\text{Ga}(\text{OH})_3$ [196], the $\text{Ga}(\text{OH})_3$ is formed initially and this later reacts with OH^- in the reaction medium to form $\text{Ga}(\text{OH})_4^-$. As concentration of Eu^{3+} ions are much smaller compared to Ga^{3+} , it is quite possible that each Eu^{3+} ion will have number of $\text{Ga}(\text{OH})_4^-$ species in their vicinity. For the purpose of charge neutrality minimum of three anionic species ($\text{Ga}(\text{OH})_4^-$) must be surrounding the Eu^{3+} ions. On decomposition of $\text{Eu}^{3+}-3\text{Ga}(\text{OH})_4^-$ species to GaOOH:Eu at $\sim 100^\circ\text{C}$, Eu^{3+} ions can either migrate to Ga^{3+} site in the GaOOH lattice or it can occupy the space between the layers of GaOOH. Due to smaller ionic radius of Eu^{3+} compared to inter layer spacing of GaOOH ($\sim 2.5 \text{ \AA}$) [197], Eu^{3+} ions/ species have a tendency to get incorporated at the inter-layers of GaOOH wherein it can preferentially interact with OH groups to form europium hydroxide species. Formation of such hydroxide species

destabilizes the layered structure of GaOOH. As each Eu^{3+} ions can react with three OH groups, small amounts of Eu^{3+} in GaOOH is sufficient to create significant destabilization of the lattice leading to collapse of its structure and associated amorphization. These changes are schematically shown in Fig.24. There is another possibility that the protons of the OH linkages can undergo ion exchange with the Eu^{3+} ions and this in turn can lead to the collapse of the layered GaOOH structure. In order to check this aspect, ion exchange studies were carried out and are described below.

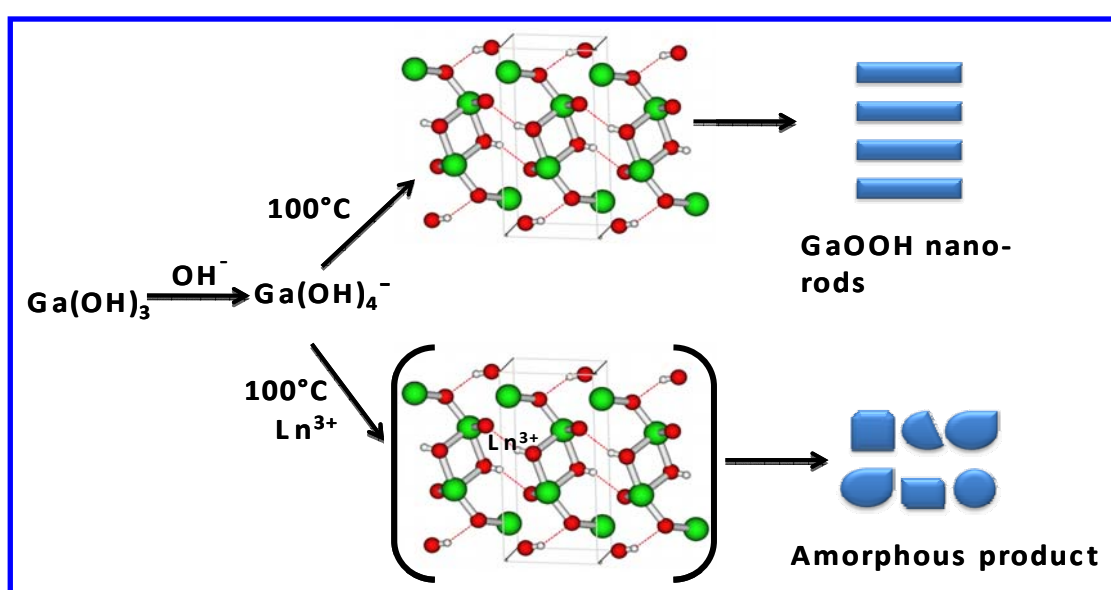


Fig.24. GaOOH structure obtained using the software MOLDRAW, depicting the interaction of Eu^{3+} ions with GaOOH lattice and collapse of its layered structure to form amorphous gallium and europium hydroxide. Colour code: Green spheres represent Gallium, red spheres represent oxygen and white spheres represent hydrogen. Dotted red lines represent hydrogen bonding.

Figure 25 shows the XRD patterns of the product obtained by mixing GaOOH nanorods with aqueous solution of europium nitrate heated in the presence of urea for 30 minutes and 2 hours around 100°C (samples were isolated after treatment by centrifugation). XRD patterns of the samples obtained after 30 minutes and 2 hours of heat treatment are primarily GaOOH together with europium hydroxide carbonate (Fig.25 (b and c)) and the formation of the latter increases with increasing reaction time. For the purpose of

comparison, Eu^{3+} ions alone in water is subjected to urea treatment as described above for two hours and XRD pattern of the precipitate is shown in Fig.25 (d). The pattern matches well with that of crystalline europium hydroxide carbonate (PC-PDF-No: 43-0603). These results further confirm that ion exchange process is not responsible for the collapse of the layered structure of GaOOH instead Eu^{3+} incorporation at the inter layer spacing and its reaction with OH groups at the inter layer spacing may be a reason for amorphisation. Such amorphisation process is also expected to have significant effect on the luminescence properties of lanthanide ions and hence detailed luminescence studies were carried out for these samples and are described below.

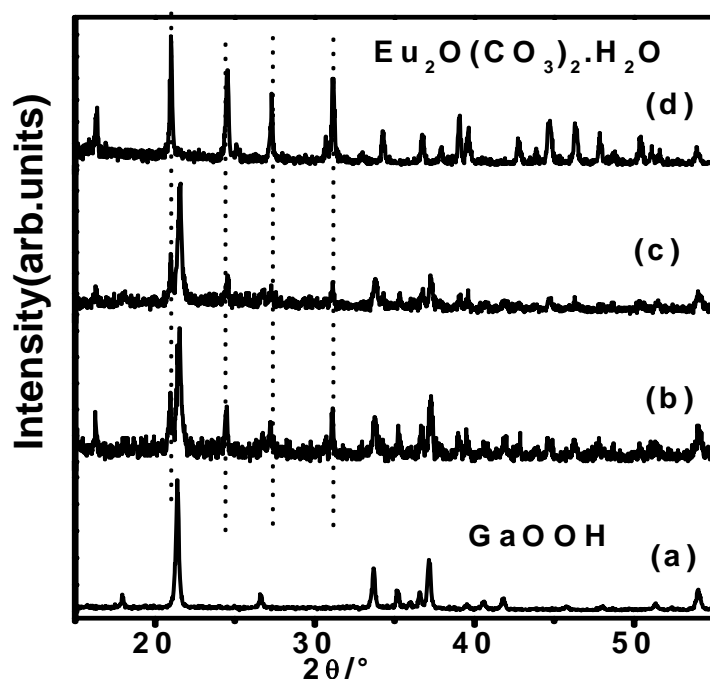


Fig.25. XRD patterns corresponding to GaOOH nanorods treated with aqueous solution of Eu^{3+} ion in presence of urea $\sim 100^\circ\text{C}$ for (a) 0 minutes (b) 30 minutes (c) 2 hours. The corresponding pattern obtained only with Eu^{3+} ions in the absence of GaOOH is shown in Fig.25 (d).

Figure 26 shows the emission and excitation spectrum of as prepared GaOOH nanorods synthesized in the absence of lanthanide ions (Eu^{3+}). The emission spectrum matches well with that reported by Huang and Yeh [182]. Emission spectrum is characterized by a peak around 435 nm, which is arising from the electronic transition involving Ga-O

bonds in the GaO₆ octahedra. Based on photoluminescence studies of a variety of gallium compounds containing GaO₆ octahedra [182, 198-201] the emission around 435 nm has been attributed to recombination of electrons trapped at oxygen vacancies and hole trapped at Ga³⁺ vacancies present in GaOOH. Peaks around 360 and 280 nm characterize corresponding excitation spectrum. UV-visible optical absorption studies [182] have revealed that GaOOH has an optical band gap of ~ 4.4 eV (~280 nm) and hence the excitation peak around 280 nm is assigned to the excitation of electron from valence band to conduction band of GaOOH. The other excitation peak around 360 nm is attributed to excitation of electrons from valence band to defect levels (oxygen vacancies) present in the lattice. Existence of energy transfer from hosts like Ga₂O₃ to lanthanide ions is used as criteria to confirm the lanthanide ion incorporation in host. In order to find out whether lanthanide ions are incorporated in the GaOOH lattice, detailed luminescence experiments were carried out for lanthanide ions doped GaOOH samples and are described below.

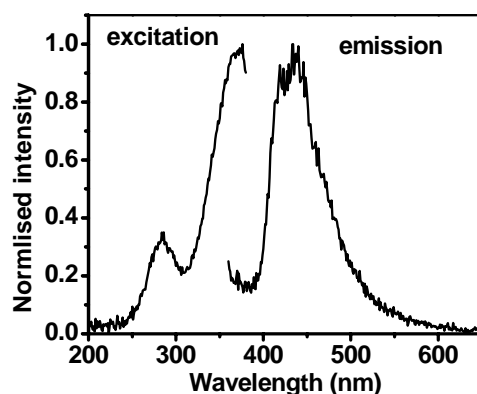


Fig.26. Emission spectrum obtained after 280 nm excitation and excitation spectrum corresponding to 435 nm emission from GaOOH nanorods prepared in the absence of any Eu³⁺ ions.

Figure 27 (right) shows the emission spectrum of GaOOH nanorods prepared in the presence of different concentrations of Eu³⁺ ions. Peaks around 590 and 615 nm, which are due to the magnetic, characterize the emission spectrum and electric dipole allowed ⁵D₀→⁷F₁ and ⁵D₀→⁷F₂ transitions, respectively of Eu³⁺ ions. The emission spectrum is the same for all

the samples, suggesting that Eu^{3+} environment is not changing with increase in Eu^{3+} content in the medium. The relative intensity ratio of ${}^5\text{D}_0 \rightarrow {}^7\text{F}_2$ (615 nm) to ${}^5\text{D}_0 \rightarrow {}^7\text{F}_1$ (590 nm) transition, known as the asymmetric ratio of luminescence, is found to be around 2.6 for all the samples further confirming that the Eu^{3+} environment is same in all the samples. The excitation spectrum corresponding to 615 nm emission from these samples is shown in Fig. 27(left). The patterns essentially consist of sharp peaks characteristic of the intra 4f transitions along with broad peaks centered ~ 265 and 360 nm. The peak at 265 nm arises due to the Eu-O charge transfer process. This peak overlaps with that of host excitation peak around 280 nm whereas the peak ~ 360 nm is due to excitation of electrons to the defect levels present in GaOOH host as can be clearly seen in the excitation spectrum corresponding to GaOOH nanorods prepared in the absence of Eu^{3+} ions (Fig.26).

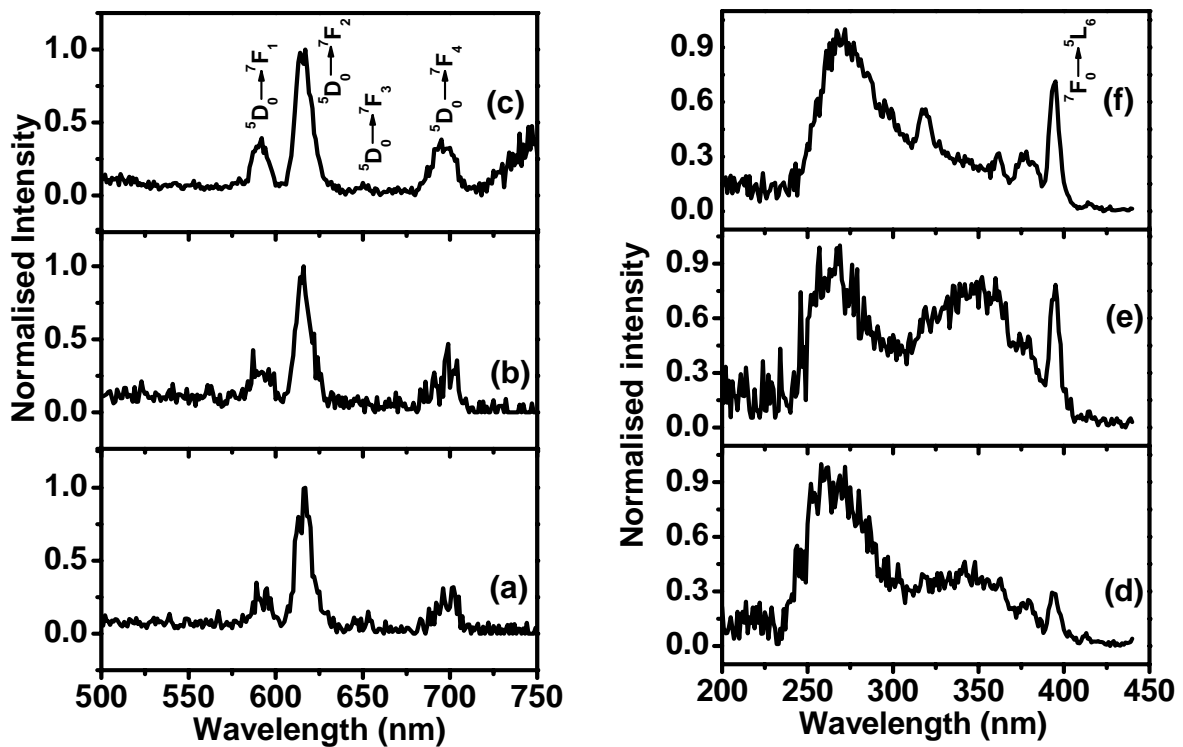


Fig.27. Emission spectrum (left) obtained at 350 nm excitation and excitation spectrum (right) corresponding to 615 nm emission from GaOOH nanorods prepared in the presence of (a and d) 0.5 at % Eu^{3+} , (b and e) 0.75 at % Eu^{3+} , (c and f) 2 at % Eu^{3+} .

Appearance of a broad host excitation peak ~ 360 nm in the excitation spectrum by monitoring Eu^{3+} emission around 615 nm suggests that Eu^{3+} emission can be observed by exciting the host at 360 nm. This is possible only when excited charge carriers in GaOOH host transfers its energy to Eu^{3+} ions. In other words, energy transfer occurs from host GaOOH nanorods to Eu^{3+} species. Similar results were also observed with GaOOH: Tb^{3+} and GaOOH: Dy^{3+} samples. Representative emission and excitation spectra from GaOOH: Dy^{3+} (1 at % Dy^{3+}) are shown in Fig.28.

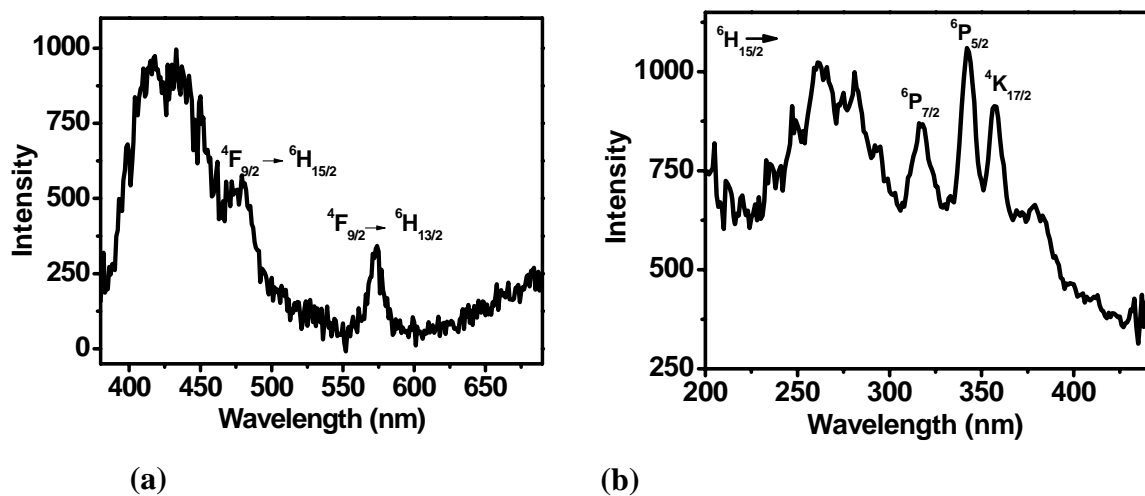


Fig.28. (a) Emission spectrum obtained by exciting the samples at 280 nm and (b) excitation spectrum for the emission at 575 nm from GaOOH nanorods prepared in the presence of 1 at % Dy^{3+} ions.

Energy transfer efficiency (η) has been calculated from the emission spectrum of GaOOH and GaOOH: Dy^{3+} nanorods based on the equation, $\eta = 1 - I_d/I_{d0}$, where I_d and I_{d0} are intensity of emission in presence and absence of Dy^{3+} ions, respectively [56]. The efficiency is $\sim 32\%$ for GaOOH: Dy^{3+} . Generally, high values of energy transfer efficiency (of the order of 90%) are observed for lanthanide ions when incorporated in hosts like Ga_2O_3 . Such a low value of energy transfer efficiency indicates that the lanthanide ions are not incorporated in GaOOH host, but forms a separate Ln^{3+} species, which is intimately mixed with the GaOOH/amorphous gallium hydroxide phase. Due to this intimate mixing there can be some Ln^{3+} species close to the surface of GaOOH and this leads to the weak energy transfer.

These inferences are further substantiated by decay curves corresponding to 5D_0 level of Eu^{3+} (Fig.29 (a)) from these samples. The decay has been found to be single exponential for all the samples with lifetime value around $340\mu\text{s}$. The values are higher than that of Europium hydroxide ($250\mu\text{s}$) prepared by the identical method as that of GaOOH. Identical lifetime values corresponding to the 5D_4 level of Tb^{3+} ions (1.2 ms (80%) and $388\mu\text{s}$ (20%)) are also observed for GaOOH samples containing different amounts of Tb^{3+} (Fig.29 (b)). Hence from the decay curves and emission spectra, it is inferred that lanthanide hydroxide phase is finely mixed with amorphous gallium hydroxide and crystalline GaOOH phase. These results are further supported by the thermo-gravimetry and differential thermal analysis studies on the samples.

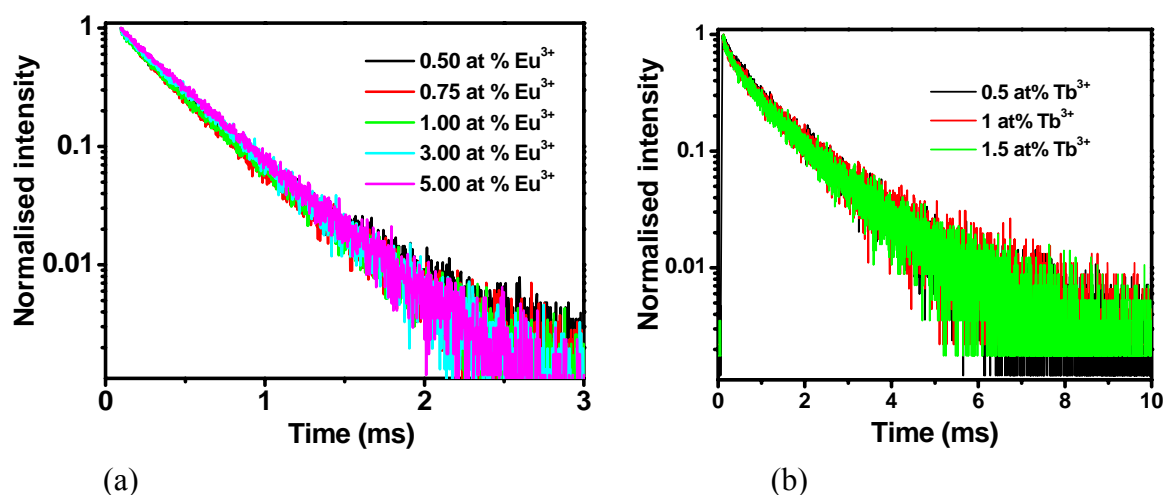


Fig.29. Decay curves corresponding to (a) 5D_0 level of Eu^{3+} ions (b) 5D_4 level of Tb^{3+} ions from GaOOH samples prepared with different concentrations of Eu^{3+} and Tb^{3+} ions, respectively. ($\lambda_{\text{exc}} = 270, 255\text{ nm}$ and $\lambda_{\text{em}} = 615, 545\text{ nm}$ for Eu^{3+} and Tb^{3+} doped GaOOH, respectively)

Thermo gravimetric (TG) and differential thermal analysis (DTA) patterns of the GaOOH sample prepared in the presence of different concentrations of Eu^{3+} ions are shown in Fig.30. GaOOH sample prepared in the absence of any Eu^{3+} ions is characterised by two stages of weight losses in its thermogram (Fig.30 (a)). They are in the range of $200\text{-}280^\circ\text{C}$ and $350\text{-}420^\circ\text{C}$ and have been attributed to dehydration of surface bound hydroxyl groups

and constitutional hydroxyl groups respectively present with GaOOH samples. The weight loss is around 9% in the range of 350 to 420°C, confirming the dehydration from GaOOH phase [27]. Such dehydration processes are characterised by endothermic peaks around 230 and 400°C in the corresponding DTA pattern. Beyond 420°C, there is no significant change in the weight with increase in temperatures as is clear from the straight line with negligible slope observed beyond 420°C in the TG pattern shown in Fig.30 (a). However, the DTA pattern showed a broad exothermic peak in the region 640 to 1040°C. This is due to the conversion of α -Ga₂O₃ phase to β -Ga₂O₃.

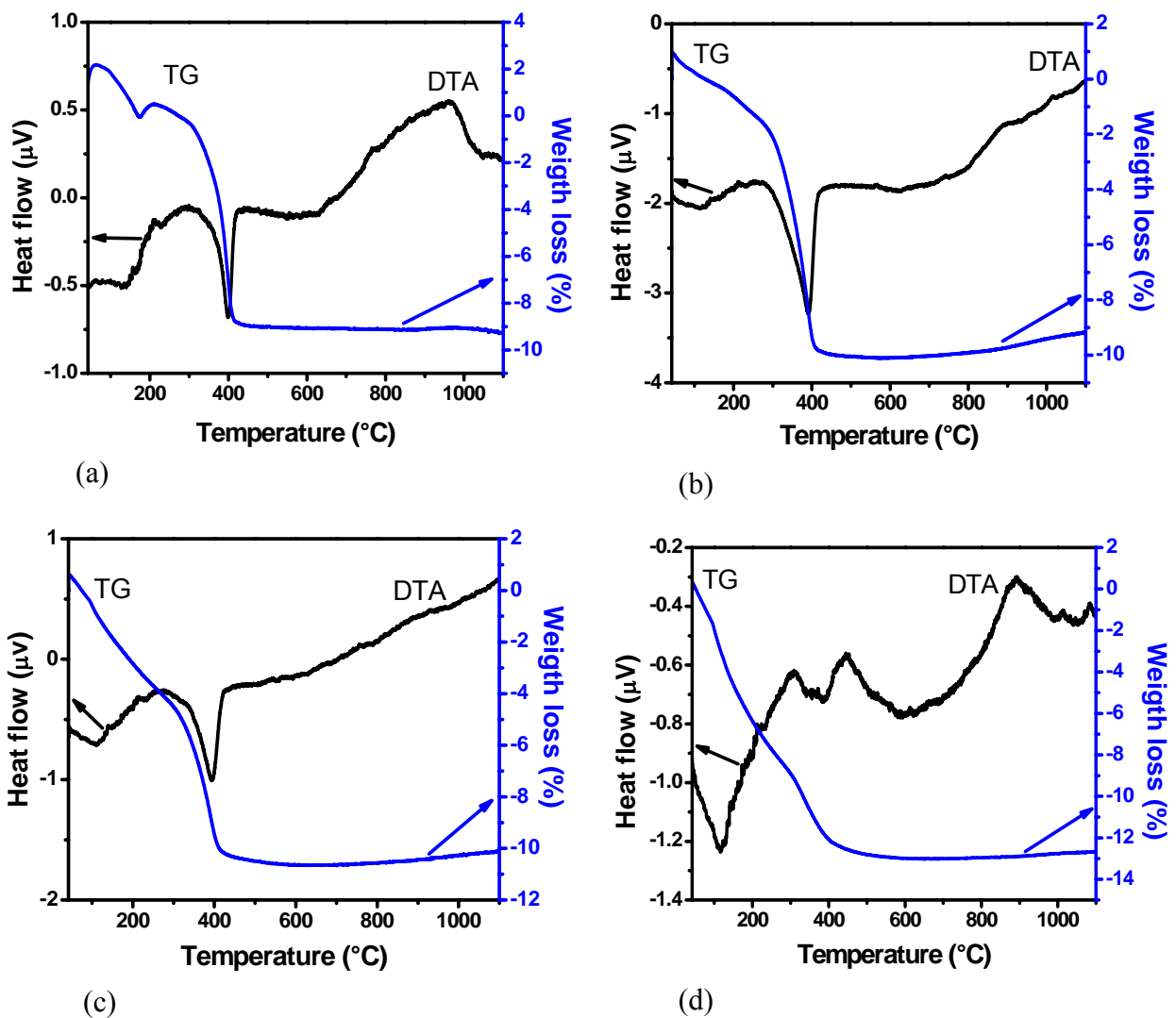


Fig.30. TG-DTA patterns of GaOOH nanorods prepared in presence of (a) 0 at % (b) 0.5 at % (c) 0.75 at % and (d) 1 at % Eu³⁺ ions.

Similar DTA peaks have been reported earlier [189, 192] for decomposition of GaOOH. The GaOOH sample prepared in presence of 0.5 at % Eu^{3+} ions (Fig.30 (b)), both TG and DTA patterns are essentially similar to that of GaOOH nanorods shown in Fig.30 (a). However, the DTA peaks are slightly broadened for the Eu^{3+} containing sample as can be seen from Fig.30 (b). Broadening of the peak has been attributed to distortion taking place with the Ga-O bonds associated with Ga-OH linkages brought about by its interaction with Eu^{3+} ions. The percentage loss of weight is found to be around 9% over the region of 230 to 400°C, which is characteristic of the dehydration process in GaOOH. The initial dehydration step in the region 200-280°C is more predominant for GaOOH sample prepared with 0.75 at % Eu^{3+} ions (Fig.30 (c)) as compared to the corresponding step for the GaOOH sample prepared with 0.5 at % Eu^{3+} . In addition to this, the weight loss below 400°C is ~10 %, suggesting that another hydroxide species along with GaOOH phase is present with the sample. This is namely the $\text{Ga}(\text{OH})_3$ phase formed by the collapse of a part of the layered GaOOH structure. But the DTA pattern is comparable with that of GaOOH sample prepared with 0.5 at % Eu^{3+} . For GaOOH sample prepared with 1 at % Eu^{3+} ions, both DTA and TG patterns significantly changed (Fig.30 (d)). The weight loss of ~12% is indicative of an increase in the extent of gallium hydroxide phase along with the GaOOH phase. The DTA pattern (Fig.30 (d)) is similar to that obtained for a group 13 metal hydroxides like $\text{In}(\text{OH})_3$ [202, 203] and can be considered as overlapping of the DTA patterns of $\text{Ga}(\text{OH})_3$ and GaOOH present in the sample. From these results it is inferred that GaOOH undergo complete decomposition in the presence of Eu^{3+} ions at a concentration >1 at % forming $\text{Ga}(\text{OH})_3$ species. Hence the TG-DTA results are in conformity with the inferences drawn from XRD and photo luminescence studies.

3.4. Effect of heat treatment on crystal phase and morphology of Ga_2O_3 and $\text{Ga}_2\text{O}_3:\text{Ln}^{3+}$ nanomaterials: GaOOH nanorods on heating get converted to rhombohedral $\alpha\text{-Ga}_2\text{O}_3$ at

500°C and monoclinic β -Ga₂O₃ at 900°C as can be seen from the XRD patterns (Fig.31). All the diffraction peaks have been assigned to corresponding planes. Average crystal size was calculated by using Debye-Scherrer formula and is 40 nm for GaOOH, 22 nm for α -Ga₂O₃ and 19 nm for β -Ga₂O₃. In order to check morphology changes occurring during heat treatment, SEM measurements were carried out and are shown in Fig.32. From these images it is clear that rod shape morphology of GaOOH is maintained even after heat treatment to form α - and β -Ga₂O₃ phases.

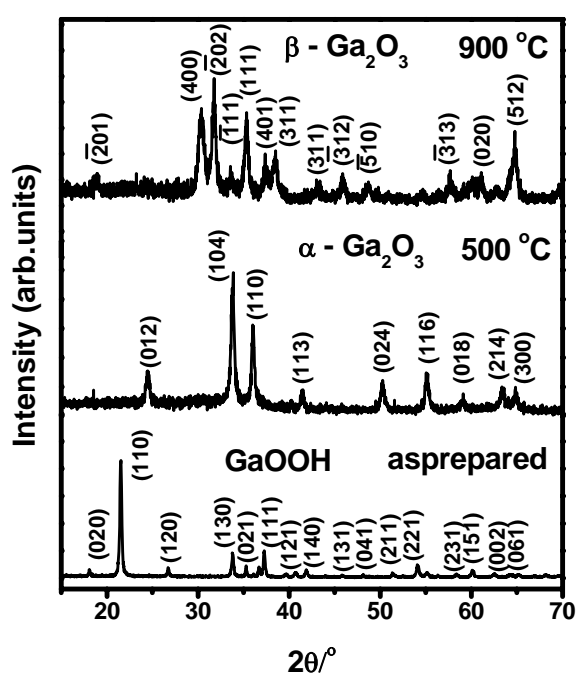
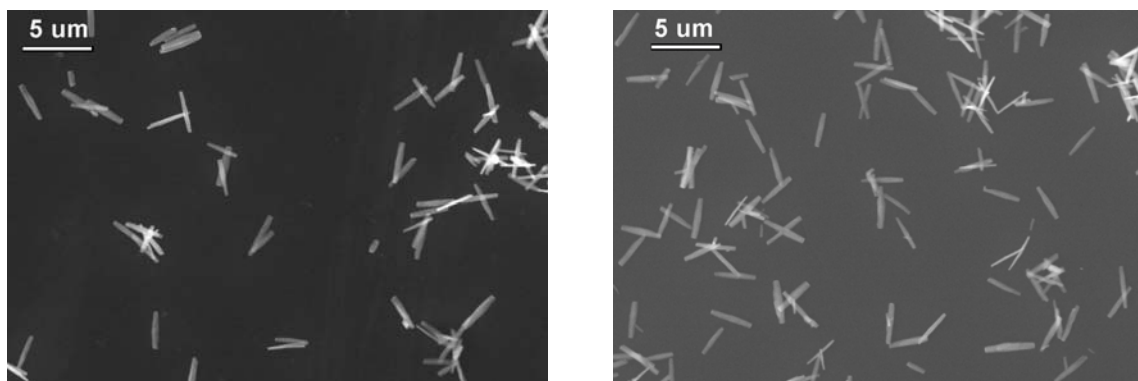


Fig.31. XRD patterns of as prepared, 500 and 900°C heated GaOOH nanorods



(a) (b)
Fig.32 SEM images of GaOOH nanorods heated at (a) 500°C and (b) 900°C

GaOOH samples doped with different amounts of lanthanide ions were heated at 500°C and their XRD patterns are shown in the Fig.33. Samples prepared with less than 1 at % Eu are crystalline in nature with α - Ga₂O₃ structure whereas above 1 at % Eu³⁺ doping leads to the formation of amorphous samples. In order to check the structural changes with Eu³⁺ incorporation, FT-IR measurements were carried out on undoped and 0.5, 0.75, 1, 2, 3 and 5 at% Eu³⁺ doped GaOOH samples which were subjected to heat treatment at 500°C (Fig.34).

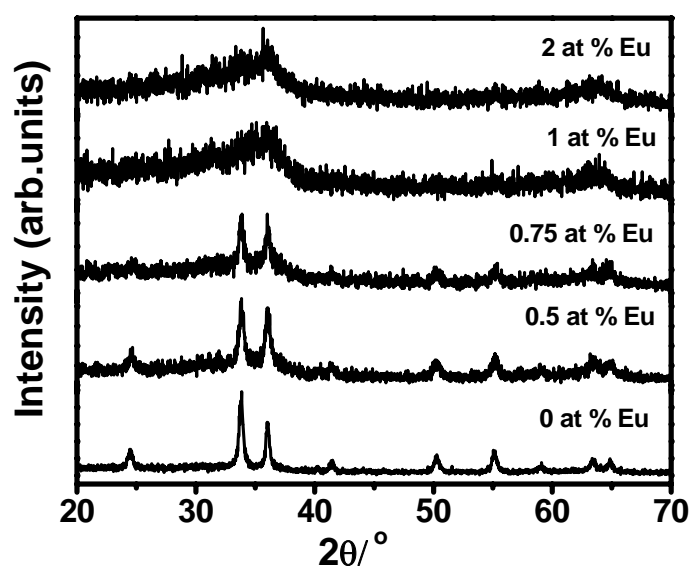


Fig.33 XRD patterns of GaOOH samples containing 0, 0.5, 0.75, 1 and 2 at % of Eu³⁺ ions after heat treatment at 500°C.

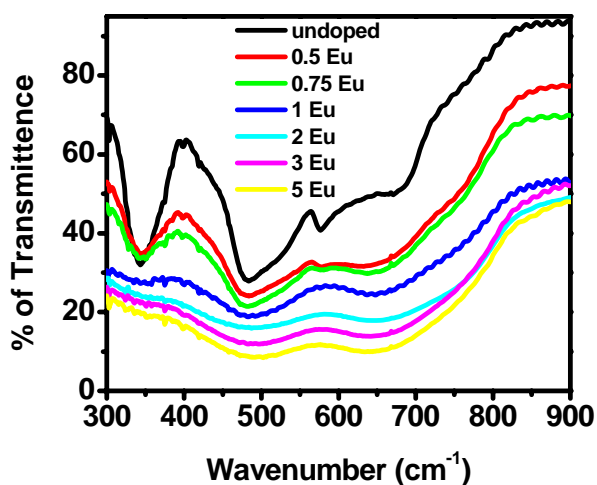


Fig.34. FT-IR spectra of GaOOH samples containing 0, 0.5, 0.75, 1, 2, 3 and 5 at % of Eu³⁺ ions after heat treatment at 500°C.

All the samples show three bands centered around 345, 482 and 675 cm^{-1} . The peak width increases with increase in Eu concentration and this has been assigned to the increased distortion in the Ga_2O_3 lattice brought about by Eu^{3+} incorporation. The bands also shifted towards lower wave numbers for the samples doped up to 0.75 at % Eu^{3+} (for the samples doped above 0.75 at %, the peak is so broad that shifting of the peak maxima could not be clearly observed). This can be explained based on the difference in the mass of gallium and lanthanide ions. Red shift in the peak maxima can be explained based on the heavier mass of Eu^{3+} ions compared to Ga^{3+} ions, indicating the formation of Ga-O-Eu type of linkages. Increase in broadening of the IR peaks beyond 0.75 at% is due to the conversion of crystalline Ga_2O_3 to an amorphous gallium oxide phase.

However, samples heated at 900°C show the crystalline nature beyond 1 at % lanthanide ions doping (Fig.35). For the samples doped with 3 at % or more Eu^{3+} , a small peak started appearing at 2θ value of 28.4° and 32.2°. These peaks are attributed to Eu_2O_3 . Unit cell parameters are calculated by least square fitting of XRD patterns of 900°C heated samples (Table 3).

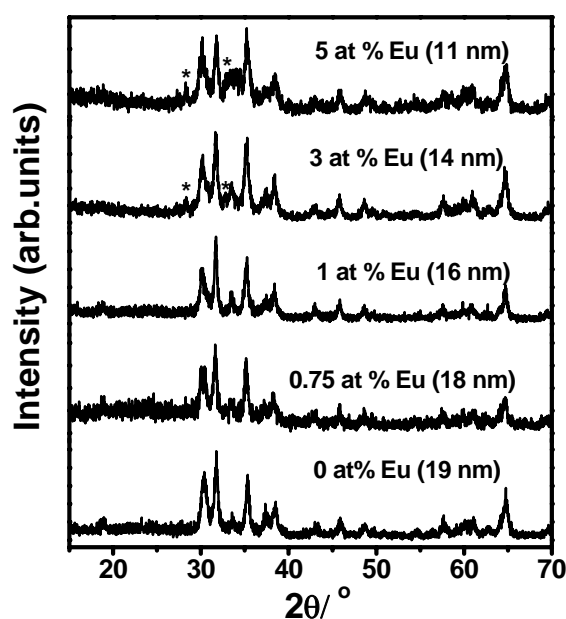


Fig.35. XRD patterns of $\beta\text{-Ga}_2\text{O}_3$ doped with 0, 0.75, 1, 3 and 5 at % of Eu^{3+} (peak marked * correspond to Eu_2O_3). Values in brackets show average crystallite size.

The cell parameters increases with increase in the lanthanide ion concentration up to 0.75 at % and above that they started decreasing. Although, lattice parameters start decreasing, they are larger than the undoped sample. From the above results, it is inferred that lanthanide ions are replacing Ga^{3+} ions up to 0.75 at % and above that a separate phase namely Eu_2O_3 is formed. The average crystallite size calculated by using Scherrer formula for samples doped with different percentage of lanthanide ions are given in the Table 3. The average crystallite size decreases with increase in the lanthanide ions concentration. To confirm this fact, TEM measurements were carried out and the results are discussed below.

Table.3. Variation in the lattice parameters of β - Ga_2O_3 samples prepared in presence of different amounts of Eu^{3+} ions. Numbers in bracket indicate the errors.

at % Eu^{3+}	Avg. Crystal size (nm)	β - Ga_2O_3				
		a (Å)	b (Å)	c (Å)	β (°)	Cell volume (Å ³)
0	19	12.237(1)	3.031(2)	5.802(2)	103.865(3)	208.93(2)
0.5	19	12.242(2)	3.038(1)	5.809(3)	103.940(2)	209.70(1)
0.75	18	12.249(1)	3.042(3)	5.820(2)	104.018(2)	210.40(2)
1	16	12.249(2)	3.039(2)	5.812(1)	104.012(1)	209.94(2)
2	15	12.242(2)	3.038(3)	5.809(2)	103.875(2)	209.67(3)
3	14	12.240(3)	3.038(1)	5.810(1)	104.077(3)	209.60(3)
5	11	12.210(2)	3.038(2)	5.807(2)	103.969(3)	209.04(2)

Figure 36 shows the TEM images of 900°C heated samples containing different concentrations of Eu^{3+} ions. The shape and size of the Ga_2O_3 nanomaterials changed after doping with lanthanide ions. Undoped Ga_2O_3 shows uniform nanorods with length 2.3-2.8 μm and width 0.2-0.3 μm . whereas 0.75 at % Eu doped samples exhibit the formation of both nanorods and nanoparticles with a broad size distribution. For the Ga_2O_3 samples with 3 at % Eu^{3+} ions, only nanoparticles with irregular shapes are observed instead of nanorods. The size of the nanoparticles is further reduced on increasing the Eu^{3+} concentration to 5 at %. This can be explained based on structural changes taking place in $GaOOH$ lattice after doping with

lanthanide ions. Doping of lanthanide ions into GaOOH lattice causes structural destruction due to incorporation of lanthanide ions in between the GaO₆ octahedral layers at the expense of hydrogen bonds and the resulting product mainly contains finely mixed Ga(OH)₃ and Eu(OH)₃. During heat treatment, Eu³⁺ ions can diffuse into the lattice and forms Eu³⁺ doped Ga₂O₃.

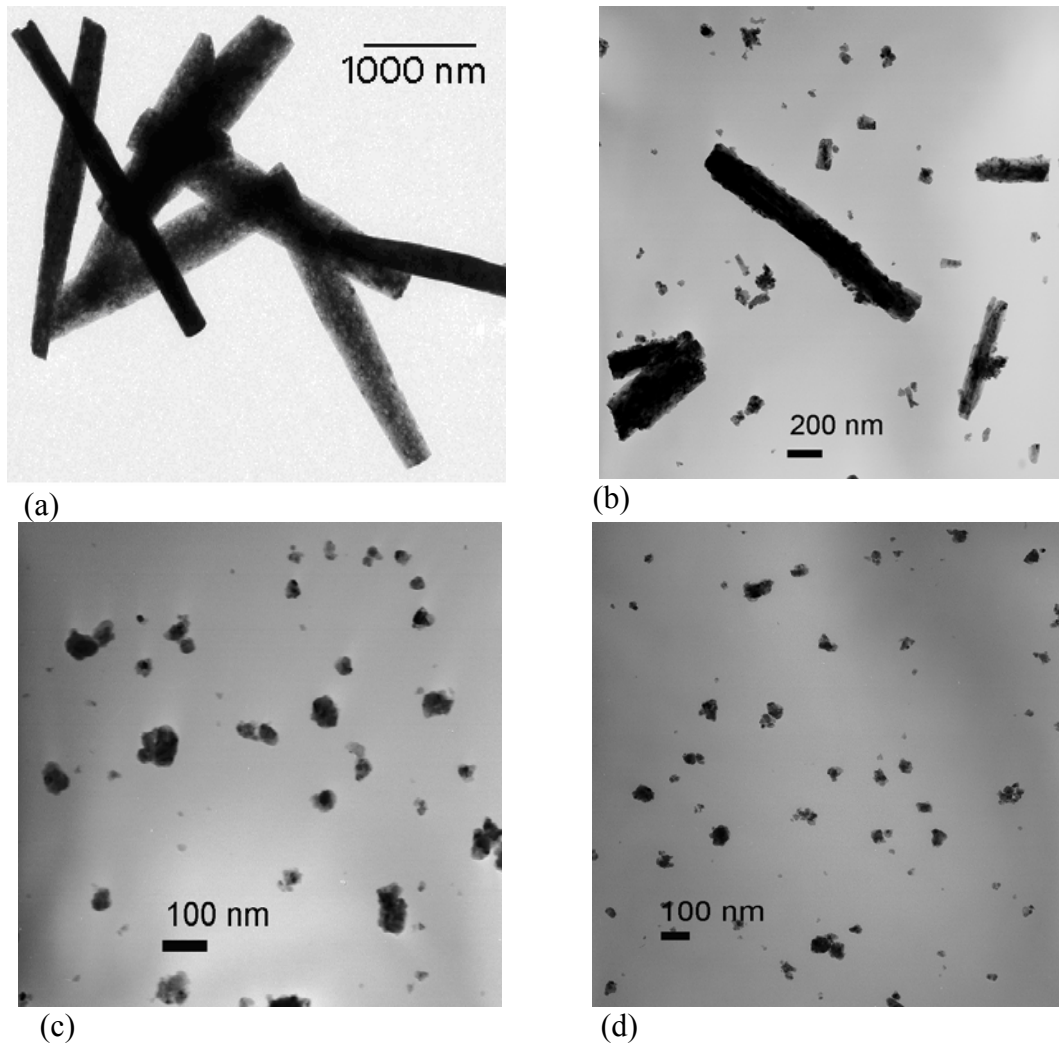


Fig.36. TEM images of (a) 0, (b) 0.75, (c) 3 and (d) 5 at % Eu doped β - Ga₂O₃.

3.5 Effect of heat treatment on luminescence of Ga₂O₃:Ln³⁺ nanomaterials: Figure 37 (a) shows the emission spectra of Tb³⁺ doped GaOOH, α -Ga₂O₃ and β -Ga₂O₃ nanomaterials. All samples displayed four peaks ~ 489, 543, 588 and 622 nm corresponding to ⁵D₄→⁷F₆, ⁵D₄→⁷F₅, ⁵D₄→⁷F₄ and ⁵D₄→⁷F₃ transitions of Tb³⁺ ions. Tb³⁺ doped α -Ga₂O₃ sample shows

strong emission compared to corresponding GaOOH and β -Ga₂O₃ samples. The low emission intensity of Tb³⁺ in GaOOH can be attributed to the quenching of Tb³⁺ excited state due to hydroxyl groups and that in β -Ga₂O₃ can be attributed to the formation of Ga₃Tb₅O₁₂/terbium oxide phase due to heat treatment at 900°C. The decay curves correspond to ⁵D₄ level of Tb³⁺ ions in the sample are shown in Fig.37 (b) and measured lifetime values are given in Table 4. The excited state of Tb³⁺ decays single exponentially in GaOOH and α -Ga₂O₃ and bi-exponentially in β -Ga₂O₃. These results indicate that Tb³⁺ ions are having only one type of environment in GaOOH and α -Ga₂O₃ lattices whereas it is more than one type of environments in β -Ga₂O₃. This is further supported by the formation of Ga₃Tb₅O₁₂/terbium oxide phase in Tb³⁺ doped samples as confirmed by XRD studies.

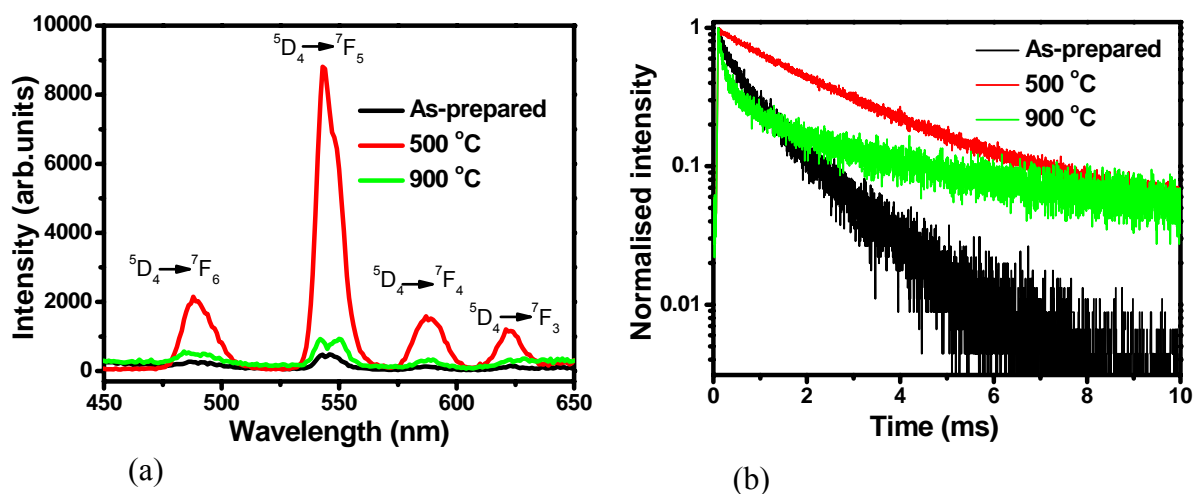


Fig.37. (a) Emission spectra, (b) decay curve corresponding to ⁵D₄ level of Tb³⁺ in 0.5 at % Tb³⁺ doped GaOOH, α -Ga₂O₃ and β -Ga₂O₃ nanomaterials. ($\lambda_{exc} = 255$ nm and $\lambda_{em} = 544$ nm)

Table 4. Lifetime values corresponding to ⁵D₄ level of Tb³⁺ from GaOOH:Tb³⁺ heated at different temperatures.

Sample	τ_1 (μ s)	τ_2 (μ s)
As prepared GaOOH:Tb ³⁺	326 (14%)	1284 (86%)
500°C (α -Ga ₂ O ₃ : Tb ³⁺)	2389 (100%)	
900°C (β -Ga ₂ O ₃ : Tb ³⁺)	258 (13%)	2872 (87%)

Figure 38 (a) shows the emission spectra of β -Ga₂O₃ doped with 0, 0.5, 1 and 2 at % Tb³⁺ obtained after excitation at 255 nm. Undoped (0 at % Tb) β -Ga₂O₃ sample shows a broad band centered around 455 nm and is assigned to emission from oxygen defect levels present in the host matrix. The emission intensity reduces with increase in Tb³⁺ percentage in the sample. This is explained based on the energy transfer from host to Tb³⁺ ions. The excitation spectra corresponding to host and Tb³⁺ emission are shown in Fig.38 (b).

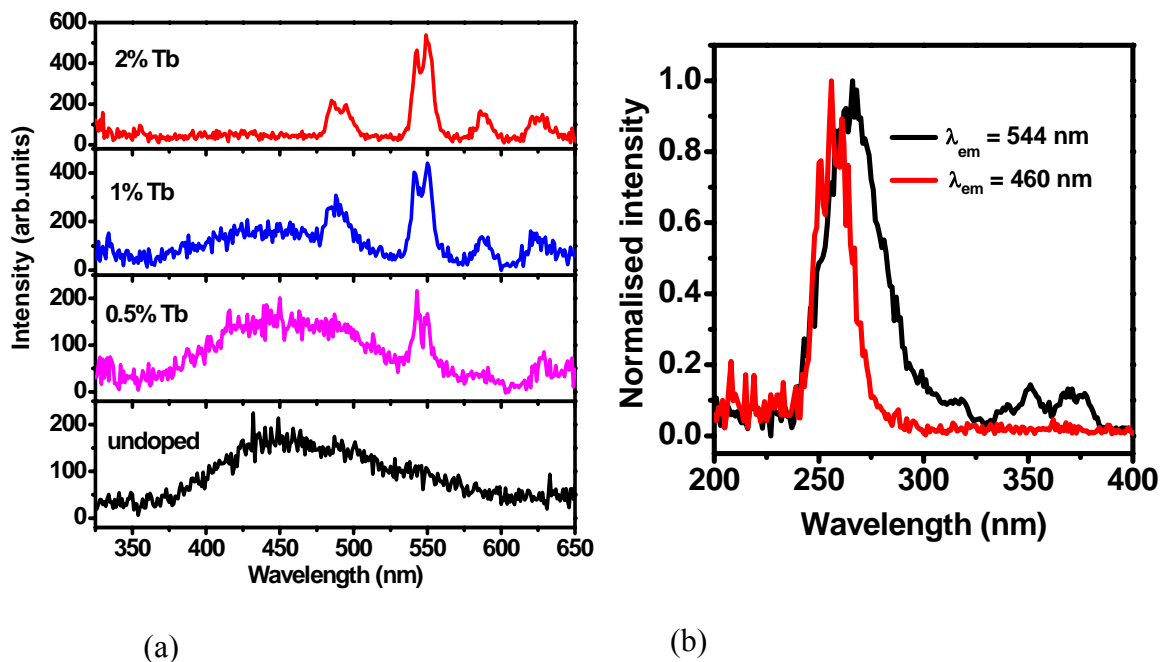


Fig.38 (a) Emission spectra of β -Ga₂O₃ nanomaterials doped with 0, 0.5, 1 and 2 at % Tb³⁺ ions. The corresponding excitation spectra for 1 at % Tb³⁺ doped sample, monitored at 460 and 544 nm emission, are shown in Fig. 38 (b)

The excitation spectra corresponding to host emission exhibits only one band at 255 nm whereas excitation spectra corresponding to Tb³⁺ emission is characterized by strong band at 275 nm having shoulder at 255 nm along with weak bands above 350 nm. The broadband \sim 275 nm is assigned to 4f to 5d transition of Tb³⁺, the shoulder peak to host absorption and peaks above 350 nm are due to f-f transitions of Tb³⁺ ions. Based on the excitation spectra, it is confirmed that energy transfer takes place from host to Tb³⁺ ions in these samples. This is further supported by the excited state lifetime values corresponding to host emission observed from samples with different Tb³⁺ contents. The corresponding decay

curves are shown in Fig.39. Lifetime values corresponding to host emission decreased with increase in the terbium ion concentration (Table 5). The decrease in lifetime values with increase in Tb^{3+} concentration confirms the energy transfer from host to lanthanide ion.

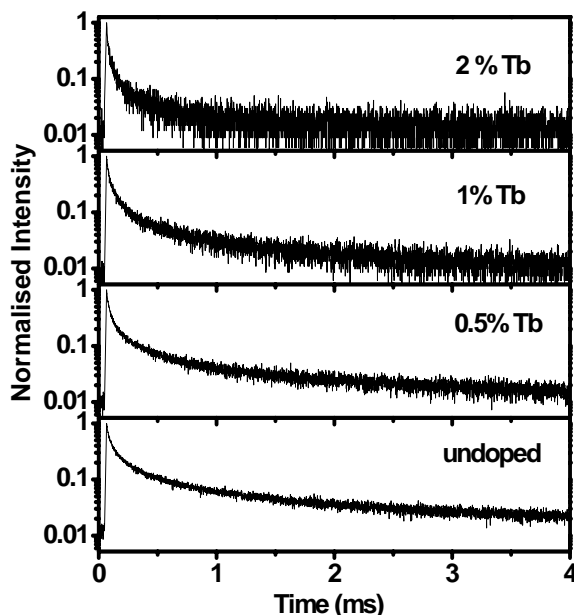


Fig.39 Decay curves corresponding to excited state of the host emission of $\beta\text{-Ga}_2\text{O}_3$ nanomaterials doped with 0, 0.5, 1 and 2 at % Tb^{3+} ions.

Table 5 Excited state lifetime values of host emission from $\beta\text{-Ga}_2\text{O}_3\text{:Tb}$ nanomaterials after doping with different amounts of Tb^{3+} ions.

Sample	τ_1 (μs)	τ_2 (μs)
$\beta\text{-Ga}_2\text{O}_3$	110 (24%)	885 (76%)
$\beta\text{-Ga}_2\text{O}_3\text{: 0.5% Tb}$	100 (26%)	811 (74%)
$\beta\text{-Ga}_2\text{O}_3\text{: 1% Tb}$	94 (29%)	827 (71%)
$\beta\text{-Ga}_2\text{O}_3\text{: 2% Tb}$	65 (32%)	590 (68%)

The emission and excitation spectra from a representative $\beta\text{-Ga}_2\text{O}_3\text{:Dy}$ and $\beta\text{-Ga}_2\text{O}_3\text{:Eu}$ samples are shown in Fig.40(a-d). Emission spectrum shown in Fig. 40 (a) corresponds to $\beta\text{-Ga}_2\text{O}_3\text{:Dy}$ nanorods and is obtained by exciting the host at 260 nm. Sharp emission peaks due to intra 4f transitions of Dy^{3+} ions characterize the spectrum. Corresponding excitation spectrum obtained by monitoring Dy^{3+} emission at 575 nm is

shown in Fig.40 (b). While monitoring Dy^{3+} emission, observation of host absorption around 260 nm confirms that energy transfer occurs from host to Dy^{3+} ions in $\beta\text{-Ga}_2\text{O}_3:\text{Dy}^{3+}$ nanorods. A comparison of this emission and excitation spectrum with that of $\text{GaOOH}:\text{Dy}^{3+}$ samples (Fig.28) reveals that the energy transfer is relatively stronger in $\text{Ga}_2\text{O}_3:\text{Dy}^{3+}$ system compared to $\text{GaOOH}:\text{Dy}^{3+}$ system. The efficiency of energy transfer has been calculated and found to be around 92 % in this case. Possible reason for the improved energy transfer is the combined effect of migration of lanthanide ions in the lattice of Ga_2O_3 as well as removal of hydroxyl groups by heat treatment. These observations are in agreement with those reported on lanthanide ions (Dy^{3+}) doped Ga_2O_3 nanomaterials [56].

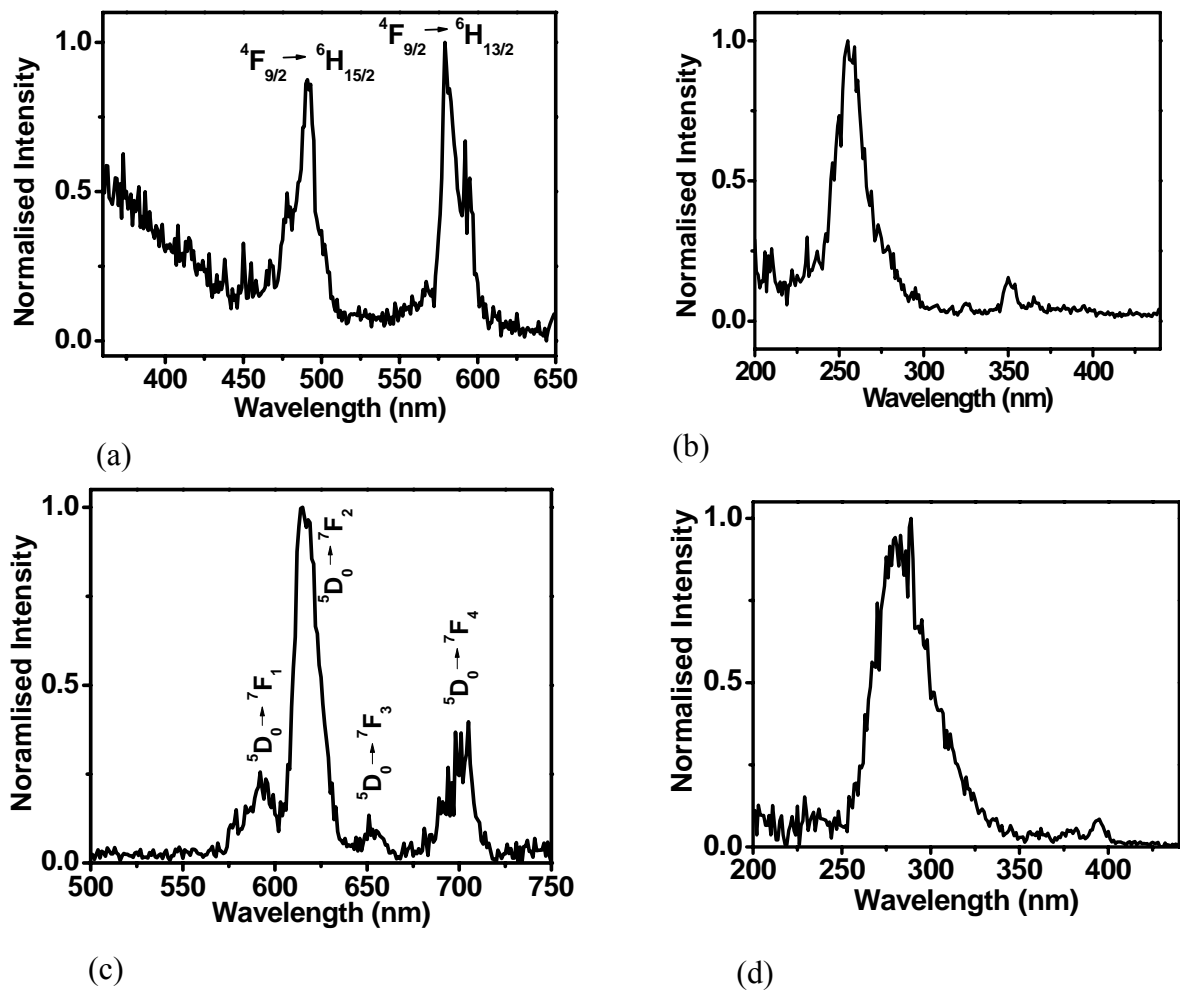


Fig.40. Emission spectrum (a) obtained after 260 nm excitation and excitation spectrum (b) corresponding to 575 nm emission from $\beta\text{-Ga}_2\text{O}_3:\text{Dy}^{3+}$ nanomaterials. Corresponding emission ($\lambda_{\text{exc}} = 280$ nm) and excitation ($\lambda_{\text{em}} = 613$ nm) spectrum from $\text{Ga}_2\text{O}_3:\text{Eu}$ nanorods are shown in Fig.40 (c and d).

Similar results are also observed from β -Ga₂O₃:Eu nanorods obtained after the decomposition of GaOOH:Eu nanorods at 900°C, as can be seen from the emission and excitation spectra shown in Fig.40 (c and d). The patterns match well with that reported for β -Ga₂O₃:Eu films by Mizunashi and Fujihara [204]. Unlike the excitation spectrum observed for Ga₂O₃:Dy nanorods (Fig.40 (b)), the excitation spectrum corresponding to Ga₂O₃:Eu nanorods is characterised by a broad peak with emission maximum around 280 nm. This has been attributed to the overlapping of Eu-O charge transfer band with the Ga₂O₃ host excitation peak.

Figure 41 shows the emission and excitation spectra of Er³⁺ doped Ga₂O₃ nanomaterials. Emission spectrum (Fig.41 (a)) after excitation at 380 nm shows strong peak at 1535 nm corresponding to ⁴I_{13/2} → ⁴I_{15/2} transition of Er³⁺ ions present in the Ga₂O₃ lattice. The excitation spectrum (Fig.41 (b)) corresponding to 1535 nm emission consists of many sharp peaks and are attributed to f-f transitions of Er³⁺ ion in the Ga₂O₃ lattice. Based on these studies it is confirmed that β -Ga₂O₃ is an ideal host for doping lanthanide ions. Efficient energy transfer from host to lanthanide ions helps to improve photoluminescence from lanthanide ions.

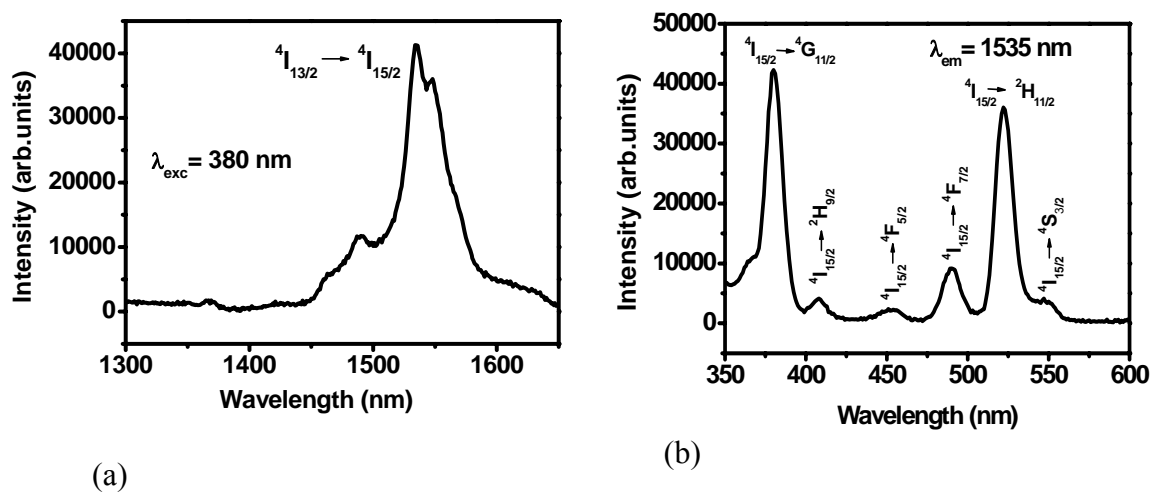


Fig.41. (a) Emission spectrum and (b) excitation spectrum from Ga₂O₃:Er³⁺ nanorods. The excitation and emission wavelengths are 380 and 1535 nm, respectively.

3.6 Structural and luminescence studies on antimony oxide nanomaterials: Antimony oxide nanomaterials were prepared by hydrolysis of antimony trichloride by aqueous ammonia solution in iso-propanol, at room temperature. As prepared samples were heated at 100, 200 and 400°C for 5 hours. The XRD patterns of these samples (room temperature, heated at 100, 200 and 400°C) corresponds to orthorhombic form of Sb_2O_3 (Fig.42). However, the sample heated at 400°C showed an additional Sb_2O_4 phase ($2\theta=29.03^\circ$) [156]. Sharp diffraction peaks indicate crystalline nature of Sb_2O_3 samples. The average particle size was calculated by using Debye–Scherrer formula and found to be around 40 nm. Lattice parameters were calculated for the as prepared sample and found to be $a = 4.916(1) \text{ \AA}$, $b = 12.471(2) \text{ \AA}$ and $c = 5.418(2) \text{ \AA}$. Corresponding values for bulk Sb_2O_3 are $a = 4.918(3) \text{ \AA}$, $b = 12.453(2) \text{ \AA}$ and $c = 5.427(2) \text{ \AA}$.

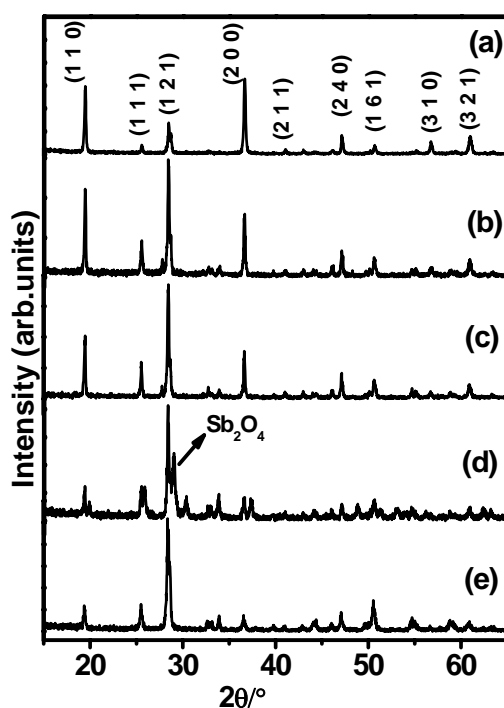


Fig.42. XRD pattern of (a) Sb_2O_3 sample prepared at room temperature in isopropanol medium. Corresponding patterns from the samples heated at 100, 200 and 400°C along with that of bulk Sb_2O_3 are shown in (b)–(e), respectively.

For bulk Sb_2O_3 sample the highest intensity peak corresponds to (121) plane around a 2θ value of 28.42° (Fig.42 (e)). However, for samples prepared in isopropanol the highest

intensity of XRD peaks correspond to (110) and (200) planes around 2θ values 19.66 and 36.62° , respectively. These results indicate a preferred crystallographic orientation existing in the sample prepared by iso-propanol route which leads to selective enhancement in the intensity of some of the Bragg reflections. A similar increase in intensity for (110) and (200) planes has also been observed by Deng, et al. for Sb_2O_3 nanorods prepared by oxidation of antimony metal [64]. On annealing it is observed that the intensity of the super-lattice peaks at 2θ values corresponding to (110) and (200) reflections systematically decreases. This indicates that the preferred crystallographic orientation associated with the sample is slowly destroyed (Fig.42 (b and c)). In addition to the orientation changes, annealing at 400°C also leads to partial conversion of Sb_2O_3 to Sb_2O_4 cervantite phase (Fig.42 (d)). In order to check the morphology and preferred crystallographic orientation existing with the sample, atomic force and transmission electron microscopic (AFM and TEM) measurements were carried out.

Figure 43 (a and b) shows the AFM images of methanol dispersion of as prepared Sb_2O_3 samples obtained by iso-propanol route. The images consist of long rod shaped species with a length around 3– 4 μm and width around 100–200 nm. Several such rods can be clearly seen from the images. A closer look at the image demonstrate that in addition to the long rods there also exist small rods having length roughly in the range of around 1 μm . A representative TEM image along with the selected area electron diffraction patterns of the sample is shown in Fig.43 (c and d). Dimension of the nanorods obtained from TEM images agree well with that obtained from AFM images. As the SAED pattern taken along the [100] zone axis consists only spots, it is confirmed that each nanorod is a single crystal of Sb_2O_3 with [100] orientation. For the purpose of comparison bulk material was also dispersed in methanol and TEM images were recorded for the supernatant solution (Fig.43 (e and f)). These particles are aggregated and are having size in the broad range of 50–500 nm.

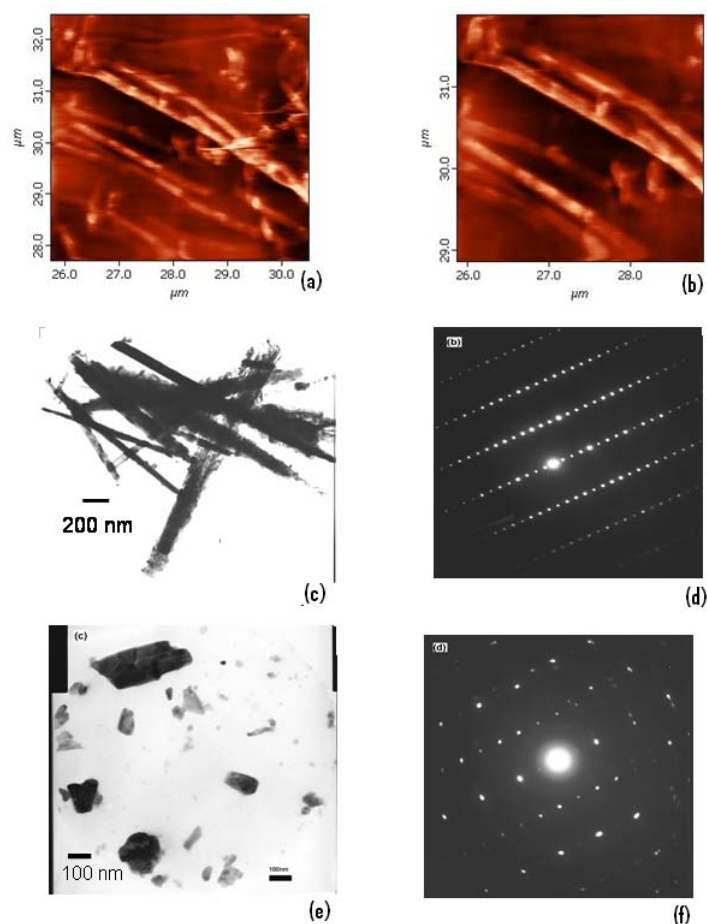


Fig.43. (a and b) AFM images showing the nanorods of Sb_2O_3 at two representative regions of the sample. TEM and SAED images for the nanorods along with that of bulk sample are shown in (c)–(f), respectively.

3.7 Effect of morphology on the luminescence of Sb_2O_3 : Figure 44 (a and b) shows the emission spectra from Sb_2O_3 nanorods and bulk material as a function of temperature (in the range ~ 77 – 300 K). Line shapes corresponding to the emission spectrum from both nanorods and bulk materials remained same at all the temperatures. A broad emission at ~ 390 nm has been observed for Sb_2O_3 nanorods and bulk materials at all the temperatures. Considering the band gap energy values of Sb_2O_3 (~ 3.3 eV) [64] and based on previous Sb^{3+} luminescence studies [163, 64], the peak around 390 nm has been attributed to the near band edge emission arising from Sb_2O_3 . However for nanorods in addition to the band edge emission around 390 nm, an additional broad peak which appears as a doublet with peak maxima around 545 and 592 nm is also observed. These two peaks have significant intensity in the case of nanorods

compared to the bulk material and are arising due to the defect levels present in the band gap of Sb_2O_3 . These can be the oxygen vacancies, the surface dangling bonds or the surface defects. Similar defect emission with comparable line shape has also been observed in semiconductors like TiO_2 , ZnO , etc. [205, 206]. Lifetime corresponding to the excited state of these emission centers could not be accurately measured as the decay is faster than the experimental time resolution of the luminescence set up (~ 1 ns). Thus, it can be concluded that the excited state lifetime is of the order of sub-nanoseconds, similar to what has been observed in the case of ZnO nanorods [206]. At this stage, it is difficult to understand the exact origin of defects levels. It is worth while to mention here that Deng, et al. [64] have observed blue emission around 433 nm from Sb_2O_3 nanobelts, and they have attributed this to the oxygen related defect emission from the nanorods. In the case of ZnO nanorods [206], it has been demonstrated that the orange, red and green defect related emission originate from them depending on the preparation method, annealing temperature and atmospheres.

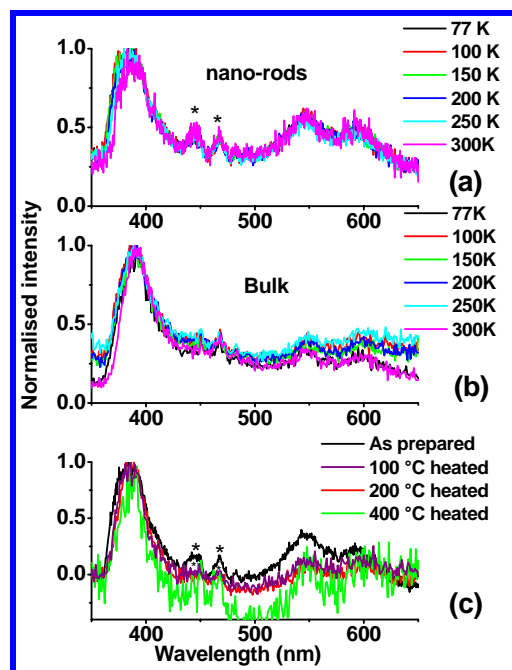


Fig.44. Emission spectra of (a) Sb_2O_3 nanorods and (b) bulk Sb_2O_3 as a function of temperature. Room temperature emission spectra of as prepared Sb_2O_3 nanorods annealed at different temperatures are shown in (c). Excitation wavelength was 220 nm. Peaks marked * are artifacts.

On annealing the nanorods at 100 and 200°C, emission intensity of the 545 and 592 nm peaks relative to the band edge emission has been found to decrease as can be seen from Fig.44 (c). Based on the luminescence and XRD studies of the as prepared nanorods and the nanorods annealed at different temperatures it is inferred that the morphological changes are taking place in Sb₂O₃ nanorods during annealing and they are responsible for the change in intensity of 545 and 592 nm peaks. To further confirm the morphological assisted changes and the associated structural changes in Sb₂O₃ nanorods on annealing, Raman spectroscopic studies of both (as prepared and annealed) samples were carried out and the results are described below. Figure 45 (a) shows Raman spectrum of the as prepared nanorods. The sample shows peaks at 143, 191, 218, 256, 297, 445, 503, 596 and 681 cm⁻¹, characteristic of the orthorhombic valentinite form of Sb₂O₃, which agrees well with the reported by data [64, 207–209]. Similar spectra are also observed from bulk and nanorods annealed at different temperatures. The Raman spectra of the annealed samples show a strong luminescence background, intensity of which systematically increases as the annealing temperature is increased. Thus, the broad emission background dominates the sample annealed at 400°C. The major differences between the patterns corresponding to as prepared nanorods, the one annealed at different temperatures and the bulk, are depicted by the Raman peaks at ~260 cm⁻¹ (Fig.45 (b)), 445 cm⁻¹ (Fig.45 (c)) and ~ 710 cm⁻¹ (Fig.45 (d)). The peak at ~ 260 cm⁻¹ (peak A) in bulk Sb₂O₃ is clearly seen to have evolved into two peaks for nanorods; one at 256 cm⁻¹ (peak A1) and another at 259 cm⁻¹ (peak A2). The peak A1 is relatively sharper (line width approximately ~1/3rd) than peak A2. As the nanorods are annealed, the intensity of this peak reduces and that of A2 increases; while their widths remain almost constant. Similar inferences are drawn for the peak at ~ 445 cm⁻¹ (peak B in Fig.45 (c)). In case of nanorod sample this shows a triplet, with peaks at ~ 435 cm⁻¹ (peak B1), 443 cm⁻¹ (peak B2) and 451 cm⁻¹ peak (B3). The B2 peak is most intense, followed by B3 and B1. The widths of peak B2

is almost 1½ times that of peak B1 and B3. As the samples are annealed (say at 100°C and 200°C), these peaks are merged and appear as a one single peak similar to the one observed from the bulk sample. The morphology change is further clear from the shoulder peak ~ 710 cm⁻¹ (as shown by the encircled region in Fig.45 (d)) observed for nanorods, which is successively broadened with increasing annealing temperature.

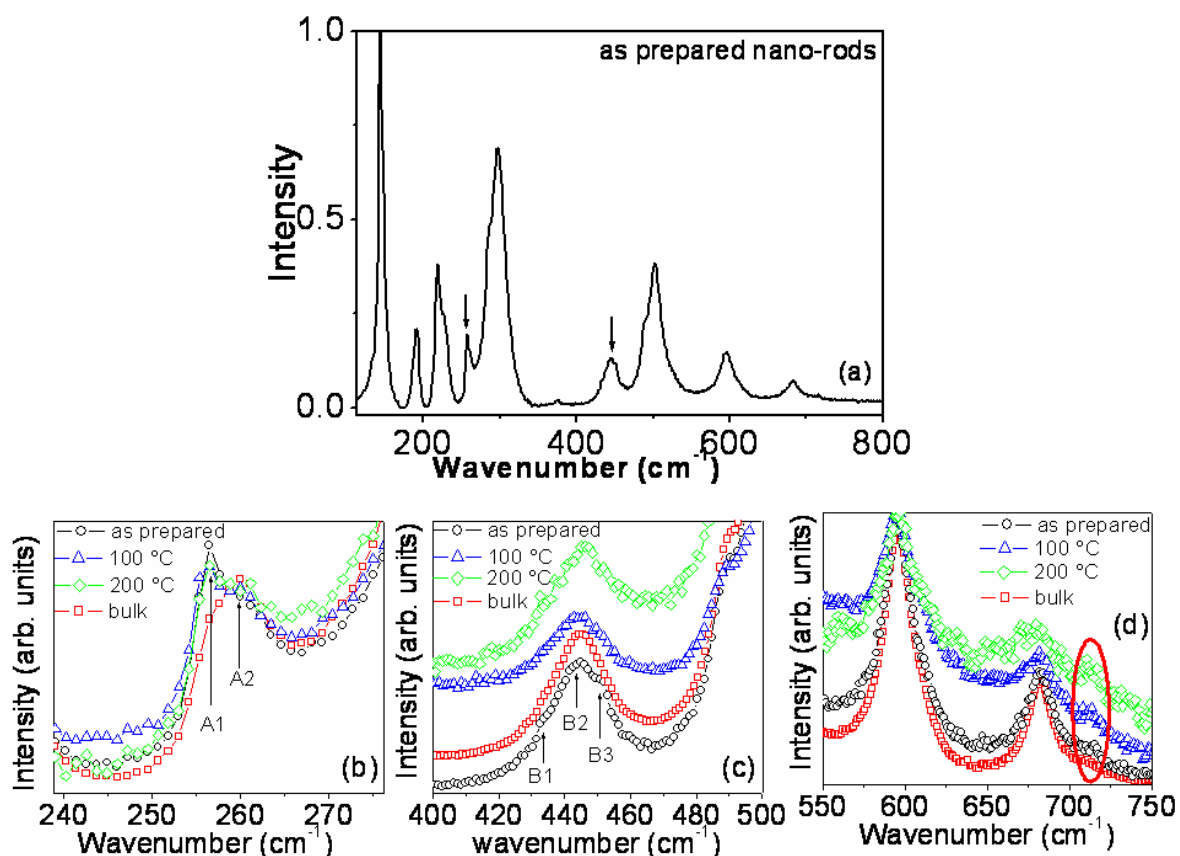


Fig.45. Raman spectrum of (a) as prepared Sb₂O₃ nanorods. The changes related to morphology/annealing are shown by arrows at ~260 cm⁻¹ and ~445 cm⁻¹. Enlarged view of the Raman spectrum corresponding to Sb–O–Sb stretching (b, d) and bending (c) modes of Sb₂O₃ nanorods annealed at various temperatures along with that of bulk sample are also shown. Fig.45 (b) shows peaks ‘A1’ and ‘A2’ for the 260 cm⁻¹ peak and Fig.45 (c) shows ‘B1’, ‘B2’ and ‘B3’ for the 445 cm⁻¹ peak. Encircled region in Fig.45 (d) shows the changes in the Sb–O–Sb stretching vibrations at various annealing temperatures.

The Sb₂O₃ comprises of four SbO₃ (E) pyramids (E being lone pair of electrons) arranged into the Sb₄O₆ molecular ring structure with a Td symmetry [209,210]. Each oxygen is bridged between two SbO₃ pyramids. According to Gilliam, et al. [210], the molecular

vibration of the Sb_4O_6 ring is decomposed into $2A_1 + 2E + 2T_1 + 4T_2$ of which A_1 , E and T_2 are Raman active modes. These modes are further classified into Sb–O–Sb stretch, Sb–O–Sb bend and Sb–O–Sb wag modes [210]. The most affected modes in the nanorods (compared to bulk Sb_2O_3) are the Sb–O–Sb stretching (A_1 type) appearing at $\sim 256 \text{ cm}^{-1}$ and the Sb–O–Sb bending (A_1 type) appearing at $\sim 445 \text{ cm}^{-1}$. Another peak at $\sim 710 \text{ cm}^{-1}$, also corresponds to Sb–O–Sb stretching with T_2 symmetry. As reported above, the shape selective nature of the nanorods results in only few of the modes that are affected, rest being unaltered. In comparison to the bulk material, the oriented Sb_2O_3 nanorods are expected to have Raman activity in terms of the dynamic polarizability tensor. The A_1 type of vibrations include polarizability of the kind $\alpha_{xx} + \alpha_{yy} + \alpha_{zz}$, while T_2 type of vibrations includes the non-diagonal components like α_{xy} , α_{yz} , α_{zx} [211]. Thus, the arrangement of the Sb_4O_6 molecular units in Sb_2O_3 nanorods is associated with the selective excitation of some of these polarizability tensors over the others, leading to enhanced Raman activity for a particular peak over the other. This results in appearance of additional peak at $\sim 256 \text{ cm}^{-1}$ and a triplet at $\sim 445 \text{ cm}^{-1}$ for oriented samples. The A_1 type of modes have highest Raman activity ($16 \text{ \AA}^4 \text{ amu}^{-1}$) as compared to E , T_1 and T_2 type [210]. Moreover, these shape selective changes in the dynamic polarizability tensor is further regained to its bulk value (or at least tries to regain) by annealing the nanorods at 100 and 200°C . Thus, the Raman and XRD investigations suggest a clear morphological change in the Sb_2O_3 , from nanorods to bulk particles. The structural changes associated with morphological change are responsible for the change in luminescence properties.

In the following section brief description regarding the interaction of these luminescent nanorods with lanthanide ions are discussed. Eu^{3+} ions are used as representative lanthanide ions in the present study as its luminescence properties with respect to different environments are well understood.

3.8 Interaction of Eu^{3+} ions with Sb_2O_3 nanorods: Figure 46 shows the XRD patterns of Sb_2O_3 nanorods prepared both the XRD patterns of Sb_2O_3 nanorods prepared in both the presence and absence of Eu^{3+} ions. Sharp peaks in the XRD patterns indicate crystalline nature of the samples. The peak positions in the XRD patterns confirm that the Sb_2O_3 samples crystallize in the orthorhombic structure. From the line width of diffraction peaks, average crystallite sizes was calculated using Debye-Scherrer formula and found to be around 40 nm, for the nanorods. Lattice parameters were calculated based on the least square fitting of the diffraction peaks. The values are $a = 4.916(1) \text{ \AA}$, $b = 12.471(2) \text{ \AA}$, $c = 5.418(2) \text{ \AA}$. Corresponding values for Sb_2O_3 nanorods prepared in the presence of Eu^{3+} are $a = 4.918(3) \text{ \AA}$, $b = 12.453(2) \text{ \AA}$, $c = 5.427(2) \text{ \AA}$. The values are comparable within error limits for both type of samples (i. e., prepared in presence and absence of Eu^{3+} ions). The Eu^{3+} ions do not have any effect on the crystallinity and orientation of the nanorods as revealed by the identical line width and intensity corresponding to the diffraction peaks for Sb_2O_3 nanorods prepared in both the presence and absence of Eu^{3+} ions.

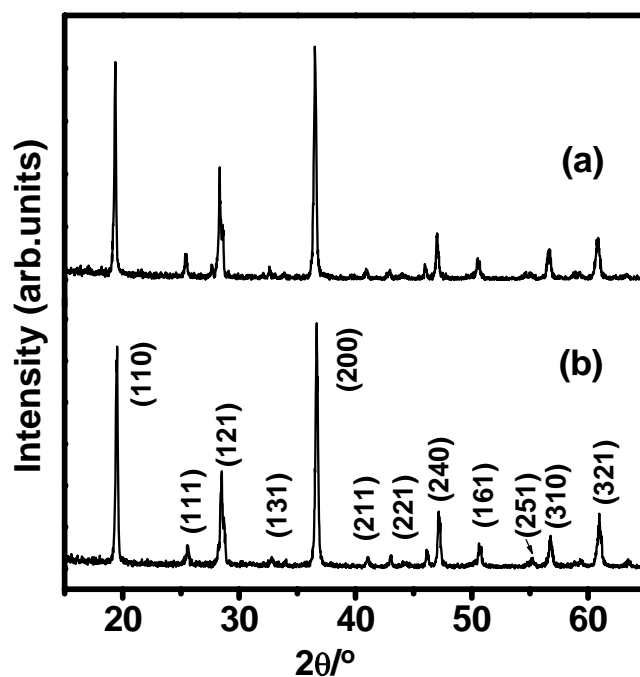


Fig.46. XRD patterns of Sb_2O_3 nanorods prepared in presence of (a) 0 at % Eu^{3+} and (b) 5 at % Eu^{3+} .

Figure 47 (a) shows room temperature emission spectrum of Sb_2O_3 nanorods prepared in presence of Eu^{3+} ions obtained after excitation at 220 nm. A broad emission at ~ 390 nm has been observed from the sample. Considering the band gap energy values of Sb_2O_3 (~ 3.3 eV) and based on previous Sb^{3+} luminescence studies the peak around 390 nm has been attributed to the near band edge emission arising from Sb_2O_3 . Since on excitation at 220 nm no characteristic emission of Eu^{3+} ions is observed from Sb_2O_3 nanorods prepared in presence of Eu^{3+} ions suggests that Eu^{3+} ions are not getting incorporated into the Sb_2O_3 lattice and also there is no energy transfer between the Sb_2O_3 host and Eu^{3+} ions. Figure 47 (b) shows the emission spectrum of Sb_2O_3 nanorods prepared in presence of Eu^{3+} ions obtained after excitation at 395 nm along with the excitation spectrum monitored at 615 nm emission (as an inset).

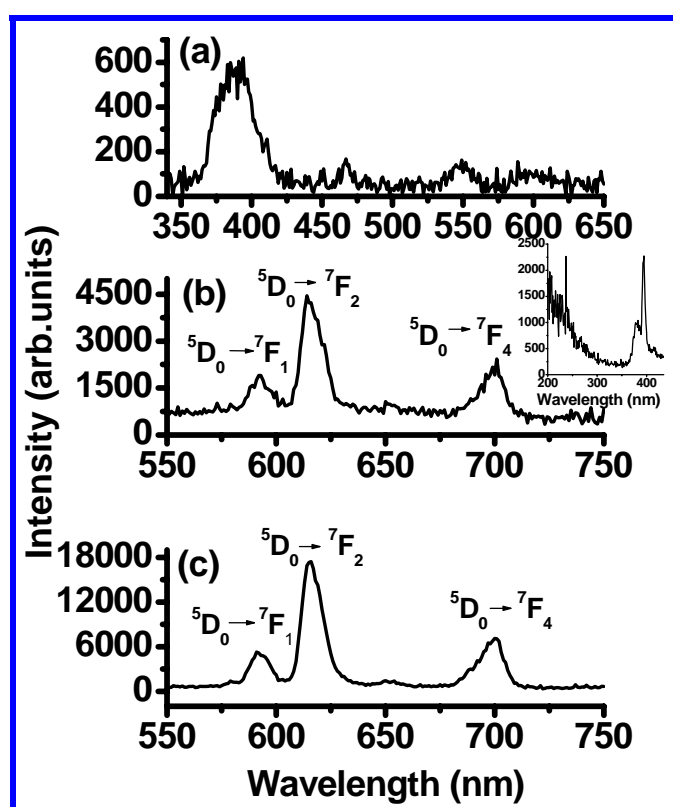


Fig.47 Emission spectrum from Sb_2O_3 nanorods prepared in presence of 5 at % Eu^{3+} and obtained after (a) 220 nm excitation and (b) 395 nm excitation. The corresponding pattern from bulk Sb_2O_3 prepared in presence of 5 atom % Eu^{3+} obtained after 395 nm excitation is shown in Fig.47 (c). The inset of Fig.47 (b) shows the excitation spectrum monitored at 615 nm emission.

The spectrum shows strong emission peaks around 590 and 615 nm, which are characteristic of magnetic and electric dipole allowed ${}^5D_0 \rightarrow {}^7F_1$ and ${}^5D_0 \rightarrow {}^7F_2$ transitions, respectively of Eu^{3+} . Besides this peak, there are two more weak peaks centered at 651 and 700 nm due to ${}^5D_0 \rightarrow {}^7F_3$ and ${}^5D_0 \rightarrow {}^7F_4$ transitions, respectively of Eu^{3+} ions. The relative intensity ratio of the electric to magnetic dipole allowed transition, known as the asymmetric ratio of luminescence, is a sensitive parameter, which depends on the electronic environment around Eu^{3+} ions. The asymmetric ratio of luminescence is found to be 3.4 and is comparable with the value observed for of bulk Sb_2O_3 samples (~ 3.3) prepared in presence of Eu^{3+} ions (Fig.47 (c)). The higher intensity of electric dipole transition compared to the magnetic dipole transition and associated high asymmetric ratio value shows that the Eu^{3+} ions are in a non-centro symmetric environment.

To confirm the fact that the Eu^{3+} ions are not forming separate europium oxide/hydroxide phase, Eu^{3+} ions were subjected to the same chemical treatment as that done for Sb^{3+} for preparing Sb_2O_3 nanorods and the precipitate was subjected to luminescence measurements. XRD and infrared patterns of precipitate indicated that the product is amorphous europium hydroxide. Figure 48 shows the emission spectrum from the as prepared europium hydroxide sample subjected to 395 nm excitation. The pattern is found to be quite different from the Sb_2O_3 sample prepared in presence of Eu^{3+} ions. The asymmetric ratio of luminescence is calculated to be ~ 1.6 . The higher asymmetric ratio of Eu^{3+} emission, in Sb_2O_3 sample prepared in presence of Eu^{3+} ions, compared to europium hydroxide phase (prepared by the same procedure as that of Sb_2O_3) shows that Eu^{3+} ions in Sb_2O_3 sample have a different environment and are not existing as separate europium hydroxide phase. The excitation spectrum (inset in Fig.48) also reveals that the Eu^{3+} ions have different environment in both the samples. These results are further supported by the lifetimes corresponding to the 5D_0 level of Eu^{3+} ions in the sample, as shown in Fig.49.

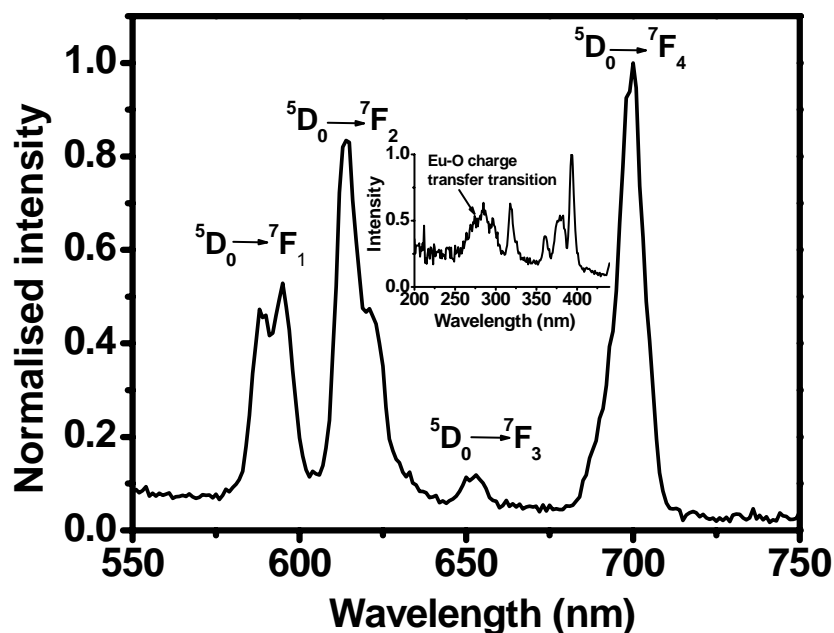


Fig.48. Emission spectrum obtained after excitation at 395 nm from europium hydroxide sample prepared by the same procedure as adopted for antimony oxide nanorods. The excitation spectrum corresponding to 615 nm emission is shown in the inset.

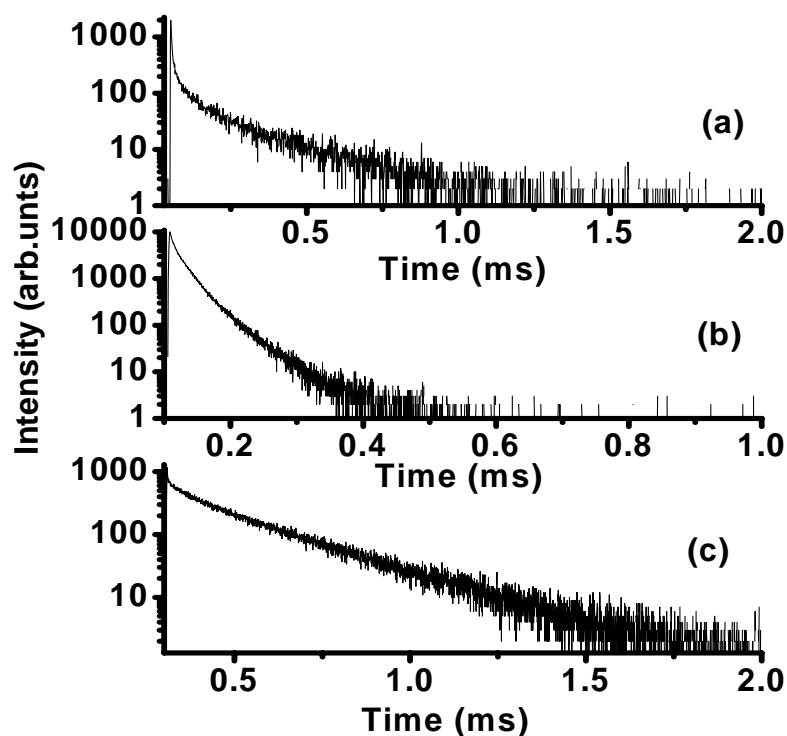


Fig.49. Decay curves corresponding to 5D_0 level of Eu^{3+} in (a) Sb_2O_3 nanorods prepared in presence of Eu^{3+} (b) Europium hydroxide sample prepared by the identical procedure as adopted for Sb_2O_3 nanorods and (c) bulk Sb_2O_3 prepared in presence of Eu^{3+} . Samples were excited at 395 nm and emission was monitored at 615 nm.

The decay curves are found to be bi-exponential for all the samples. The corresponding life times are 7.4 μs (30%) and 177 μs (70%) for Sb_2O_3 nanorods synthesized in the presence of 5 at % Eu^{3+} ions, 13 μs (49%) and 37 μs (51%) for europium oxide, prepared by the identical procedure as that of Sb_2O_3 nanorods and 46 μs (10%) and 238 μs (90%) for bulk Sb_2O_3 synthesized in the presence of 5 at % Eu^{3+} ions. The higher lifetime values corresponding to the Eu^{3+} present in Sb_2O_3 nanorods and bulk Sb_2O_3 compared to the europium hydroxide support our previous inference that Eu^{3+} ions are in a different environment in the Sb_2O_3 sample and is not existing as separate europium hydroxide phase. In other words, Eu^{3+} ions are undergoing reaction with Sb^{3+} to form europium antimony hydroxide compound.

To further substantiate the fact that Eu^{3+} ions are not incorporated in Sb_2O_3 lattice, structural studies were carried out on Sb_2O_3 samples prepared with different concentrations of Eu^{3+} ions and the results are described below. Figure 50(a) shows the FT-IR patterns of Sb_2O_3 nanorods prepared in the presence of Eu^{3+} with concentrations 0, 2, 5 and 10 at % (with respect to Sb^{3+} ions) over the range of ~ 270 to 1200 cm^{-1} . Sb_2O_3 nanorods prepared both in presence and in absence of Eu^{3+} ions are characterized by mainly 5 peaks, with identical peak maximum and line shape. It may be noted that these positions agree well with that of the bulk Sb_2O_3 as reported by Cody, et al. [208] and Deng, et al. [65].

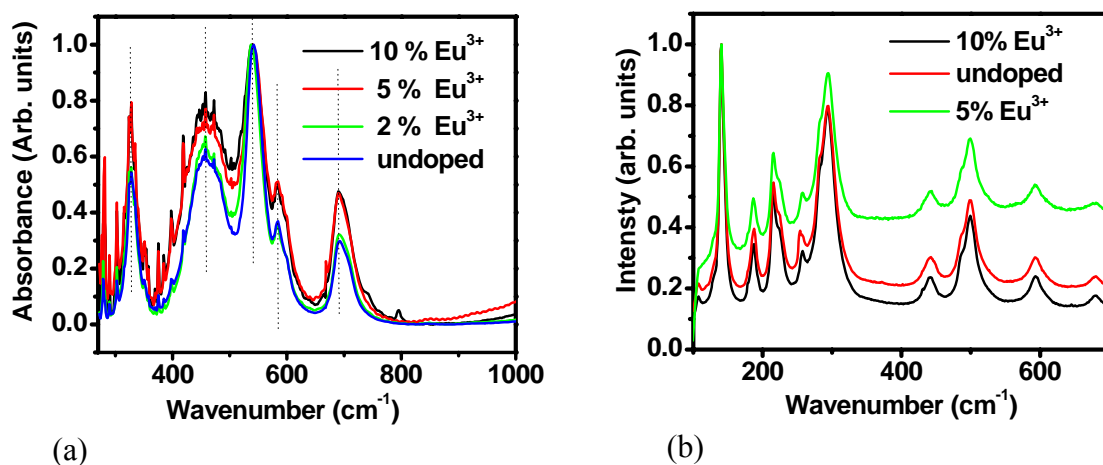


Fig.50. FT-IR patterns (a) and Raman Spectra (b) of Sb_2O_3 nanorods prepared in presence of different Eu^{3+} concentrations.

In addition, these peaks represent the characteristics of the different vibrational modes of Sb-O-Sb linkages in Sb_2O_3 . The peak maxima and line shapes are identical for all the samples, prepared with different amount of Eu^{3+} ions. Raman studies carried out over the region $130\text{-}1000\text{ cm}^{-1}$ (Fig.50 (b)) for Sb_2O_3 nanorods prepared both in presence and absence of Eu^{3+} ions show peaks characteristic of the orthorhombic valentinite form of Sb_2O_3 , which agrees well with the literature values [208-210]. As seen in Fig.50 (b), the peak position in the Raman spectrum is similar to what has been observed in IR spectrum. The fact that the line shape and peak position over the low frequency range (~ 100 to 1000 cm^{-1}) remain unaffected by increasing Eu^{3+} concentration, clearly suggests that the Eu^{3+} is not replacing the Sb^{3+} in the Sb_2O_3 lattice. Had it been the case, the stretching and bending vibrations of the Sb-O-Sb structural units would have affected leading to changes in the line shape and the peak position, which is not observed in the present study. On the other hand if there is a hydroxide formation between Sb^{3+} and Eu^{3+} ions, signatures corresponding to OH vibration from this compound should be seen in the IR spectrum for the Eu^{3+} containing sample. Hence, FT-IR patterns over the region of $2500\text{-}4000\text{ cm}^{-1}$ were recorded for both the undoped and highest Eu^{3+} doped sample (10%) (Fig.51).

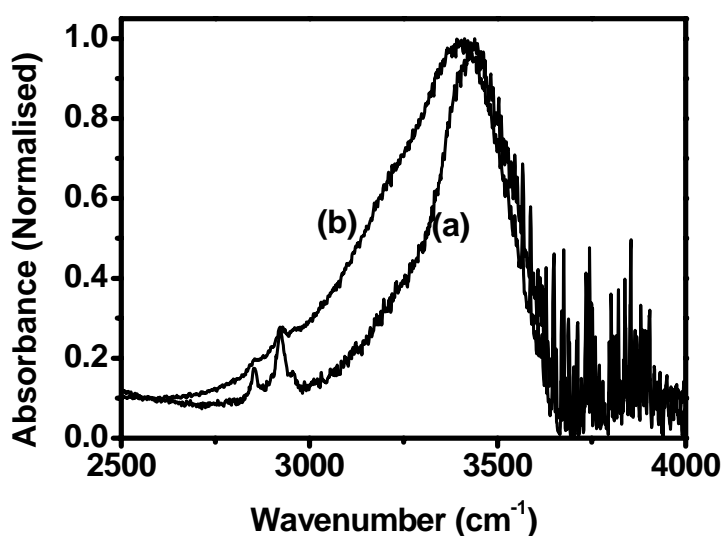


Fig.51. FT-IR patterns for the region corresponding to the OH stretching vibrations from (a) Sb_2O_3 nanorods (b) Sb_2O_3 nanorods with 10 at % Eu^{3+} .

As prepared undoped Sb_2O_3 sample is characterised by broad asymmetric peak centered around 3440 cm^{-1} . This has been attributed to the stretching vibrations of the OH groups present on the surface of the Sb_2O_3 nanorods. In addition, sharp peaks in the form of a triplet associated with the $-\text{C}-\text{H}$ stretching vibrations of the isopropanol molecule (as a stabilizing ligand on the surface of Sb_2O_3) is also observed around 2920 cm^{-1} . For the sample with 10% Eu^{3+} , this OH band is shifted to 3398 cm^{-1} , together with a considerable increase in the asymmetry towards lower wave numbers. This suggests the possibility of the formation of europium antimony hydroxide compound in the Eu^{3+} containing Sb_2O_3 nanorods which is further supported by the luminescence results discussed above.

To understand the nature of compound formation taking place between Sb^{3+} and Eu^{3+} ions, stoichiometric concentrations of Sb^{3+} and Eu^{3+} ions ($\text{Sb}^{3+}:\text{Eu}^{3+}$ ratio is maintained at 5:3, as $\text{Sb}_5\text{Eu}_3\text{O}_{12}$ is the only phase formed between Sb^{3+} and Eu^{3+} reported in the literature) were allowed to react under same experimental conditions as adopted for the synthesis of Sb_2O_3 nanorods. Figure 52 shows the XRD patterns of the reaction product obtained by the reaction between Sb^{3+} and Eu^{3+} ions along with the same product subjected to heat treatments at 500 and 900°C. As prepared and 500°C heated samples are amorphous (Fig.52 (a and b)), however on heating to 900°C, hydrated Sb_2O_5 phase along with HSb_3O_8 and Eu_2O_3 are formed as can be seen from the XRD patterns shown in Fig.52 (c). If there is no interaction between Sb^{3+} and Eu^{3+} ions, as prepared sample should contain highly crystalline Sb_2O_3 nanorods and that should have reflected in the XRD pattern shown in Fig.52 (a). This is not observed in the present study further supporting the antimony europium hydroxide compound formation. On heating the compound, antimony europium hydroxide, result in its decomposition or oxidation to form HSb_3O_8 , hydrated Sb_2O_5 and Eu_2O_3 .

Figure 53 shows the emission spectrum and decay curves from the hydrated europium antimony oxide heated at different temperatures. As prepared and 500°C heated samples gave

strong emission characteristic of Eu^{3+} ions, whereas on heating to 900°C the emission intensity got significantly reduced as can be seen from Fig.53 (a). The $^5\text{D}_0$ level of Eu^{3+} ion in all the samples has been found to decay bi-exponentially (Fig.53 (b)). The bi-exponential nature indicates the presence of more than one type of Eu^{3+} environment in the sample. The lifetime is systematically reduced with increase in heat treatment temperature. For the as prepared sample the values are found to be $143\ \mu\text{s}$ (20%) and $258\ \mu\text{s}$ (80%). These values are comparable with that of bulk Sb_2O_3 sample prepared in presence of Eu^{3+} ions. The observed weak luminescence and short lifetime for the 900°C heated samples have been attributed to formation of Eu_2O_3 phase.

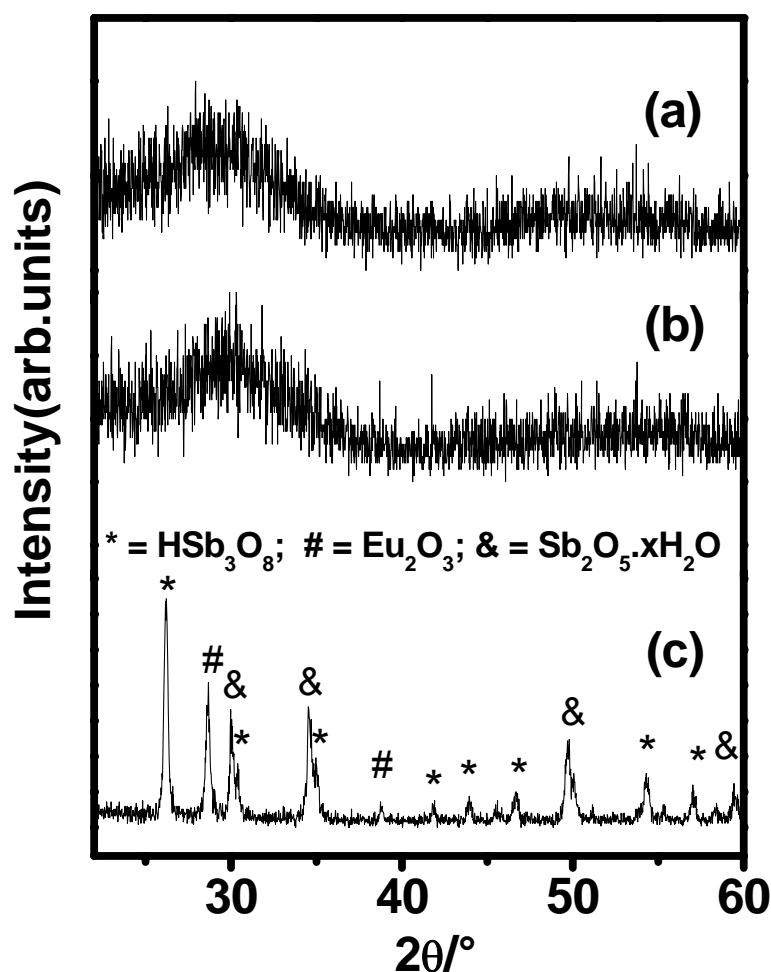


Fig.52. XRD patterns for the product obtained by the reaction between Sb^{3+} and Eu^{3+} ions taken in stoichiometric amounts and heated at different temperatures: (a) as prepared (b) 500°C and (c) 900°C .

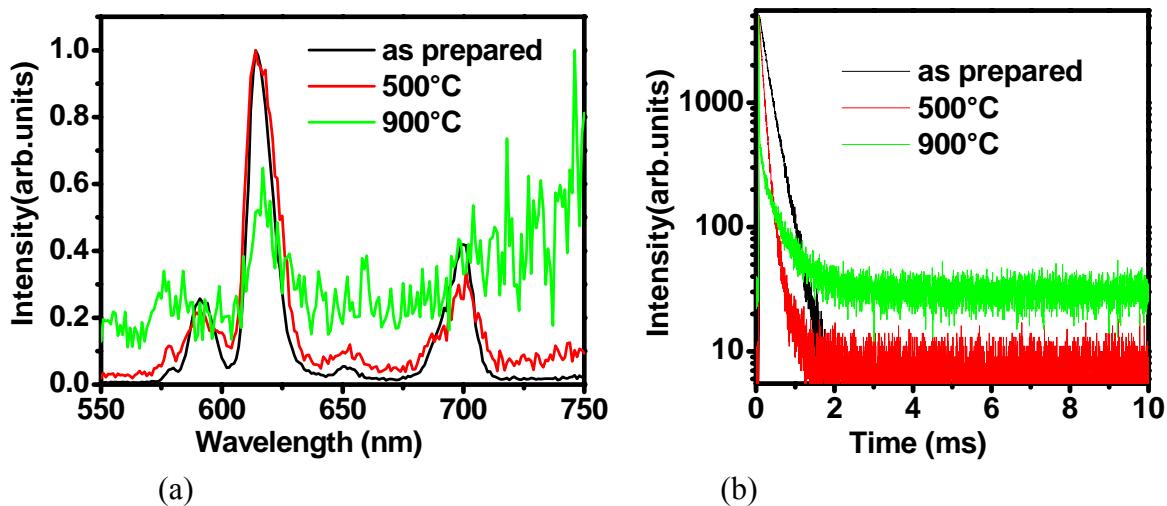


Fig.53. Emission spectra (a) and decay curves corresponding to the 5D_0 level of Eu^{3+} (b) for the product obtained by the reaction between Sb^{3+} and Eu^{3+} ions taken in the stoichiometric ratio. Samples were excited at 395 nm and emission was monitored at 612nm.

Hence based on the detailed luminescence and XRD studies, it is confirmed that Eu^{3+} and Sb^{3+} forms an amorphous antimony europium hydroxide. This amorphous compound undergoes decomposition on heating around 900°C , leading to the formation of mainly Eu_2O_3 and hydrated Sb(V) oxides.

CHAPTER 4: Phosphates

4.1. Introduction: Phosphates of Ga^{3+} , Sb^{3+} and Bi^{3+} are of interest because of their potential technological applications [212-220]. For example, GaPO_4 is a good piezo-electric material whereas SbPO_4 and BiPO_4 are used as catalysts as well as in optical/ photonic devices [221-225]. Doping lanthanide ions in such phosphates is an attractive option for making materials with multi functional applications. Under ambient conditions, GaPO_4 exists in hexagonal form whereas SbPO_4 and BiPO_4 adopt a monoclinic structure. BiPO_4 is also known to exist in hexagonal form [226, 227]. Unlike this, LnPO_4 (Ln = lanthanide) exist mainly in two crystalline modifications, viz. monazite and xenotime [228]. Monazite structure is adopted by lanthanide phosphates with relatively larger lanthanide ions (i.e., La^{3+} - Gd^{3+}) while xenotime structure is formed by smaller lanthanide ions (i.e., Tb^{3+} - Lu^{3+}). Essential difference in both the structures is that in the xenotime structure, Ln^{3+} ions exist as regular LnO_8 polyhedra whereas in the monazite structure, lanthanide ions (Ln^{3+}) exist as LnO_9 polyhedra [228]. For making lanthanide ions based luminescent materials using phosphate hosts like GaPO_4 , SbPO_4 and BiPO_4 , it will be ideal if solid solution formation between these phosphates and lanthanide phosphates exist. The major problem with the solid solution formation in this system is the large difference in the ionic radii of the cations and difference in their coordination numbers, particularly for Ga^{3+} and Sb^{3+} ions in GaPO_4 and SbPO_4 respectively. Further, the solubility product values are significantly different for GaPO_4 (10^{-21}), BiPO_4 (10^{-23}) and LnPO_4 ($\sim 10^{-26}$ to 10^{-25}) [229-231] which prevent the formation of solid solution between these compounds through co-precipitation techniques. However, if the metal phosphate nanoparticles are prepared under alkaline conditions in aqueous or alcoholic solutions, the surface hydroxyl groups on nanoparticles may undergo ion exchange with lanthanide ions. Such an ion exchange process will lead to the formation of nanoparticles

having surface lanthanide ions. This is particularly valid for GaPO₄, as the Ga³⁺ ionic radius is much smaller as compared to lanthanide ions, besides significant difference in the coordination numbers around the cations. Situation is slightly different for SbPO₄ nanomaterials as the ionic radius of Sb³⁺ (0.76Å) [177] is expected to be comparable with that of lanthanide ions with coordination number four, although lanthanide ions with such low coordination are not commonly observed. In contrast to this, Bi³⁺ ions in BiPO₄ have comparable ionic size to that of lanthanide ions and crystal structure of BiPO₄ is similar to that of lanthanide phosphates, there by facilitating the improved solubility of lanthanide ions in BiPO₄.

In the present study Eu³⁺, Ce³⁺, Tb³⁺, Dy³⁺, Sm³⁺ ions were chosen for doping in the above mentioned hosts. The luminescence characteristics of Eu³⁺ with respect to different environments are well understood and hence can be used as a probe to monitor the structural changes taking place with a host lattice. The ions Ce³⁺ and Tb³⁺ are known to have strong absorption in the UV region with Tb³⁺ ions emitting strongly in the visible region. In addition Ce³⁺ is an efficient sensitizer to Tb³⁺ (due to energy transfer from Ce³⁺ to Tb³⁺ ions) and therefore materials doped with Ce³⁺ and Tb³⁺ have been developed to generate efficient green light for display applications. This energy transfer between Ce³⁺ and Tb³⁺ ions is very sensitive to the crystal structure of the host, surface modification, etc. [112, 113, 232]. For example in CePO₄:Tb³⁺ and CePO₄:Dy³⁺ nanomaterials strong energy transfer has been observed from Ce³⁺ to Tb³⁺ or Dy³⁺ ions. However, in Ce³⁺ co-doped YAG:Tb³⁺ nanoparticles, energy transfer occurs from Tb³⁺ to Ce³⁺ [94]. Furthermore, in Ce³⁺ co-doped Y₂Sn₂O₇:Tb³⁺ nanoparticles, strong energy transfer from Ce³⁺ to Tb³⁺ occurs only after covering the nanoparticles with SiO₂ [233]. This has been attributed to the diffusion of lanthanide ions towards the interface region between Y₂Sn₂O₇ nanoparticles and silica.

This chapter is divided into three sections. The first section deals with structural and luminescence properties of GaPO₄ nanoparticles having different concentration of Eu³⁺ ions. The results obtained from this study is used to understand the luminescence properties of other lanthanide ions (Tb³⁺, Dy³⁺, Er³⁺, etc.) doped nanoparticles. The second section describes synthesis and optical properties of lanthanide doped SbPO₄ nanomaterials. Incorporation of lanthanide ions in such low symmetry environments (coordination number 4) and their luminescence properties are discussed. Vibrational spectroscopy has been used to confirm incorporation of lanthanides ions in the SbPO₄ host. Changes in the experimental conditions like synthesis temperature, doping concentration and varying the relative volume of solvent, etc., on the vibrational and luminescence properties from such nanomaterials are investigated. Luminescence properties of these nanomaterials are compared with the lanthanide ions doped bulk materials obtained by solid-state reaction. Energy transfer between Ce³⁺ and Tb³⁺ ions and its effect on the decay profiles of the excited state of Tb³⁺ ions in SbPO₄ host is also discussed in this section. In the third section synthesis and characterization of lanthanide doped BiPO₄ nanomaterials is discussed in detail. Lanthanide ions doped BiPO₄ nanomaterials with different crystal structures have been prepared at a relatively low temperatures and the effect of crystal structure on luminescence properties of the lanthanide ions is also investigated.

4.2. Studies on GaPO₄ and lanthanide ions containing GaPO₄ nanomaterials: GaPO₄ nanoparticles were prepared at 140°C in glycerol by precipitating Ga³⁺ with ammonium dihydrogen phosphate. For europium containing samples, appropriate concentration of Eu³⁺ is also used along with Ga³⁺ ions.

4.2.1. XRD, FT-IR and TEM study: XRD patterns of GaPO₄ nanoparticles containing 0, 2.5 and 5 at % Eu³⁺ ions are shown Fig.54. For the purpose of comparison XRD pattern of a standard hexagonal GaPO₄ (JCPDS file no. 080497) is also included in this figure. The

diffraction patterns from the GaPO₄ nanoparticles match well with the pattern reported in JCPDS data. The lattice parameters were calculated and are found to be $a = 4.900(2) \text{ \AA}$ and $c = 11.041(3) \text{ \AA}$ with a unit cell volume $229.5(2) \text{ \AA}^3$ for un-doped GaPO₄ nanoparticles. The lattice parameters are unchanged with increase in Eu³⁺ content in the sample suggesting that GaPO₄ lattice is unaffected by increase in Eu³⁺ concentration in the sample.

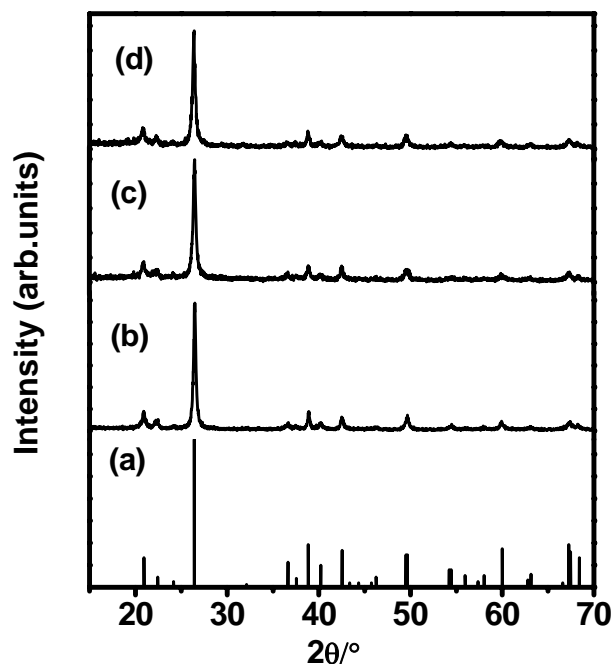


Fig.54. XRD patterns of (a) hexagonal GaPO₄ standard corresponding to JCPDS file no. 080497 (b) GaPO₄ nanoparticles, (c and d) GaPO₄ nanoparticles with 2.5 and 5 at % Eu³⁺, respectively.

The average crystal size of GaPO₄ nanoparticles was calculated from the line width of highest intense XRD peak by using Debye–Scherrer formula and is found to be ~ 30 nm. The particle size is also unaffected by increasing the Eu³⁺ contents in GaPO₄ samples. From the XRD results, it can be inferred that Eu³⁺ ions are not replacing Ga³⁺ ions in GaPO₄ lattice. Had it been the case, the lattice parameters of GaPO₄ nanoparticles would have increased significantly due to the higher ionic radii of Eu³⁺ (0.947Å) compared to Ga³⁺ (0.62Å) [172]. In order to characterize the nanocrystalline nature of the above samples detailed TEM studies have been carried out.

Figure 55 shows the representative TEM image and selected area electron diffraction (SAED) pattern from as prepared GaPO₄ nanoparticles. The particle sizes are in the range of 25-35 nm. There are also some particle aggregates having size in the range of 40 - 65 nm. The SAED patterns consist of dots, which are characteristic of randomly oriented single crystalline nanoparticles. The TEM images of 2.5 at % Eu³⁺ containing GaPO₄ sample is comparable with that of the undoped GaPO₄ nanoparticles (not shown). Based on the TEM studies it is inferred that as prepared Eu³⁺ containing sample consists of crystalline GaPO₄ nanoparticles of average size of 30 nm. This suggests that Eu³⁺ doping has no effect on the particle size of GaPO₄ nanoparticles. Even though the particle size and crystallinity of the GaPO₄ nanoparticles containing different amounts of Eu³⁺ ions are same, it is quite possible that the photoluminescence properties of Eu³⁺ ions can change significantly depending on the interaction of Eu³⁺ ions with the GaPO₄ nanoparticles. To understand such interactions, detailed luminescence studies have been carried out on these samples.

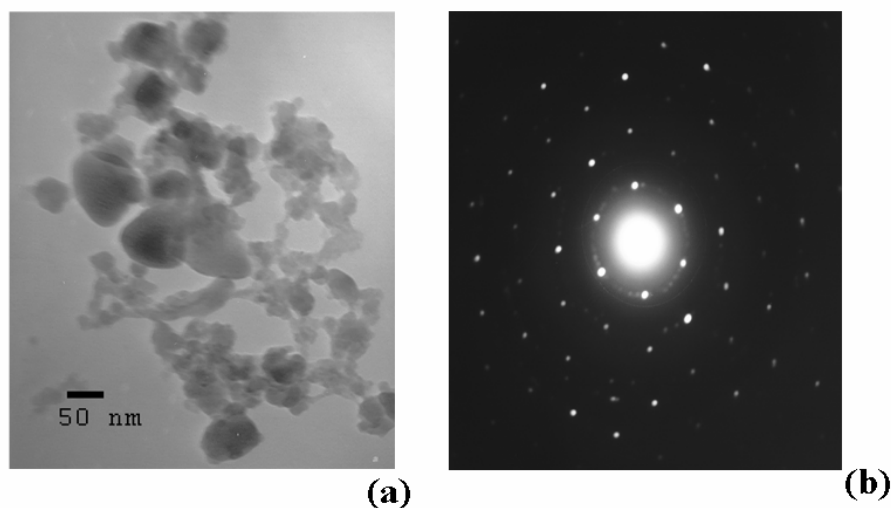


Fig.55. TEM images of (a) GaPO₄ nanoparticles. The selected area electron diffraction pattern from nanoparticles is shown in Fig.55 (b)

4.2.2. Luminescence studies: Figure 56 shows the emission spectra from GaPO₄ nanoparticles containing 2.5 and 5 at % Eu³⁺ along with that from pure EuPO₄ nanoparticles obtained after excitation at 260 nm. All the patterns are characterised by transitions from ⁵D₀

level to 7F_1 , 7F_2 , 7F_3 and 7F_4 levels of Eu^{3+} ions. The transitions ${}^5D_0 \rightarrow {}^7F_1$ and ${}^5D_0 \rightarrow {}^7F_2$ are purely magnetic and electric dipole allowed respectively. The relative intensity ratio of ${}^5D_0 \rightarrow {}^7F_2$ to ${}^5D_0 \rightarrow {}^7F_1$ transition, known as the asymmetric ratio of luminescence, is a very sensitive parameter which depends on the environment around Eu^{3+} ions [234, 235]. The value is found to be 2.2 for 2.5 at % Eu^{3+} containing sample. With increasing Eu^{3+} content (i.e. for 5 at % Eu^{3+} containing sample) the asymmetric ratio decreases to 1.0 (Fig.56 (b)). Significant change in the asymmetric ratio of luminescence indicates a drastic change in the environment around Eu^{3+} ions, which could be due to the formation of separate Eu^{3+} containing phase. It can be either the pure EuPO_4 or a complex of Eu^{3+} formed with ligands (glycerol) present in the reaction medium.

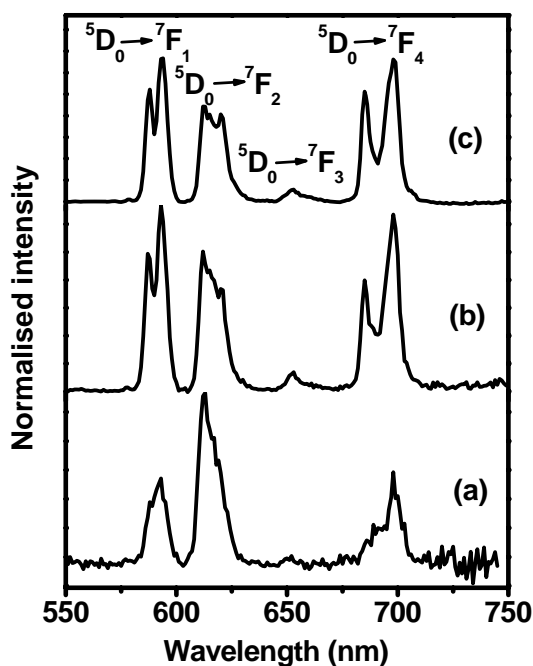


Fig.56. Emission spectrum from GaPO_4 nanoparticles containing (a) 2.5 at % and (b) 5 at % Eu^{3+} ions. The corresponding pattern from EuPO_4 nanoparticles is shown in Fig.56 (c). All samples were excited at 260 nm.

To check this aspect, emission spectrum from pure EuPO_4 sample prepared in an identical method as that used for GaPO_4 nanoparticles is shown in Fig.56 (c). The pattern is same as that of 5 at % Eu^{3+} containing GaPO_4 nanoparticles. The asymmetric ratio of luminescence is

found to be 0.97. A comparison of the emission spectrum shown in Fig.56 (b and c) suggests that Eu^{3+} ions exist as a separate EuPO_4 phase in 5 at % Eu^{3+} containing sample. However, for 2.5 at % Eu^{3+} containing sample, the asymmetric ratio of luminescence is quite different from EuPO_4 phase, suggesting that Eu^{3+} ions are in a different environment in GaPO_4 nanoparticles containing 2.5 at % Eu^{3+} . Presence of Eu^{3+} ions during precipitation reaction to form GaPO_4 can either lead to the formation of europium hydroxide phase or result in replacing protons of the surface hydroxyl groups attached to surface gallium or phosphorus species present on the nanoparticles.

In order to check the first possibility, Eu^{3+} ions were subjected to hydrolysis in glycerol medium using urea as the reagent for hydroxide formation (urea and not ammonium dihydrogen phosphate was used for precipitation to prevent the formation of EuPO_4 phase). Emission spectrum from the sample obtained after 260 nm excitation is shown in Fig.57. The asymmetric ratio of luminescence is found to be 4.2 which is significantly higher than the value 2.2 observed from GaPO_4 nanoparticles containing 2.5 at % Eu^{3+} ions. These data suggest that Eu^{3+} ions do not exist as europium hydroxide phase along with the GaPO_4 nanoparticles.

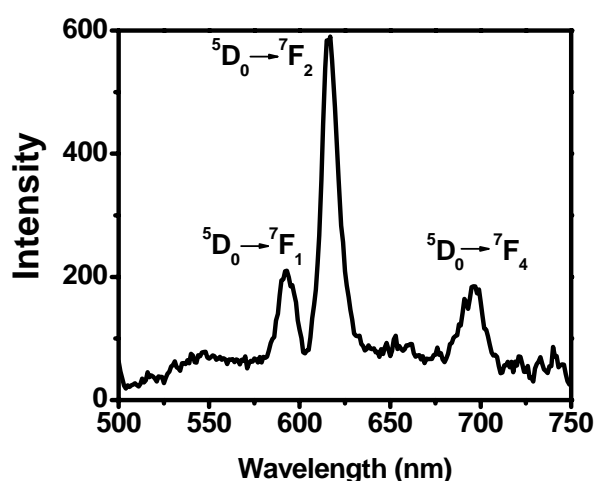


Fig.57 Emission spectrum of europium hydroxide sample prepared in glycerol medium by the identical method as that employed for GaPO_4 and EuPO_4 nanoparticles, except that urea rather than ammonium dihydrogen phosphate was used to create the alkaline environment and to prevent the formation of EuPO_4 phase.

The second possibility is the exchange of protons of OH groups attached to phosphorus or gallium ion at the surface of GaPO₄ nanoparticles. Such ion exchange process is expected to affect the electronic environment around P and this will be reflected in the ³¹P Magic Angle Spinning Nuclear Magnetic Resonance (MAS NMR) spectrum of the samples. Hence the ³¹P MAS NMR patterns of the samples were recorded and are described below.

4.2.3 ³¹P MAS NMR studies: Figure 58 shows the ³¹P MAS NMR patterns of GaPO₄ nanoparticles containing different amounts of Eu³⁺ ions. As prepared GaPO₄ sample showed a sharp peak around δ -10 ppm with weak shoulder around -6 ppm in the ³¹P MAS NMR spectrum (Fig.58 (a)). Based on the previous ³¹P MAS NMR studies on GaPO₄ and Al_xGa_{1-x}PO₄ samples [236, 237] the peak at -10 ppm has been attributed to the P structural units having four Ga³⁺ ions as its next nearest neighbors (first neighbor being the oxygen atom). The weak shoulder has been attributed to P structural units existing at the surface of the nanoparticles which have got linkages with the OH groups. Shoulder peak is more broadened compared to the main peak, due to the strong dipolar interaction between ³¹P and ¹H nuclei. With incorporation of 2.5 at % Eu³⁺, the peak maximum of the main and shoulder peaks remained same, however their line widths are higher compared to GaPO₄ nanoparticles (Fig.58 (b)). With increase in Eu³⁺ concentration, the line width of the peak increases and the shoulder is merged with the main peak around -10 ppm (Fig.58 (c and d)) due to increased line broadening. The peak maximum is found to be same for all the samples confirming that neither there is any solid solution formation between GaPO₄ and EuPO₄ nor there is any formation of P-O-Eu³⁺ linkages. Broadening of the peaks can be attributed to the existence of paramagnetic europium species along with the GaPO₄ nanoparticles. EuPO₄ phase formation, as revealed by luminescence studies for samples containing higher Eu³⁺ contents (5% or more), could not be confirmed by ³¹P MAS NMR as it showed no resonance signal due to the higher extent of paramagnetic broadening brought about by the presence of four europium

ions as next nearest neighbors around P in orthophosphate structural units. Significantly different values of solubility product for $\text{Ga}(\text{OH})_3$ (7.3×10^{-36}) and $\text{Eu}(\text{OH})_3$ (9.4×10^{-27}) further suggests that the ion exchange process is quite favorable in these system [177].

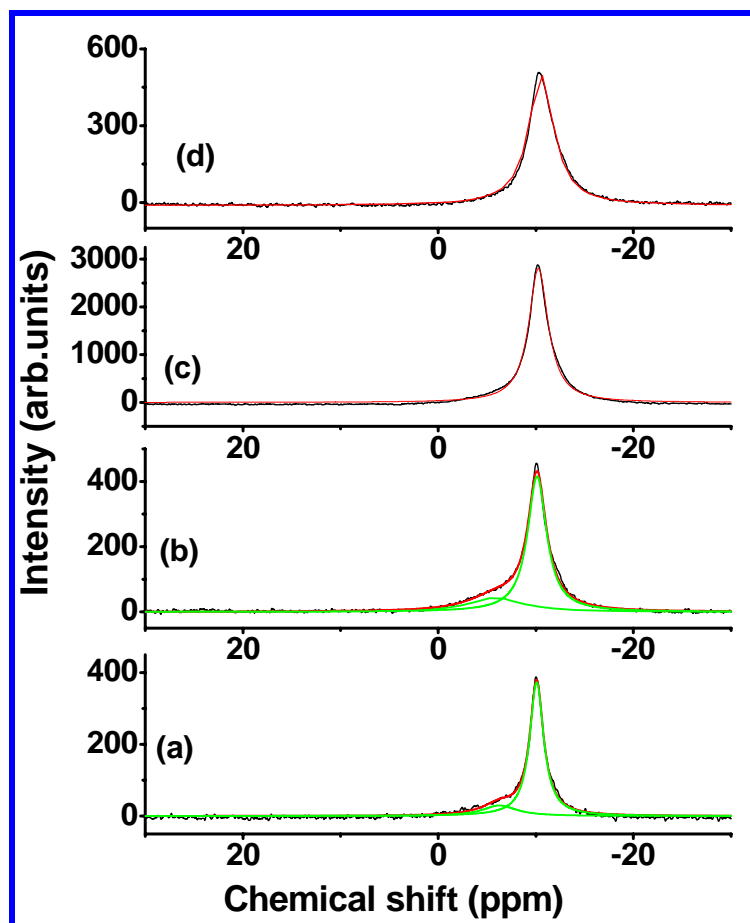


Fig.58. ^{31}P MAS NMR patterns of GaPO_4 nanoparticles containing (a) 0 at %, (b) 2.5 at %, (c) 5 at % and (d) 10 at % Eu^{3+} ions. Samples were spun at 10000Hz.

To get insight regarding the electronic environment around P in these samples, principal values of the ^{31}P chemical shift anisotropy tensor (δ_{11} , δ_{22} and δ_{33}) for GaPO_4 nanoparticles containing different amounts of Eu^{3+} ions have been calculated from the intensity of spinning sidebands observed in the ^{31}P MAS NMR patterns (recorded at a spinning speed of 5000 Hz) (Table 6). The anisotropy parameter has been calculated from the difference of δ_{11} and δ_{33} values and found to be around 20 ppm for GaPO_4 and 27 ppm for 2.5 at % Eu^{3+} containing GaPO_4 nanoparticles. For 5 and 10 at % Eu^{3+} containing sample, the

chemical shift anisotropy is much higher and the value significantly increases with increase in Eu^{3+} content in the sample (viz. Table 6). Comparable values of chemical shift anisotropy for both GaPO_4 and 2.5 at % Eu^{3+} incorporated GaPO_4 nanoparticles, further confirm the absence of P-O- Eu^{3+} linkages in the sample. In other words Eu^{3+} ions are not in the near vicinity of P and must be in the vicinity of Ga^{3+} ions, as Ga-O-Eu linkages formed by undergoing surface ion exchange with protons of the Ga-OH linkages. For GaPO_4 nanoparticles with higher Eu^{3+} concentrations (5 at % and more), there is an increase in fluctuating magnetic field created around P by paramagnetic EuPO_4 nanoparticles. Similar increase in the side band intensities and anisotropy values are also observed in ^{29}Si and ^{27}Al MAS NMR patterns of aluminosilicates containing paramagnetic iron compounds [238, 239]. A schematic diagram showing the ion exchange process leading to the formation of Ga-O-Eu linkages is shown in Fig.59. No separate peaks corresponding to EuPO_4 phase is seen in the XRD patterns for sample corresponding to more than 2.5 atom % Eu^{3+} . This is because of its relatively smaller concentration and poor crystallinity associated with its nanophase nature.

Table 6. The anisotropy parameter ($\Delta\delta$) obtained from the components of the chemical shift tensor (δ_{11} , δ_{22} and δ_{33}) which are calculated from the side band intensities observed from the ^{31}P MAS NMR patterns of GaPO_4 sample containing different amounts of Eu^{3+} ions. The line width of the peak (Γ) is also given in the table. Error in the chemical shift values is ± 1 ppm.

Structural Configuration of ^{31}P	Value of δ_{iso} (ppm)	Value of Γ (Hz)	Value of δ_{11} (ppm)	Value of δ_{22} (ppm)	Value of δ_{33} (ppm)	Value of $\Delta\delta$ (ppm) $ \delta_{33}-\delta_{11} $
GaPO_4	-10	344	2	-14	-18	20
GaPO_4 with 2.5 at % Eu^{3+}	-10.3	472	7	-17	-20	27
GaPO_4 with 5 at % Eu^{3+}	-10.3	516	21	-23	-29	50
GaPO_4 with 10 at % Eu^{3+}	-10.3	626	29	-24	-36	65

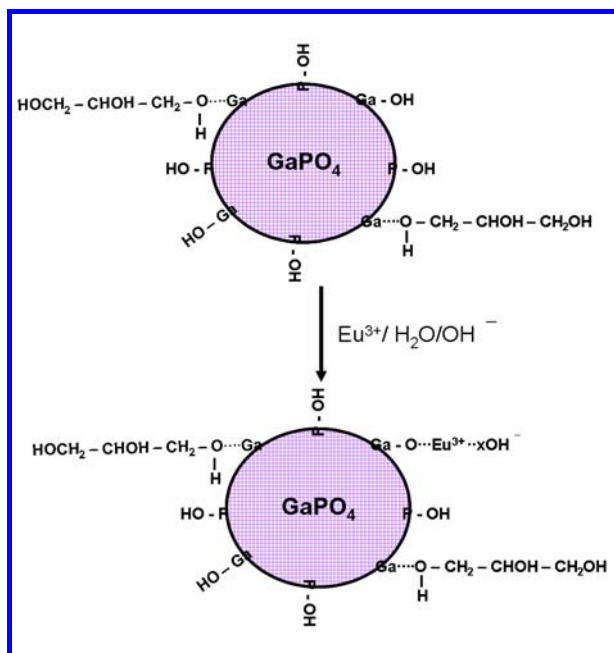


Fig.59. Schematic diagram of Eu³⁺ species present on the surface of the GaPO₄ nanoparticles.

For understanding the nature of interaction of ligands (glycerol molecule) with the surface Ga³⁺/Eu³⁺ species present in GaPO₄ nanoparticles, FT-IR spectra were recorded for both GaPO₄ nanoparticles and GaPO₄ nanoparticles containing 2.5 at % Eu³⁺ ions and are shown in Fig.60. Both the patterns are identical with peak positions around 3403, 2948, 2117, 2356 and 1654 cm⁻¹ as can be seen from Fig.60. In fact, the spectra for the 5 and 10 atom % Eu³⁺ containing samples are also same as that of undoped GaPO₄ nanoparticles. The peaks centered around 3403 and 1654 cm⁻¹ correspond to stretching and bending vibrations respectively of O-H groups present on the surface of the nanoparticles as well as from glycerol molecule [240]. The less intense peak ~ 2948 cm⁻¹ is assigned to asymmetric and symmetric stretching vibrations of C-H linkages of the stabilizing glycerol molecules. The weak peaks around 2117 and 2356 cm⁻¹ can be considered as the overtones of the δ(OH) bending vibrations [241]. There is no change in the line shape and peak positions of the peaks corresponding to the different vibrational modes of the ligand molecules present with both undoped and 2.5 at % Eu³⁺ containing GaPO₄ nanoparticles. This suggests that Eu³⁺ ions do

not have strong interaction with the ligand molecules. Hence from the luminescence, FT-IR and ^{31}P MAS NMR spectrum, it is confirmed that up to 2.5 at % Eu^{3+} containing GaPO_4 nanoparticles, Eu^{3+} replaces protons of the Ga-OH linkages, forming Ga-O-Eu type of linkages and beyond which separate EuPO_4 phase is formed.

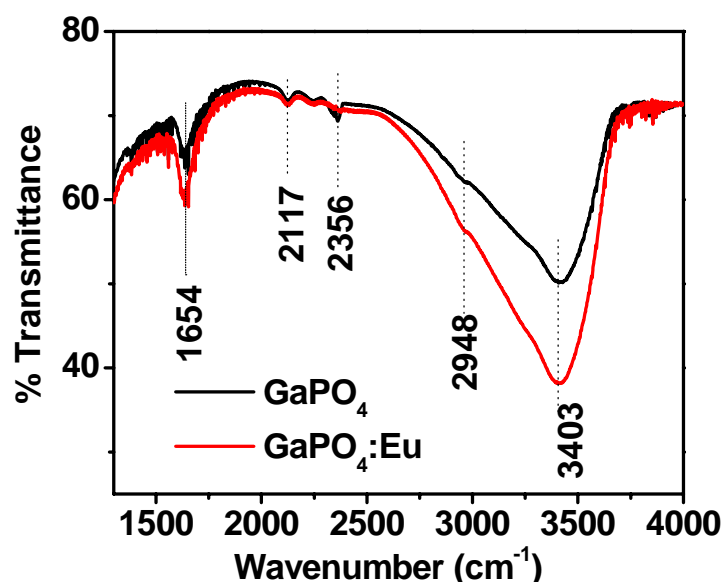


Fig.60. FT-IR spectrum of GaPO_4 nanoparticles containing 0 % and 2.5 at % Eu^{3+}

4.3. Studies on Antimony phosphate nanomaterials: Antimony phosphate nanomaterials were prepared at 130°C by precipitating Sb^{3+} using ammonium dihydrogen phosphate in ethylene glycol, glycerol and mixture of them.

4.3.1. Effect of ethylene glycol to glycerol ratio on size and shape of $\text{SbPO}_4:\text{Ln}$ nanomaterials: Figure 61 shows XRD patterns of as prepared SbPO_4 sample, obtained by using pure glycerol, mixtures of glycerol and ethylene glycol and pure ethylene glycol. For samples prepared in glycerol as well as mixture of glycerol and ethylene glycol, crystalline SbPO_4 with monoclinic structure has been observed. It should be noted here that for samples prepared in pure ethylene glycol, no sharp peak characteristic of crystalline material is observed revealing that reaction in pure ethylene glycol leads to the formation of an amorphous product. Average crystallite sizes as calculated from the line width of the XRD

peaks are found to decrease with increase in ethylene glycol content in the reaction medium. Table 7 shows the variation in average crystallite size as a function of relative amounts of ethylene glycol and glycerol in the reaction medium. From these results, it is inferred that the average crystallite size can be tuned by varying the relative amounts of ethylene glycol and glycerol in the reaction medium. The observed variation in the crystallite size with change in the relative concentration of the solvent has been explained based on the increase in viscosity of the medium with increase in the relative concentration of glycerol and associated increase in growth rate. XRD patterns are least square fitted to determine the lattice parameters. The values for un-doped SbPO_4 samples are $a = 5.099(1) \text{ \AA}$, $b = 6.767(2) \text{ \AA}$, $c = 4.749(1) \text{ \AA}$ with $\beta = 94.73$. Corresponding values for the 5% Tb^{3+} doped nanoparticles are $a = 5.093(1) \text{ \AA}$, $b = 6.769(2) \text{ \AA}$, $c = 4.733(1) \text{ \AA}$ with $\beta = 94.69$. There is no significant change in the values of lattice parameters for both doped and un-doped samples. This can be attributed to the comparable ionic radii of Sb^{3+} and Tb^{3+} under a coordination number of four. In order to check the nature of amorphous product obtained when pure ethylene glycol is used as the solvent, IR patterns were recorded for the amorphous product and it is compared with the patterns obtained from crystalline SbPO_4 sample. Figure 62 shows IR spectra of as prepared SbPO_4 sample obtained by using pure ethylene glycol, pure glycerol and a mixture of glycerol and ethylene glycol (10 ml each).

Table.7. Effect of variation volume of solvents on the average crystallite size of SbPO_4 nanomaterials.

Volume of glycerol (ml)	Volume of ethylene glycol (ml)	Average crystallite size (nm)
20	0	46
10	10	28
8	12	12
0	20	-

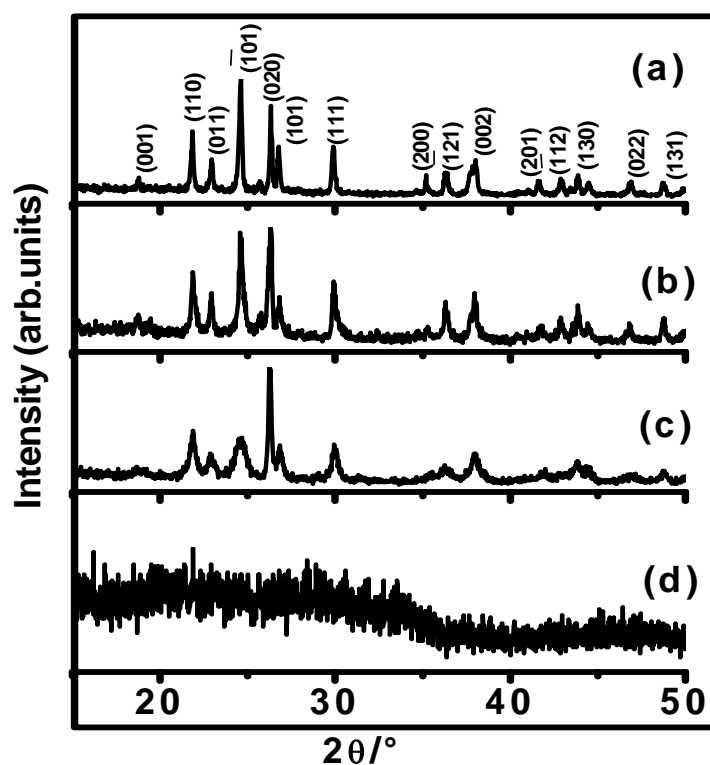


Fig.61. XRD Patterns of $\text{SbPO}_4:\text{Tb}^{3+}$ nanomaterials synthesized from (a) 20 ml glycerol, (b) 10 ml ethylene glycol and 10 ml glycerol, (c) 12 ml ethylene glycol and 8 ml glycerol and (d) 20 ml ethylene glycol.

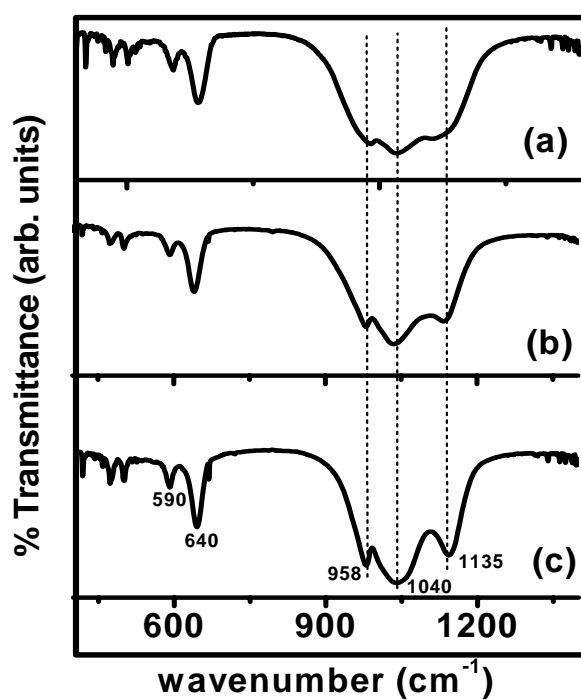


Fig.62. FT-IR Spectra of $\text{SbPO}_4:\text{Tb}^{3+}$ samples obtained in (a) ethylene glycol medium, (b) glycerol medium and (c) mixture of ethylene glycol and glycerol medium (10 ml each).

All the patterns were characterized by three intense peaks centered around 958, 1040 and 1135 cm^{-1} . Based on previous investigations [242-244] these peaks have been assigned to three non-degenerate P-O stretching vibrations of P-O-Sb³⁺ linkages. The peaks around 640 and 590 cm^{-1} have been attributed to the stretching vibration of Sb-O linkages present in P-O-Sb³⁺ linkages [244]. Peaks are slightly broadened in the case of amorphous product, indicating the higher extent of disorder present in the sample. The FT-IR pattern indicates that the product obtained from pure ethylene glycol is amorphous SbPO₄:Tb³⁺.

Figure 63 shows the TEM images of SbPO₄: Tb³⁺ samples prepared by using ethylene glycol-glycerol mixture. The images indicate the presence of both nanoribbons and nanoparticles of SbPO₄: Tb³⁺. The ribbons have length and width in the ranges of 500-700 and 100-200 nm, respectively (Fig.63 (a)). The images also have very fine nanoparticles of the size varying between 2 and 5 nm Fig.63 (b). Selected area electron diffraction patterns of both nanoribbons and particles showed crystalline nature of the samples (Fig.63 (c)). Further symmetry in the SAED patterns indicate the preferential orientation/ alignment of the nanoribbons existing in the sample. This is also in agreement with the powder XRD results (Fig.61). High-resolution image from a nanoparticle is shown in Fig.63 (d). The line spacing of 3.39 ± 0.05 Å between the lattice fringes matches well with the distance between the (020) planes of SbPO₄ lattice. Depending on the relative percentages of ethylene glycol and glycerol, the tunability in the morphology of SbPO₄ can be achieved. For example, carrying out the reaction in pure ethylene glycol leads to the formation of very small particles of SbPO₄ whereas carrying out the reaction in pure glycerol yields primarily nanoribbons. Anisotropic growth mechanism generally leads to the formation of nanorods or nanoribbons whereas the isotropic growth mechanism gives nanoparticles. This change in morphology has been again attributed to the wide difference in the viscosity of ethylene glycol and glycerol. Lower viscosity of ethylene glycol favors a faster diffusion of the precursor ions to the

growth centre compared to higher viscosity glycerol. This leads to the isotropic growth of the material in ethylene glycol compared to glycerol.

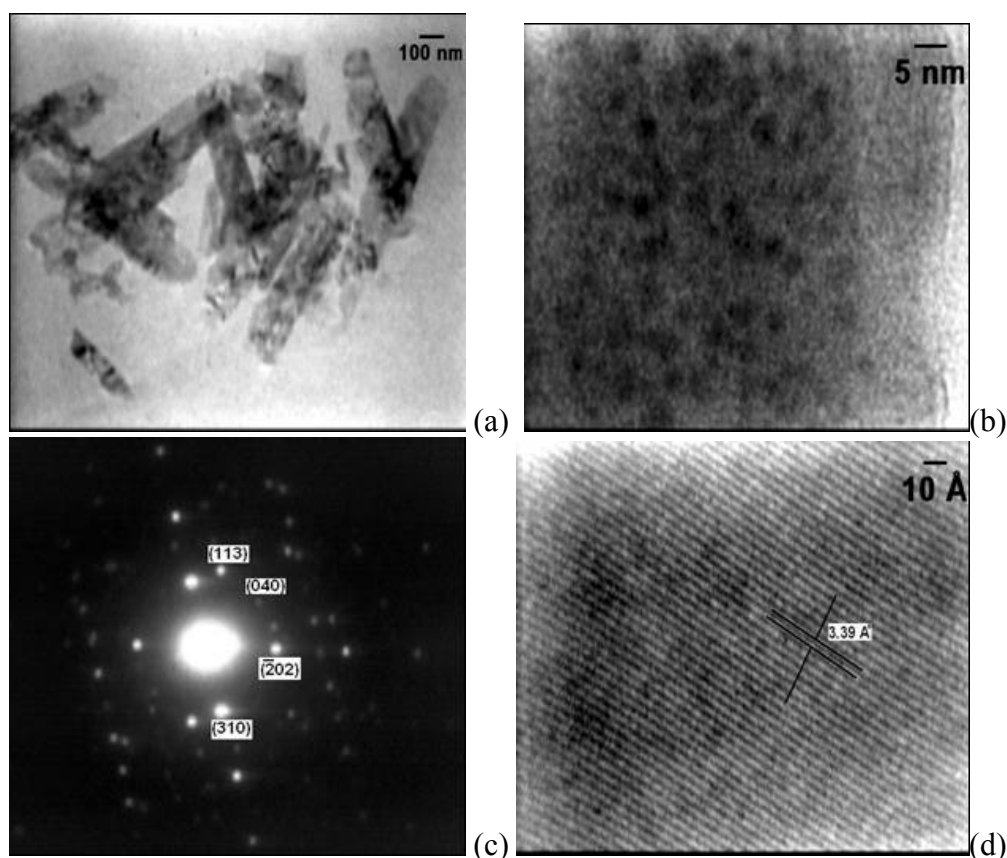


Fig.63. TEM images of (a) $\text{SbPO}_4:\text{Tb}^{3+}$ nanoribbons and (b) $\text{SbPO}_4:\text{Tb}^{3+}$ nanoparticles. The selected area electron diffraction pattern from the sample and the high resolution TEM image of a nanoribbon is shown in Fig.63 (c and d) respectively.

4.3.2 Luminescence studies on $\text{SbPO}_4:\text{Ln}$ nanoparticles/ nanoribbons: Luminescence property of these nanomaterials needs to be understood before incorporating them into different matrices like glassy materials or thin films for various optical applications. Figure 64(a and b) shows the emission spectra of $\text{SbPO}_4:\text{Eu}^{3+}$ (5%) and $\text{SbPO}_4:\text{Tb}^{3+}$ (5%) nanoparticles/ nanoribbons. For Eu^{3+} doped samples, the spectrum consists of mainly two peaks around 590 and 616 nm. The peak around 590 nm is characteristic of magnetic dipole (${}^5\text{D}_0 \rightarrow {}^7\text{F}_1$) transition and that around 616 nm is characteristic of electric dipole (${}^5\text{D}_0 \rightarrow {}^7\text{F}_2$) transition. Asymmetric ratio of luminescence (defined as the ratio of the relative intensity of

$^5D_0 \rightarrow ^7F_2$ to $^5D_0 \rightarrow ^7F_1$ transition) is calculated from the emission spectrum and found to be 1.14. The excitation spectrum corresponding to 616 nm emission is shown as an inset in Fig.64 (a). In addition to the sharp peaks characteristic of intra 4f transitions of Eu^{3+} ions, a broad asymmetric peak centered on 250 nm with a shoulder around 220 nm is observed in the excitation spectrum. Based on detailed luminescence studies on Eu^{3+} doped and un-doped SbPO_4 nanoparticles/ nanoribbons, the broad peak centered on 250 nm has been attributed to the Eu-O charge transfer process and the weak shoulder around 220 nm to the host absorption. Eu^{3+} emission has been observed from these samples after excitation at 250 and 220 nm indicating that there is energy transfer from the host to Eu^{3+} ions.

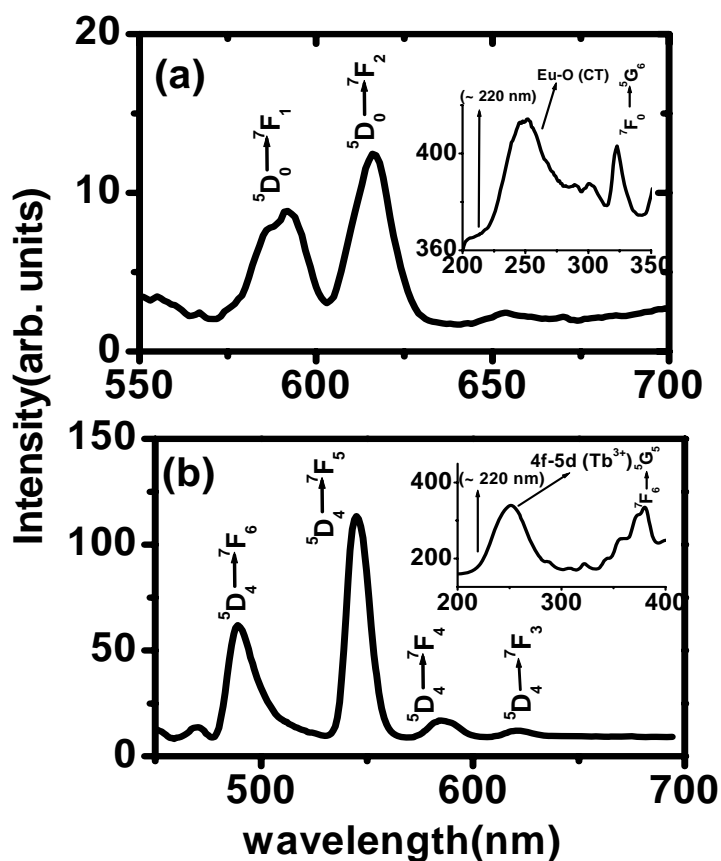


Fig.64. Emission spectrum of (a) $\text{SbPO}_4:\text{Eu}^{3+}$, (b) $\text{SbPO}_4:\text{Tb}^{3+}$ nanoparticles/ nanoribbons obtained after 220nm excitation. Insets show corresponding excitation spectrum monitored at 616 and 545 nm emission.

For Tb^{3+} doped SbPO_4 nanoparticles/ nanoribbons (Fig.64 (b)), strong Tb^{3+} emission characteristic of $^5D_4 \rightarrow ^7F_3$, $^5D_4 \rightarrow ^7F_4$, $^5D_4 \rightarrow ^7F_5$ and $^5D_4 \rightarrow ^7F_6$ transitions have been

observed after excitation at 250 and 220 nm. Excitation spectrum corresponding to 545 nm emission from these nanoparticles/ nanoribbons is shown as an inset in Fig.64 (b). Along with less intense sharp peaks characteristic of intra 4f transitions of Tb^{3+} ions, broad peak around 250 nm, which is characteristic of $4f \rightarrow 5d$ transition of Tb^{3+} ions is also observed. The host absorption around 220 nm characteristic of $SbPO_4$ is not clearly observed as it is masked under the intense $4f \rightarrow 5d$ transition peak. The intensity of 250 nm peak increases with increasing Tb^{3+} concentration in $SbPO_4$ nanoparticles/ nanoribbons.

To confirm incorporation of lanthanide ions in the $SbPO_4$ host, pure $EuPO_4$ and $TbPO_4$ samples were prepared in a manner identical to the synthesis of $SbPO_4:Eu^{3+}$ and $SbPO_4:Tb^{3+}$. No emission could be seen from $TbPO_4$ sample under all excitation wavelengths, whereas weak emission with asymmetric ratio of luminescence 0.78 has been observed from $EuPO_4$ sample (Fig.65).

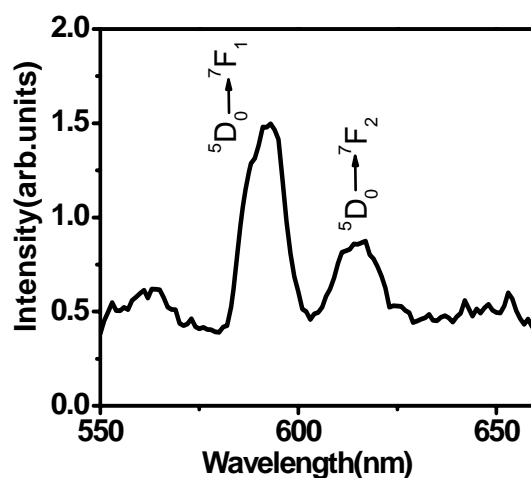


Fig.65. Emission spectrum of $EuPO_4$ sample obtained after 250 nm excitation.

Poor emission from these samples has been attributed to the significant quenching due to decreased $Eu^{3+}-Eu^{3+}$ distance brought about by high lanthanide ion concentration. The asymmetric ratio of luminescence, which is very sensitive to the Eu^{3+} local environment, is quite different for $EuPO_4$ (0.78) as compared to $SbPO_4:Eu$ (1.14). Observation of strong Eu^{3+} and Tb^{3+} emission from $SbPO_4:Eu^{3+}$ and $SbPO_4:Tb^{3+}$ along with quite different values of

asymmetric ratios of luminescence for $\text{SbPO}_4:\text{Eu}^{3+}$ and EuPO_4 samples confirm that no separate $\text{EuPO}_4/\text{TbPO}_4$ phase is formed, instead lanthanide ions like Tb^{3+} and Eu^{3+} are incorporated in SbPO_4 host. Had these ions formed separate phase, strong Tb^{3+} and Eu^{3+} emission would not have been observed from the lanthanide ions doped SbPO_4 samples. Final confirmation for the lanthanide ion incorporation in the SbPO_4 host comes from the lifetime values of $^5\text{D}_0$ level of Eu^{3+} in $\text{SbPO}_4:\text{Eu}^{3+}$ and EuPO_4 . The $^5\text{D}_0$ lifetime of Eu^{3+} is 2.0 ms (97%) and 0.004 ms (3%) for $\text{SbPO}_4:\text{Eu}^{3+}$ and the corresponding values are 0.8 ms (73%) and 0.42 ms (27%) for EuPO_4 . Significantly higher $^5\text{D}_0$ lifetime value corresponding to Eu^{3+} ion in $\text{SbPO}_4:\text{Eu}^{3+}$ compared to that of EuPO_4 further substantiate the fact that Eu^{3+} ions are incorporated in the SbPO_4 host and not existing as separate EuPO_4 .

With a view to compare the photoluminescence intensities of $\text{SbPO}_4:\text{Ln}^{3+}$ nanoparticles/ nanoribbons with that of bulk materials, $\text{SbPO}_4:\text{Eu}^{3+}$ and $\text{SbPO}_4:\text{Tb}^{3+}$, bulk materials were prepared by solid-state reaction between Sb_2O_3 and ammonium dihydrogen phosphate at 500°C . XRD patterns of the reaction product confirmed formation of crystalline SbPO_4 . Figure 66 shows the emission and excitation spectra from these samples. For the same amount of sample, photoluminescence intensities of bulk materials are comparable with that of nanomaterials. (Host absorption around 220 nm is more clearly seen in the inset of Fig.66 (a)). Based on these results it is inferred that the luminescent SbPO_4 nanomaterials prepared at low temperature are equally good as bulk materials and has an added advantage of dispersability in methanol and water.

Luminescence measurements were also carried out for SbPO_4 nanoparticles/ nanoribbons as a function of Tb^{3+} doping concentration. Figure 67 shows the emission spectrum from SbPO_4 nanoparticles/ nanoribbons containing different amounts of Tb^{3+} ions and excited at 250 nm. The emission intensity is maximum for 2 atom % Tb^{3+} doped samples and it systematically decreased with further increasing Tb^{3+} concentration due to

concentration quenching. Tb^{3+} luminescence improves by co-doping of Ce^{3+} in $SbPO_4:Tb^{3+}$ nanomaterials. This has been attributed to the energy transfer from Ce^{3+} to Tb^{3+} ions in the lattice. In the following section, structure, morphological and luminescence characteristic of Ce^{3+} co-doped $SbPO_4:Tb^{3+}$ nanomaterials are discussed.

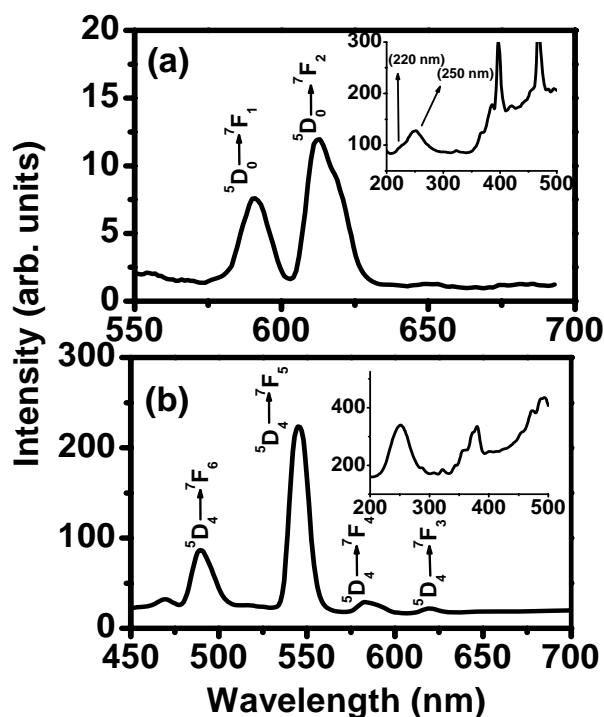


Fig.66. Emission spectrum of (a) $SbPO_4:Eu^{3+}$ and (b) $SbPO_4:Tb^{3+}$ bulk materials prepared by solid state reaction (excitation wavelength was 220 nm). Insets show corresponding excitation spectrum monitored at 616 and 545 nm emission.

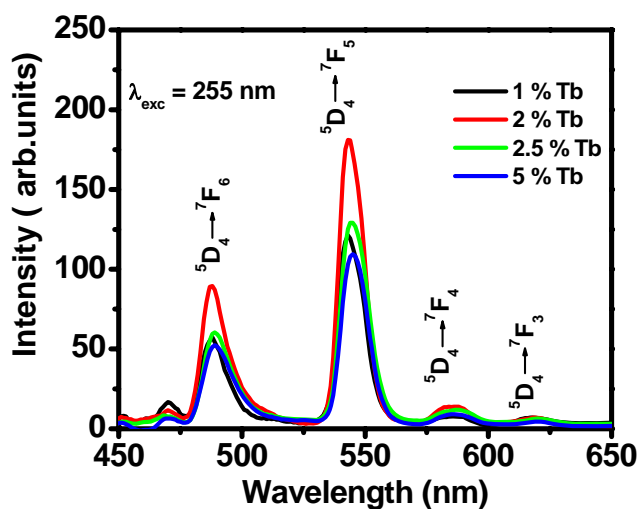


Fig.67. Emission spectra of $SbPO_4$ nanoparticles/ nanoribbons doped with 1, 2, 2.5, and 5 at % Tb^{3+} ions. Samples were excited at 250 nm.

4.3.3 Studies on Ce^{3+} co-doped $\text{SbPO}_4:\text{Tb}^{3+}$ nanomaterials and their dispersion in silica:

Figure 68 shows TEM images of $\text{SbPO}_4:\text{Ce}^{3+}(2.5\%),\text{Tb}^{3+}(5\%)$ samples dispersed in SiO_2 . The ribbons are shown in Fig.68 (a). Their length and width are in the range of 700-800 and 20-50 nm, respectively. In addition to these nanorods, nanoparticles of size 2-5 nm are also present as revealed by the TEM image (Fig.68 (b)). Nanoribbons are aggregated and are surrounded by silica, as can be seen from the contrast difference observed in the TEM image arising due to the high refractive index of SbPO_4 compared to silica. Selected area diffraction from the sample is shown in the Fig.68 (c).

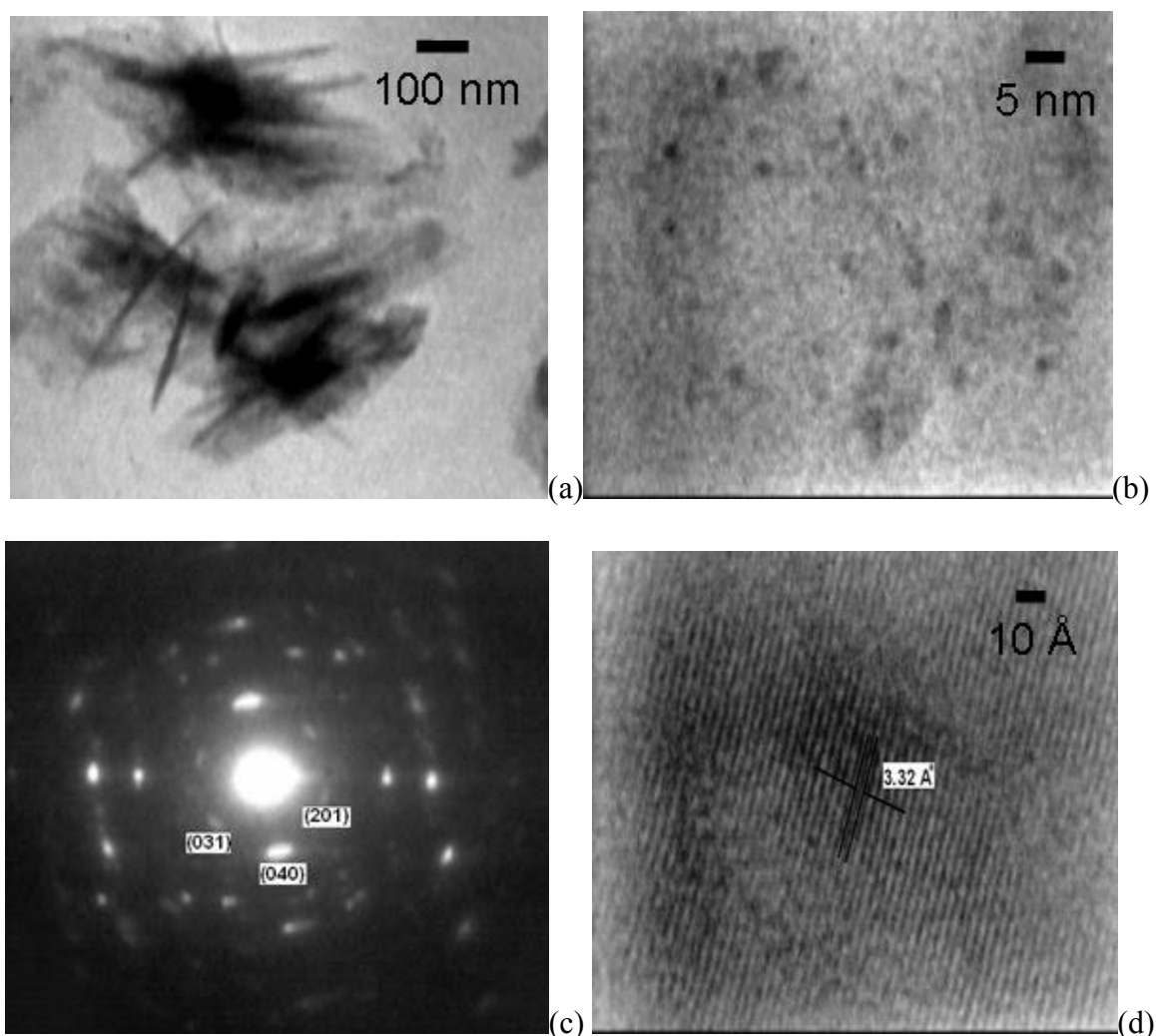


Fig.68. TEM images of (a) $\text{SbPO}_4:\text{Ce}^{3+}(2.5\%),\text{Tb}^{3+}(5\%)$ nanoribbons in silica and (b) $\text{SbPO}_4:\text{Ce}^{3+}(2.5\%),\text{Tb}^{3+}(5\%)$ nanoparticles in silica. A representative selected area electron diffraction pattern and a high resolution TEM image from these nanoribbon are shown in Fig.68 (c and d), respectively.

Compared to the selected area electron diffraction pattern shown in Fig.63 (c), the dots corresponding to the diffraction patterns observed in Fig.68 (c) are not symmetrically placed, indicating that there exists lesser extent of preferential orientation in the sample after dispersion in silica. High-resolution image of a nanoparticle is shown in Fig.68 (d). Lattice fringes can be clearly seen in the image. The distance between the lattice planes, 3.32 ± 0.05 Å, match well with the (020) plane of SbPO₄ phase. XRD and TEM studies do not give any indication regarding the incorporation of the lanthanide ions in SbPO₄ lattice. In order to confirm this aspect, detailed structural studies have been carried out using infrared and Raman spectroscopic techniques.

4.3.4 Proof for the incorporation of lanthanide ions into SbPO₄ lattice: Figure 69 shows the Raman spectrum of un-doped SbPO₄, SbPO₄:Ce³⁺(2.5%),Tb³⁺(5%), SbPO₄:Ce³⁺(2.5%),Tb³⁺(5%)-SiO₂ samples. The patterns appear identical for all the samples. All the patterns are characterised by sharp peaks at ~ 210, 350, 471, 578, 618, 971 and 1048 cm⁻¹. In addition to this, broad peaks at ~ 437, 664, 770 and 931 cm⁻¹ are observed. The position of these peaks is in close agreement with those reported by Nalin, et al. [245]. The SbPO₄ crystallize in C_{2h}² space group and comprises of PO₄ tetrahedral units bound to the Sb(III) polyhedral units (trigonal bipyramidal configurations) through asymmetrical bridging oxygen atoms [246]. The isolated PO₄ groups with T_d symmetry, when placed at C_{2h} sites, (corresponding to the monoclinic SbPO₄ unit cell) results in the decomposition of the vibrational species into the following modes.

$$A_1: A_g + B_u, \quad 2F_2: 4A_g + 4B_u + 2A_u + 2B_g, \quad E: A_g + B_u + A_u + B_g$$

Among these, the six A_g and three B_g modes are Raman active while the 3A_u and 6B_u modes are IR active. The peaks at ~ 355, 623, 976 and 1053 cm⁻¹ are of the A_g type, while peaks at ~ 476 and 583 cm⁻¹ are of the B_g type. Replacement of Sb³⁺ by lanthanide ions (Ce³⁺ or Tb³⁺) is expected to have significant effect on the P-O stretching modes of PO₄ units in SbPO₄. We

have noticed that the peak maximum at $\sim 1053 \text{ cm}^{-1}$ characteristic of the asymmetric stretching vibration of PO_4 structural units, decreases with doping lanthanide ions in the SbPO_4 lattice, as can be seen from Fig.69 (b). Shifting of the peak maximum corresponding to the asymmetric P-O stretching mode of PO_4 units to lower wave numbers has been attributed to the combined effect of heavier mass of Ce^{3+} and Tb^{3+} ions compared to Sb^{3+} ion and decrease in the covalency of P-O linkages brought about by replacement of Sb^{3+} by Ce^{3+} and Tb^{3+} ions in SbPO_4 lattice.

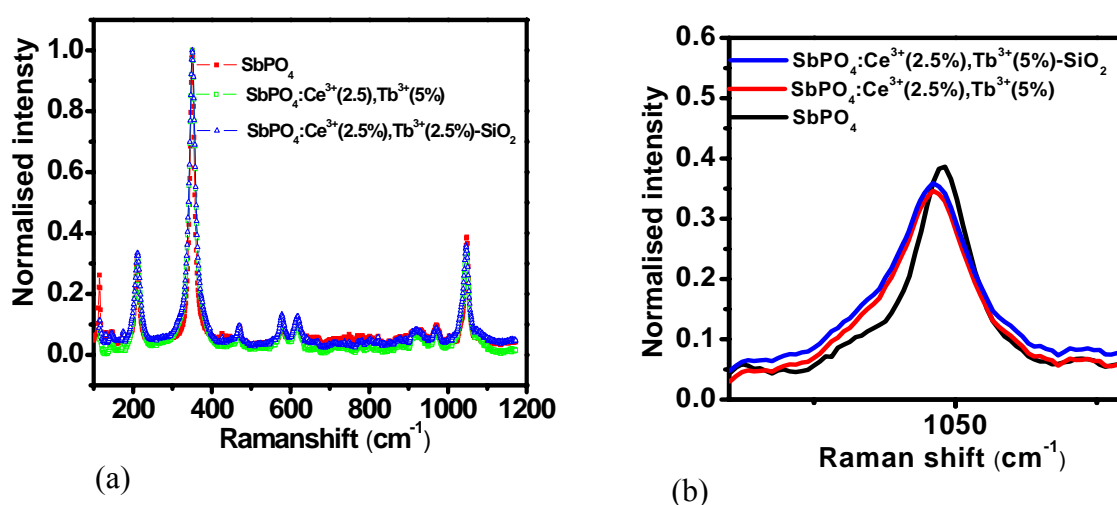


Fig.69. Raman spectrum over the entire region (a) corresponding to un-doped SbPO_4 , $\text{SbPO}_4:\text{Ce}^{3+}(2.5\%),\text{Tb}^{3+}(5\%)$ and $\text{SbPO}_4:\text{Ce}^{3+}(2.5\%),\text{Tb}^{3+}(5\%)$ samples dispersed in silica. The peak corresponding to the asymmetric stretching vibrations of PO_4 tetrahedra in these samples observed over the region of 1000-1080 cm^{-1} is shown in Fig.69 (b).

Similar trend is also observed for the asymmetric stretching vibration of the PO_4 units in the IR spectrum (Fig.70 (a)). In addition to the vibrations of PO_4 stretching, the vibrations characteristic of Sb-O linkages (peak observed $\sim 640 \text{ cm}^{-1}$) is also affected (Fig.70 (b)). The peak at 640 cm^{-1} shows a systematic lowering with increase in lanthanide ion concentration in SbPO_4 . This is not very clear in the Raman spectrum due to weak intensity for peak corresponding to Raman mode of Sb-O linkages. Hence based on the IR and Raman studies it is established that lanthanide ions such as Ce^{3+} and Tb^{3+} replace Sb^{3+} ions in the SbPO_4

lattice. Lanthanide ions occupying such a low symmetry environments (coordination number 4) in inorganic hosts is observed for the first time.

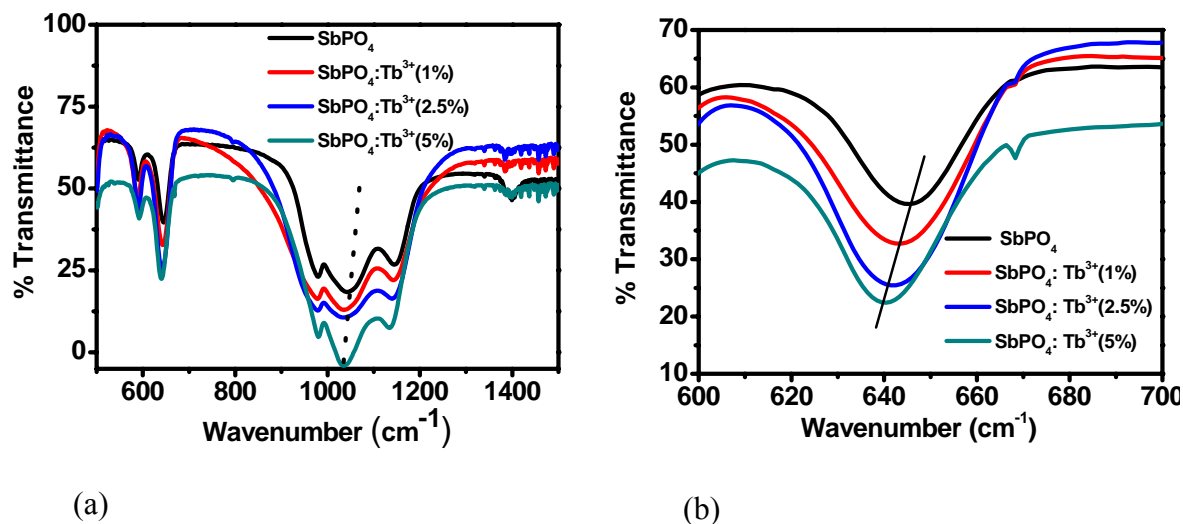


Fig.70. FT-IR patterns corresponding to SbPO_4 nanoribbons/ nanoparticles containing different concentrations of Tb^{3+} ions. The peak corresponding to the Sb-O stretching vibration in these samples observed over the region of $600\text{-}700\text{ cm}^{-1}$ is shown in Fig.70 (b).

The effect of SiO_2 coating is very clearly seen in the symmetric PO_4 stretching mode at $\sim 930\text{ cm}^{-1}$ (Fig.71). The peak at $\sim 930\text{ cm}^{-1}$ for undoped SbPO_4 and $\text{SbPO}_4:\text{Ce}^{3+}(2.5\%),\text{Tb}^{3+}(5\%)$ sample remains unchanged. The increased width in silica coated $\text{SbPO}_4:\text{Ce}^{3+}(2.5\%),\text{Tb}^{3+}(5\%)$ sample is due to random distribution of phosphate structural units in the SiO_2 matrix. The presence of Si attached with the PO_4 tetrahedra (P-O-Si linkages) results in weakening of the ν_{sym} vibrational group frequencies at $\sim 930\text{ cm}^{-1}$. In fact, a careful analysis of the 930 cm^{-1} peak (Fig.71 (c)) indicates that there are two overlapping peaks, one at $\sim 930\text{ cm}^{-1}$ similar to what is observed for the undoped and $\text{SbPO}_4:\text{Ce}^{3+}(2.5\%),\text{Tb}^{3+}(5\%)$ sample and another at $\sim 921\text{ cm}^{-1}$ which represent the changed bonding configuration of the PO_4 units in the silica matrix. Thus, the phosphate groups are present in two different environments. One such possible change in the bonding environment is the terminal O atoms of surface PO_4 tetrahedron of SbPO_4 nanoribbons/ nanoparticles

being bonded with the Si atoms (i.e. P-O-Si type of linkages). Phosphorus being more electronegative than Si, this will result in a reduction in the force constants, and hence lowering of Raman frequency. This effect is more prominent for the symmetric PO₄ vibration and hence we observe two peaks in the present case.

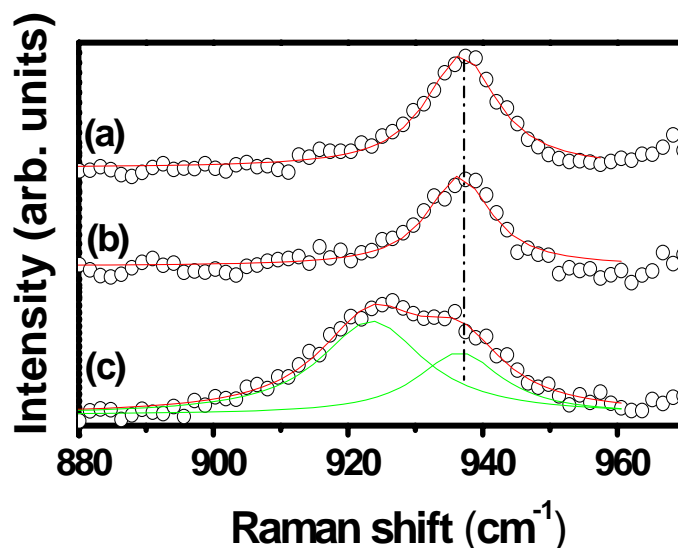


Fig.71 Raman spectrum corresponding to symmetric PO₄ stretching mode of (a) un-doped SbPO₄ (b) SbPO₄:Ce³⁺(2.5%),Tb³⁺(5%) and (c) SbPO₄:Ce³⁺(2.5%),Tb³⁺(5%) samples dispersed in silica.

4.3.5 Luminescence studies on SbPO₄:Ce, Tb and effect of incorporation of nanomaterials in silica: Figure 72 shows the emission spectra of SbPO₄:Tb³⁺(5%), SbPO₄:Ce³⁺(2.5%),Tb³⁺(5%) and SbPO₄:Ce³⁺(2.5%),Tb³⁺(5%)-SiO₂ obtained after 250 nm excitation. The peaks observed ~ 489, 543, 585, and 621 nm correspond to transitions from ⁵D₄ level to ⁷F₆, ⁷F₅, ⁷F₄ and ⁷F₃ levels, respectively of Tb³⁺ ion. It is worth noting that, unlike Tb³⁺ or Ce³⁺-Tb³⁺ doped SbPO₄ samples, pure TbPO₄ prepared by the identical method as that of SbPO₄:Tb³⁺ samples did not show any emission (inset of Fig.72). This aspect substantiate the fact that Tb³⁺ ions are getting incorporated in SbPO₄ lattice and do not exist as separate TbPO₄ phase, a fact which is also confirmed from the vibrational studies described above. It is also observed that Ce³⁺ ion shows very weak emission in the UV region. A representative Ce³⁺ emission spectrum from SbPO₄:Ce³⁺(2.5%),Tb³⁺(5%) sample

obtained after 275 nm excitation is shown as an inset in Fig.72. Weak emission has been attributed to the enhanced non-radiative decay of Ce^{3+} ions in the present host.

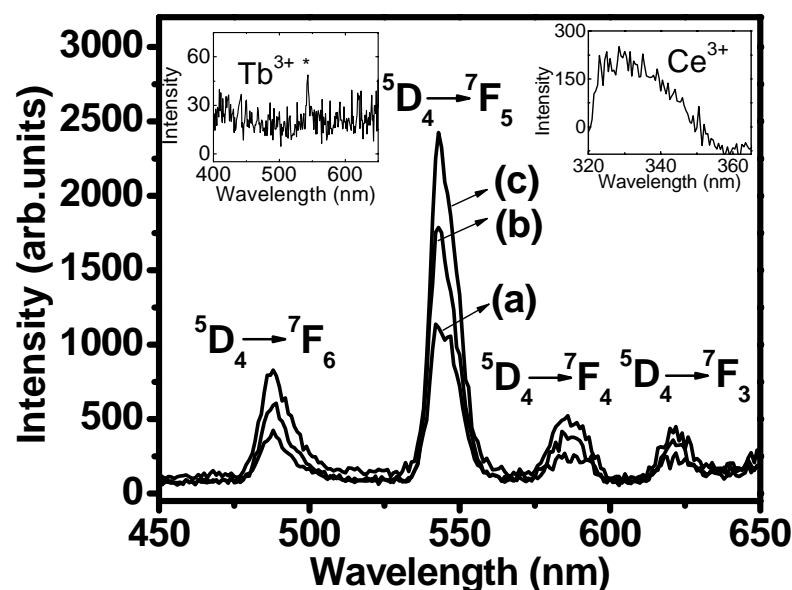


Fig.72. Emission spectrum from nanoribbons/ nanoparticle of (a) $\text{SbPO}_4:\text{Tb}^{3+}(5\%)$, (b) $\text{SbPO}_4:\text{Ce}^{3+}(2.5\%),\text{Tb}^{3+}(5\%)$, and (c) $\text{SbPO}_4:\text{Ce}^{3+}(2.5\%),\text{Tb}^{3+}(5\%)$ dispersed in silica. Samples were excited at 250 nm. Inset at the left side shows the emission spectrum of TbPO_4 samples prepared by the identical method as that adopted for other samples and the inset at the right side shows the Ce^{3+} emission from $\text{SbPO}_4:\text{Ce}^{3+}(2.5\%),\text{Tb}^{3+}(5\%)$ sample obtained after 278 nm excitation. The peak marked “*” in the left inset is an artifact.

Since the samples are powder in nature, it is not very accurate to compare the peak intensities of the emission spectra, while comparing their luminescence properties. Instead, the lifetime of the $^5\text{D}_4$ level of Tb^{3+} in these samples can be compared for judging their luminescent efficiencies. The decay curve corresponding to the $^5\text{D}_4$ level of Tb^{3+} obtained after exciting the samples at ~ 250 nm ($4f \rightarrow 5d$ transition of Tb^{3+}) and monitoring the emission at ~ 544 nm ($^5\text{D}_4 \rightarrow ^7\text{F}_5$ transition of Tb^{3+}) for these samples are shown in Fig.73. The decay curves are found to be bi-exponential in nature for both $\text{SbPO}_4:\text{Tb}^{3+}(5 \text{ at } \%)$ and $\text{SbPO}_4:\text{Ce}^{3+}(2.5\%),\text{Tb}^{3+}(5\%)$ nanoribbons/ nanoparticles, and single exponential in nature for $\text{SbPO}_4:\text{Ce}^{3+}(2.5\%),\text{Tb}^{3+}(5\%)$ nanoribbons/ nanoparticles incorporated in silica. The measured

lifetime values along with their relative contribution to the over all decay profile are shown in Table 8. The lifetime values of the 5D_4 level of Tb^{3+} in the $SbPO_4:Tb^{3+}$ (2.5 at %) sample are 0.4 ms (τ_1) and 2.1 ms (τ_2) and the values corresponding to Ce^{3+} co-doped $SbPO_4:Tb^{3+}$ (5 at%) sample are 0.4 ms (τ_1) and 2.4 ms (τ_2) with their relative contribution in the ratio $\sim 22 : 78$ for both the samples. In the case of $SbPO_4:Ce^{3+}$ (2.5 at %), Tb^{3+} (5 at %)- SiO_2 samples, the faster component is absent.

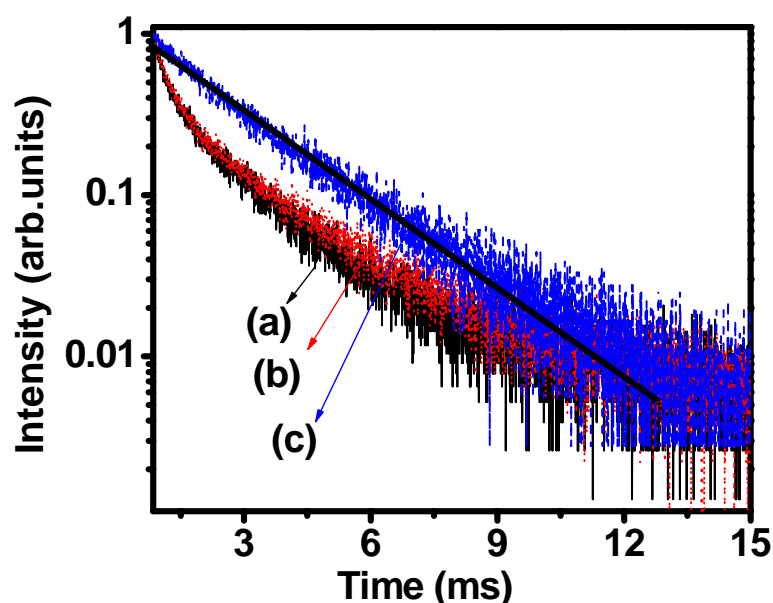


Fig.73. Decay curves corresponding to the 5D_4 level of Tb^{3+} ions from nanoribbons / nanoparticles of (a) $SbPO_4:Tb^{3+}$ (5 at %), (b) $SbPO_4:Ce^{3+}$ (2.5 at %), Tb^{3+} (5 at %) and (c) $SbPO_4: Ce^{3+}$ (2.5 at %), Tb^{3+} (5 at %) dispersed in silica. The samples were excited at 250 nm and emission was monitored at 544 nm.

Table 8. The lifetime values corresponding to the 5D_4 level of Tb^{3+} ions in $SbPO_4:Ce^{3+}$, Tb^{3+} nanoribbons/ nanoparticles along with the χ^2 values obtained from fitting. The numbers in brackets give the relative concentration of each lifetime components. Error in the lifetime values are within 5% as revealed by the duplicate measurements

Sample name	Lifetime values			Effective lifetime (ms)
	τ_1 (ms)	τ_2 (ms)	χ^2	
$SbPO_4:Tb^{3+}$ (5%)	0.4 (23%)	2.1 (77%)	1.1	3.09
$SbPO_4:Ce^{3+}$ (2.5%), Tb^{3+} (5%)	0.4 (22%)	2.4 (78%)	1.2	3.28
$SbPO_4:Ce^{3+}$ (2.5%), Tb^{3+} (5%) - SiO_2	-	2.2(100%)	1.1	3.01

The luminescence dynamics associated with multiple lifetime components can be better pictured through effective lifetime (τ_{eff}). The effective lifetime (τ_{eff}), which is measure of the average environment around the Tb^{3+} ions in the sample, is calculated based on the equation (20).

$$\tau_{\text{eff}} = \frac{\int_0^{\infty} tI(t)dt}{\int_0^{\infty} I(t)dt} \dots\dots\dots (20)$$

where I(t) is the intensity at any time t

From Table 8 it is evident that, Ce^{3+} co-doping in $\text{SbPO}_4:\text{Tb}^{3+}$, leads to slight increase in the τ_2 component of the decay corresponding to the $^5\text{D}_4$ level of Tb^{3+} ions. This increase in the τ_2 component is responsible for the increased τ_{eff} values. The bi-exponential nature of the decay curves of $\text{SbPO}_4:\text{Tb}^{3+}(5\%)$ and $\text{SbPO}_4:\text{Ce}^{3+}(2.5\%),\text{Tb}^{3+}(5\%)$ nanoribbons/ nanoparticles can be attributed to the presence of Tb^{3+} ions in at least in two different environments, namely the one at the bulk and the other at the surface of the nanoribbons/ nanoparticles. The luminescence originating from the surface of the nanoribbons/ nanoparticles is responsible for the τ_1 component whereas that originating from the bulk is responsible for τ_2 component. The lanthanide ions at the surface will undergo faster quenching compared to the ones at the bulk due to the presence of stabilising ligands at the surface. The vibrations associated with the C-H, O-H and C-O linkages of the stabilising ligands are responsible for the non-radiative decay of the lanthanide ions excited states. The presence of stabilising ligand with the SbPO_4 nanoribbons/ nanoparticles has been confirmed from IR pattern of the sample. Thus an increased component of the non-radiative transition in case of samples which are not incorporated in silica, results in a shorter lifetime component. However, when the nanoribbons/ nanoparticles are dispersed in silica, the ligands are removed from the surface, thereby leading to the appearance of a single exponential decay curve. The similar τ_1 values

that are observed for both the $\text{SbPO}_4:\text{Tb}^{3+}$ (5%) and $\text{SbPO}_4:\text{Ce}^{3+}$ (2.5%), Tb^{3+} (5%) samples further support that the faster component (τ_1) is originating from the lanthanide ions present at the surface of the nanoribbons/ nanoparticles. Replacement of the ligands from the surface of the nanoparticles by silica matrix is schematically shown in Fig.74.

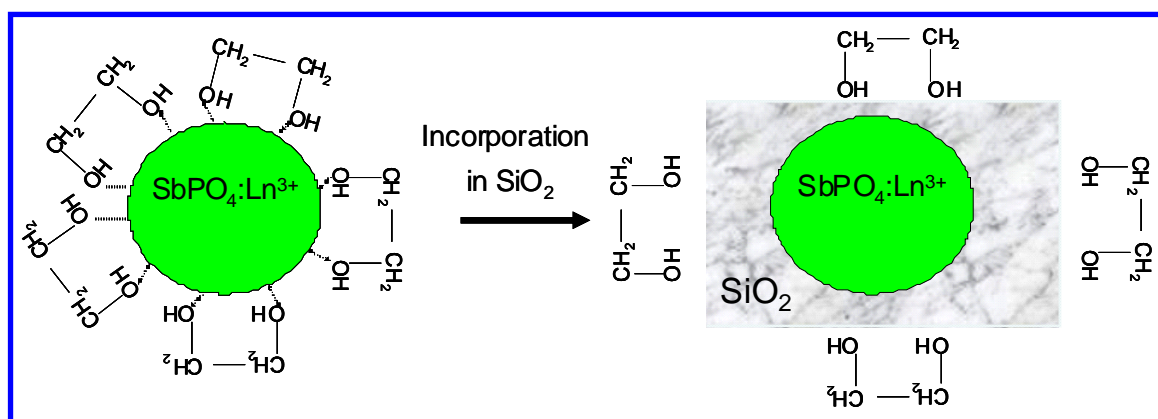


Fig.74. Schematic representation showing the effect of incorporation of nanoparticles in silica matrix.

In order to confirm whether energy transfer is taking place between Ce^{3+} and Tb^{3+} ions in the $\text{SbPO}_4:\text{Ce}^{3+}$, Tb^{3+} nanoribbons/ nanoparticles, excitation spectra were recorded by monitoring the $^5\text{D}_4 \rightarrow ^7\text{F}_5$ transition of Tb^{3+} ions at 545 nm (Fig.75). The excitation spectrum of $\text{SbPO}_4:\text{Tb}^{3+}$ (5%) (Fig.75 (a)) has a broad and intense band at ~ 250 nm and sharp and weak features at 284, 303, and 318 nm. The former broad band at ~ 250 nm corresponds to allowed 4f to 5d transition of Tb^{3+} and latter sharp peaks belong to intra 4f transitions of Tb^{3+} ion. The lower intensity of latter peaks is because of forbidden nature of f-f transitions. The shielding of 4f electrons by 5s and 5p electrons from surroundings results in the relatively sharper peaks. Co-doping $\text{SbPO}_4:\text{Tb}^{3+}$ (5%) nanoribbons/ nanoparticles with Ce^{3+} results in an additional peak centered around 278 nm with two shoulders. As 4f \rightarrow 5d transition of Tb^{3+} and Ce^{3+} ions have very high value of oscillator strength and assuming comparable transition probabilities for the 4f \rightarrow 5d transition of Tb^{3+} and Ce^{3+} ions, the excitation spectrum has been de-convoluted based on a Gaussian fit. De-convolution of the excitation spectrum revealed

that the broad peak can be resolved into three peaks, with an intense peak centered at 278 nm and two less intense peaks around 300 and 257 nm.

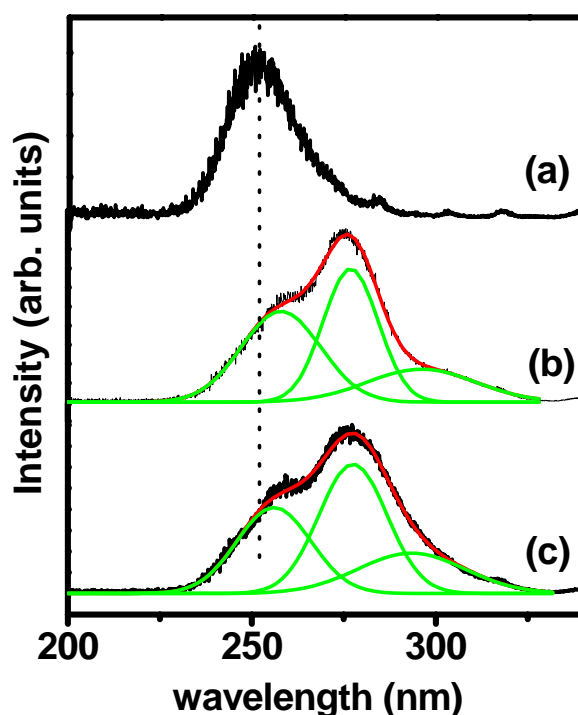


Fig.75. Excitation spectrum corresponding to the $^5D_4 \rightarrow ^7F_5$ transition of Tb^{3+} ions (544 nm) from nanoribbons/ nanoparticles of (a) $SbPO_4:Tb^{3+}(5\%)$, (b) $SbPO_4:Ce^{3+}(2.5\%), Tb^{3+}(5\%)$ and (c) $SbPO_4:Ce^{3+}(2.5\%), Tb^{3+}(5\%)$ dispersed in silica.

Based on the comparison of the spectra shown in Fig.75, it is inferred that the peak around 257 nm is due to the $4f \rightarrow 5d$ transition of Tb^{3+} and the remaining two peaks are due to the $4f \rightarrow 5d$ transition of Ce^{3+} . This is further confirmed from the excitation spectrum of $SbPO_4:Ce^{3+}(5\%)$ which gave an excitation peak centered around 278 nm with an asymmetry around 300 nm (not shown). Slight red shift (~ 7 nm) in the excitation peak maximum of $4f \rightarrow 5d$ transition of Tb^{3+} can be attributed to the changes in the $SbPO_4$ lattice brought about by both Tb^{3+} and Ce^{3+} ions doping. Observation of $4f \rightarrow 5d$ excitation peaks for both Tb^{3+} and Ce^{3+} ions in the excitation spectrum obtained by monitoring Tb^{3+} emission around 544 nm confirms the existence of energy transfer from Ce^{3+} to Tb^{3+} ions in Ce^{3+} co-doped $SbPO_4:Tb^{3+}$ nanoribbons/ nanoparticles. The relative intensity of $4f \rightarrow 5d$ transition of Tb^{3+} to

Ce³⁺ ions is in the ratio of around 40:60 for both SbPO₄:Ce³⁺ (2.5%), Tb³⁺ (5%) nanoribbons/nanoparticles as well as the nanoribbons/nanoparticles dispersed in silica, suggesting that the extent of energy transfer is approximately 60 %. The values are comparable with the energy transfer efficiency estimated from the Ce³⁺ emission in SbPO₄ host using the equation $\eta = 1 - I/I_0$, where I and I₀ are the intensities of Ce³⁺ emission in the presence and absence, respectively of Tb³⁺ ions. The comparable efficiency of energy transfer for the as prepared nanomaterials and nanomaterials incorporated in silica matrix are understandable as the phonon energies are comparable for both SbPO₄ and SiO₂ lattices. Hence, identical extent of quenching is expected for lanthanide ion excited states from these matrices. However, the silica covering on the nanoribbons/nanoparticles have additional advantage of removing the asymmetric environment created at the surface by the stabilising ligands. Energy transfer must also reflect in the Ce³⁺ excited state lifetimes. However, the decay curves obtained corresponding to the excited state of Ce³⁺ were close to the instrument response (less than 1 ns) and hence the values could not be accurately calculated from the decay curves.

It will be interesting to understand the mechanism of the energy transfer between the Ce³⁺ and Tb³⁺ ions. The energy transfer between Ce³⁺ and Tb³⁺ depends on extent of overlap between donor (D) emission peak (Ce³⁺ emission peak in the present case) and acceptor (A) absorption peak (Tb³⁺ excitation peak in the present case) and expressed by the equation 21 [69],

$$P_{DA} = \frac{4\pi}{h} |\langle D, A^* | H_{DA} | D^*, A \rangle|^2 \int g_D(E) \cdot g_A(E) dE \dots \dots \dots (21)$$

where, P_{DA} is the rate of energy transfer from donor to acceptor. The first term in the above expression represents the transition dipole moment between the |D*, A> and |D, A*> states via the interaction Hamiltonian H_{DA}. D* and A* represent the excited state of the donor and acceptor, H_{DA} is the interaction Hamiltonian. The parameters g_D(E) and g_A(E) are normalized population density function representing the optical line shapes of donor and acceptor

respectively. Value of this integral depends on the extent of overlap between the donor emission and acceptor absorption profiles. P_{DA} depends strongly on the critical distance between donors, as well as on their excited state lifetimes. The critical distance is the minimum distance between donor and acceptor above which no energy transfer between them is possible. In the $SbPO_4$ lattice, each SbO_4 polyhedron is separated by PO_4 tetrahedron and the minimum average distance between Sb^{3+} ions is around 5.01\AA [226]. As only 2.5 at % of Ce^{3+} and 5 atom % of Tb^{3+} are randomly distributed at the Sb^{3+} site in the lattice the average distance between Ce^{3+} and Tb^{3+} ions will be significantly higher than 5.01\AA thereby resulting in an increased distance between the donor and acceptor. Hence, the possibility of energy transfer either by the exchange mechanism or by the multi-polar interactions is ruled out. Based on these results, it is inferred that a long-range energy migration from different Ce^{3+} to Tb^{3+} ions is taking place in $SbPO_4:Ce^{3+}, Tb^{3+}$ nanomaterials.

The steady state and time resolved luminescence studies described above establish that covering the nanoribbons/ nanoparticles with silica matrix is very effective in reducing the surface contribution to luminescence from nanomaterials. Further, these studies also confirmed that the energy transfer takes place from Ce^{3+} to Tb^{3+} ions, which are occupying Sb^{3+} site in $SbPO_4$ lattice, a low symmetric environment with a coordination number of four

4.4 Bismuth phosphate nanomaterials: Different forms of $BiPO_4$ nanomaterials were prepared by adding ammonium dihydrogen phosphate solution to ethylene glycol containing bismuth nitrate followed by refluxing at various temperature for two hours.

4.4.1 Effect of reaction temperature on the particle size, shape and crystal structure:

Figure 76 shows the XRD patterns Eu^{3+} doped $BiPO_4$ nanomaterials prepared at different temperatures namely room temperature, 100, 125 and 185°C . For samples prepared at room temperature, XRD pattern is characteristic of hydrated hexagonal form of $BiPO_4$. With increase in the reaction temperature, it slowly converted to anhydrous hexagonal $BiPO_4$ at

100°C. On further increasing the reaction temperature (at 125°C) the hexagonal form gets partially converted to monoclinic phase and at 185°C it transforms completely into monoclinic BiPO₄. The average crystallite sizes are calculated by using Debye-Scherrer formula and are found to be 25, 47 and 51 nm for hydrated hexagonal BiPO₄, hexagonal BiPO₄ and monoclinic BiPO₄, respectively. The increase in crystal size may be explained based on the Ostwald ripening phenomenon where in, with increase temperature, bigger particles starts growing at the expense of smaller particles.

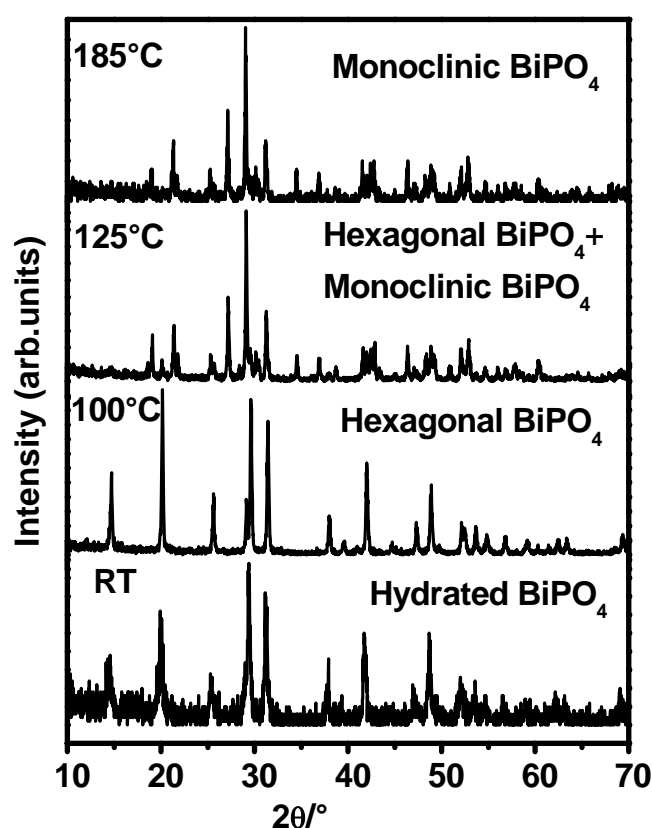


Fig.76. XRD patterns of 2.5 at % Eu³⁺ doped BiPO₄ samples prepared at room temperature, 100, 125 and 185°C.

In order to evaluate the conversion of hydrated hexagonal BiPO₄ to hexagonal and then to monoclinic from combined thermo-gravimetric and differential thermal analysis (TG-DTA) patterns of hydrated BiPO₄ sample were recorded (Fig.77). In TG, the weight losses are obtained mainly in the ranges of 50-180°C and 200-750°C. The former corresponds to the loss of water molecules adsorbed on the surface and the latter to the decomposition of

ethylene glycol moiety (stabilizing ligand). In DTA pattern mainly a sharp exothermic peak centered at 600°C was observed which is attributed to the phase transformation from hexagonal BiPO₄ to monoclinic BiPO₄.

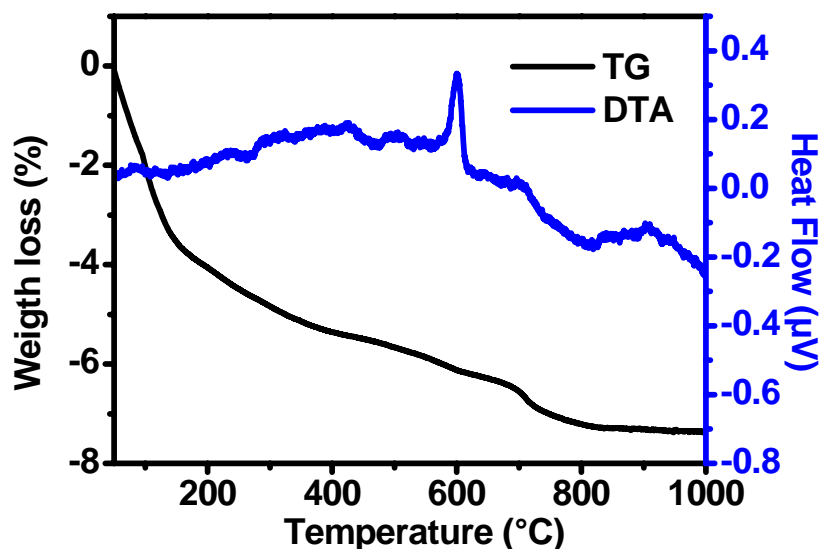


Fig.77. TG-DTA pattern of BiPO₄ sample prepared at room temperature.

In order to understand structural changes occurring during the synthesis of BiPO₄ nanomaterials at different temperature, FT-IR spectra were recorded for these samples (Fig.78). The BiPO₄ nanomaterials prepared at room temperature and 100°C show similar spectra with sharp peaks at 539 and 600 cm⁻¹ together with broad bands centered around 1000 cm⁻¹ and 3500 cm⁻¹ (3500 cm⁻¹ band is not shown). The strong band centered at 1000 cm⁻¹ is due to ν_3 stretching vibration of the PO₄ tetrahedra and the peaks at 600 and 539 cm⁻¹ correspond to $\delta(0-P-O)$ and $\nu_4(PO_4)$, respectively [227]. Samples prepared at 125 and 185°C show similar spectra except splitting of peaks corresponding PO₄ stretching vibrations. The fine structure of the bands corresponding to PO₄ vibrations has been assigned to the reduction of the crystal symmetry from pseudo T_d to C₁. In order to check, whether the variation in reaction temperature and crystalline phase has any effect on the particle size and morphology of BiPO₄, detailed TEM studies were carried out. Figure 79 shows the TEM images of BiPO₄

nanomaterials prepared at different temperatures and their insets show the corresponding SAED patterns.

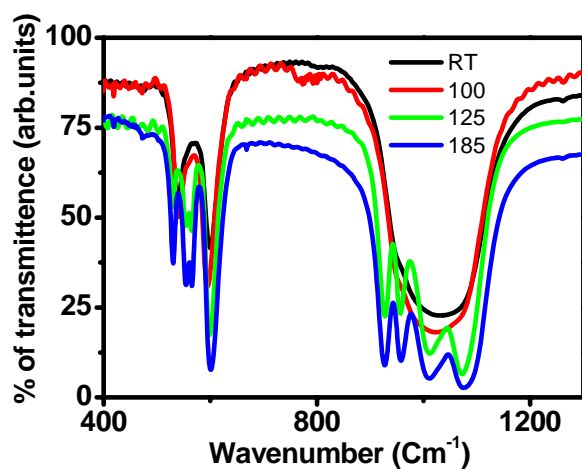


Fig.78. FT-IR spectra of BiPO₄ samples prepared at room temperature, 100, 125 and 185°C

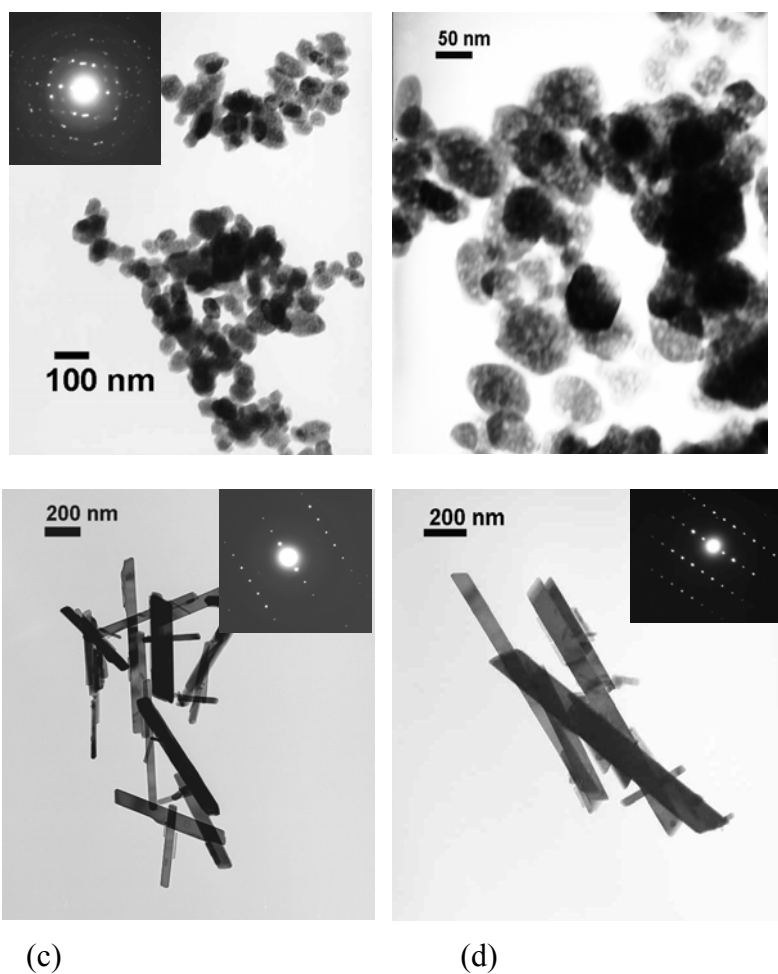


Fig.79. TEM images of BiPO₄ samples prepared at (a) room temperature, (b) 100, (c) 125 and (d) 185°C. Inset shows the SAED patterns of corresponding samples.

Room temperature and 100°C synthesized samples showed particles with size in the range of 50-80 nm and 70-100 nm, respectively. BiPO₄ samples prepared at 125 and 185°C shows rod shaped morphology with lengths in the range ~ 450-750 and 1000-1200 nm with corresponding widths ~ 50-120 and 100-170 nm, respectively. The SAED patterns show that these nanomaterials are single crystalline in nature and their crystallinity increases with increase in the reaction temperature. The possible reason for change in morphology with increase in temperature is the increasing concentration of nuclei and associated anisotropic growth brought about by the reaction temperature.

4.4.2 Effect of particle size and crystal structure on Eu³⁺ emission from BiPO₄:Eu³⁺ nanomaterials:

Figure 80 (a) shows the emission spectra of Eu³⁺ doped hydrated hexagonal BiPO₄, anhydrous hexagonal BiPO₄, and monoclinic BiPO₄ nanomaterials on 270 nm excitation. The intensity of Eu³⁺ luminescence increases with increase in the reaction temperature. It has been attributed to the combined effect of improved crystallinity and removal of water molecules present in the lattice. Water molecules quench the excited state of Eu³⁺, thereby reducing its luminescence intensity. Europium ions in the BiPO₄ lattice show four intense emission peaks at 590, 615, 650 and 700 nm and are due to ⁵D₀ → ⁷F₁, ⁵D₀ → ⁷F₂, ⁵D₀ → ⁷F₃ and ⁵D₀ → ⁷F₄ transitions of Eu³⁺. Improved crystallinity of BiPO₄ samples with increase in temperature of synthesis is also clear from the fine structure of the emission spectrum (Fig 80 (a)), particularly for the 185°C heated samples. The corresponding excitation spectra monitored at 615 nm emission from the samples is shown in Fig.80 (b). It shows broad intense band centered at 270 nm with a shoulder at 255 nm along with many sharp peaks in the wavelength range of 310 - 420 nm. The broad band centered at 270 nm is due to the Eu-O charge transfer process and the shoulder at 255 nm is due to host absorption. Observation of host excitation peak while monitoring Eu³⁺ emission from the sample confirm that the energy transfer takes place from host to Eu³⁺ ions. The sharp peaks in the wavelength

range of 310 – 420 nm are assigned to the f-f transitions of Eu^{3+} ions. It is necessary at this stage to find out whether the Eu^{3+} ions goes to the lattice of BiPO_4 and replaces the Bi^{3+} ions or exist at the interstitial or surface sites of BiPO_4 nanomaterials. Hence BiPO_4 nanomaterials were prepared with different concentrations of La^{3+} ions (Eu^{3+} ions are not used as the unpaired electrons in Eu^{3+} can broaden the solid state NMR spectrum) and characterized by XRD, FT-IR and ^{31}P MAS NMR techniques.

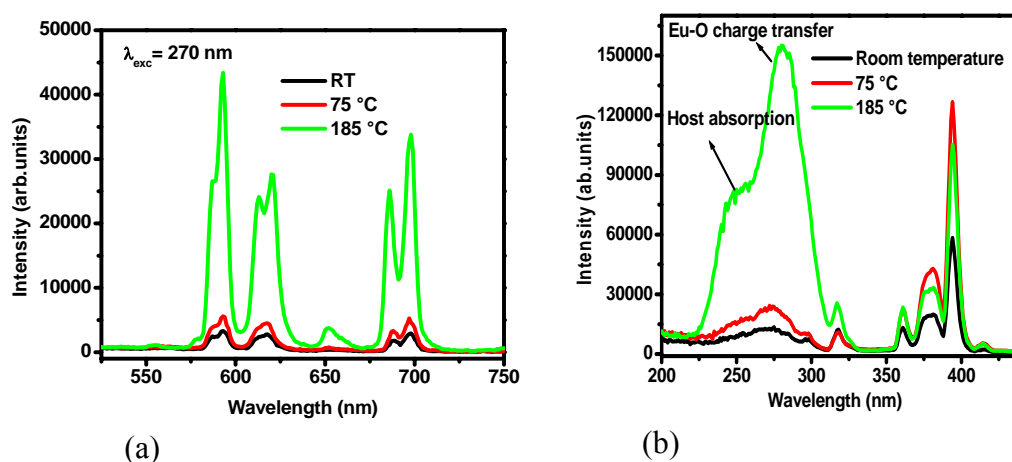


Fig.80 (a) Emission spectra of BiPO_4 samples prepared at room temperature, 75 and 185°C after excitation at 270 nm and (b) corresponding excitation spectra monitored at 615 nm emission.

4.4.3 Solid solution formation between bismuth and lanthanide phosphates: XRD

patterns corresponding to $\text{Bi}_{1-x}\text{La}_x\text{PO}_4$ ($x = 0, 0.3, 0.5, 0.7, 1$) are shown in the Fig.81. All the samples are found to have monoclinic phase. The diffraction peaks have been shifted to lower 2θ values with increasing the lanthanum concentration. This has been attributed to the higher ionic radius of La^{3+} compared to the Bi^{3+} and associated lattice expansion.

Figure 82 (a and b) shows the FT-IR spectra of $\text{Bi}_{1-x}\text{La}_x\text{PO}_4$ ($x = 0, 0.3, 0.5, 0.7, 1$) nanomaterials prepared at 185°C. The peaks present over the region 480-680 cm^{-1} (Fig.82 (a)) are mainly due to the PO_4 bending vibrations whereas absorption in the region 750-1330 cm^{-1} (Fig.82 (b)) is due to PO_4 stretching vibrations. Both the regions show systematic shift towards the higher frequency with increase in the La^{3+} content in the lattice. Bismuth is

heavier metal ion as compared to La^{3+} ion and hence it is expected that as La^{3+} replaces Bi^{3+} in BiPO_4 lattice there can be a blue shift in the peak maximum corresponding to PO_4 vibrations. These results also confirm the solid solution formation between the BiPO_4 and LaPO_4 lattices.

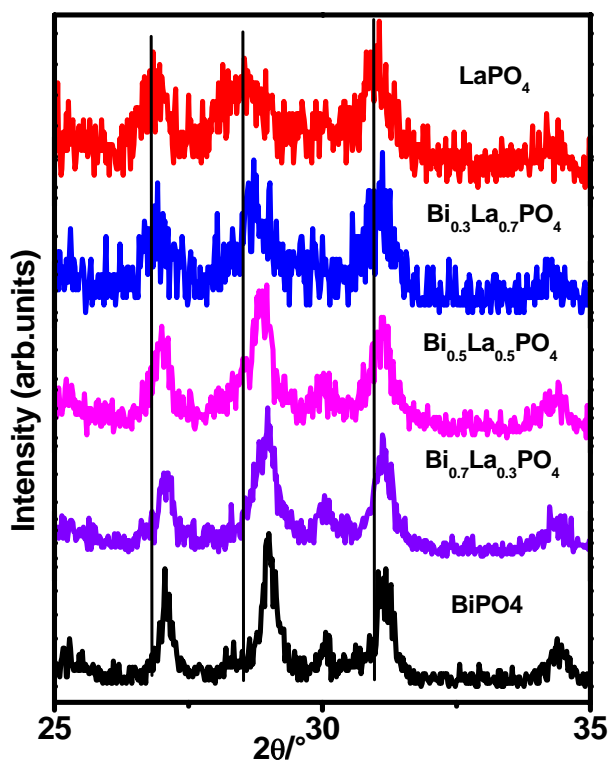


Fig.81. XRD patterns of $\text{Bi}_{1-x}\text{La}_x\text{PO}_4$ ($x = 0, 0.3, 0.5, 0.7, 1$) nanomaterials prepared at 185°C .

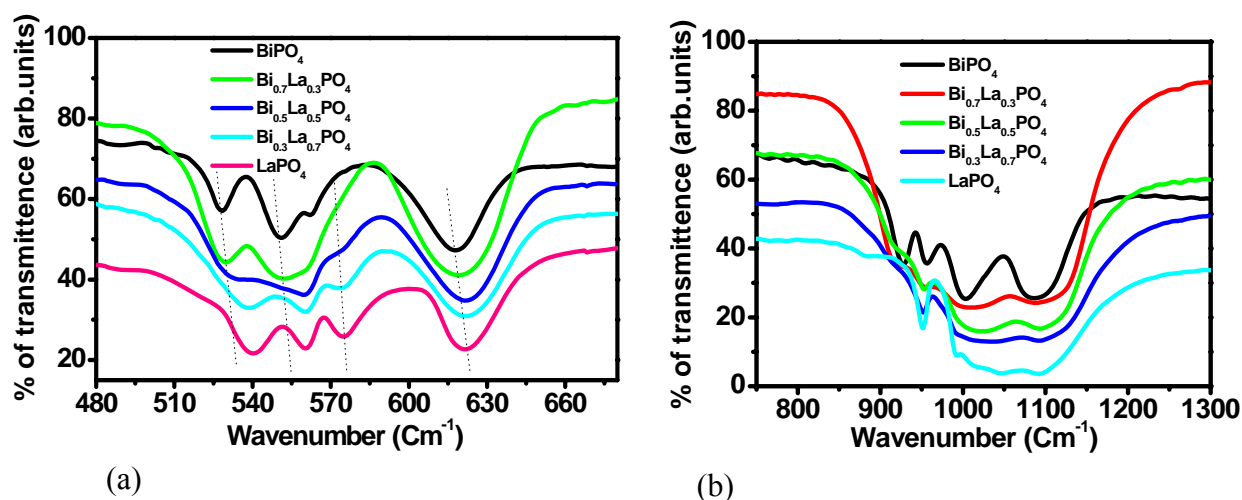


Fig.82. FT-IR patterns of $\text{Bi}_{1-x}\text{La}_x\text{PO}_4$ ($x = 0, 0.3, 0.5, 0.7, 1$) nanomaterials prepared at 185°C showing the regions (a) $480 - 680 \text{ cm}^{-1}$ and (b) $750 - 1300 \text{ cm}^{-1}$.

Figure 83 shows the ^{31}P MAS-NMR spectra of $\text{Bi}_{1-x}\text{La}_x\text{PO}_4$ ($x = 0, 0.3, 0.5, 0.7, 1$) nanomaterials prepared at 185°C . With increase in La^{3+} content in BiPO_4 , there is a significant change in the line shape is observed. The line width of the peak increases significantly and peak maxima shift towards higher chemical shift (δ) values with increase in La^{3+} content in the lattice. This can be understood by considering the difference in the charge to radius ratio (2.46 and 2.56 for La^{3+} and Bi^{3+} , respectively) between Bi^{3+} and La^{3+} ions. The lower charge to radius ratio of La^{3+} compared to Bi^{3+} leads to shifting of peak maxima towards higher δ values when Bi^{3+} is replaced by La^{3+} in BiPO_4 lattice. The sharpening of the peaks with increase in the La^{3+} concentration can be explained based on the environment around 'P' in the solid solution. It is known that Bi^{3+} is heavier ion compared to La^{3+} and when heavier ions surround the probe nucleus (^{31}P), anisotropy in chemical environment around 'P' will be higher as compared to the situation in which 'P' is surrounded by lighter ions. Higher the anisotropy in chemical environment, greater will be the line width of the NMR absorption peak. These results further substantiate the solid solution formation between BiPO_4 and LaPO_4 .

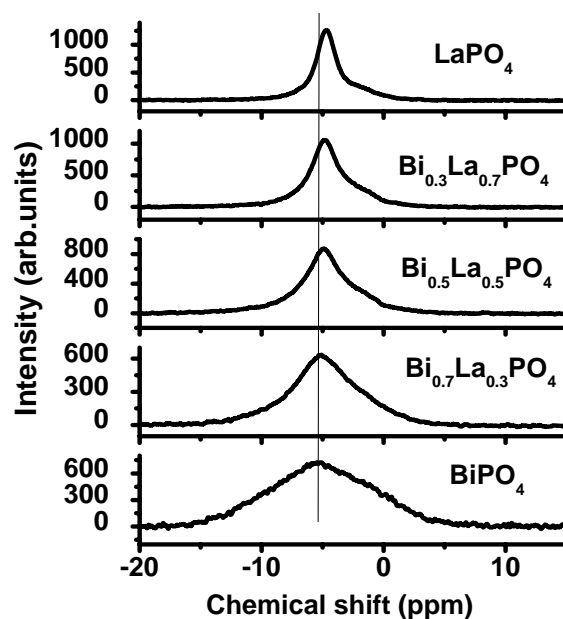


Fig.83. ^{31}P MAS-NMR patterns of $\text{Bi}_{1-x}\text{La}_x\text{PO}_4$ ($x = 0, 0.3, 0.5, 0.7, 1$) nanomaterials prepared at 185°C .

Similar studies were also carried out for other lanthanide ions like Tb^{3+} and the results are discussed below. Tb^{3+} is chosen in the present study for doping because unlike $BiPO_4$ and $LaPO_4$ which have got monoclinic structure, $TbPO_4$ exists in the tetragonal form. Hence solid solution formation between $BiPO_4$ and $TbPO_4$ will be quite interesting both with respect to fundamental aspect as well as with respect to light emitting applications. Figure 84 shows the XRD patterns of $BiPO_4$ nanomaterials containing different amounts of Tb^{3+} . With increase in Tb^{3+} to Bi^{3+} ratio, the peaks maxima are shifted to higher 2θ values. This is explained based on the lattice contraction brought about by the replacement of the larger ionic radius Bi^{3+} (1.11 Å) with the smaller ionic radius Tb^{3+} (1.04 Å) ions. In pure $TbPO_4$ case, it is an entirely different crystalline phase with tetragonal structure (Fig.84). Hence, based on XRD, FT-IR and ^{31}P MAS NMR studies of $BiPO_4:Ln^{3+}$ nanomaterials, it is confirmed that extensive solid solution formation occurs with $BiPO_4$ and $LnPO_4$. In the following section, luminescence properties of Ln^{3+} doped $BiPO_4$ nanorods are discussed.

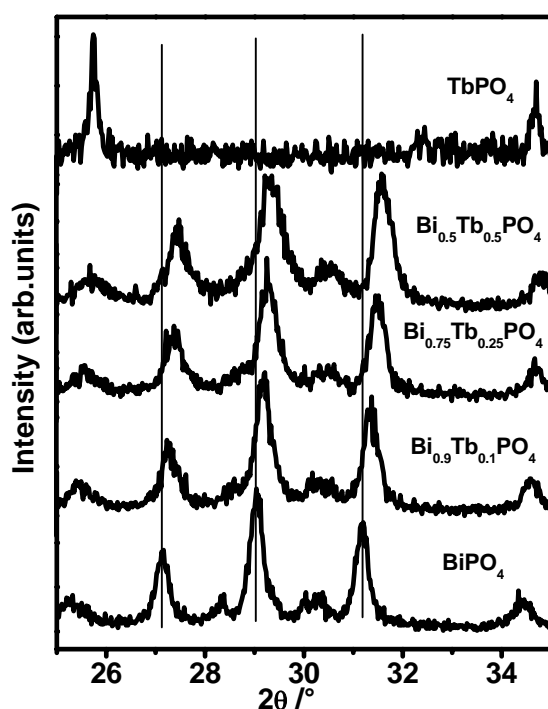


Fig.84. XRD patterns of $Bi_{1-x}Tb_xPO_4$ ($x = 0, 0.1, 0.25, 0.5, 1$) nanomaterials prepared at $185^\circ C$

4.4.4 Luminescence studies on Eu^{3+} doped BiPO_4 nanomaterials: Figure 85 (a) shows the emission spectra of 1, 2, 2.5 and 5 atom% Eu doped BiPO_4 nanorods excited at 275 nm. Strong orange and red emission is observed from the sample. The 590, 612, 650 and 700 nm peaks are due to $^5\text{D}_0 \rightarrow ^7\text{F}_1$, $^5\text{D}_0 \rightarrow ^7\text{F}_2$, $^5\text{D}_0 \rightarrow ^7\text{F}_3$ and $^5\text{D}_0 \rightarrow ^7\text{F}_4$ transitions of Eu^{3+} , respectively. The fine structure observed in the emission peaks shows the crystalline nature of host lattice. As the concentration of Eu^{3+} increases, the emission intensity initially increases up to 2.5 atom % and then decreases. Initially with increase in doping concentration, the number of luminescent centers increases and as a result, emission intensity increases. However, above certain doping concentration there is non-radiative decay due to energy transfer (migration) among different Eu^{3+} ions until it reaches a quenching centre. As a result, emission intensity decreases. These results are further supported by the decay curve corresponding to the $^5\text{D}_0$ level of Eu^{3+} in these samples.

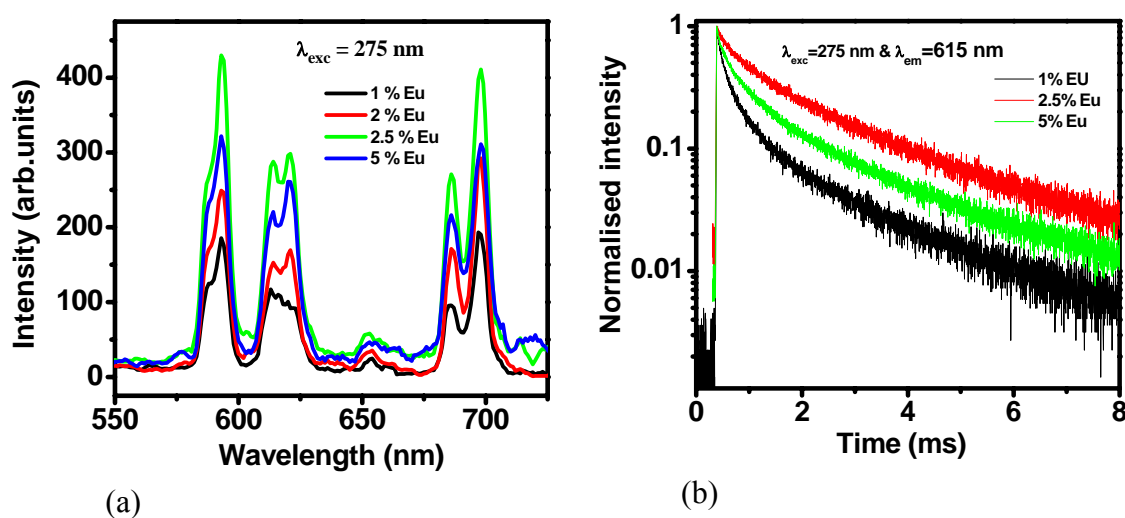


Fig.85. (a) Emission spectra obtained after excitation at 275 nm, (b) decay curves corresponding to $^5\text{D}_0$ level of Eu^{3+} from $\text{BiPO}_4:\text{Eu}^{3+}$ nanomaterials containing different amounts of Eu^{3+} .

The decay curves corresponding to $^5\text{D}_0$ level of Eu^{3+} from these samples are shown in Fig.85 (b) and their corresponding lifetime values are given in Table 9. All these curves are bi-exponential in nature and based on the explanation given in the previous chapters, the

faster decay component is assigned to the surface Eu^{3+} ions and slower component to Eu^{3+} ions present in the bulk of the nanomaterials. Values of ${}^5\text{D}_0$ lifetimes increase with increase in Eu^{3+} concentration up to 2.5 atom% and above this concentration the lifetime values started decreasing (Table 9 and Fig.85 (b)). Thus, the lifetime values support the inferences drawn from emission spectra.

Table 9. Lifetime values corresponding to ${}^5\text{D}_0$ level of Eu^{3+} in BiPO_4 nanorods doped with different amounts of Eu^{3+} ions.

% of Eu^{3+}	${}^5\text{D}_0$ lifetime values of Eu^{3+}	
	τ_1 (ms)	τ_2 (ms)
1 atom %	0.18 (35 %)	1.63 (65 %)
2.5 atom %	0.31 (13%)	2.0 (87%)
5 atom %	0.34 (30 %)	1.72 (70%)

4.4.5 Luminescence studies on Tb^{3+} doped BiPO_4 nanorods: Figure 86 (a) shows the emission spectra of 1, 2.5, and 5 atom% Tb^{3+} doped BiPO_4 nanorods. Emission peaks centered at ~ 487 , 543, 585 and 621 nm correspond to transitions from ${}^5\text{D}_4$ level to ${}^7\text{F}_6$, ${}^7\text{F}_5$, ${}^7\text{F}_4$ and ${}^7\text{F}_3$ levels respectively of Tb^{3+} ions present in the BiPO_4 lattice.

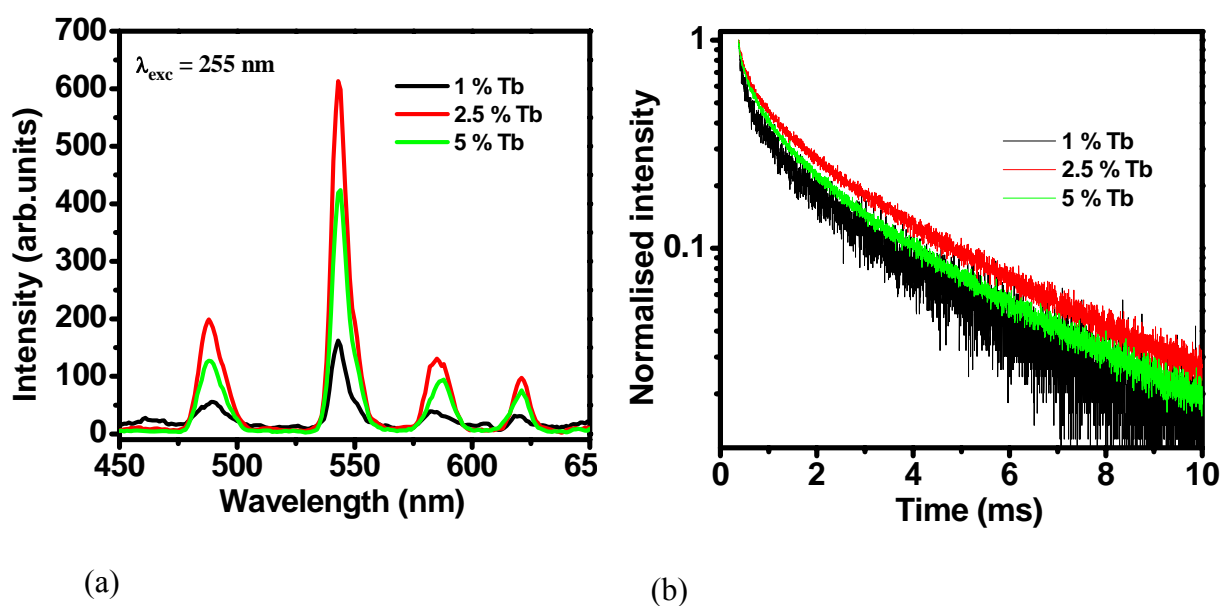


Fig.86. (a) Emission spectra obtained after excitation at 255 nm, (b) decay curves corresponding to ${}^5\text{D}_4$ level of Tb^{3+} ion from BiPO_4 : Tb^{3+} nanorods prepared at 185°C .

With increasing Tb^{3+} ion concentration up to 2.5 atom%, the green emission (peak at 545 nm) intensity increases and above that concentration it started decreasing. The decrease in emission intensity beyond 2.5 at % is attributed to concentration quenching. Fig.86 (b) shows the decay curves corresponding to 5D_4 level of Tb^{3+} from $BiPO_4:Tb^{3+}$ nanorods. All the samples showed bi-exponential decay and the lifetime values are given in the Table 10. Optimum lifetime values are obtained for 2.5 at % Tb^{3+} doped $BiPO_4$ nanorods.

Table 10. Lifetime values of 5D_4 level of Tb^{3+} from $BiPO_4$ nanorods doped with different amounts of Tb^{3+} ion.

% of Tb^{3+}	5D_4 lifetime values of Tb^{3+}	
	τ_1 (ms)	τ_2 (ms)
1 atom %	0.24 (13 %)	2.23 (87 %)
2.5 atom %	0.32 (11%)	2.62 (89%)
5 atom %	0.36 (15 %)	2.44 (85%)

4.4.6 Energy transfer from Tb^{3+} to Eu^{3+} ions in Tb^{3+} co-doped $BiPO_4:Eu^{3+}$ nanorods:

Figure 87 (a) shows the emission spectra of $BiPO_4:Eu^{3+}$ (5 at %) and 5 at % Tb^{3+} co-doped $BiPO_4:Eu^{3+}$ (5 at %) nanorods obtained after excitation at 255 nm. It is observed that Tb^{3+} emission intensity decreases after co-doping with Eu^{3+} . This indicates that energy transfer takes place from Tb^{3+} to Eu^{3+} ions in the co-doped samples. Fig.87 (b) shows the excitation spectra corresponding to Eu^{3+} emission from both Eu^{3+} single doped and Tb^{3+} co-doped $BiPO_4:Eu^{3+}$ nanorods. Excitation spectrum corresponding to Eu^{3+} emission from co-doped sample showed peaks characteristic of both Eu-O charge transfer and 4f-5d transitions of Tb^{3+} . Unlike this the excitation spectrum corresponding to Tb^{3+} emission at 545 nm from the sample showed only 4f-5d transition of Tb^{3+} . These results confirm that energy transfer takes place from Tb^{3+} to Eu^{3+} . This is also understandable by considering the energy values corresponding to 4f-5d transition of Tb^{3+} and Eu-O charge transfer transition of Eu^{3+} . Figure 87 (c) shows the decay curve corresponding to 5D_4 level of Tb^{3+} in the presence and absence of Eu^{3+} ion. It is observed that lifetime of Tb^{3+} ions decreases after doping with Eu^{3+} ions. On

the other hand the Eu^{3+} lifetime has been found to increase after co-doping with Tb^{3+} ions. The lifetime values are given in the Table 11. The increase in lifetime corresponding to $^5\text{D}_0$ level of Eu^{3+} and decrease in lifetime corresponding to $^5\text{D}_4$ level of Tb^{3+} in co-doped samples compared to singly doped samples further confirms the energy transfer from Tb^{3+} ions to Eu^{3+} ions.

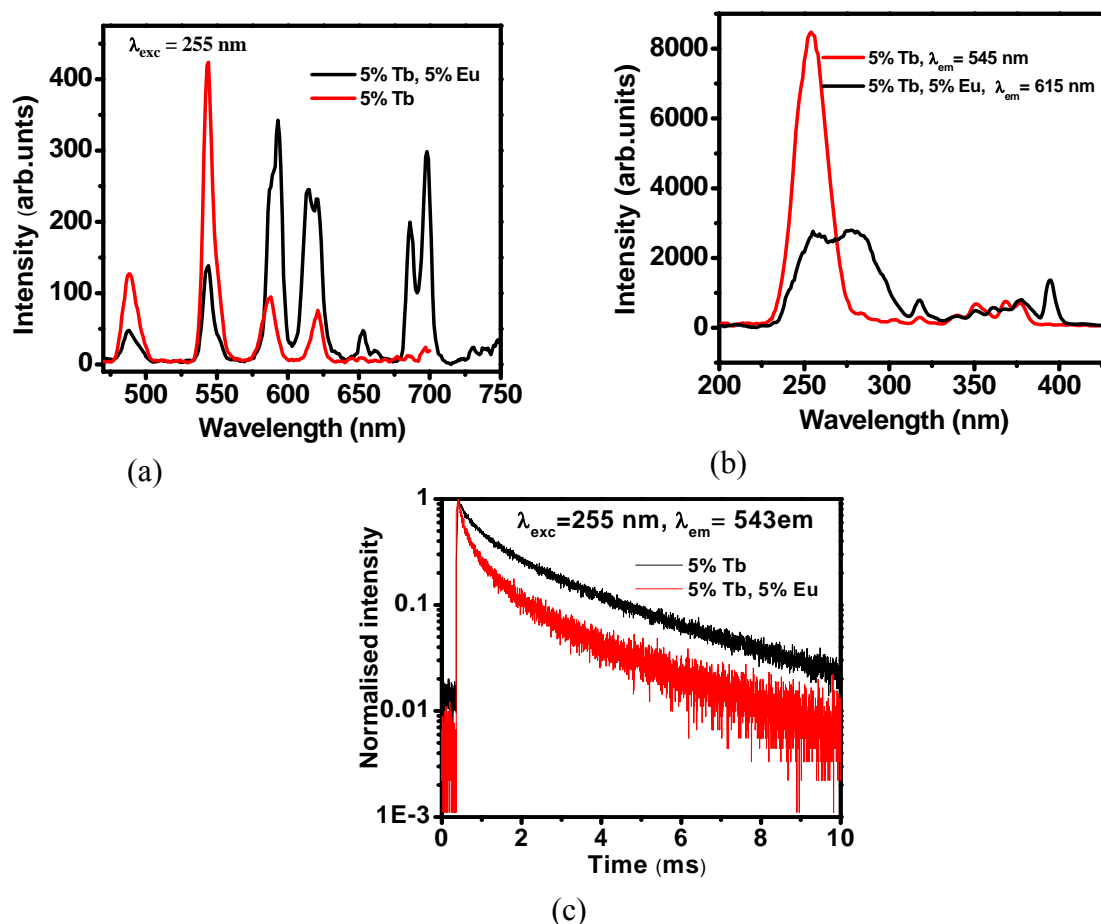


Fig.87. (a) Emission spectra from $\text{BiPO}_4:\text{Tb}^{3+}$ (5 at%) and $\text{BiPO}_4:\text{Eu}^{3+}$ (5 at%), Tb^{3+} (5 at%) nanomaterials after excitation at 255 nm. The corresponding excitation spectrum is shown in Fig.87 (b). Decay curve corresponding to $^5\text{D}_4$ level of Tb^{3+} from these samples are shown in Fig 87 (c).

Table 11. Lifetime values of excited states of Tb^{3+} and Eu^{3+} ions in BiPO_4 nanorods.

sample	Lifetime of	τ_1 (ms)	τ_2 (ms)
$\text{BiPO}_4:5\% \text{Eu}^{3+}$	$^5\text{D}_0$ level of Eu^{3+}	0.34 (30 %)	1.72 (70 %)
$\text{BiPO}_4:5\% \text{Tb}^{3+}$	$^5\text{D}_4$ level of Tb^{3+}	0.36 (15 %)	2.44 (85 %)
$\text{BiPO}_4:5\% \text{Eu}^{3+}, 5\% \text{Tb}^{3+}$	$^5\text{D}_4$ level of Tb^{3+}	0.19 (27%)	1.77 (73%)
	$^5\text{D}_0$ level of Eu^{3+}	0.66 (14 %)	2.8 (86%)

4.4.7 Luminescence studies on Dy³⁺ doped BiPO₄ nanorods: Figure 88 (a) shows the emission spectrum from BiPO₄ nanorods doped with 2.5 at % of Dy³⁺ obtained after excitation at 350 nm. It consists of two peaks at 478, 573 nm corresponding to ⁴F_{9/2}→⁶H_{15/2} and ⁴F_{9/2}→⁶H_{13/2} transitions, respectively of Dy³⁺ ion in BiPO₄ nanorods. The corresponding excitation spectra monitored at 573 nm emission is shown in Fig.88 (b). It consists of a broad band centered at 255 nm along with sharp transitions above 300 nm. The broad band at 255 nm is due to host absorption. Observation of host absorption peak while monitoring Dy³⁺ emission confirms the energy transfer from host to Dy³⁺ ions. The less intense sharp peaks in the excitation spectrum are arising due to f-f transitions of Dy³⁺ ion present in the lattice. The decay curve corresponding to ⁴F_{9/2} level of Dy³⁺ ion is shown in Fig.88 (c). It is a bi-exponential in nature with lifetime component 22 μs (15%) and 793 μs (85%).

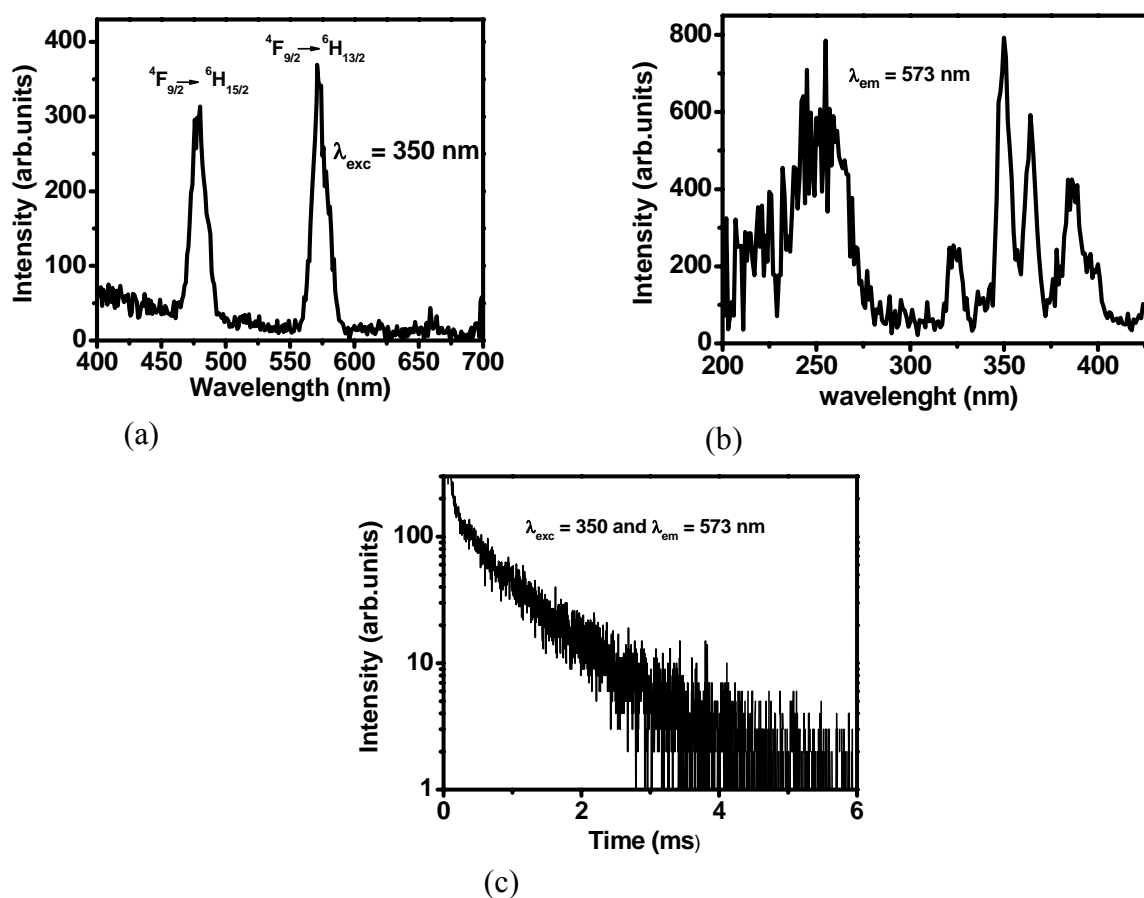


Fig.88 (a) Emission spectrum obtained after excitation at 350 nm (b) excitation spectra monitored at 573 nm emission and (c) decay curve corresponding to ⁴F_{9/2} level of Dy³⁺ ion in BiPO₄:Dy³⁺ nanorods.

4.4.8 Luminescence studies on Sm³⁺ doped BiPO₄ nanorods: Figure 89 (a) shows the emission spectrum of Sm³⁺ ions doped in BiPO₄ nanorods obtained after excitation at 402 nm. The spectrum consist of four peaks at 560, 597, 645 and 706 nm corresponding to ⁴G_{5/2} → ⁶H_{5/2}, ⁴G_{5/2} → ⁶H_{7/2}, ⁴G_{5/2} → ⁶H_{9/2} and ⁴G_{5/2} → ⁶H_{11/2} transitions, respectively of Sm³⁺ ion present in the BiPO₄ lattice.

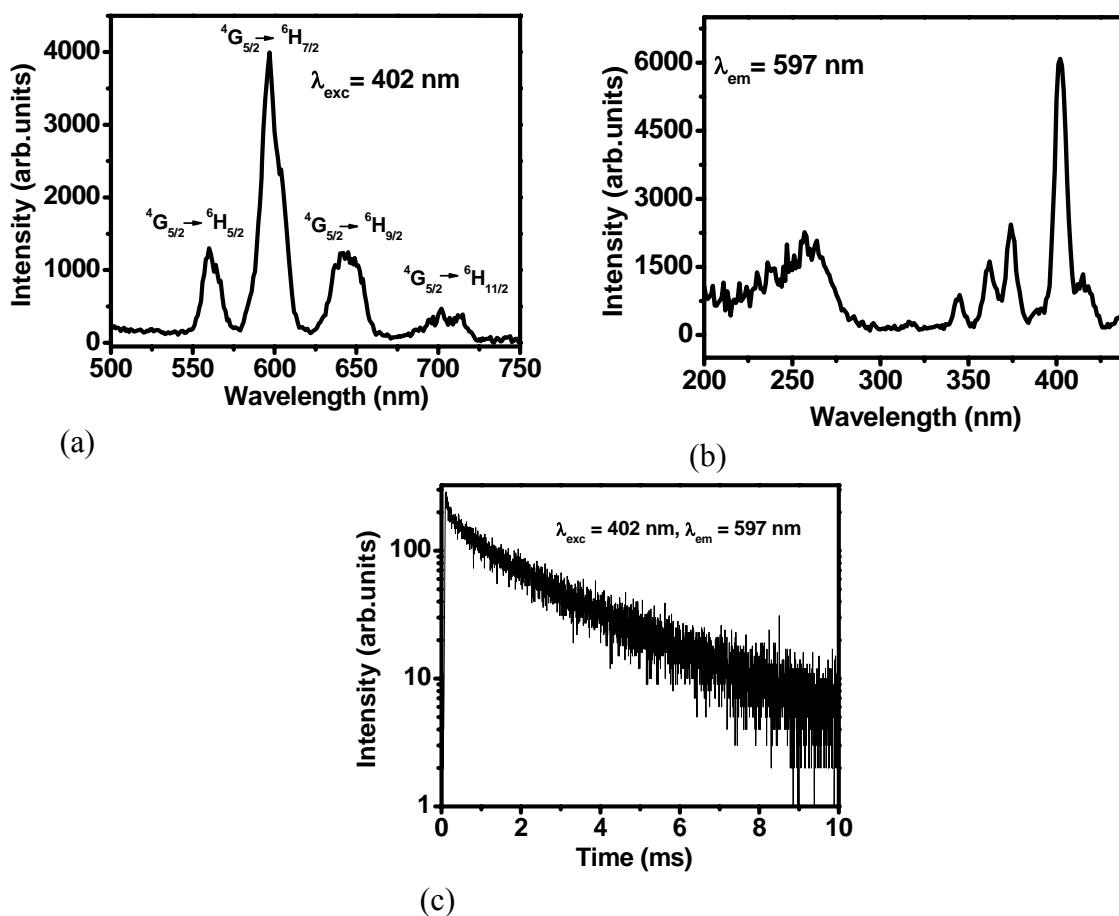


Fig.89. (a) Emission spectrum obtained after 402 nm excitation, (b) excitation spectra monitored at 597 nm emission and (c) decay curve corresponds to ⁴G_{5/2} level of Sm³⁺ in BiPO₄:Sm³⁺ nanorods.

The corresponding excitation spectrum monitored at 597 nm is shown in Fig.89 (b). The spectrum is similar to that of BiPO₄:Dy³⁺ samples and consists of broad band centered at 255 nm along with sharp peaks above 320 nm. As explained in the case of BiPO₄:Dy³⁺ samples, the broad band is arising due to energy transfer from host to Sm³⁺ ion and the sharp peaks

corresponds to f-f transition of Sm^{3+} ion. The decay curve corresponding to ${}^4\text{G}_{5/2}$ level of Sm^{3+} has been shown in Fig.89 (c). Bi-exponential nature of the decay curve has been attributed to Sm^{3+} ions present on the surface and in bulk of the nanorods.

CHAPTER 5: Zinc gallate (ZnGa_2O_4)

5.1. Introduction: Zinc gallate (ZnGa_2O_4) belongs to the class of inorganic compounds having spinel structure. It crystallises in cubic structure with a space group of $\text{Fd}\bar{3}\text{m}$ [247]. ZnGa_2O_4 is an insulator with a band gap of 4.4 eV and has potential applications as materials for low voltage field emission displays (FEDs), electro-luminescent devices (ELDs) and vacuum fluorescent displays (VFDs) [247-254]. ZnGa_2O_4 exhibits higher chemical stability under high electric field and strong electron bombardment when compared with conventional sulfide based phosphors [251, 254]. Blue emission has been observed from ZnGa_2O_4 and is due to a transition via a self-activation centre under UV or low voltage electron excitations [255]. The intensity and wavelength maximum corresponding to blue emission vary with the nature of dopants. For example detailed studies are available regarding the luminescent properties of ZnGa_2O_4 when partially substituted with metal ions like Cd^{2+} (for Zn^{2+}) and In^{3+} (for Ga^{3+}) [256-258]. If nanoparticles of such luminescent materials are prepared with sufficient dispersability in organic solvents, then polymer based luminescent materials can be made out of them. Polymer based materials can be converted into devices by using cheap fabrication techniques. Primary requirement for incorporating nanoparticles in polymer matrix is to make them highly dispersible in organic solvents by stabilizing the nanoparticles with bulky organic ligands. However, such ligand-stabilised nanoparticles can be obtained only when the synthesis temperature is less than 250°C , so that as to prevent decomposition coordinated ligand. Hirano, et al. prepared ZnGa_2O_4 nanoparticles at a relatively low temperature of 90°C from aqueous solution of ZnSO_4 and $\text{Ga}_2(\text{SO}_4)_3$ by using precipitating agents like urea, aqueous ammonia and hexamethyl tetramine [248]. However, in this method ligand stabilization is difficult, as H_2O being a solvent with low viscosity and poor coordinating characteristics does not prevent aggregation of the nanoparticles. Many methods are reported for the synthesis of ZnGa_2O_4 nanomaterials in the form of nanowires, helical

structures and thin films [259-264]. In this study ZnGa_2O_4 nanoparticles with different sizes with tuneable photoluminescent properties were prepared at 120°C by co-precipitation method. Ions like In^{3+} , Eu^{3+} , Tb^{3+} and Ce^{3+} could also be doped in ZnGa_2O_4 nanoparticles with a view to prepare nanomaterials with multicolour emission characteristics. Some of these nanoparticles are also incorporated in polymers like polymethyl methacrylate (PMMA) matrix by in situ polymerization reaction and their luminescence characteristics have been investigated.

5.2. Effect of ethylene glycol (EG) - H_2O solvent ratio on particle size and photoluminescence of ZnGa_2O_4 nanoparticles: Viscosity of the solvent is known to play an important role in the nucleation and growth of nanoparticles. In order to check whether this is applicable for the synthesis of ZnGa_2O_4 nanoparticles, experiments were carried out by changing the viscosity of solvent by varying the relative concentration of ethylene glycol (EG) and H_2O in the reaction medium and the corresponding XRD patterns are shown in Fig.90.

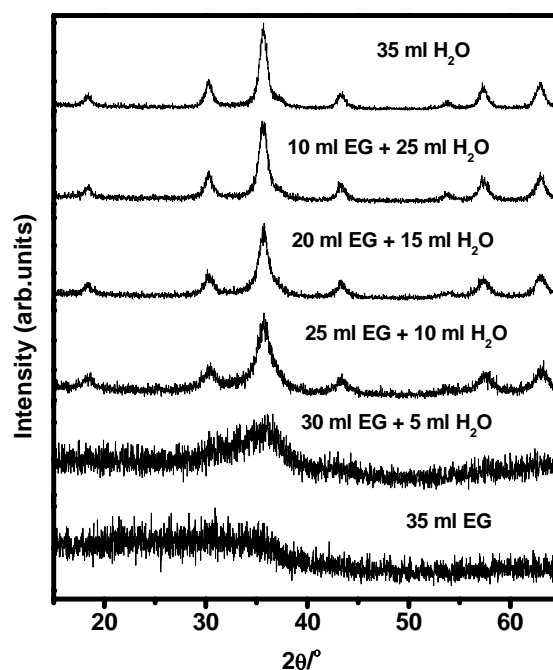


Fig.90. XRD patterns of ZnGa_2O_4 nanoparticles prepared in solvents containing different values of EG- H_2O ratios

In pure EG an amorphous product is formed. As volume of H₂O increases in the reaction medium, the crystallinity of nanoparticles also increasing as can be seen from the line width of the diffraction peaks. In pure H₂O, average crystal size is found to be the highest. Average crystallite size of ZnGa₂O₄ nanoparticles obtained with different EG-water solvent ratio is given in Table 12. The increase in particle size with increase in water to solvent ratio can be explained based on two aspects. The first one is as that with increase in water content urea hydrolysis becomes more effective and the second one is that the viscosity decreases with increase in water content facilitating diffusion of monomer towards the growth site.

Table 12: Calculated average crystallite size of ZnGa₂O₄ nanoparticles as a function of EG-H₂O ratio.

No. of moles of Zn ²⁺ (mmol)	No. of moles of Ga ³⁺ (mmol)	Vol. of H ₂ O (ml)	Vol. of EG (ml)	Crystallite size (nm)
1.43	2.86	35	0	10
1.43	2.86	25	10	8
1.43	2.86	15	20	7
1.43	2.86	10	25	5
1.43	2.86	5	30	1
1.43	2.86	0	35	-

To confirm the nature of product obtained while EG only was used as the solvent, FT-IR studies were carried out on the sample and the pattern is compared with that of samples prepared with EG-water mixture and are shown in Fig.91. Nanoparticles prepared in pure water shows two bands at 450 and 600 cm⁻¹ and are attributed to Ga-O and Zn-O stretching vibrations, respectively of ZnGa₂O₄ [265]. The samples prepared in 25 ml EG and 10 ml water displayed these bands but appeared at a slightly higher frequency. Further, two other bands at 850 and 1050 cm⁻¹ also appeared (Fig.91). The 1050 cm⁻¹ peak is assigned to the C-H bending of EG molecules present on the surface of nanoparticles. The bands at 450 and 600 cm⁻¹ shifted to higher frequency and have become broader with increase in the EG to water ratio in the solvent. This is attributed to the reduction of particle size with increase in

the EG to water ratio. For samples prepared in pure EG, FT-IR spectra is similar to that of samples prepared in solvents containing both EG and water. Hence, it is confirmed that the product formed when EG alone is used as the solvent is also ZnGa_2O_4 . Poor crystallinity can be due to the very small particle size of ZnGa_2O_4 when EG alone is used as solvent. Further, the relative intensity of band corresponding to C-H vibration increases with increase in the EG volume in the solvent. It indicates that the nanoparticles are stabilized effectively by EG molecules. The increase in line width and blue shift of the peaks can be explained as follows. With decrease in particle size, number of atoms on the surface (which are having unsaturated coordination) increases and this leads to distortion in the lattice of ZnGa_2O_4 nanoparticles. Further, small particles of ZnGa_2O_4 in general must have higher electronic/vibrational energy levels compared to bulk ZnGa_2O_4 . These two effects lead to broadening of the IR absorption peak and shifting of its maximum to higher frequency values.

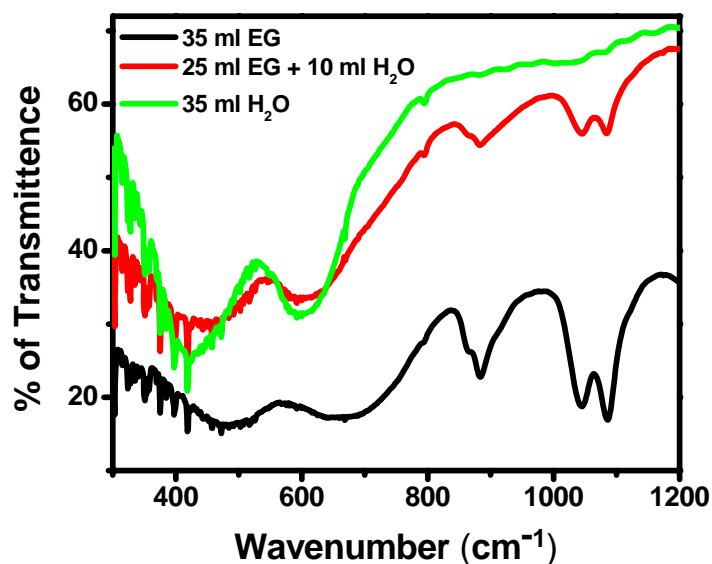


Fig.91. FTIR spectra of ZnGa_2O_4 nanoparticles prepared in solvents containing different amounts of EG and water.

Photoluminescence spectra of all these samples obtained after excitation in the range of 250-300 nm are shown in Fig.92 (a) and the corresponding excitation spectra are shown in Fig.92 (b). The emission maximum is found to vary from 385 to 455 nm with increase in the

water content in the reaction medium. Similar red shift is also observed in the excitation spectrum with increase in water content.

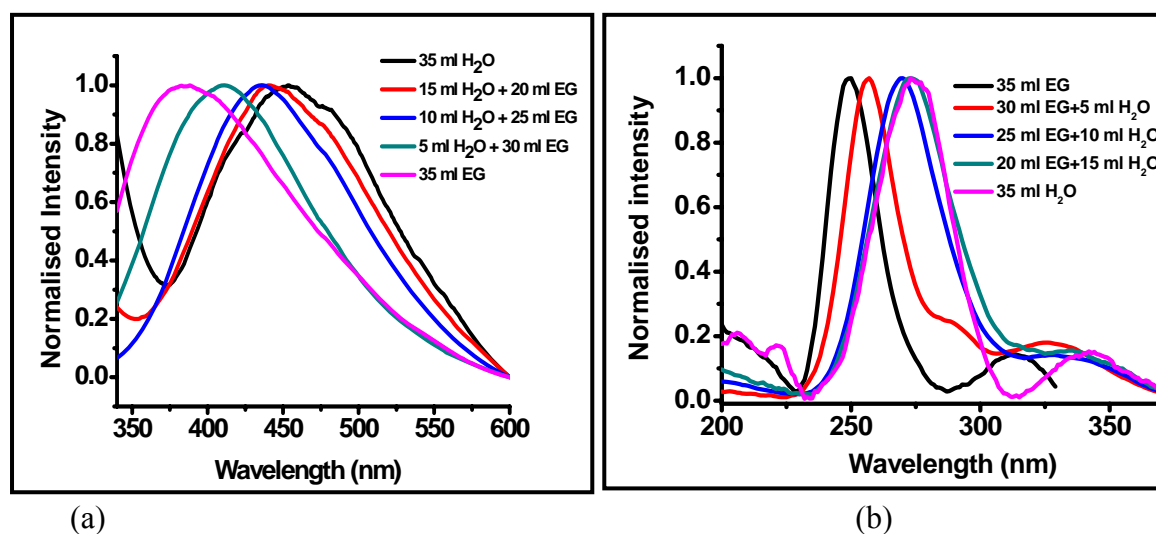


Fig.92.(a) Emission spectra of ZnGa₂O₄ nanoparticle prepared in solvents containing different ratios of EG and H₂O. Corresponding excitation spectra are shown in Fig.92 (b)

Based on the previous studies, emission in the region of 385 to 455 nm has been attributed to the de-excitation of energy levels characteristic of GaO₆ motif present in the ZnGa₂O₄ lattice [255]. The peak observed over the region of 250-290 nm in the excitation spectrum has been attributed to the excitation of electrons from valence band to the conduction band of ZnGa₂O₄ lattice. As particle size decreases, energy values corresponding to GaO₆ units also increases and this will lead to shifting of emission maxima towards lower wavelength values. The same trend has also been observed in the excitation spectra, i.e., excitation maxima shifted from 250 to 275 nm with increase in particle size (Fig.92 (b)). The excitation spectra also show a weak band which shifts from 310 to 345 nm with increase in the particle size. This peak has been attributed to the localised levels corresponding to GaO₆ units in the band gap of ZnGa₂O₄ lattice. Excitation of ZnGa₂O₄ around 260 nm leads to creation of charge carriers namely electrons in conduction band and holes in valance band. The electron gets de-excited and reaches the localised levels created by the GaO₆ structural

units. Radiative recombination of this trapped electron with hole in valance band leads to emission in the region 385 to 455 nm as schematically shown in Fig.93.

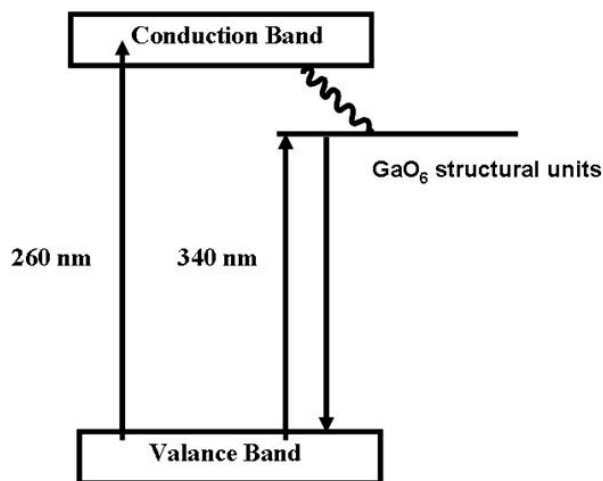


Fig.93. Schematic representation of possible energy transitions in ZnGa_2O_4 nanoparticles.

5.3. Effect of precursor concentration on particle size: ZnGa_2O_4 nanoparticles were prepared in 25 ml EG and 10 ml water with different concentrations of reactants namely gallium chloride and zinc acetate and XRD patterns of the resulting compounds are shown in Fig.94. For samples prepared with 0.14 mmol of gallium, XRD patterns revealed the formation of an amorphous product. This is probably due to very small size of the nanoparticles of ZnGa_2O_4 (as confirmed by FT-IR studies previously described). As the precursor concentration increases, particle size increases up to certain concentration, i.e., 1.44 mmol of gallium and above that its starts decreasing and finally again giving rise to an amorphous product at 22.96 mmol of gallium. The calculated crystal sizes are given in the Table 13 as a function of the gallium concentration. This observed variation can be explained based on nucleation and growth processes involved for the formation of ZnGa_2O_4 particles. At lower Ga^{3+} concentration, both nucleation and growth are slower because ions are far away and attaining the super-saturation condition is difficult. As a result, the particle sizes are smaller. With increase in gallium concentration, growth becomes faster as compared to

nucleation, thereby leading to increase in the particle size. After certain concentration, due to super-saturation, nucleation is expected to be much faster than the growth and as a result particle size starts decreasing with increase in Ga^{3+} concentration.

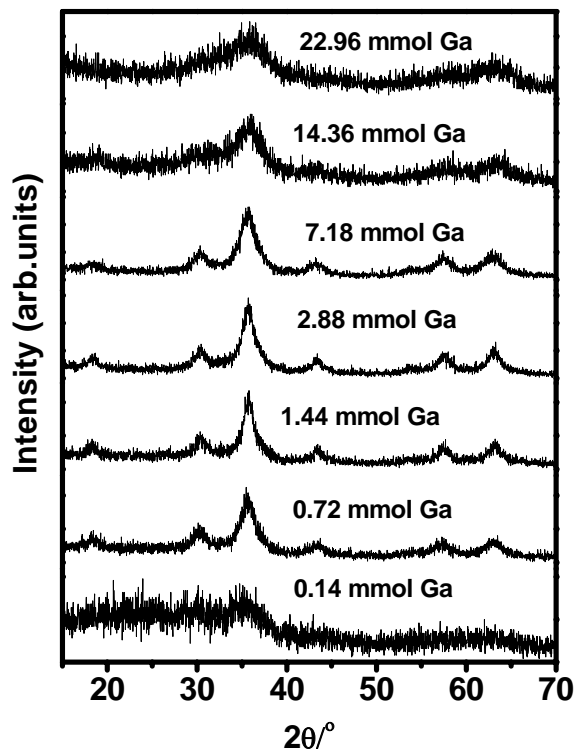


Fig.94. XRD patterns of ZnGa_2O_4 nanoparticles prepared with different concentration of Ga^{3+} ions.

Table 13: Calculated crystallite size of ZnGa_2O_4 nanoparticles as a function of increasing the reactants concentration.

No. of moles of Zn^{2+} (mmol)	No. of moles of Ga^{3+} (mmol)	Vol. of H_2O (ml)	Vol. of EG (ml)	Crystallite size (nm)
0.07	0.14	10	25	-
0.36	0.72	10	25	4
0.72	1.44	10	25	5
1.44	2.88	10	25	4
3.59	7.18	10	25	3
7.18	14.36	10	25	2
11.48	22.96	10	25	-

In order to check the phase formed at high concentration of reactants, FT-IR spectra were recorded and representative spectra were shown in the Fig.95. It has been observed that all

the compounds shows similar characteristics, except the broadening and shifting of the band position corresponding to Ga-O vibrations to higher wave numbers with increase in precursor concentration. Again based on the same logic mentioned in the previous section, this has been attributed to the reduction in the particle size with increasing the concentration of the reactants

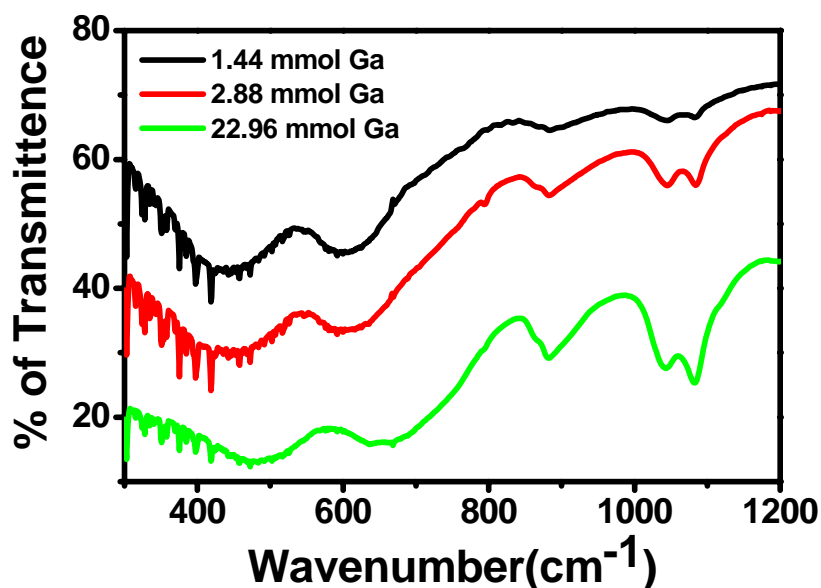


Fig.95. FT-IR spectra of ZnGa₂O₄ nanoparticles prepared with different amounts of starting material.

In order to check the morphology of these nanoparticles, TEM measurements for representative samples have been carried out and the images are shown in Fig.96. TEM measurements (Fig.96 (a)) revealed that samples prepared with 1.44 mmol Ga and 0.72 mmol Zn consist of particles with diameter around 4-6 nm. The distance between the lattice fringes from HRTEM image (Fig.96 (b)) has been measured and found to be matching with that of (311) plane of crystalline ZnGa₂O₄ phase. Concentric rings in SAED pattern (Fig.96 (c)) also confirm nanocrystalline nature of the sample. The TEM image of sample prepared with 22.96 mmol of Ga and 11.48 mmol of Zn is shown in Fig.96 (d). From the image, presence nanoparticles having size in the range of 2-3 nm can be confirmed. The corresponding HRTEM (Fig.96 (e)) and SAED pattern (Fig.96 (f)) further confirm the smaller size of the

particles. Thus the TEM studies also confirm the observed variation in particle size as a function of Ga concentration.

Photoluminescence spectra of ZnGa_2O_4 nanoparticles prepared with different Ga^{3+} concentration are shown in Fig.97 (a) and corresponding excitation spectra are shown in Fig.97 (b). The emission spectra (Fig.97 (a)) clearly reveal that with increasing the Ga concentration, from 0.14 to 1.44 mmol, emission maxima shifts from 420 nm to 435 nm and for further higher concentration of gallium, it starts shifting to lower wavelength side. This again can be explained by considering the changes in the particle size with reactants concentration. The host absorption (Band edge absorption) also shows similar trend as evident from the excitation spectra (Fig.97 (b)) where the peak maximum shifts from 260 to 270 and then to 255 nm. Wavelength maximum corresponding to localised centres present in ZnGa_2O_4 nanoparticles also varied in a similar fashion.

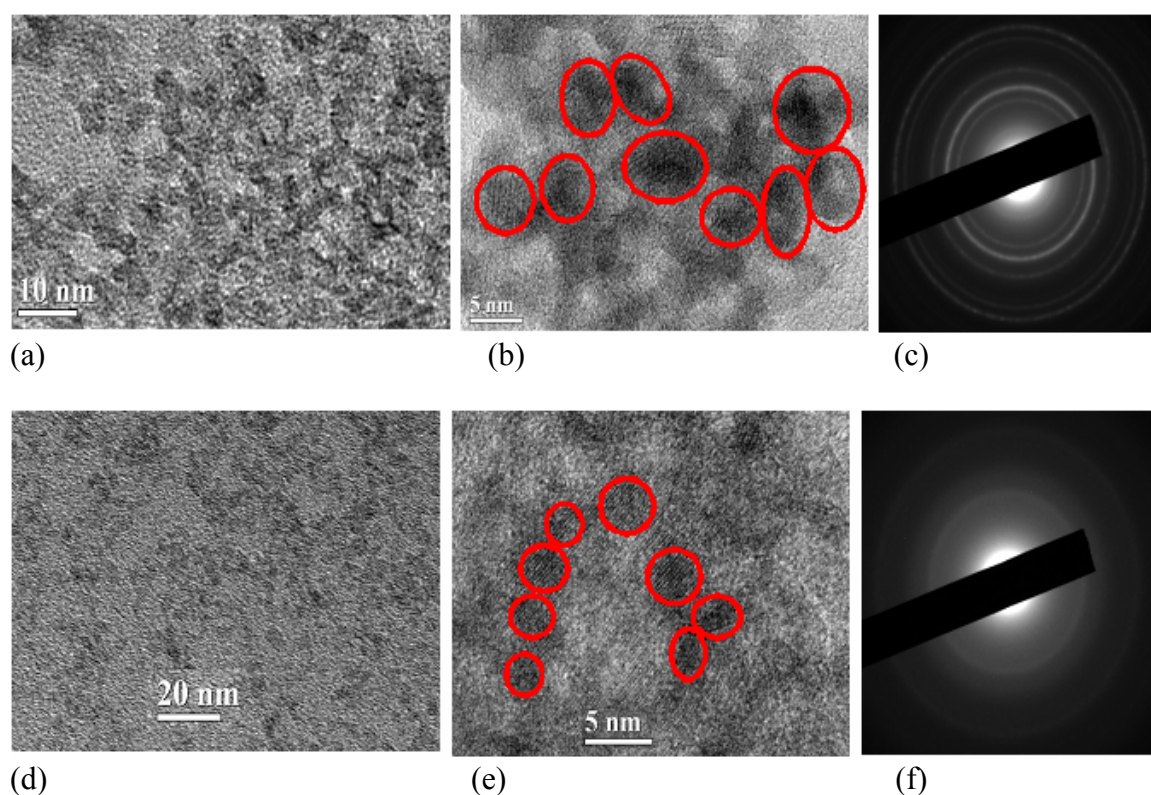


Fig.96. TEM images (a, d), HREM images (b, e), SAED patterns (c, f) of ZnGa_2O_4 nanoparticles prepared with 1.44 and 22.96 mmol Ga, respectively.

From the above studies, it is inferred that the host emission from ZnGa_2O_4 can be tuned by varying the particle size. It is interesting to know the variation in emission maximum with iso-valent ions substitution at the Ga^{3+} site in the ZnGa_2O_4 lattice. Such substitution can modify the levels due to GaO_6 octahedra in the band gap of ZnGa_2O_4 . Keeping this in mind ZnGa_2O_4 nanoparticles have been doped with In^{3+} and their emission characteristics were measured as a function of In^{3+} concentration and the results are described below. In^{3+} ion is chosen in the present study, as it is iso-valent with Ga^{3+} ion and due its heavier mass, it is expected to reduce the energy level corresponding to Ga/InO_6 units. This can lead to the shifting of the emission maximum towards higher wavelength.

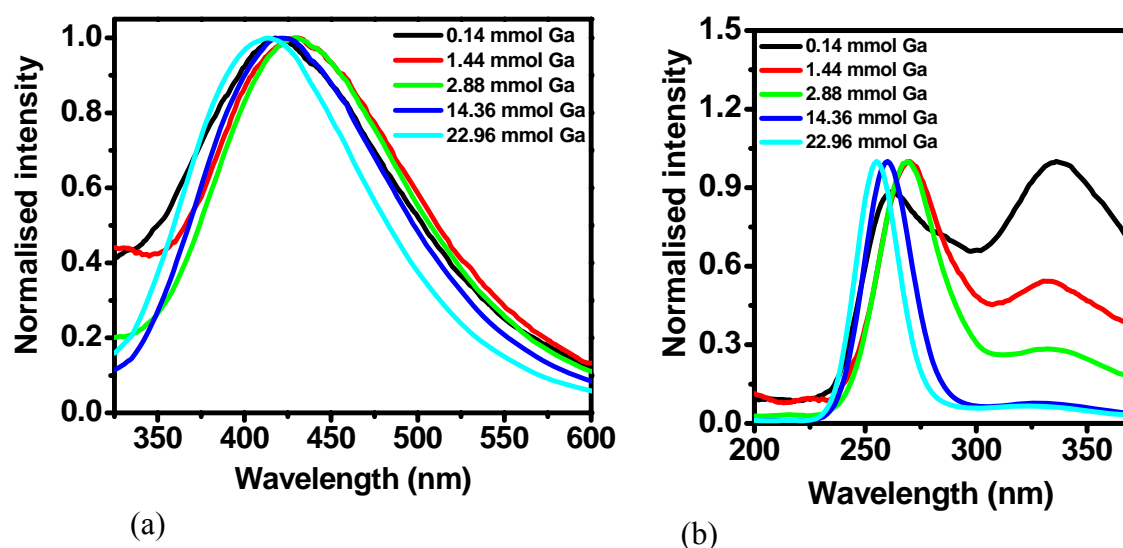


Fig.97. (a) Emission spectra of ZnGa_2O_4 nanoparticles prepared by using different concentrations Ga^{3+} after exciting the samples in the range of 250-290 nm and (b) corresponding excitation spectra.

5.4. Effect of Indium doping on crystallinity and photoluminescence of ZnGa_2O_4 :

$\text{ZnGa}_{2-x}\text{In}_x\text{O}_4$ ($x = 0, 0.05, 0.1, 0.2, 0.3, 0.5$) nanoparticles have been prepared in a mixture of 25 ml EG and 10 ml water with 0.716 mmol of Zn and 1.44 mmol of Ga and In together at 110°C . The corresponding XRD patterns for In^{3+} doped ZnGa_2O_4 nanoparticles are shown in Fig.98. With increase in the In^{3+} content, XRD peak becomes broader and shifts to lower 2θ

value. The lattice parameters calculated from the XRD patterns increase with increasing In^{3+} content in the sample. This is understandable as the ionic size of In^{3+} (0.81) is larger than that of Ga^{3+} (0.6) and incorporation of In^{3+} at Ga^{3+} site leads to lattice expansion thereby shifting the diffraction peak maximum to lower 2θ value. The broadening of the diffraction peaks can be attributed to the distortion in the lattice brought about by incorporation of larger ionic radii In^{3+} at the expense of Ga^{3+} . Thus based on XRD studies it is confirmed that In^{3+} gets incorporated into the ZnGa_2O_4 lattice and forms solid solutions of type $\text{ZnGa}_{2-x}\text{In}_x\text{O}_4$.

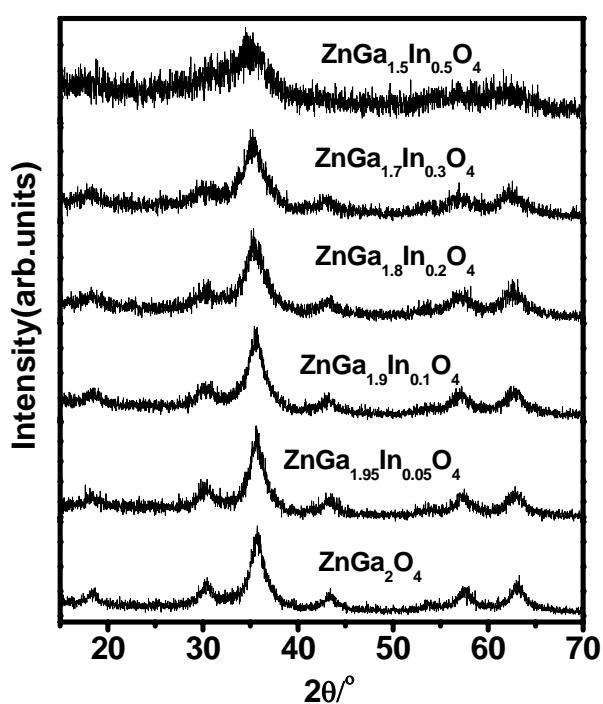


Fig.98. XRD patterns of $\text{ZnGa}_{2-x}\text{In}_x\text{O}_4$ ($x = 0, 0.05, 0.1, 0.2, 0.3, 0.5$) nanoparticles.

TEM image of $\text{ZnGa}_{1.5}\text{In}_{0.5}\text{O}_4$ nanoparticles is shown in Fig.99. Very fine particles with size in the range of 4-6 nm can be seen in the image. Corresponding SAED pattern is shown in the inset of the Fig.99 (a). The SAED pattern has been conformity with the formation of nanocrystalline $\text{ZnGa}_{2-x}\text{In}_x\text{O}_4$ phase.

Emission spectra of these samples are given in the Fig.100 (a). It is clearly seen that the emission maximum is shifted towards higher wavelength side from 430 to 455 nm with increase in the In^{3+} content in the sample and this has been attributed to the presence of In^{3+}

in the ZnGa_2O_4 lattice. It is known that In^{3+} is heavier than Ga^{3+} , as a result the energy corresponding to GaO_6 unit in the $\text{ZnGa}_{2-x}\text{In}_x\text{O}_4$ nanoparticles will be less than that in ZnGa_2O_4 . Hence, the λ_{max} corresponding to emission and excitation of GaO_6 level shifts to higher values with increase in the In^{3+} content. The decay curve corresponding to the excited state of blue emission from $\text{ZnGa}_{1.5}\text{In}_{0.5}\text{O}_4$ nanoparticles is shown in Fig.100 (b). It is found to be bi-exponential in nature with lifetime values $0.49 \mu\text{s}$ (56 %) and $1.85 \mu\text{s}$ (44 %). The faster component is due to surface GaO_6 units and longer component is due to GaO_6 present in the bulk of the $\text{ZnGa}_2\text{O}_4:\text{In}^{3+}$ lattice. Since surface GaO_6 units are directly bound to EG moiety, they will decay faster than bulk GaO_6 structural units.

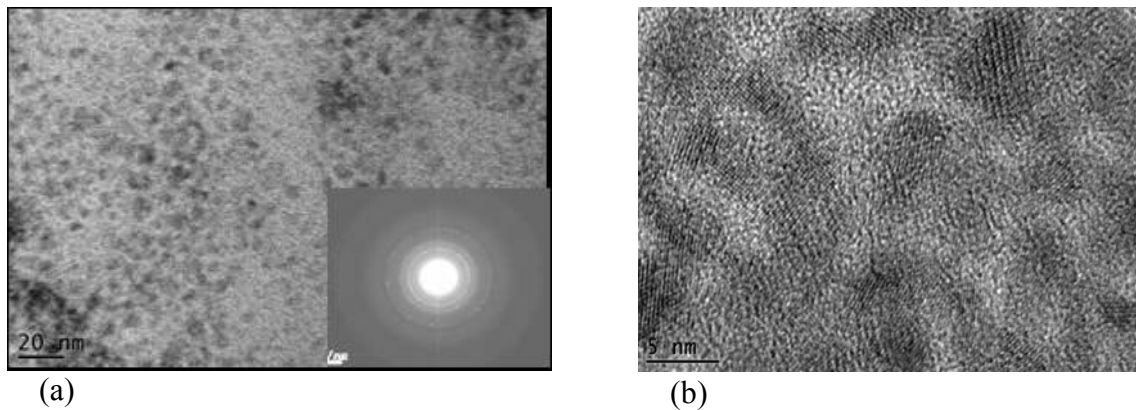


Fig.99. (a) TEM image, (b) HRTEM image of $\text{ZnGa}_{1.5}\text{In}_{0.5}\text{O}_4$ nanoparticles. SAED pattern from these nanoparticles is shown in the inset of Fig.99 (a)

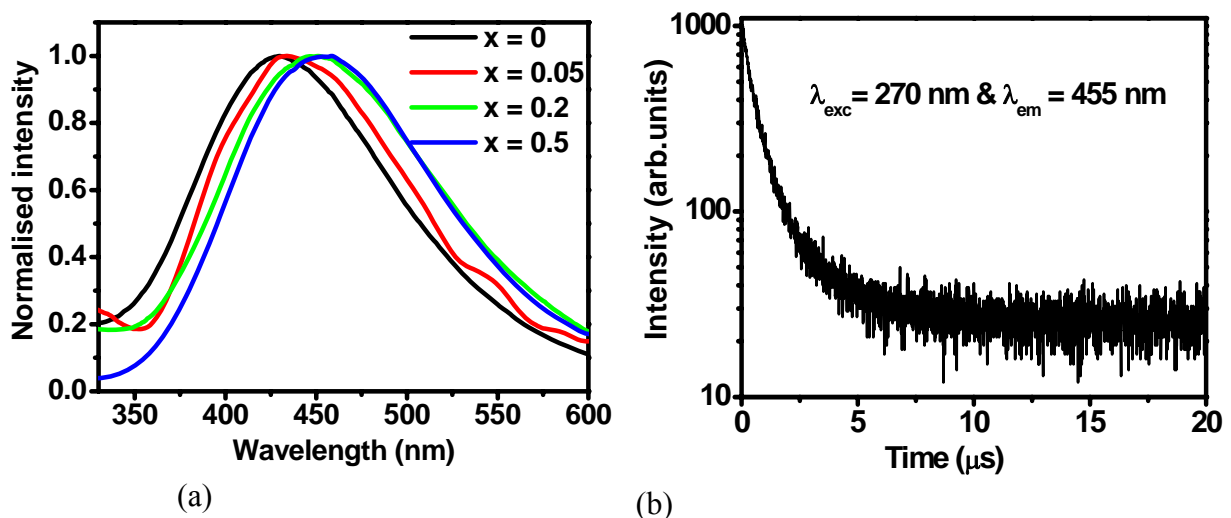


Fig.100. (a) Emission spectra of $\text{ZnGa}_{2-x}\text{In}_x\text{O}_4$ ($x = 0, 0.05, 0.2, 0.5$) nanoparticles after exciting samples in the UV region (260 to 280 nm). (b) Decay profile corresponding to blue emission from $\text{ZnGa}_{1.5}\text{In}_{0.5}\text{O}_4$ nanoparticles.

Quantum yield of the blue emission was measured using integrating sphere by dispersing the nanoparticles in methanol and the maximum quantum yield of around 10% was observed for $\text{ZnGa}_{1.5}\text{In}_{0.5}\text{O}_4$ nanoparticles. These nanoparticles were incorporated into poly methyl methacrylate (PMMA) matrix by in situ polymerization of methyl methacrylate (MMA) using AIBN as radical initiator at 72°C . The resultant polymer is soluble in organic solvents like CHCl_3 , toluene, CCl_4 , etc. The polymer was dissolved in CHCl_3 and spin coated on a quartz plate at 2500 rpm. The film was exposed to 270 nm light and the blue emission coming from the nanoparticles incorporated film is photographed and is shown in Fig.101. These results establish the potential of these nanoparticles for polymer based display applications. In addition to the host emission, the scope of ZnGa_2O_4 as a luminescent material will further improve if lanthanide ions can be incorporated in the lattice of ZnGa_2O_4 .



Fig.101. Photograph of blue light emission from thin film of PMMA containing $\text{ZnGa}_{1.5}\text{In}_{0.5}\text{O}_4$ nanoparticles, on a quartz substrate. The excitation wavelength was 270 nm.

5.5. Photoluminescence from lanthanide doped ZnGa_2O_4 nanoparticles:

5.5.1. Ce^{3+} doped ZnGa_2O_4 nanoparticles: Figure 102 shows XRD patterns of undoped ZnGa_2O_4 and 5 atom % Ce^{3+} doped ZnGa_2O_4 nanoparticles. The XRD peaks of Ce^{3+} doped ZnGa_2O_4 nanoparticle are broader and can be explained based on the difference in the ionic sizes of Ga^{3+} (0.61\AA) and Ce^{3+} (1.15\AA) under six coordination. Replacement of Ga^{3+} ion by

Ce³⁺ in the lattice leads to significant strain in the lattice due to large ionic size of Ce³⁺ ion compared to Ga³⁺ ion.

Emission spectrum of 5 atom % Ce³⁺ doped ZnGa₂O₄ nanoparticles after exciting at 265 nm light is shown in the Fig.103 (a) along with the corresponding excitation spectrum monitored at 350 nm emission. Emission spectrum shows broad band at 350 nm and is assigned to the 5d-4f transition of Ce³⁺ ion in the ZnGa₂O₄ host. The corresponding excitation spectrum shows a band at 265 nm and is arising due to the 4f-5d transition of Ce³⁺ ion. The decay curve corresponding to Ce³⁺ emission at 350 nm is shown in Fig.103 (b). The decay is single exponential with lifetime of 17.3 ns. Based on the studies it can be inferred that Ce³⁺ doping in ZnGa₂O₄ will be helpful for making bright luminescent materials showing emission in the UV region.

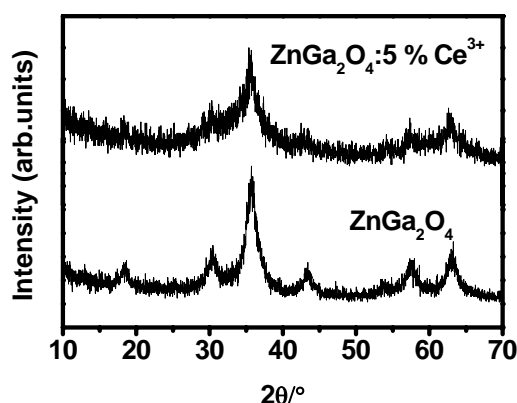


Fig.102. XRD patterns of undoped ZnGa₂O₄ and 5 at % Ce³⁺ doped ZnGa₂O₄ nanoparticles.

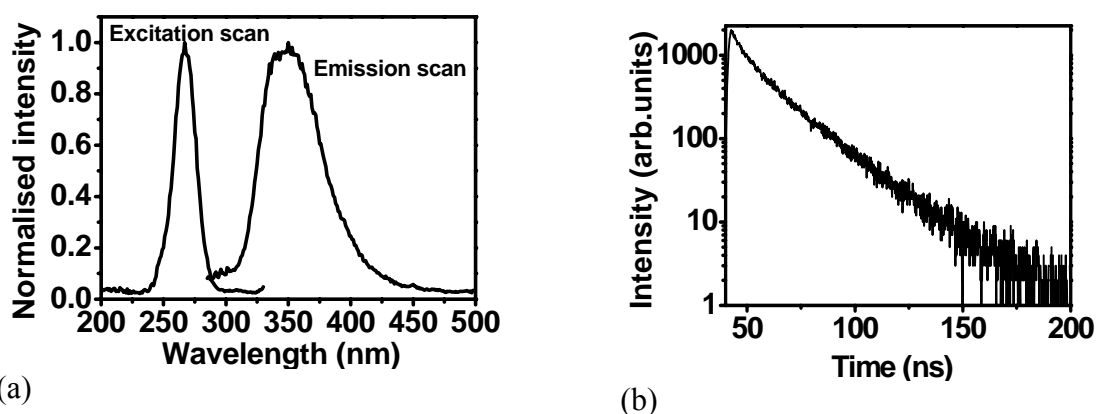


Fig.103. (a) Emission and excitation spectra of 5 at % Ce³⁺ doped ZnGa₂O₄ nanoparticles and (b) excited state decay profile of Ce³⁺ emission (λ_{exc} =265 nm, λ_{em} =350 nm).

5.5.2. Eu^{3+} doped $\text{ZnGa}_{1.5}\text{In}_{0.5}\text{O}_4$ nanoparticles: Emission spectrum of Eu^{3+} doped $\text{ZnGa}_{1.5}\text{In}_{0.5}\text{O}_4$ nanoparticles excited at 280 nm is shown in Fig.104 (a). It consists of a broad band around 460 nm over which sharp peaks $\sim 590, 615, 700$ nm are superimposed. The broad band is a characteristic emission of $\text{ZnGa}_{1.5}\text{In}_{0.5}\text{O}_4$ host material and sharp peaks correspond to $^5\text{D}_0 \rightarrow ^7\text{F}_1$, $^5\text{D}_0 \rightarrow ^7\text{F}_2$ and $^5\text{D}_0 \rightarrow ^7\text{F}_4$ transitions of Eu^{3+} ion. Excitation spectra were monitored at 460 and 615 nm emissions (Fig.104 (b)).

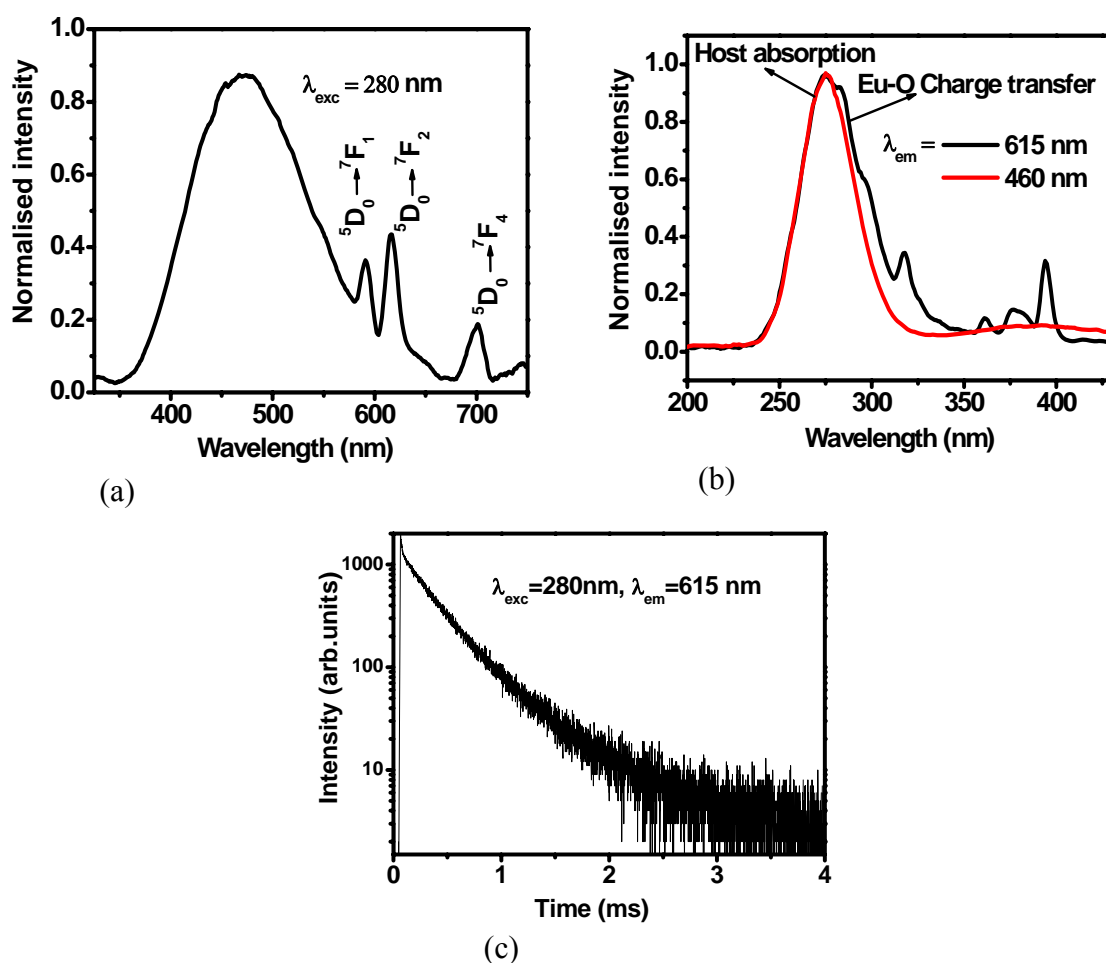


Fig.104. (a) Emission spectrum obtained after 280 nm excitation and (b) excitation spectra obtained after monitoring 615 nm and 460 nm emissions along with (c) the decay curve corresponding to $^5\text{D}_0$ level of Eu^{3+} in $\text{ZnGa}_{1.5}\text{In}_{0.5}\text{O}_4$ nanoparticles.

The excitation spectrum monitored at 460 nm emission showed only one peak at 280 nm corresponding to host absorption of the material. Unlike this excitation spectrum monitored at 615 nm emission consists of sharp peaks above 300 nm along with broad

asymmetric band at 280 nm. The broad band is a combination of host absorption and Eu-O charge transfer transition whereas the sharp peaks are characteristic f-f transitions of Eu^{3+} ion. The decay corresponding to the $^5\text{D}_0$ level of Eu^{3+} in the sample is shown in the Fig.104 (c). It is bi-exponential in nature with lifetime components 200 μs (45%) and 526 μs (55%). The faster and slower components are due to surface and bulk Eu^{3+} ions, respectively present in ZnGa_2O_4 nanoparticles.

5.5.3 Tb^{3+} doped $\text{ZnGa}_{1.5}\text{In}_{0.5}\text{O}_4$ nanoparticles: Emission spectrum of Tb^{3+} doped $\text{ZnGa}_{1.5}\text{In}_{0.5}\text{O}_4$ nanoparticles excited at 280 nm is shown in Fig.105 (a). The spectrum consists of a broad band at 460 nm along with sharp peaks at 490, 545, 585 and 620 nm. This broad band is the characteristic of the host emission and the sharp peaks are due to $^5\text{D}_4 \rightarrow ^7\text{F}_6$, $^5\text{D}_4 \rightarrow ^7\text{F}_5$, $^5\text{D}_4 \rightarrow ^7\text{F}_4$ and $^5\text{D}_4 \rightarrow ^7\text{F}_3$ transitions of Tb^{3+} , respectively. $^5\text{D}_4$ decay profile of Tb^{3+} (Fig.105 (b)) is a single exponential with lifetime of 1.39 ms.

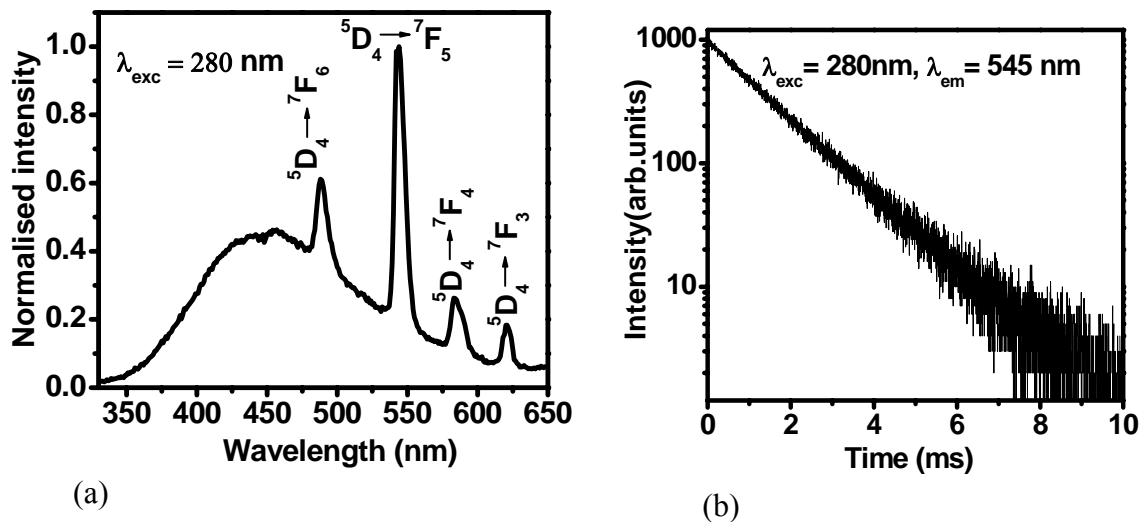


Fig.105. (a) Emission spectrum and (b) $^5\text{D}_4$ decay profile of Tb^{3+} , from Tb^{3+} doped $\text{ZnGa}_{1.5}\text{In}_{0.5}\text{O}_4$ nanoparticles. The excitation and emission wavelengths are 280 and 545 nm, respectively.

CHAPTER 6: Tungstates [MWO₄ (M = Ca, Sr, Ba)]

6.1. Introduction: The tungstate materials have attracted much attention over the past two decades due to their important properties and applications in photoluminescence, microwave devices, optical fibers, scintillator materials, humidity sensors and catalysis [266-270]. They are expressed by the general formula of MWO₄ and can exist in two different crystalline modifications depending on the size of cations [271, 272]. Tungstates of relatively larger bivalent cations (ionic radius >0.99 Å) such as Ca, Ba, Pb and Sr exist in the scheelite structure, where the tungsten atom adopts tetrahedral coordination. Unlike this tungstates of smaller bivalent cations (ionic radius <0.77 Å) like Fe, Mn, Co, Ni, Mg and Zn belong to wolframite structure, where the tungsten atom adopts an octahedral coordination. Calcium tungstate is known as a good scintillator and is blue light emitting material [69]. Preparing them in nanosize dimension and understanding their optical properties will be of interest and will be relevant for developing different types of optical materials for various applications. Further, lanthanide ions once incorporated in the lattice can result in energy transfer from host to lanthanide ions, thereby leading to improved luminescence from such materials. Due to similarities in coordination number and ionic sizes of ions like calcium with trivalent lanthanide ions [172], it is easy to replace Ca²⁺ ion by Ln³⁺ ion in the MWO₄ lattice. Conventionally both doped and undoped MWO₄ particles have been prepared by solid-state reactions. However, low temperature synthesis of MWO₄ nanomaterials using co-precipitation and solvo-thermal techniques has been reported recently [273-278]. It will be interesting if lanthanide doped MWO₄ nanoparticles can be obtained at low temperature with suitable ligand stabilization, so that they can be dispersed in different solvents for further processing. Such nanoparticles are also expected to have different luminescence properties compared to those prepared through solid-state method. Keeping this in mind, in the present study a number of MWO₄ nanoparticles doped with Eu³⁺, Tb³⁺, Dy³⁺, Sm³⁺ and Er³⁺ have

been prepared. Synthesis and luminescence properties of these nanoparticles are discussed in this chapter. Tungstate nanomaterials were prepared at room temperature in ethylene glycol by adding sodium tungstate to the metal nitrate solution.

6.2. Effect of nature of metal ion on the particle size: Figure 106 shows XRD patterns of MWO_4 ($M = Ca, Sr, Ba$) nanomaterials. All the peaks are characteristic of nanocrystalline tetragonal MWO_4 with scheelite structure. The shifting of XRD peak maximum to lower 2θ values from Ca to Ba through Sr is due to the increase in the ionic radii of cation and associated lattice expansion. Line widths of diffraction peaks are also found to decrease with increase in the ionic radii of the metal ion. Average crystallite size was calculated by using Debye-Scherrer formula and is found to be 7, 10, 20 nm for $CaWO_4$, $SrWO_4$ and $BaWO_4$, respectively.

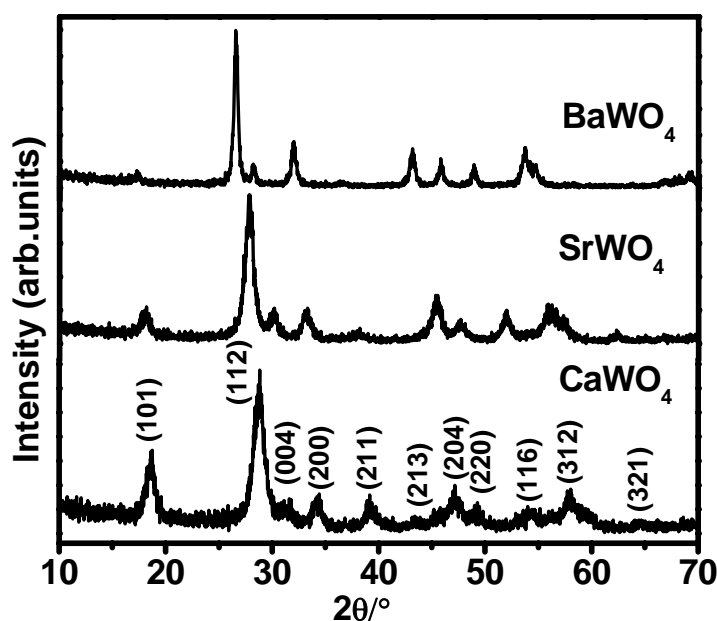


Fig.106. XRD patterns of MWO_4 ($M = Ca, Sr, Ba$) nanoparticles.

Lattice parameters were calculated by least squares fitting of the XRD patterns. These are found to be $a = 5.240 \text{ \AA}$, $c = 11.381 \text{ \AA}$ for $CaWO_4$, $a = 5.415 \text{ \AA}$, $c = 11.951 \text{ \AA}$ for $SrWO_4$ and $a = 5.613 \text{ \AA}$, $c = 12.703 \text{ \AA}$ for $BaWO_4$ nanoparticles. The increase in the lattice parameters are due to increase in the ionic sizes of metal ions. Increase in particle size with increase in

ionic radius of the metal cation can be explained based on the difference in the extent of stabilization of ligand (EG moiety) on the surface of MWO_4 nanoparticles. As the stabilization of EG moiety on the nanoparticles occurs through cations like Ca^{2+} , Sr^{2+} and Ba^{2+} , the extent of stabilization of ligand will be the highest for $CaWO_4$ nanoparticles and lowest for $BaWO_4$ nanoparticles, due to the so called hard-hard and soft-soft interactions. Extent of stabilization of ligands with $SrWO_4$ is in between that of $CaWO_4$ and $BaWO_4$. Higher the extent of stabilization, lower will be the extent of growth and this result in smaller particles.

TEM images of $CaWO_4$, $SrWO_4$ and $BaWO_4$ nanomaterials are shown in Fig.107. $CaWO_4$ nanoparticles are relatively small with size in the range 5-10 nm and have uniform size distribution as can be seen in Fig.107 (a). The SAED pattern from these nanoparticles is shown in the inset of Fig.107 (a). The pattern consists of several rings, which are characteristic of very fine particles that are randomly oriented. HRTEM image of $CaWO_4$ nanoparticles is shown in Fig.107 (b). Distance between lattice fringes is found to be 3.1 Å and this matches well with that of (112) plane of $CaWO_4$. TEM image of $SrWO_4$ nanoparticles is shown in Fig.107 (c). It is clear from the image that particles have homogeneous size distribution with sizes in the range of 15-25 nm. Corresponding SAED pattern is shown in the inset of Fig.107 (c), consists of both rings, and dots characteristic of nanocrystalline $SrWO_4$ phase with slight aggregation. TEM image of $BaWO_4$ nanoparticles is shown in Fig.107 (d). These particles are having rice shape with length around 500-1000 nm. SAED pattern from $BaWO_4$ nanoparticles is shown in the inset of Fig.107 (d) and the pattern mainly consists of dots and is characteristic of single crystalline nature of $BaWO_4$ nanomaterials. Based on XRD and TEM studies it is inferred that $CaWO_4$ nanoparticles are extremely small in size compared to other two tungstates. It would be of interesting to assess the MWO_4 nanomaterials which can give optimum luminescence on lanthanide ion doping.

In order to check this aspect, these nanomaterials are doped with representative lanthanide ion namely the Eu^{3+} and their luminescence properties are described in the following section.

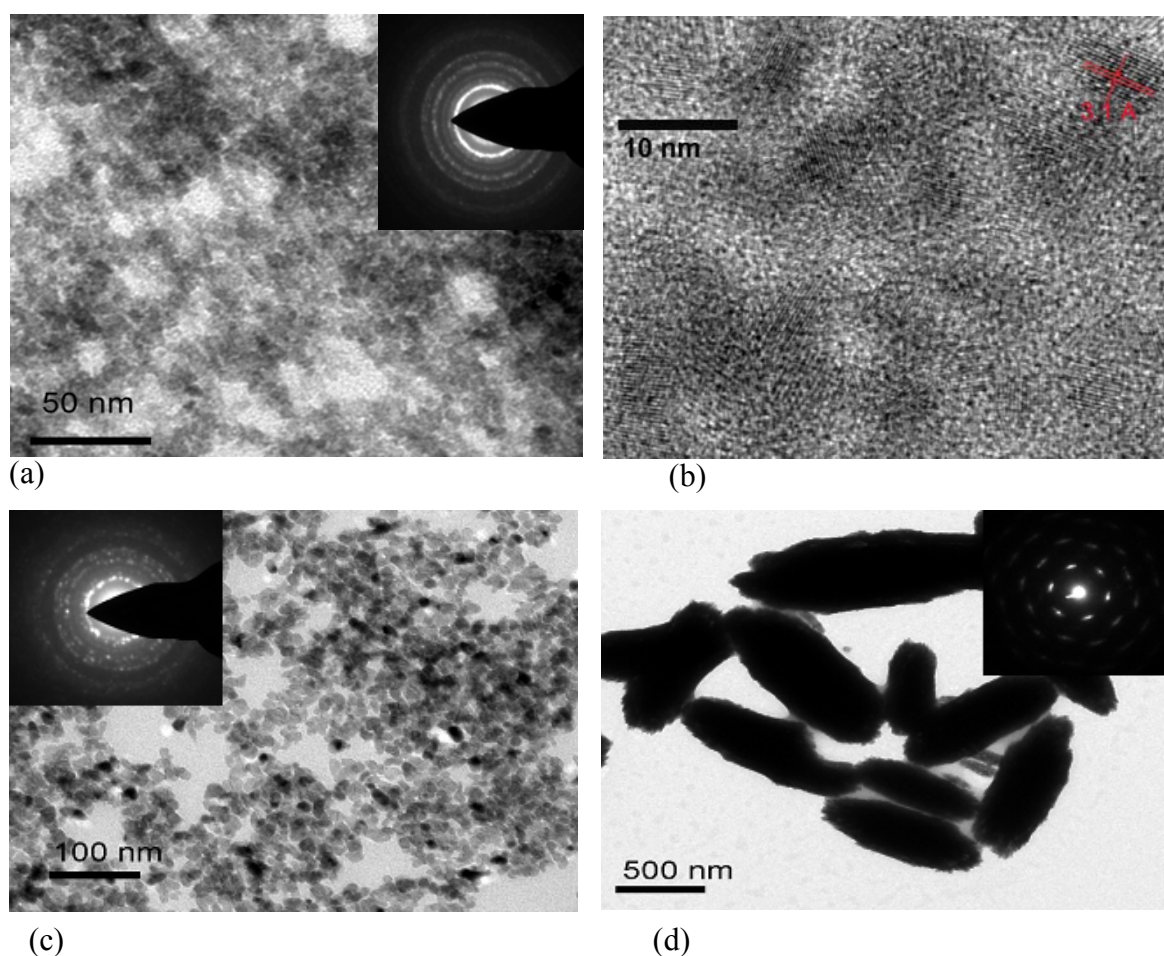


Fig.107. TEM image of (a and b) CaWO_4 , (c) SrWO_4 and (d) BaWO_4 nanomaterials and inset of the images shows corresponding SAED pattern.

6.3. Effect of metal ion on luminescence of $\text{MWO}_4:\text{Eu}^{3+}$ nanoparticles: Emission spectra of Eu^{3+} doped MWO_4 ($\text{M} = \text{Ca}, \text{Sr}, \text{Ba}$) nanoparticles excited at 270 nm is given in the Fig.108 (a). It consists of four peaks at 590, 615, 650 and 700 nm and are attributed to $^5\text{D}_0 \rightarrow ^7\text{F}_1$, $^5\text{D}_0 \rightarrow ^7\text{F}_2$, $^5\text{D}_0 \rightarrow ^7\text{F}_3$ and $^5\text{D}_0 \rightarrow ^7\text{F}_4$ transitions of Eu^{3+} ions present in the lattice. The $^5\text{D}_0 \rightarrow ^7\text{F}_2$ transition is electric dipole allowed transition. It is hypersensitive and is highly dependent on the symmetry around the Eu^{3+} ion. Unlike this, $^5\text{D}_0 \rightarrow ^7\text{F}_1$ transition is a magnetic dipole allowed transition and is independent of the symmetry around Eu^{3+} ion in the

lattice. Asymmetric ratio is ~ 12 for all the three tungstates. High value of asymmetric ratio indicates that Eu^{3+} ion occupies a highly asymmetric environment in MWO_4 ($\text{M} = \text{Ca}, \text{Sr}, \text{Ba}$) crystal lattice. The intensity of Eu^{3+} emission decreases with increase in the ionic size of the alkaline earth metal cations. Similar effect was observed by Blasse, et al. for UO_6 emission in the tungstate host [69]. Presence of ions with large radius around the luminescent center is equivalent to soft surroundings. With increase in the softness of surroundings, stokes shift increases and as a result the excited tungstate group decays by a non-radiative route to ground state instead of transferring energy to lanthanide ions. This explains the decrease in luminescence intensity when going from CWO_4 to SrWO_4 and then to BaWO_4 . It is also known that with increase in the stiffness of the lattice, non-radiative process decreases.

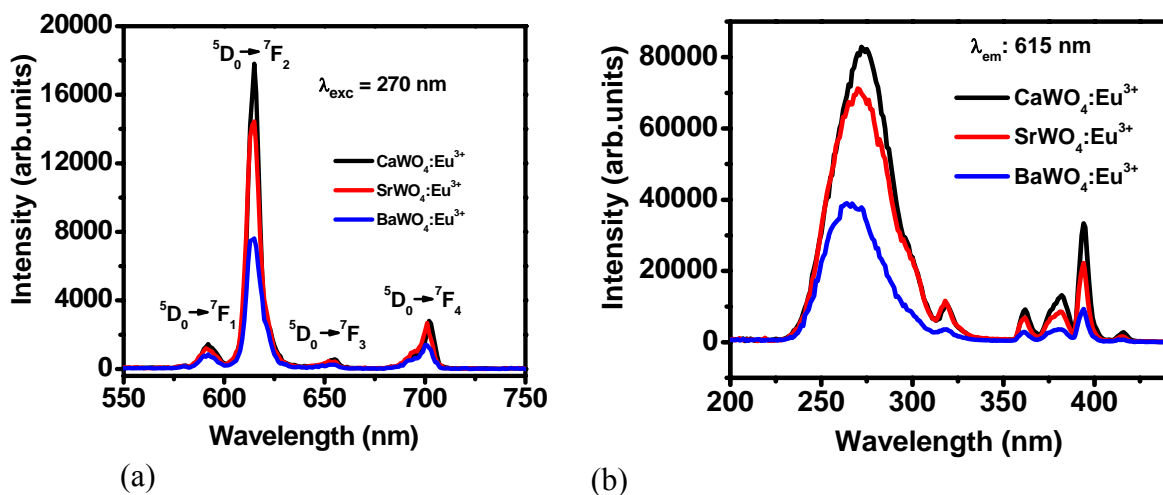


Fig.108. (a) Emission spectra and (b) excitation spectra from $\text{CaWO}_4:\text{Eu}^{3+}$, $\text{SrWO}_4:\text{Eu}^{3+}$, $\text{BaWO}_4:\text{Eu}^{3+}$ nanoparticles. ($\lambda_{\text{exc}} = 270 \text{ nm}$ and $\lambda_{\text{em}} = 615 \text{ nm}$)

In the present case the ionic radii of metal ion increases while going from CaWO_4 to SrWO_4 and then to BaWO_4 . Hence, the stiffness of the lattice decreases in the same order and this explains the observed maximum in the luminescence intensity from CaWO_4 as compared to SrWO_4 and BaWO_4 . Values of lattice parameters further confirm this. The excitation spectra corresponding to Eu^{3+} emission is shown in Fig.108 (b). The patterns consist of broad peak centered at 270 nm and sharp peaks above 310 nm. The broad band is assigned to the Eu-O

charge transfer transition and sharp peaks to f-f transitions of Eu^{3+} ion present in the lattice. Eu^{3+} doped CaWO_4 nanoparticles showed highest luminescence intensity as compared to Eu^{3+} doped SrWO_4 and BaWO_4 . Hence, detailed studies were carried out on luminescence properties of undoped and different lanthanide doped CaWO_4 nanoparticles.

6.4. Luminescence studies on un-doped CaWO_4 nanoparticles: Emission spectrum observed from undoped CaWO_4 nanoparticles after exciting with 253 nm light is shown in Fig.109 (a). The spectrum is characterized by a broad band extended over a region of 325 to 600 nm with maximum ~ 425 nm. A photograph of the emission (blue) observed from the sample dispersed in methanol after shining with 253 nm light is shown in Fig.109 (b). Excitation spectrum from the sample corresponding to 425 nm emission is shown in Fig.109 (c). The spectrum consists of a broad peak centered at 253 nm and arises from the charge transfer transitions within the WO_4^{2-} tetrahedra of CaWO_4 [69]. From the view point of molecular orbital theory, the excitation and emission from CaWO_4 nanoparticles can be attributed to transitions involving $^1\text{A}_1$ ground state and ^1B ($^1\text{T}_2$) excited state of WO_4^{2-} ion. Excited state [^1B ($^1\text{T}_2$)] decay profile of the WO_4^{2-} ion monitored at 425 nm emission is shown in Fig.109 (d). The decay is found to be bi-exponential with lifetime components 0.5 μs (25%) and 2.6 μs (75%). The shorter component has been assigned to the emission originating from the surface tungstate groups and longer component to the emission originating from bulk tungstate groups. Stabilizing ligands on the surface quenches the excited state of WO_4^{2-} structural units and thereby leading to reduced lifetime of the corresponding excited state. In order to check whether the emission due to WO_4^{2-} group is sensitive to the particle size of CaWO_4 , as prepared samples were heated at different temperatures and their structural and luminescent properties were investigated. The results are described below.

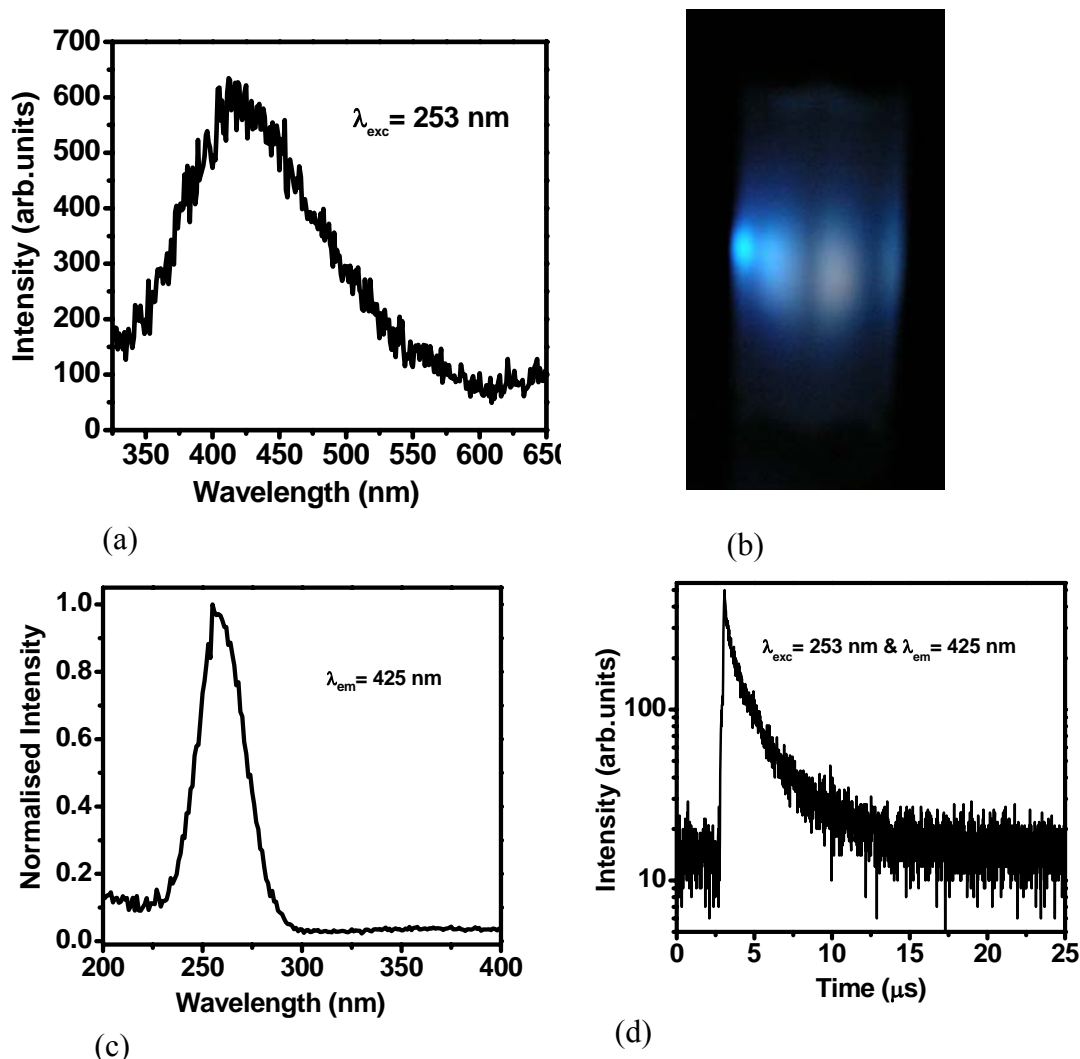


Fig.109. Emission spectrum (a) and photograph of emission (b) obtained from $\text{CaWO}_4:\text{Eu}$ nanoparticles after excitation at 253 nm. The corresponding excitation spectrum and decay curve, both monitored at 425 nm emission are shown in Fig.109 (c) and (d) respectively.

6.5. Effect of heat treatment on particle size: CaWO_4 nanoparticles prepared at room temperature were heated at different temperatures ranging from 300 to 900°C in air for 8 hours and their XRD patterns are shown in Fig.110. All the samples show characteristic peaks of scheelite structure with tetragonal unit cell. With increase in the heating temperature, XRD peaks become sharper. This is due to the increase in the average crystallite size on aggregation. Average crystallite size has been calculated by using Debye-Scherrer formula (Table 14) and found to increase from 7 to 99 nm as temperature increases from room temperature to 900°C.

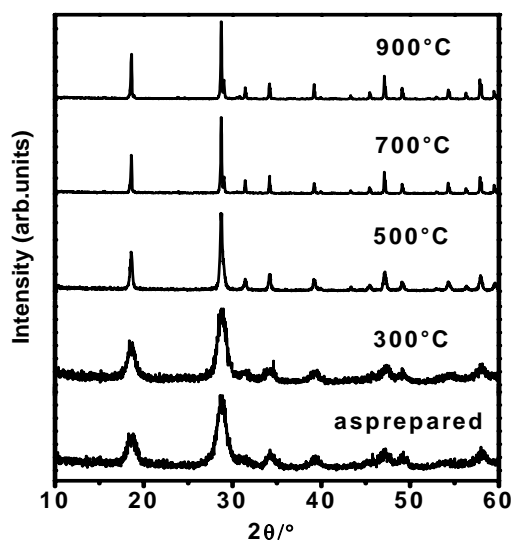


Fig.110. XRD patterns of as prepared, 300, 500, 700 and 900°C heated CaWO₄ nanoparticles.

Table 14. Average crystallite size of CaWO₄ nanoparticles as a function of heat treatment temperatures.

Temperature (°C)	Avg. crystallite size (in nm)
As prepared (Room temperature)	7
300	8
500	26
700	90
900	99

6.6. Effect of particle size on photoluminescence of CaWO₄ nanoparticles: Emission spectra of CaWO₄ nanoparticles heated at different temperatures obtained after excitation at 253 nm is shown in Fig.111 (a). As prepared (particle size 7 nm) and 300°C heated (particle size 8 nm) samples show weak emission and are having almost same intensity. Unlike this samples heated at 700°C (particle size 90 nm) and 900°C (particle size 99 nm) show bright luminescence and their intensities are almost same. Luminescence of 500°C (26 nm) heated samples is slightly higher than 300°C heated sample, but much lower than 700°C heated sample. Based on these results, it is inferred that photoluminescence of CaWO₄ nanoparticles increases with increase in the particle size and crystallinity and associated decrease in the concentration of surface quenching sites.

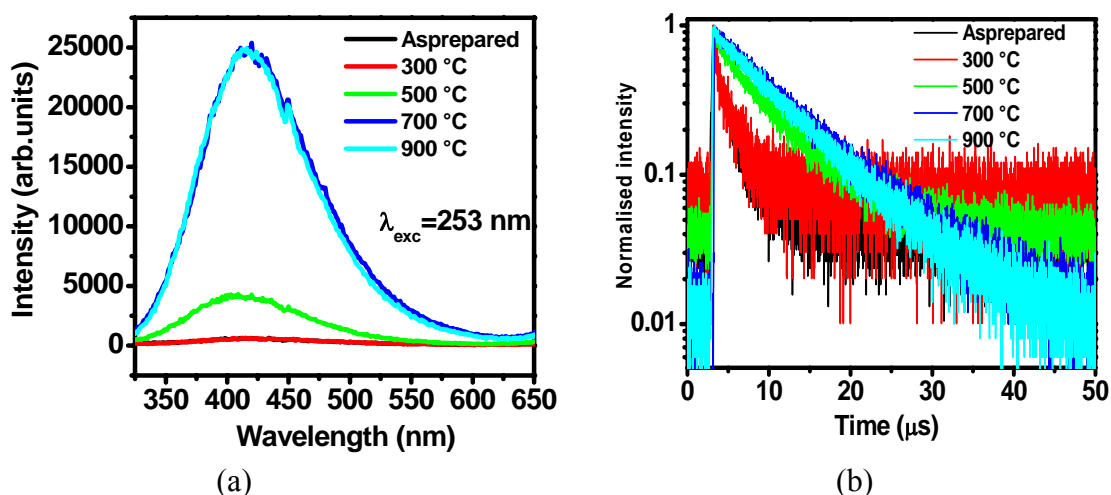


Fig.111. Emission spectra (a) and excited state decay curves (b) of CaWO_4 nanoparticles as a function of heat treatment temperatures (particle size). ($\lambda_{\text{exc}} = 253 \text{ nm}$ and $\lambda_{\text{em}} = 425 \text{ nm}$)

To confirm above inferences, decay curves corresponding to the excited state for the emission (425 nm) is recorded for different samples and are shown in Fig.111 (b). The corresponding lifetime values and their relative percentages are given in the Table 15. Decay curves corresponding to as prepared, 300 and 500°C heated CaWO_4 nanoparticles are found to be bi-exponential in nature, whereas that of 700 and 900°C heated samples are found to be single exponential. In the case of samples showing bi-exponential decay curves, the shorter lifetime values are assigned to surface WO_4^{2-} and longer lifetime values due to bulk WO_4^{2-} structural units.

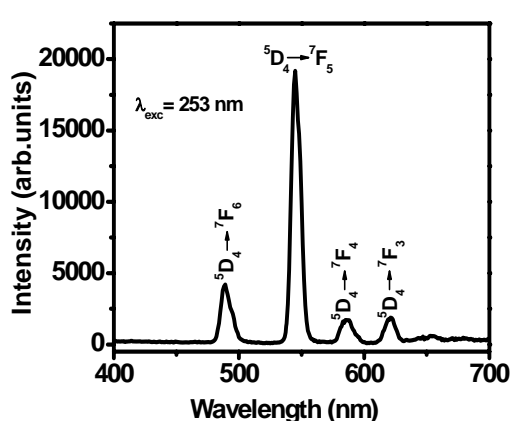
Table 15. Excited state lifetime values of CaWO_4 nanoparticles as a function of heat treatment temperature and particle size.

Sample	Avg. crystallite size (in nm)	Lifetime values	
		τ_1 (μs)	τ_2 (μs)
As prepared	7	0.5 (25%)	2.602 (75 %)
300°C	8	0.398 (13%)	2.798 (87 %)
500°C	26	1.661 (9%)	7.004 (91 %)
700°C	90	8.214 (100%)	-
900°C	99	7.829 (100%)	-

The lifetime value increases and relative percentage of shorter component decreases with increase in heat treatment temperatures. Hence from the steady state and lifetime

measurements, it is confirmed that increase in particle size and associated decrease in the concentration of surface quenching sites are responsible for the improved emission from the nanoparticles heated at high temperatures. In continuation of this work, detailed studies were carried out on lanthanide doped CaWO_4 nanoparticles and their luminescence properties are described below.

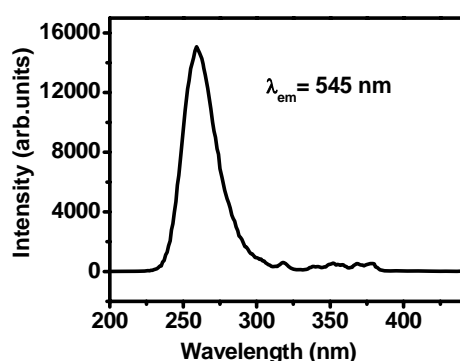
6.7. Luminescence studies on Tb^{3+} doped CaWO_4 nanoparticles: Emission spectrum from as prepared 2 at% Tb^{3+} doped CaWO_4 nanoparticles excited at 253 nm is shown in Fig.112 (a). The spectrum consists of four sharp peaks at 490, 545, 590 and 621 nm and are attributed to the $^5\text{D}_4 \rightarrow ^7\text{F}_6$, $^5\text{D}_4 \rightarrow ^7\text{F}_5$, $^5\text{D}_4 \rightarrow ^7\text{F}_4$ and $^5\text{D}_4 \rightarrow ^7\text{F}_3$ transitions, respectively of Tb^{3+} ions present in the CaWO_4 lattice.



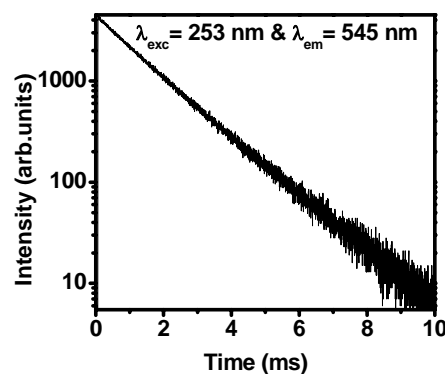
(a)



(b)



(c)



(d)

Fig.112. Emission spectra (a) and photograph of emission (b) obtained after excitation at 253 nm from $\text{CaWO}_3:\text{Tb}^{3+}$ nanoparticles. The corresponding excitation spectrum and decay curve monitored at 545 nm emission are shown in Fig.112 (c and d), respectively.

Strong green emission has been observed from Tb³⁺ doped CaWO₄ nanoparticles in methanol after exciting at 253 nm (Fig.112 (b)). Excitation spectra corresponding 545 nm emission is shown in Fig.112 (c) and consist of a strong peak between 230 and 300 nm, with a maximum ~260 nm along with less intense sharp peaks above 300 nm. The strong band is due to the overlap of host absorption and 4f-5d transition of Tb³⁺ ions present in the lattice. Sharp peaks above 300 nm are assigned to f-f transitions of Tb³⁺ ion. The decay curve corresponding to ⁵D₄ level of Tb³⁺ is shown in Fig.112 (d). The decay curve is bi-exponential in nature with lifetime components 0.978 ms (23%) and 1.59 ms (77 %). The shorter and longer lifetime component has been attributed to the surface and bulk Tb³⁺ ions, respectively present in the nanoparticles.

6.8. Luminescence studies on Dy³⁺ doped CaWO₄ nanoparticles: Emission spectrum from 2 at % Dy³⁺ doped CaWO₄ nanoparticles obtained after exciting the sample at 253 nm is shown in Fig.113 (a). It consist of peaks at 478, 574 and 665 nm and are due to ⁴F_{9/2} → ⁶H_{15/2}, ⁴F_{9/2} → ⁶H_{13/2} and ⁴F_{9/2} → ⁶H_{9/2} transitions, respectively of Dy³⁺ ions present in the lattice. Strong greenish yellow emission is observed from the Dy³⁺ doped CaWO₄ nanoparticles in methanol after exciting at 253 (Fig.113 (b)). Excitation spectrum corresponding to 574 nm emission of Dy³⁺ is shown in Fig.113 (c). The spectrum consists of a strong band at 253 nm along with weak peak at 350 nm and the latter is due to f-f transition of Dy³⁺ ion. The strong band is characteristic of the host and is arising due to charge transfer absorption of host as there is no absorption band for Dy³⁺ in this region. Observation of host absorption peak in the excitation spectrum corresponding to Dy³⁺ emission at 574 nm confirms that the absorbed energy of the host get transferred to Dy³⁺ ions. The decay curve corresponding to ⁴F_{9/2} excited state of Dy³⁺ is shown in Fig.113 (d). The decay is found to be bi-exponential with lifetime components 0.1 ms (24%) and 0.36 ms (76%). Similar to the explanation given to the ⁵D₄ decay of Tb³⁺ from CaWO₄:Tb³⁺ nanoparticles, the faster and

slower lifetime components are attributed to Dy^{3+} ions present at the surface and bulk of the nanoparticles, respectively.

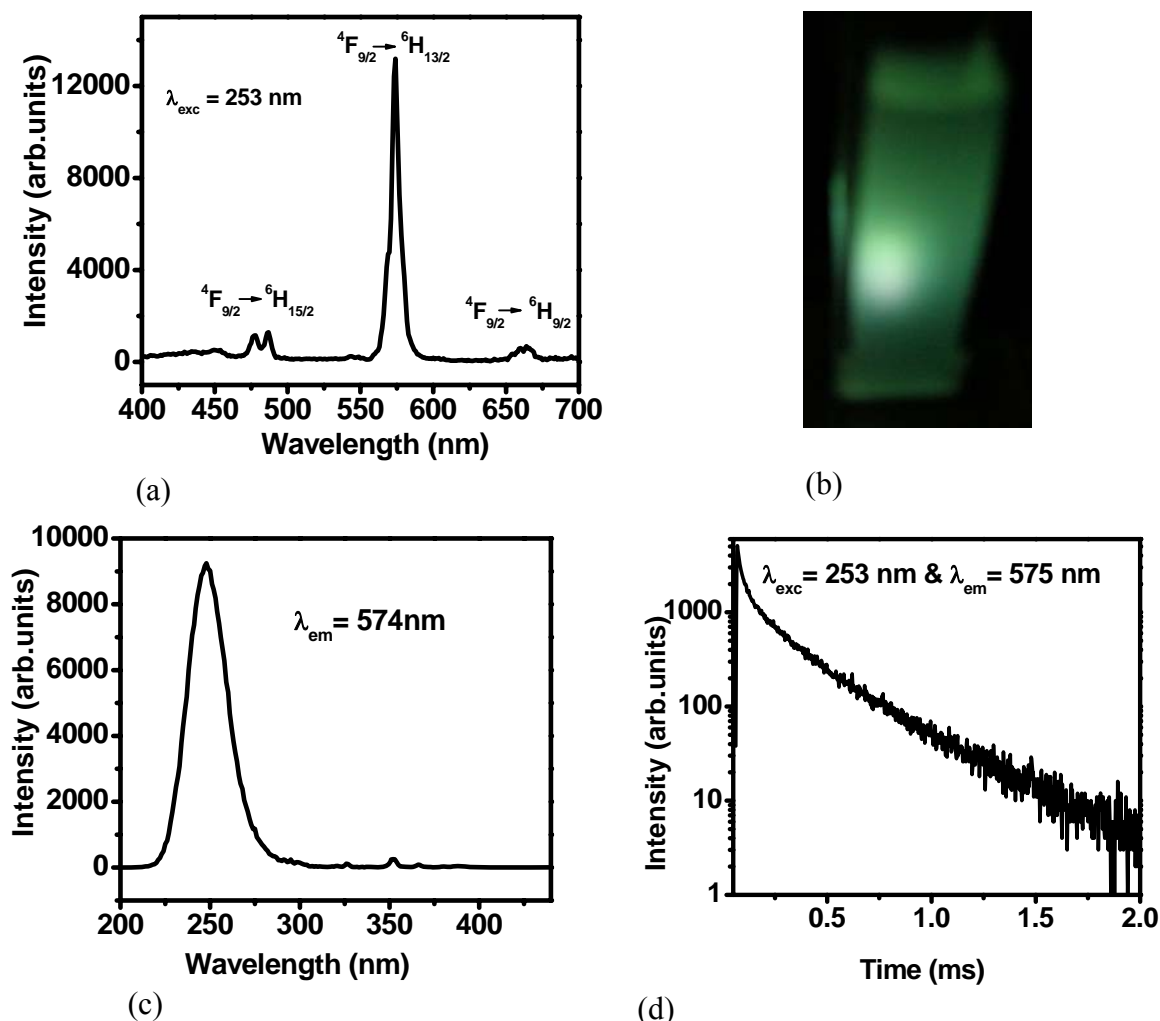


Fig.113. Emission spectrum (a) and photograph of emission (b) obtained after excitation at 253 nm from $\text{CaWO}_4:\text{Dy}^{3+}$ nanoparticles. Corresponding excitation spectrum and decay curve monitored at 574 nm emission are shown in Fig.113 (c and d).

6.9. Luminescence studies on Sm^{3+} doped CaWO_4 nanoparticles: Emission spectrum obtained from 2 at % Sm^{3+} doped CaWO_4 nanoparticles after excitation at 253 nm is shown in Fig.114 (a). The spectrum consists of three peaks at 565, 602 and 645 nm and is attributed to ${}^4\text{G}_{5/2} \rightarrow {}^6\text{H}_{5/2}$, ${}^4\text{G}_{5/2} \rightarrow {}^6\text{H}_{7/2}$ and ${}^4\text{G}_{5/2} \rightarrow {}^6\text{H}_{9/2}$ transitions, respectively of Sm^{3+} present in the CaWO_4 lattice. Orange emission visible to naked eye, observed from Sm^{3+} doped CaWO_4 nanoparticles in methanol is clear from the photograph shown in the Fig.114 (b). The excitation spectrum monitored at 602 nm emission of Sm^{3+} is shown in Fig.114 (c). It

consists of strong band at 255 nm along with weak peaks above 350 nm and the former is assigned to the charge transfer transition of the WO_4^{2-} group whereas latter to f-f transitions of Sm^{3+} ions present in the lattice. The results are similar to that of $\text{CaWO}_4:\text{Dy}^{3+}$ samples. The results on $\text{CaWO}_4:\text{Sm}^{3+}$ samples also establish that strong energy transfer takes place from host to the Ln^{3+} ions in the CaWO_4 nanoparticles. The decay curve corresponding to $^4\text{G}_{5/2}$ level of Sm^{3+} is shown in Fig.114 (d). The decay is bi-exponential in nature with lifetime components 18.5 μs (33%) and 67.8 μs (67%).

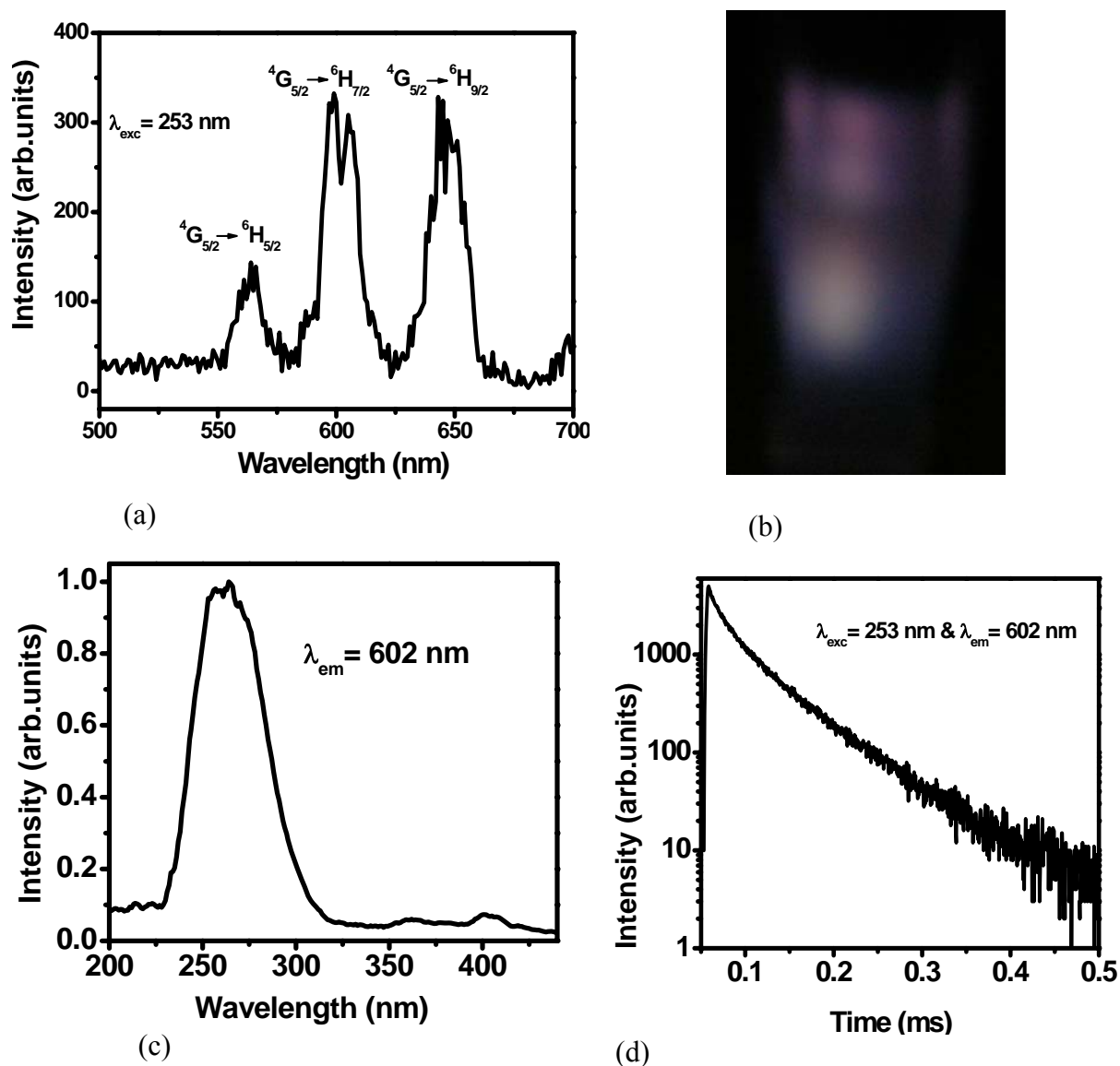


Fig.114. Emission spectrum (a) and photograph of emission (b) obtained after excitation at 253 nm from $\text{CaWO}_4:\text{Sm}^{3+}$ nanoparticles. Corresponding excitation spectrum and decay curve monitored at 602 nm emission are shown in Fig.114 (c and d).

Purity of the observed colour from a sample is decided by the CIE coordinates, which can be calculated from the emission spectrum. The abbreviation CIE stands for the French word Commission Internationale de l'éclairage and is an international governing body on light, illumination, color and color spaces. The CIE coordinates have been calculated for the undoped, Eu^{3+} , Tb^{3+} , Dy^{3+} and Sm^{3+} doped CaWO_4 nanoparticle from corresponding emission spectra obtained by exciting samples at 253 nm. These values are plotted in the standard CIE diagram (Fig.115) and they are showing blue, red, green, greenish yellow and orange for undoped, Eu^{3+} , Tb^{3+} , Dy^{3+} and Sm^{3+} doped samples, respectively.

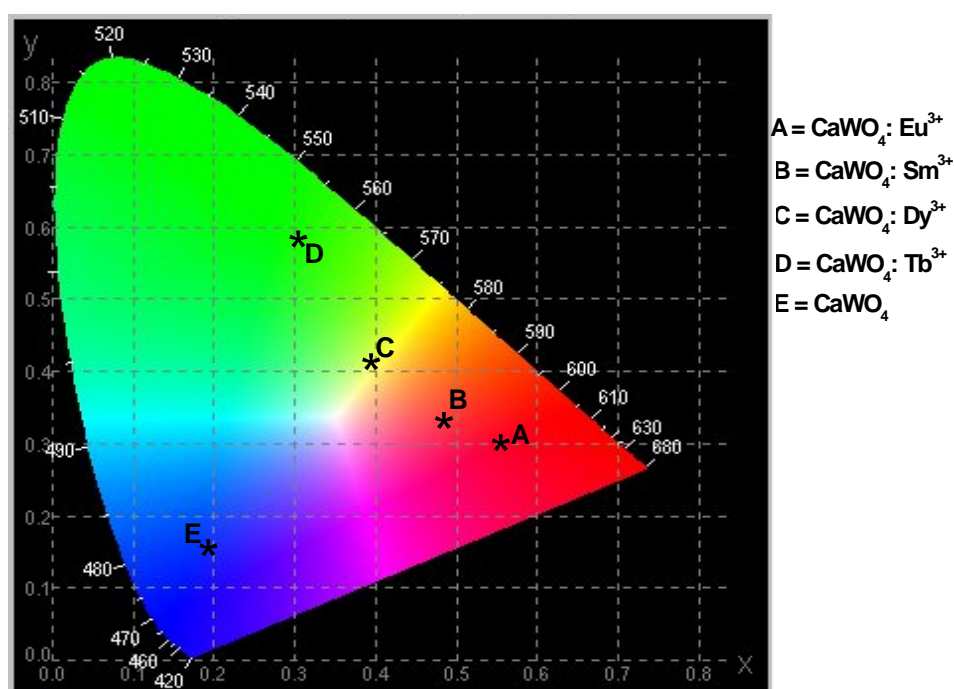


Fig.115. CIE diagram. A, B, C, D and E in the diagram represent the color coordinates corresponding to different $\text{CaWO}_4:\text{Ln}$ nanoparticles.

6.11. Luminescence studies on Er^{3+} doped CaWO_4 nanoparticles: Emission spectra from Er^{3+} doped CaWO_4 nanoparticles excited at 255, 380 and 522 nm are shown in the Fig.116 (a). Strong NIR emission centered at 1535 nm is observed from these nanoparticles. Highest emission intensity is observed after exciting at 380 nm light. This emission can be assigned to ${}^4\text{I}_{13/2} \rightarrow {}^4\text{I}_{15/2}$ transition of Er^{3+} ion in the CaWO_4 nanoparticles. The splitting in the emission

peak can be attributed to the crystal field effect on the Er^{3+} energy levels. Excitation spectrum corresponding to 1536 nm emission of Er^{3+} ions is shown in Fig.116 (b). It consists of a broad peak at 255 nm along with sharp peaks at 380, 488 and 522 nm. The broad band is due to the charge transfer process in WO_4^{2-} structural units and sharp peaks are due to f-f transitions of Er^{3+} ion in the CaWO_4 lattice. The appearance of 255 nm band in the excitation spectrum corresponding to Er^{3+} emission indicates that energy transfer is taking place from host to Er^{3+} ions.

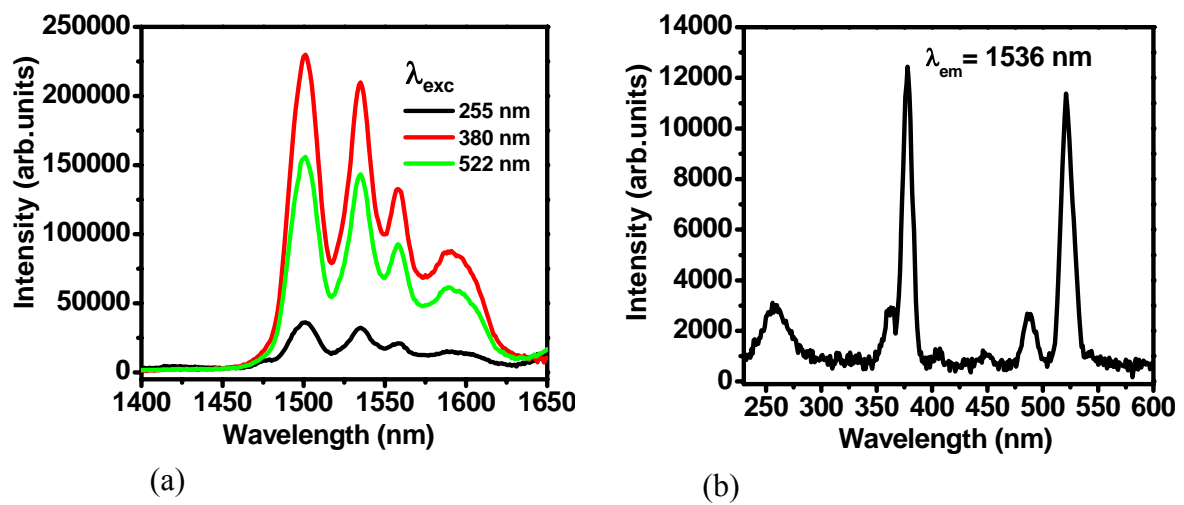


Fig.116. (a) Emission spectrum and (b) excitation spectrum of Er^{3+} doped CaWO_4 nanoparticles.

CHAPTER 7: Summary and Conclusions

The work presented in this thesis deals with the synthesis and characterization of a variety of inorganic luminescent nanomaterials based on oxides, phosphates, gallates and tungstates. Luminescent and structural properties of these materials before and after doping with lanthanide ions have been investigated by using XRD, TEM, SEM, FT-IR, Raman, TG-DTA, ^{31}P MAS NMR and photoluminescence techniques. A brief introduction about nanomaterials, their luminescence properties and different types of luminescent materials are described in chapter 1. Basic principles of different experimental techniques used for the characterization of the prepared nanomaterials are discussed in chapter 2. Subsequent chapters (chapters 3-6) deal with the synthesis of lanthanide doped nanomaterials and investigation of their structural and luminescent properties. The last chapter summarizes the work of the present investigation.

GaOOH nanorods with different aspect ratios were prepared by changing the urea concentration in the reaction medium. Lanthanide doping (~ 1 at %) in GaOOH nanorods causes significant structural and morphological changes leading to amorphisation of crystalline GaOOH. Based on XRD, SEM and vibrational studies it is concluded that the lanthanide ions interact with hydroxyl groups present at the inter-layers of GaOOH to form europium hydroxide, thereby disrupting the OH groups, which stabilizes the layered structure of GaOOH. This leads to the formation of finely mixed europium and gallium hydroxides. Existence of energy transfer between GaOOH and dopant lanthanide ions confirms the fine dispersion of lanthanide hydroxides with GaOOH. On heating, the nanorods maintain their morphology and lanthanide ions diffuses into the Ga_2O_3 lattice as revealed by the existence of strong energy transfer between the Ga_2O_3 and lanthanide ions. Strong NIR emission (~ 1535

nm) is observed from Er^{3+} doped Ga_2O_3 nanomaterials. These materials have potential applications in fabrication of optoelectronic devices and optical amplifiers.

Orthorhombic Sb_2O_3 nanorods were prepared at room temperature. A distinct photoluminescence band is observed over the region of 500–600 nm for Sb_2O_3 nanorods and has been attributed to the morphology of Sb_2O_3 nanorods. Changes occurring in the $\text{Sb}^{3+}\text{--O--Sb}^{3+}$ stretching and bending modes of vibration in the Raman spectrum at ~ 260 and 445 cm^{-1} further confirm their shape selective nature. Lanthanide ions like Eu^{3+} if present during the room temperature synthesis of Sb_2O_3 nanorods, leads to its interaction with Sb^{3+} ions to form amorphous europium antimony hydroxide. The amorphous compound on heating at high temperatures leads to decomposition, giving Eu_2O_3 and hydrated Sb(V) oxides as major phases.

Hexagonal GaPO_4 nanoparticles were prepared at a relatively low temperature of 130°C in glycerol medium. Based on the ^{31}P MAS NMR studies on undoped and lanthanide doped GaPO_4 it is concluded that upto 2.5 at % Eu^{3+} , protons of the surface Ga-OH linkages are replaced by Eu^{3+} ions and beyond which a separate EuPO_4 phase is formed along with GaPO_4 nanoparticles.

Nanoparticles and nanoribbons of lanthanide ions doped SbPO_4 were prepared at a low temperature of 120°C in mediums like ethylene glycol and glycerol. Morphology has been found to vary with the relative concentration of the solvents used for preparation of the sample. Based on the detailed infrared and Raman studies it has been confirmed that lanthanide ions are replacing Sb^{3+} ions from the SbPO_4 lattice. Energy transfer from Ce^{3+} to Tb^{3+} has been observed from Ce^{3+} co-doped $\text{SbPO}_4\text{:Tb}$ nanomaterials. The efficiency of energy transfer is around 60% in both $\text{SbPO}_4\text{:Ce}^{3+}(2.5\%),\text{Tb}^{3+}(5\%)$ nanomaterials and $\text{SbPO}_4\text{:Ce}^{3+}(2.5\%),\text{Tb}^{3+}(5\%)$ incorporated in silica ($\text{SbPO}_4\text{:Ce}^{3+}(2.5\%),\text{Tb}^{3+}(5\%)\text{-SiO}_2$). However, incorporating these nanomaterials into silica matrix leads to the effective shielding

of surface Tb^{3+} ions from stabilizing ligands resulting in a single exponential decay curve corresponding to the $^5\text{D}_4$ level of Tb^{3+} from the sample.

BiPO_4 nanomaterials with hexagonal and monoclinic crystal structures have been prepared in ethylene glycol medium at a relatively low temperature. There exist solid solution formation between BiPO_4 and different Ln^{3+} ions (like La^{3+} , Eu^{3+} and Tb^{3+}) as confirmed from XRD, FTIR and solid-state MAS NMR experiments. This type of solid solutions formation is highly desirable for making efficient light emitting and light harvesting materials. Orange, red, green and yellow emission has been observed from Sm^{3+} , Eu^{3+} , Tb^{3+} and Dy^{3+} doped BiPO_4 nanomaterials, respectively. In the case of Eu^{3+} - Tb^{3+} co-doped samples energy transfer has been observed from Tb^{3+} to Eu^{3+} .

ZnGa_2O_4 nanoparticles with tunable sizes have been prepared at a relatively low temperature of 120°C . Particle size of ZnGa_2O_4 nanoparticles can be tuned by either varying the precursor concentration or by varying the viscosity of the reaction medium. Photoluminescence from these nanoparticles can be tuned from 385 nm to 470 nm by varying the particle size. Luminescence from the ZnGa_2O_4 nanoparticles also gets tuned by In^{3+} doping in the lattice. Intense blue emission with quantum yield of $\sim 10\%$ is observed from $\text{ZnGa}_{1.5}\text{In}_{0.5}\text{O}_4$ nanoparticles. These nanoparticles were incorporated in PMMA matrix and such composite materials are useful for developing polymer based display devices. Doping lanthanide ions like Eu^{3+} , Tb^{3+} and Ce^{3+} in ZnGa_2O_4 nanoparticles lead to the development of multicolour light emitting nanoparticles

Un-doped and lanthanide ions doped MWO_4 ($\text{M} = \text{Ca}, \text{Sr}, \text{Ba}$) nanoparticles were prepared at room temperature in ethylene glycol medium. Under identical conditions, particle size increases with increase in ionic size of the metal ions. Blue emission is observed from CaWO_4 nanoparticles and this emission intensity increases with increase in particle size. Bright orange, red, green and greenish yellow emissions are obtained from Sm^{3+} , Eu^{3+} , Tb^{3+}

and Dy^{3+} doped CaWO_4 nanoparticles, respectively. Energy transfer from host to lanthanide ions in $\text{CaWO}_4:\text{Ln}^{3+}$ nanoparticles are responsible for its bright luminescence. Strong NIR (1536 nm) emission is observed from Er^{3+} doped CaWO_4 nanoparticles. These materials are expected to have potential application in the fields of telecommunication and lasers.

Future work: As an extension of this work, it is proposed that further work needs to be carried out for the development of ZnGa_2O_4 and CaWO_4 nanoparticles doped with lanthanide ions like Er^{3+} for employing them in NIR imaging as well as in polymer based optical amplifiers. The nanoparticles should have high dispersability in different organic medium for incorporating them in different polymers. Using bulky organic ligands as capping agents during the synthesis is one of the options. Optical amplifier will amplify the optical signal without converting into electrical signal. In optical amplifiers, lanthanide ions act as gain medium, which can amplify the optical signal. Optical amplifiers are widely used in telecommunication applications. However, polymer based optical amplifiers will have advantages like easy and economic fabrication as well as improved mechanical flexibility compared to the already existing thin film based devices. A schematic representation of optical amplifier is given in the Fig.117.

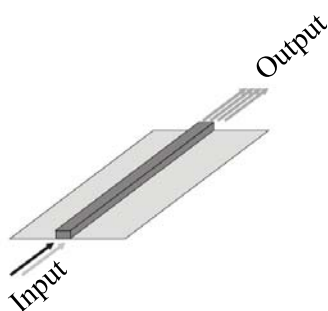


Fig.117. Schematic representation of an optical amplifier.

Some of the phosphates like SbPO_4 has layered structure which can accommodate/ intercalate different types of ions in the inter layer spacing. This property can be used for separation of different types of ions or species from solution. There are also some studies on the ion

exchange properties of the nanomaterials. For example Dong, et al. [279] have demonstrated that when GdF_3 nanoparticles dispersed in water are exposed to excess of La^{3+} ions, rapid ion exchange of Gd^{3+} from GdF_3 lattice by La^{3+} ions in aqueous solution takes place, resulting in the formation of LaF_3 nanoparticles and aqueous solution of Gd^{3+} ions. It is observed that lanthanide ions in the left of the periodic table (for example La^{3+}) can replace the ones from the right (for example Gd^{3+}) present in a lattice. In a recent study [280] it is also observed that rapid cation exchange takes place between Ce^{3+} ions in CePO_4 host and Eu^{3+} and Y^{3+} ions in solution. Hence, in order to understand the potential of nanomaterials for separation applications, it is proposed to carry out detailed ion exchange studies on phosphate based nanomaterials synthesized in the present study.

It is also proposed to carry out work on electro-luminescence properties of the nanomaterials like ZnGa_2O_4 , CaWO_4 , Sb_2O_3 , etc., after incorporating them in suitable polymers. This will be helpful for the development of polymer based display devices. The general approach used for electroluminescence devices is given in the Fig.118. It consists of anode (generally ITO coated glass), hole injector, emissive layer and cathode. Electrons will be injected from cathode while holes will be injected from anode. They will recombine in the emissive layer which is nanoparticles incorporated polymer film.

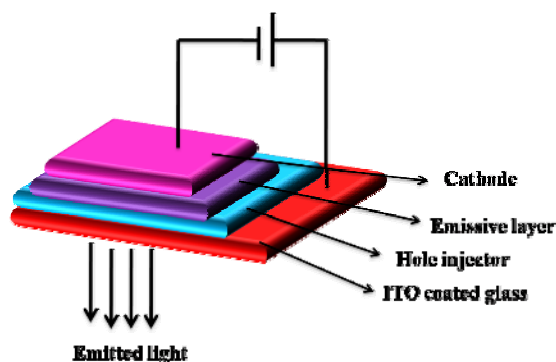


Fig. 118. Schematic diagram of an electro-luminescent device.

REFERENCES

1. D. J. Barber, I. C. Freestone, *Archaeometry*, 32 (1990) 33.
2. J. Yacamán, L. Rendon, J. Arenas, M. C. S. Puche, *Science*, 273 (1996) 223.
3. http://www.britishmuseum.org/explore/highlights/highlight_objects/pe_mla/t/the_lycurgus_cup.aspx
4. <http://aveburybooks.com/faraday/catalog.html>
5. M. Faraday, *Philos. Trans. R. Soc., London*, 147 (1857) 145.
6. G. Bredig, *Z. Angew. Chem.*, 11 (1898) 951.
7. J. Donau, *Monatsh*, 25 (1905) 525.
8. R. Zsigmondy, *Z. Phys. Chem.*, 56 (1906) 65.
9. R. Feynman, lecture entitled “There's Plenty of Room at the Bottom” given at American Physical Society meeting at Caltech on December 29, 1959.
10. E. Drexler, “Nanosystems: Molecular Machinery, Manufacturing and Coputation”, Wiley, 1991, Newyork.
11. X. Peng, L. Manna, W. Yang, J. Wickham, E. Scher, A. Kadavanich, A. P. Alivisatos, *Nature*, 404 (2000) 59.
12. Y. Jun, J. Choi, J. Cheon, *Angew. Chem. Int. Ed.*, 45 (2006) 3414.
13. C. Burda, X. Chen, R. Narayanan, M. A. El-Sayed, *Chem. Rev.*, 105 (2005) 1025.
14. C. N. R. Rao, A. Muller, A. K. Cheetham, “Nanomaterials Chemistry: Recent Developments and New Directions”, WILEY-VCH Verlag GmbH & Co. KGaA, 2007, Weinheim.
15. C. N. R. Rao G. U. Kulkarni, P. J. Thomas, “Nanocrystals: Synthesis, Properties and Applications”, Springer Berlin Heidelberg, 2007, New York.
16. B. L. Cushing, V. L. Kolesnichenko, C. J. O'Connor, *Chem. Rev.*, 104 (2004) 3893.
17. J. McKittrick, L. E. Shea, C. F. Bacalski, E. J. Bosze, *Displays*, 19 (1999) 169.

18. U. Kreibig, M. Vollmer, "Optical Properties of Metal Clusters", Springer: Berlin, 1995, Germany.
19. D. Dragoman, M. Dragoman, "Optical Characterization of Solids", Springer-Verlag, Heidelberg, 2002, Germany.
20. A. Hayer, V. Halleux, A. Kolhler, A. El-Garouhy, E. W. Meijer, J. Barbera, J. Tant, J. Levin, M. Lehmann, J. Gierschner, J. Cornil, Y. H. Geerts, *J. Phys. Chem. B*, 110 (2006) 7653.
21. C. Adachi, M. A. Baldo, S. R. Forrest, *J. Appl. Phys.*, 90 (2001) 5048.
22. V. K. Jain, L. Jain, *Coord. Chem. Rev.*, 254 (2010) 2848.
23. J. Kalinowski, V. Fattori, M. Cocchi, J. A. G. Williams, *Coord. Chem. Rev.*, doi:10.1016/j.ccr.2011.01.049.
24. L. Armelao, S. Quici, F. Barigelletti, G. Accorsi, G. Bottaro, M. Cavazzini, E. Tondello, *Coord. Chem. Rev.*, 254 (2010) 487.
25. K. Binnemans, *Chem. Rev.*, 109 (2009) 4283.
26. G. E. Khalil, K. Lau, G. D. Phelan, B. Carlson, M. Gouterman, J. B. Callis, L. R. Dalton, *Rev. Sci. Instrum.*, 75 (2004) 192.
27. L. D. Carlos, R. A. S. Ferreira, V. Z. Bermudez, S. J. L. Ribeiro, *Adv. Mater.*, 21 (2009) 509.
28. J. G. Bunzli, *Chem. Rev.*, 110 (2010) 2729.
29. D. B. A. Raj, B. Francis, M. L. P. Reddy, R. R. Butorac, V. M. Lynch, A. H. Cowley, *Inorg. Chem.*, 49 (2010) 9055.
30. S. Biju, M. L. P. Reddy, A. H. Cowley, K. V. Vasudevan, *J. Mater. Chem.*, 19 (2009) 5179.
31. W. M. Yen, S. Shionoya, H. Yamamoto, "Phosphor handbook", 2nd edition, CRC Press, Taylor & Francis Group, 2007, New York.

32. K. A. Gschneidner, Jr., L. Eyring, "Handbook on the Physics and Chemistry of Rare Earths", Elsevier Science, B.V. Amsterdam Lausanne, vol. 11, 1988, New York.
33. J. E. Huheey, E. A. Keiter, R. L. Keiter, O. K. Medhi, "Inorganic Chemistry: Principles of Structure and Reactivity", 3rd edition, Dorling Kindersley (India) Pvt. Ltd., 2007
34. K.A. Gschneidner, Jr., L. Eyring, "Handbook on the Physics and Chemistry of Rare Earths, Elsevier Science", B.V. Amsterdam Lausanne, vol. 23, 1996, New York.
35. K. C. Sheng, G. M. Korenowski, J. Phys. Chem., 92 (1988) 50.
36. P. Dorenbos, Phys. Rev. B, 62 (2000) 15640.
37. G. H. Dieke, H. M. Crosswhite, Appl. Opt., 2 (1963) 675.
38. J. G. Bunzli, C. Piguet, Chem. Soc. Rev., 34 (2005) 1048.
39. L. A. Riseberg, H. W. Moos, Phys. Rev., 174 (1968) 429.
40. J. L. Kropp, M. W. Windsor, J. Chem. Phys., 42 (1965) 1599.
41. E. Nakazawa, Chem. Phys. Lett., 56 (1978) 161.
42. J. G. Sole, L. E. Bausa, D. Jaque, "An Introduction to the Optical Spectroscopy of Inorganic Solids", John Wiley & Sons Ltd, 2005, England.
43. C. K. Lin, C. M. Zhang, J. J. Lin, Phys. Chem. C, 111 (2007) 3300.
44. C. Zhang, C. Li, J. Yang, Z. Cheng, Z. Hou, Y. Fan, J. Lin, Langmuir, 25 (2009) 7078.
45. K. Joy, I. J. Berlin, P. B. Nair, J. S. Lakshmi, G. P. Daniel, P. V. Thomas, J. Phys. Chem. Solids, 72 (2011) 673.
46. J. Liopis, Phys. Status Solidi A, 119 (1990) 661.
47. P. A. Arsenev, Kh. S. Bagdasarov, A. Niklas, A. D. Rhyazantsev, Phys. Status Solidi A, 62 (1980) 395.
48. L. Binet, D. Gourier, C. Minot, J. Solid State Chem., 113 (1994), 420.
49. N. Ueda, H. Hosono, R. Waseda, H. Kawazoe, Appl. Phys. Lett., 71 (1997) 933.

50. T. Miyata, T. Nakatani, T. Minami, *Thin Solid Films*, 373 (2000) 145.
51. E. G. Villora, T. Atou, T. Sekiguchi, T. Sugawara, M. Kikuchi, T. Fukuda, *Solid State Commun.*, 120 (2001) 455.
52. M. L. Pang, W. Y. Shen, J. Lin, *J. Appl. Phys.*, 97 (2005) 033511.
53. W. Y. Shen, M. L. Pang, J. Lin, J. Fang, *J. Electrochem. Soc.*, 152 (2) (2005) H25.
54. J. S. Kim, H. E. Kim, H. L. Park, G. C. Kim, *Solid State Commun.*, 132 (2004) 459.
55. J. Hao, Z. Lou, I. Renaud, M. Cocivera, *Thin Solid Films*, 467 (2004) 182.
56. G. Li, C. Peng, C. Li, P. Yang, Z. Hou, Y. Fan, Z. Cheng, J. Lin, *Inorg. Chem.*, 2010, 49, 1449.
57. A. B. Djurisic, Y. H. Leung, K. H. Tam, Y. F. Hsu, L. Ding, W. K. Ge, Y. C. Zhong, K. S. Wong, W. K. Chan, H. L. Tam, K. W. Cheah, W. M. Kwok, D. L. Phillips, *Nanotechnology*, 18 (2007) 095702.
58. O. D. Jayakumar, V. Sudarsan, C. Sudakar, R. Naik, R. K. Vatsa, A. K. Tyagi, *Scr. Mater.*, 62 (2010) 662.
59. H. Mizoguchi, P. M. Woodward, C. H. Park, D. A. Keszler, *J. Am. Chem. Soc.*, 126 (2004) 9796.
60. H. Ogawa, A. Abe, M. Nishikawa, S. Hayakawa, *J. Electrochem. Soc.*, 128 (1981) 2020.
61. Z. M. Jarzebski, J. P. Marton, *J. Electrochem. Soc.*, 123 (1976) 299.
62. Z. M. Jarzebski, J. P. Marton, *J. Electrochem. Soc.* 123 (1976) 333.
63. F. Gu, S. F. Wang, M. K. Lü, G. J. Zhou, D. Xu, D. R. Yuan, *J. Phys. Chem. B*, 108 (2004) 8119.
64. Z. Deng, D. Chen, F. Tang, X. Meng, J. Ren, L. Zhang, *J. Phys. Chem. C*, 111 (2007) 5325.

65. Z. Deng, F. Tang, D. Chen, X. Meng, L. Cao, B. Zou, *J. Phys. Chem. B*, 110 (2006) 18225.
66. S. Y. Bae, H. W. Seo, C. W. Na, J. Park, *Chem. Commun.*, (2004) 1834.
67. D. Gingasu, I. Mindru, G. Marinescu, L. Patron, C. Ghica, *J. Alloys. Compd.*, 481 (2009) 890.
68. C. M. Rao, V. Sudarsan, R. S. Ningthoujam, U. K. Gautam, R. K. Vatsa, A. Vinu, A. K. Tyagi, *J Nanosci. Nanotechnol.*, 8 (2008) 5776.
69. G. Blasse, B. C. Grabmaier, "Luminescent Materials", Springer-Verlag, 1994, Berlin.
70. J. Dhanraj, R. Jagananthan, T. R. N. Kutty, C. H. Lu *J. Phys. Chem. B*, 105 (2001) 11098.
71. T. K. Anh, L. Q. Minh, N. Vu, T. Y. Huong, N. T. Huong, C. Barthou, W. Streck, *J. Lumin.*, 102-103 (2003) 391.
72. S. Ray, P. Pramanik, A. Singha, A. Roy, *J. Appl. Phys.*, 97 (2005) 94312.
73. P. K. Sharma, M. H. Jilavi, R. Nass, H. Schmidt, *J. Phys. Lumin.*, 82 (1999) 187.
74. P. A. Tanner, K. L. Wong, *J. Phys. Chem. B*, 108 (2004) 136.
75. T. Igarashi, M. Ihara, T. Kusunoki, K. Ohno, T. Isobe, M. Senna, *Appl. Phys. Lett.*, 76 (2000) 1549.
76. H. Peng, H. Song, B. Chen, J. Wang, S. Lu, X. Kong, *J. Chem. Phys.*, 118 (2003) 3277.
77. H. Song, J. Wang, B. Chen, S. Lu, *Chem. Phys. Lett.*, 376 (2003) 1.
78. H. Song, B. Chen, H. Peng, J. Zhang, *Appl. Phys. Lett.*, 81 (2002) 1776.
79. H. Song, B. Chen, B. Sun, J. Zhang, S. Lu, *Chem. Phys. Lett.*, 372 (2003) 368.
80. H. Song, J. W. Wang, *J. Lumin.* 118 (2006) 220.
81. J. H. Park, N. G. Back, M. G. Kwak, B. E. Jun, B. C. Choi, B. K. Moon, J. H. Jeong, S. S. Yi, J. B. Kim, *Mater. Sci. Eng. C*, 27 (2007) 998.

82. S. Mukherjee, V. Sudarsan, R. K. Vatsa, S. V. Godbole, R. M. Kadam, U. M. Bhatta, A. K. Tyagi, *Nanotechnology*, 19 (2008) 325704.
83. W. Jia, H. Liu, Y. Wang, U. Hommerich, H. Eilers, K. R. Hoffman, W. M. Yen, *J. Lumin.*, 60-61 (1994) 192.
84. D. Ravichandran, R. Roy, A. G. Chakhovakoi, C. E. Hunt, W. B. White, S. Erdei, *J. Lumin.*, 71 (1997) 291.
85. G. W. Berkstresser, J. Shmulovich, T. C. D. Huo, G. Matulis, *J. Electrochem. Soc.*, 134 (1987) 2624.
86. G. Blasse, A. Bril, *J. Chem. Phys.*, 47 (1967) 5139.
87. Z. Yang, Xu. Li, Y. Yang, X. Li, *J. Lumin.*, 122-123 (2007) 707.
88. L. Ozawa, *Cathodoluminescence: Theory and Application*, Kodansha, 1990, Tokyo.
89. A. Purwanto, W. N. Wang, I. W. Lenggoro, K. Okuyama, *J. Electrochem. Soc.*, 154 (2007) J91.
90. S. H. Yang, C. Y. Lu, *J. Electrochem. Soc.*, 154 (2007) J397.
91. Y. S. Lin, R. S. Liu, *J. Lumin.*, 122-123 (2007) 580.
92. D. Hreniak, J. Hölsa, M. Lastusaari, W. Strek *J. Lumin.*, 122-123 (2007) 91.
93. H. S. Jang, W. B. Im, D. C. Lee, D. Y. Jeon, S. S. Kim *J. Lumin.*, 126 (2007) 371.
94. S. Mukherjee, V. Sudarsan, R. K. Vatsa, A. K. Tyagi, *J. Lumin.*, 129 (2009) 69.
95. G. Y. Adachi, N. Imanaka, *Chem. Rev.*, 98 (1998) 1479.
96. A. H. Peruski, L. H. Johnson, L. F. Peruski, *J. Immunol. Methods*, 263 (2002) 35.
97. J. A. Capobianco, J. C. Boyer, F. Vetrone, M. A. Speghini, M. Bettinelli, *Chem. Mater.*, 14 (2002) 2915.
98. Y. Guo, P. Woznicki, A. Barkatt, E. E. Saad, I. G. Talmy, *J. Mater. Res.*, 11 (1996) 639.
99. F. H. Firsching, S. N. Brune, *J. Chem. Eng. Data*, 36 (1991) 93.

100. A. Rouanel, J. J. Serra, K. Allaf, V. P. Orlovskii, *Inorg. Mater.*, 17 (1981) 76.
101. R. Gratz, W. Heinrich, *Am. Mineral.*, 82 (1997) 772.
102. R. P. Rao, *J. Electrochem. Soc.*, 150 (2003) H165.
103. W. H. Di, J. Y. Chen, X. J. Wang, B. Chen, *J. Chem. Lett.*, 33 (2004) 1448.
104. P. C. D. S. Filho, O. A. Serra, *J. Phys. Chem. C*, 115 (2011) 636.
105. Y. He, M. Zhao, Y. Song, G. Zhao, X. Ai, *J. Lumin.*, 131 (2011) 1144.
106. K. Srinivasu, R. S. Ningthoujam, V. Sudarsan, R. K. Vatsa, A. K. Tyagi, P. Srinivasu, A. Vinu, *J. Nanosci. Nanotechnol.*, 9 (2009) 3034.
107. M. N. Luwang, R. S. Ningthoujam, S. K. Srivastava, R. K. Vatsa, *J. Am. Chem. Soc.*, 133 (2011) 2998.
108. S. Lucas, E. Champion, D. Bregiroux, D. B. Assollant, F. Audubert, *J. Solid State Chem.*, 177 (2004) 1302.
109. L. Karpowich, S. Wilcke, R. Yu, G. Harley, J. A. Reimer, L. C. D. Jonghe, *J. Solid State Chem.*, 180 (2007) 840.
110. M. Cao, C. Hu, Q. Wu, C. Guo, Y. Qi, E. Wang, *Nanotechnology*, 16 (2005) 282.
111. L. Zhu, X. Liu, X. Liu, Q. Li, J. Li, S. Zhang, J. Meng, X. Cao, *Nanotechnology*, 17 (2006) 4217.
112. Q. Li, V. W. W. Yam, *Angew. Chem. Int. Ed.*, 46 (2007) 3486.
113. K. Kompe, H. Borchert, J. Storz, A. Lobo, S. Adam, T. Möller, M. Hasse, *Angew. Chem. Int. Ed.*, 42 (2003) 5513.
114. A. K. Gulnar, V. Sudarsan, R. K. Vatsa, R. C. Hubli, U. K. Gautam, A. Vinu, A. K. Tyagi, *Cryst. Growth. Design*. 9 (2009) 2451.
115. K. E. Gonsalves, G. Carlson, S. P. Rangarajan, M. Benaissa, M. J. Yacaman, *J. Mater. Chem.*, 6 (1996) 1451.

116. B. D. Cullity, "Elements of X-ray diffraction", Addison-Wilson Publishing Comp. Inc., 1959, U.S.A.
117. H. P. Klug, L.E. Alexander, "X-ray diffraction procedures", Wiley-Interscience Publication, 1974, New York.
118. R. W. Cahn, P. Haasen, E. J. Kramer, "Material Science and Engineering: Characterisation of Materials", VCH Publisher Inc., 1991, New York.
119. W. Zhou, Z. L. Wang, "Scanning microscopy for nanotechnology: Techniques and applications", Springer science and business media, 2006, New York.
120. M. D. Graef, "Introduction to Conventional Transmission Electron Microscopy", Cambridge University Press, Cambridge, 2000, UK.
121. B. Fultz, J. M. Howe, "Transmission Electron Microscopy and Diffractometry of Materials", Springer Berlin Heidelberg, 2008, New York.
122. R. Wiesendanger, "Scanning probe microscopy and spectroscopy: methods and applications", Cambridge University Press, Cambridge, 1994, UK.
123. C. N. Banwell, E. M. McCash, "Fundamentals of Molecular Spectroscopy", 4th Edition, Tata McGraw-Hill publishers Ltd, 2000, New Delhi.
124. P. Boolchand, "Insulating and Semiconducting Glasses", Series on directions in condensed matter physics, Vol.17, World scientific, 2000, Singapore.
125. E. R. Andrew, A. Bradbury, R. G. Eades, Nature, 183 (1959)1802,
126. I. J. Lowe, Phys. Rev. Lett., 2 (1959) 285.
127. K. K. Rohatgi-Mukherjee, "Fundamentals of Photochemistry", New Age International Publishers, 2007, New Delhi.
128. M. Ogita, K. Higo, Y. Nakanishi, Y. Hatanaka, Appl. Surf. Sci., 175 (2001) 721.
129. K. Shimizu, A. Satsuma, T. Hattori, Appl. Catal. B, 16 (1998) 319.

130. F. Li, W. Jianhuai, L. Jiongtian, W. Bingguo, S. Shuojiang, *J. Compos. Mater.*, 41 (2007) 1487.
131. H. Sato, K. Kondo, S. Tsuge, H. Ohtan, N. Sato, *Polym. Degrad. Stab.*, 62 (1998) 4148.
132. K. Ozawa, Y. Sakka, M. Amano, *J. Mater. Res.*, 13 (1998) 830.
133. D. J. Dzimitrowicz, J. B. Goodenough, P. J. Wiseman, *Mat. Res. Bull.*, 17 (1982) 971.
134. J. H. Youk, R. P. Kambour, W. J. MacKnight, *Macromolecules*, 33 (2000) 3594.
135. B. Duh, *Polymer*, 43 (2002) 3147.
136. J. S. Zabinski, M. S. Donley, N. T. McDevittb, *Wear*, 165 (1993) 103.
137. H. Bryngelsson, J. Eskhult, L. Nyholm, M. Herranen, O. Alm, K. Edstrom, *Chem. Mater.*, 19 (2007) 1170.
138. R. Roy, V. G Hill, E. F. Osborn, *J. Am. Chem. Soc.*, 74 (1952) 719.
139. H. S. Qian, P. Gunawan, Y. X. Zhang, G. F. Lin, J. W. Zheng, R. Xu, *Cryst. Growth. Des.*, 8 (2008) 1282.
140. K. Terashima, T. Hashimoto, T. Uchino, S. H. Kim, T. Yoko, *J. Ceram. Soc. Japan*, 104 (1996) 1008.
141. D. Yan, G. Yin, Z. Huang, X. Liao, Y. Kang, Y. Yao, B. Hao, J. Gu, D. Han, *Inorg. Chem.*, 48 (2009) 6471.
142. M. Sun, D. Li, W. Zhang, X. Fu, Y. Shao, W. Li, G. Xiao, Y. He, *Nanotechnology*, 21 (2010) 355601.
143. S. Avivi, Y. Mastai, G. Hodes, A. Gedanken, *J. Am. Chem. Soc.*, 121 (1999) 4196.
144. Y. Zhao, R. L. Frost, W. N. Martens, *J. Phys. Chem. C*, 111 (2007) 16290.
145. J. Zhang, Z. Liu, C. Lin, J. Lin, *J. Cryst. Growth.*, 280 (2005) 99.
146. J. N. Cha, K. Shimizu, Y. Zhou, S. C. Christiansen, B. F. Chmelka, G. D. Stucky, D. E. Morse, *Proc. Natl. Acad. Sci., USA*, 96 (1999) 361.

147. D. Kisailus, Q. Truong, Y. Amemiya, J. C. Weaver, D. E. Morse, *Proc. Natl. Acad. Sci., USA*, 103 (2006) 5652.
148. D. Kisailus, J. H. Choi, J. C. Weaver, W. Yang, D. E. Morse, *Adv. Mater.*, 17 (2005) 314.
149. I. Lee, J. Kwak, S. Haam, S. Y. Lee, *J. Cryst. Growth.*, 312 (2010) 2107.
150. A. C. Tas, P. J. Majewski, F. Aldinger, *J. Am. Ceram. Soc.*, 85 (2002) 1421.
151. D. W. Zeng, C. S. Xie, B. L. Zhu, W. L. Song, *Mater. Lett.*, 58 (2004) 312.
152. G. J. Zhu, X. M. Feng, X. J. Yang, X. Wang, L. D. Lu, *Chin. J. Inorg. Chem.*, 21 (2005) 441.
153. L. Feng, J. Liu, L. Liao, J. Wu, *J. Chem. Ind. Eng.*, 56 (2005) 2245.
154. C. H. Xu, S. Q. Shi, C. Surya, C. H. Woo, *J. Mater. Sci.*, 42 (2007) 9855.
155. P. Christian, P. O'Brien, *J. Mater. Chem.*, 15 (2005) 4949.
156. K. Ozawa, Y. Sakka, M. Amano, *J. Mater. Res.*, 13 (1998) 830.
157. Y. Hu, H. Zhang, H. Yang, *J. Alloys Compd.*, 428 (2007) 327.
158. D. W. Zeng, B. L. Zhu, C. S. Xie, W. L. Song, A. H. Wang, *Mater. Sci. Eng. A*, 366 (2004) 332.
159. D. Sendor, T. Weirich, U. Simon, *Chem. Commun.*, (2005) 5790.
160. X. Chen, X. Wang, C. An, J. Liu, Y. Qian, *Mater. Res. Bull.*, 40 (2005) 469.
161. Y. Zhang, G. Li, J. Zhang, L. Zhang, *Nanotechnology*, 15 (2004) 762.
162. Q. Zhao, X. Zhang, Q. Yang, Y. Xie, *Can. J. Chem.*, 83 (2005) 1093.
163. Z. Zhang, B. Li, Y. Zhao, X. Xu, C. Zhang, Z. Wu, *Chem. Lett.*, 35 (2006) 1026.
164. P. Gollakota, A. Dhawan, P. Wellenius, L. M. Lunardi, J. F. Muth, Y. N. Saripalli, H. Y. Peng, H. O. Everitt, *Appl. Phys. Lett.*, 88 (2006) 221906.
165. W. Y. Shen, M. L. Pang, J. Lin, J. Fand, *J. Electro. Chem. Soc.*, 152 (2005) H25.

166. L. Fu, Z. Liu, Y. Liu, B. Han, J. Wang, P. Hu, L. Cao, D. Zhu, *J. Phys. Chem. B*, 108 (2004) 13074.
167. M. L. Pang, W. Y. Shen, J. Lin, *J. Appl. Phys.*, 97 (2005) 033511.
168. T. Biljan, A. Gajović, Z. Meić. *J. Lumin.*, 128 (2008) 377.
169. E. Nogales, B. Méndez, J. Piqueras, *Nanotechnology*, 19 (2008) 035713.
170. E. Nogales, B. Méndez, J. Piqueras, J. A. Garcia, *Nanotechnology*, 20 (2009) 115201.
171. H. Xie, L. Chen, Y. Liu, K. Huang, *Solid State Commun.*, 141 (2007) 12.
172. R. D. Shannon, *Acta Cryst.*, A32 (1976) 751.
173. X. Y. Chen, H. S. Huh, S. W. Lee, *J. Solid State Chem.*, 181 (2008) 2127.
174. E. W. J. L. Oomen, W. M. A. Smit, G. Blasse, *Phys. Rev. B*, 37 (1988) 18.
175. Y. Chen. C. Shi, G. Hu, *J. Appl. Phys.*, 87 (2000) 1503.
176. F. Wen, W. Li, Z. Liu, T. Kim, K. Yoo, S. Shin, J. H. Moon, J. H. Kim, *Solid State Commun.*, 133 (2005) 417.
177. D. R. Lide, H. P. R. Frederikse, "CRC Handbook of Chemistry and Physics", CRC Press, 1996, Boca Raton.
178. C. Svensson, *Acta Cryst. B.*, 30 (1974) 458.
179. F. Wen, W. Li, Z. Liu, T. Kim, K. Yoo, S. Shin, J. H. Moon, J. H. Kim, *Solid State Commun.*, 133 (2005) 417.
180. S. Tanabe, *J. Alloys Compd.*, 675 (2006) 408.
181. J. Expedito, C. Silva, O. L. Malta, G. F. de Sa, P. A. Santa-Cruz, *J. Lumin.*, 270 (1997) 72.
182. C. C. Huang, C. S. Yeh, *New J. Chem.*, 34 (2010) 103.
183. Y. Hu, X. Liu, Z. Xu, *Miner. Eng.*, 16 (2003) 219.
184. W. W. Rudolph, C. C. Pye, *Phys. Chem. Chem. Phys.*, 4 (2002) 4319.

185. Y. Zhao, R. L. Frost, *J. Raman Spectrosc.*, 39 (2008) 1494.
186. M. Ristić, S. Popvić, S. Musić, *Mater. Lett.*, 59 (2005) 1227.
187. X. Liu, G. Qiu, Y. Zhao, N. Zhang, R. Yi, *J. Alloys Compd.*, 439 (2007) 275.
188. S. Wang, Y. Zhao, J. Chen, R. Xu, L. Luo, S. Zhong, *Superlattices Microstruct.*, 47 (2010) 597.
189. X. Liu, G. Qiu, Y. Zhao, N. Zhang, R. Yi, *J. Alloys Compd.*, 439 (2007) 275.
190. M. Uchida, A. Okuwaki, *J. Solution Chem.*, 26 (1997) 699.
191. J. Yang, Y. Zhao, R. L. Frost, *Spectrochim. Acta*, 74 (2009) 398.
192. J. M. G. Amores, V. S. Escribano, G. Busca, *J. Mater. Chem.*, 9 (1999) 1161.
193. G. Socrates, "Infrared Characteristic Group Frequencies", Wiley, 1994, New York.
194. R. Demichelis, Y. Noel, B. Civalleri, C. Roetti, M. Ferrero, R. Dovesi, *J. Phys. Chem. B*, 111 (2007) 9337.
195. P. Ugliengo, Moldraw 2.0, version h1. www.moldraw.unito.it
196. D. R. Lide, "CRC Handbook of Chemistry and Physics", CRC Press, 2008, Boca Raton.
197. V. A. Kolesova, Y. I. Ryskin, *J. Struct. Chem.*, 3 (1962) 656.
198. L. Fu, Y. Liu, P. Hu, K. Xiao, G. Yu, D. Zhu, *Chem. Mater.*, 15 (2003) 4287.
199. J. S. Kim, H. L. Park, C. M. Chon, H. S. Moon, T. W. Kim, *Solid State Commun.*, 129 (2004) 163.
200. T. Harwig, F. Kellendonk, *J. Solid State Chem.*, 24 (1978) 255.
201. C. H. Liang, G. W. Meng, G. Z. Wang, Y. W. Wang, L. D. Zhang, S. Y. Zhang, *Appl. Phys. Lett.*, 78 (2001) 3202.
202. M. S. Y. Parast, A. Morsali, *Ultrason. Sonochem.*, 18 (2011) 375.
203. T. Sato, T. Nakumara, *Thermochim. Acta*, 53 (1982) 281.
204. T. Mizunashi, S. Fujihara, *Electrochem. Solid State Lett.*, 11 (2008) J43.

205. R. Sasikala, V. Sudarsan, C. Sudakar, R. Naik, T. Sakuntala, S. R. Bharadwaj, *Int. J. Hydrogen Energy*, 33 (2008) 4966.
206. R. Sasikala, A. Shirole, V. Sudarsan, T. Sakuntala, C. Sudakar, R. Naik, S. R. Bharadwaj, *Int. J. Hydrogen Energy*, 34 (2009) 3621.
207. A. B. Djurisic, Y. H. Leung, K. H. Tam, Y. F. Hsu, L. Ding, W. K. Ge, Y. C. Zhong, K. S. Wong, W. K. Chan, H. L. Tam, K. W. Cheah, W. M. Kwok, D. L. Phillips, *Nanotechnology*, 18 (2007) 95702.
208. C. A. Cody, L. D. Carlo, R. K. Darlington, *Inorg. Chem.*, 18 (1979) 1572.
209. G. Mestl, P. Ruiz, B. Delmon, H. Knozinger, *J. Phys. Chem.*, 98 (1994) 11276.
210. S. J. Gilliam, J. O. Jensen, A. Banerjee, D. Zeroka, S. J. Kirkby, C. N. Merrow, *Spectrochim. Acta Part A*, 60 (2004) 425.
211. M. Nalin, Y. Messaddeq, S. J. L. Ribeiro, M. Poulain, V. Briois, G. Brunklaus, C. Rosenhahn, B. D. Mosel, H. Eckert, *J. Mater. Chem.*, 14 (2004) 3398.
212. F. Yaripour, F. Baghaei, I. Schmidt, J. Perregaard, *Catal. Commun.*, 6 (2005) 542.
213. A. Ludmany, S. S. Kurek, A. Stoklosa, G. Wilczynski, A. Wojtowicz, J. Zajecki, *Appl. Catal. A: Gen.*, 267 (2004) 149.
214. J. Haines, O. Cambon, D. C. Herreillat, G. Fraysse, F. E. Mallassagne, *Solid State Sci.*, 6 (2004) 995.
215. G. Y. Adachi, N. Imanaka, *Chem. Rev.*, 98 (1998) 1479.
216. A. H. Peruski, L. H. Johnson, L. F. Peruski, *J. Immunol. Methods*, 263 (2002) 35.
217. J. A. Capobianco, J. C. Boyer, F. Vetrone, M. A. Speghini, M. Bettinelli, *Chem. Mater.*, 14 (2002) 2915.
218. Y. Guo, P. Woznicki, A. Barkatt, E. E. Saad, I. G. Talmy, *J. Mater. Res.*, 11 (1996) 639.
219. F. H. Firsching, S. N. Brune, *J. Chem. Eng. Data*, 36 (1991) 93.

220. A. Rouanel, J. J. Serra, K. Allaf, V. P. Orlovskii, *Inorg. Mater.*, 17 (1981) 76.
221. E. L. Falcão, C. A. C. Bosco, G. S. Maciel, C. B. de Araujo, H. Acioli, M. Nalin, Y. Messaddeq, *Appl. Phys. Lett.*, 83 (2003) 1292.
222. M. Nalin, Y. Messaddeq, S. J. L. Ribeiro, M. Poulain, V. Briois, *J. Optoelectron. Adv. Mater.*, 3 (2001) 553.
223. F. S. De Vicente, M. S. Li, M. Nalin, Y. Messaddeq, *J. Non-Cryst. Solids*, 330 (2003) 168.
224. T. S. Chang, L. Guijia, C. H. Shin, Y. K. Lee, S. S. Yun, *Catal. Lett.*, 68 (2000) 229.
225. M. Ruwet, S. Ceckiewicz, B. Delmon, *Ind. Eng. Chem. Res.*, 26 (1987) 1981.
226. B. Kinberger, *Acta Chem. Scand.*, 24 (1970) 320.
227. B. Romero, S. Bruque, M. A. G. Aranda, J. E. Iglesias, *Inorg. Chem.*, 33 (1994) 1869.
228. Y. Ni, J. M. Hughes, A. N. Mariano, *Am. Mineral.*, 80 (1995) 21.
229. S. Kozono, S. Takahashi, H. Haraguchi, *Anal. Bioanal. Chem.*, 376 (2002) 542.
230. M. J. Clarke, F. Zhu, D. R. Frasca, *Chem. Rev.*, 99 (1999) 2511.
231. X. Liu, R. H. Byrne, *Geochim. Cosmochim. Acta.*, 61 (1997) 1625.
232. J. W. Stouwdam, F. C. J. M. van Veggel, *Langmuir*, 20 (2004) 11763.
233. S. Nigam, V. Sudarsan, R. K. Vatsa, J. Ghattak, P. V. J. Satyam, *J. Phys.Chem. C.*, 113 (2009) 8750.
234. V. Sudarsan, F. C. J. M. van Veggel, R. A. Herring, M. Raudsepp, *J. Mater. Chem.*, 15 (2005) 1332.
235. R. S. Ningthoujam, V. Sudarsan, S. K. Kulshreshtha, *J. Lumin.*, 127 (2007) 747.
236. S. K. Kulshreshtha, O. D. Jayakumar, V. Sudarsan, *J. Phys. Chem. Solids*, 65 (2004) 1141.
237. S. K. Kulshreshtha, O. D. Jayakumar, V. Sudarsan, *J. Solid State Chem.*, 183 (2010) 1071.

238. E. Oldfield, R. A. Kinsey, K. A. Smith, J. A. Nichols, R. J. Kirkpatrick, J. Magn. Reson., 51 (1983) 325.
239. S. K. Kulshreshtha, R. Vijayalakshmi, V. Sudarsan, Stud. Surf. Sci. Catal., 113 (1998) 699.
240. R. Moleski, E. Leontidis, F. Krumeich, J. Colloid Interface Sci., 302 (2006) 246.
241. V. A. Kolesova, Y. I. Ryskin, J. Struct. Chem., 3 (1962) 656.
242. G. Alonzo, N. Bertazzi, P. Galli, M. A. Massucci, P. Patrono, F. Saiano, Mat. Res. Bull., 33 (1998) 1221.
243. G. Alonzo, N. Bertazzi, P. Galli, G. Marci, M. A. Massucci, L. Palmisano, P. Patrono, F. Saiano, Mater. Res. Bull., 33 (1998) 1233.
244. V. Sudarsan, K. P. Muthe, J. C. Vyas, S. K. Kulshreshtha, J. Alloys. Comp., 336 (2002) 119.
245. M. Nalin, Y. Messaddeq, S. J. L. Ribeiro, M. Poulain, V. Briois, G. Brunklaus, C. Rosenhahn, B. D. Mosel, H. Eckert, J. Mater. Chem., 14 (2004) 3398.
246. W. Brockner, L. P. Hoyer, Spectrochim. Acta Part A., 58 (2002) 1911.
247. J. S. Bae, K. S. Shim, B. K. Moon, B. C. Choi, J. H. Jeong, S. Yi, J. H. Kim, Thin Solid Films, 479 (2005) 238.
248. M. Hirano, S. Okumura, Y. Hasegawa, M. Inagaki, J. Solid State Chem., 168 (2002) 5.
249. H. I. Kang, J. S. Kim, M. Lee, J. H. Bahng, J. C. Choi, H. L. Park, G. C. Kim, T. W. Kim, Y. H. Hwang, S. I. Mho, S. H. Eom, Y. S. Yu, H. J. Song, W. T. Kim, Solid State Commun., 122 (2002) 633.
250. J. S. Kim, H. L. Park, C. M. Chon, H. S. Moon, T. W. Kim, Solid State Commun., 129 (2004) 163.

251. J. H. Lee, H. J. Park, K. Yoo, B. W. Kim, J. C. Lee, S. Park, J. Eur. Ceram. Soc., 27 (2007) 965.
252. X. L. Duan, D. R. Yuan, L. H. Wang, F. P. Yu, X. F. Cheng, Z. Q. Liu, S. S. Yan, J. Cryst. Growth, 296 (2006) 234.
253. J. S. Kim, A. K. Kwon, J. S. Kim, H. L. Park, G. C. Kim, S. do Han, J. Lumin., 122&123 (2007) 851.
254. Z. Xu, Y. Li, Z. Liu, Z. Xiong, Mat. Sci. Eng. B, 110 (2004) 302.
255. I. K. Jeong, H. L. Park, S. I. Mho, Solid State Commun., 105 (1998) 179.
256. T. M. Chen, Y. W. Chen, J. Solid State Chem., 150 (2000) 204.
257. S. K. Choi, H. S. Mool, S. I. Mho, T. W. Kim, H. L. Park, Mater. Res. Bull., 33 (1998) 693.
258. I. K. Jeong, H. L. Park, S. I. Mho, Solid State Commun., 108 (1998) 823.
259. L. Zou, X. Xiang, M. Wei, F. Li, D. G. Evans, Inorg. Chem., 47 (2008) 1361.
260. L. Xu, Y. Su, Q. Zhou, S. Li, Y. Chen, Y. Feng, Cryst. Growth Des., 7 (2007), 810.
261. S. Y. Bae, J. Lee, H. Jung, J. Park, J. Ahn, J. Am. Chem. Soc., 127 (2005) 10802.
262. S. Y. Bae, H. W. Seo, C. W. Na, J. Park, Chem. Commun., (2004) 1834.
263. S. Daniele, D. Tchekoukov, L. G. H. Pfalzgraf, J. Mater. Chem., 12 (2002) 2519.
264. M. Cao, I. Djerdj, M. Antonietti, M. Niederberger, Chem. Mater., 19 (2007) 5830.
265. M. Yu, J. Lin, Y. H. Zhou, S. B. Wang, Mater. Lett., 56 (2002) 1007.
266. H. W. Liao, Y. F. Wang, X. M. Liu, Y. D. Li, Y. T. Qian, Chem. Mater., 12 (2000) 2819.
267. L. F. G. D. Johnson, Boyd, K. Nassau, R. R. Soden, Phys. Rev., 126 (1962) 1406.
268. W. Carel, E. van Eijk, Nucl. Instrum. Methods Phys. Res. A, 392 (1997) 285.
269. E. S. Kim, S. H. Kim, B. I. Lee, J. Eur. Ceram. Soc., 26 (2006) 2101.
270. G. Angloher et al. Astropart. Phy., 23 (2005) 325.

271. B. G. Hyde, S. Andersson, "Inorganic Crystal Structure", Wiley, 1989, New York.
272. T. T. Kloprogge, M. L. Weier, L. C. Duong, R. L. Frost, *Mater. Chem. Phys.*, 88 (2004) 438.
273. B. A. H. Sanchez, T. J. Boyle, H. D. Pratt III, M. A. Rodriguez, L. N. Brewer, D. R. Dunphy, *Chem. Mater.*, 20 (2008) 6643.
274. W. S. Wang, L. Zhen, C. Y. Xu, L. Yang, W. Z. Shao, *J. Phys. Chem. C*, 112 (2008) 19390.
275. T. Thongtem, A. Phuruangrat, S. Thongtem, *Appl. Surf. Sci.*, 254 (2008) 7581.
276. F. Lei, B. Yan, *J. Solid State Chem.*, 181 (2008) 855.
277. Y. Su, L. Li, G. Li, *J. Mater. Chem.*, 19 (2009) 2316.
278. P. Yang, Z. Quan, C. Li, H. Lian, S. Huang, J. Lin, *Microporous Mesoporous Mater.*, 116 (2008) 524.
279. C. Dong, F. C. J. M. van Veggel, *ACS Nano*, 3 (2009) 123.
280. A. K. Gulnar, V. Sudarsan, R. K. Vatsa, T. Sakuntala, A. K. Tyagi, U. K. Gautam, A. Vinu, *Nanoscale*, 2 (2010) 2847.

List of publications in journals

1. Luminescence studies on $\text{SbPO}_4:\text{Ln}^{3+}$ (Ln = Eu, Ce, Tb) nanoparticles and nanoribbons.
B. S. Naidu, V. Sudarsan and R. K. Vatsa
J. Nanosci. Nanotechnol., 9 (2009) 2997.
2. Shape selective nature of the luminescent centers and the structural properties of Sb_2O_3 .
B. S. Naidu, M. Pandey, V. Sudarsan, R.K.Vatsa and R. Tewari
Chem. Phys. Lett., 474 (2009) 180.
3. Interaction of Sb^{3+} ions with Eu^{3+} ions during the room temperature synthesis of luminescent Sb_2O_3 nanorods.
B. S. Naidu, M. Pandey, R. Tewari, V. Sudarsan, R. K. Vatsa
J. Lumin., 131 (2011) 177.
4. Investigations of Ce^{3+} co-doped $\text{SbPO}_4:\text{Tb}^{3+}$ nanoribbons and nanoparticles by vibrational and photoluminescence spectroscopy
B. S. Naidu, M. Pandey, V. Sudarsan, J. Ghattak, R. K. Vatsa.
J. Nanosci. Nanotechnol., 11 (2011) 3180.
5. Lanthanide ions assisted structural collapse of layered GaOOH lattice.
B. S. Naidu, M. Pandey, J. Nuwad, V. Sudarsan, R. K. Vatsa, R. J. Kshirsagar, C. G. S. Pillai
Inorg. Chem., 50 (2011) 4463.
6. GaPO_4 nanoparticles with Eu^{3+} ions at their surface: Evidence from luminescence and ^{31}P MAS NMR techniques
B. S. Naidu, B. Vishwanadh, V. Sudarsan, R. K. Vatsa
J. Am. Ceram. Soc., (in press).
7. Effect of lanthanide ion (Ln) concentration on the size and shape of $\text{Ga}_2\text{O}_3:\text{Ln}$ nanomaterials.

B. S. Naidu, B. Vishwanadh, V. Sudarsan, R. K. Vatsa

(Manuscript under preparation)

8. Synthesis and characterisation of solid solutions of BiPO₄ and LnPO₄ in nano size dimensions.

B. S. Naidu, B. Vishwanadh, V. Sudarsan, R. K. Vatsa

(Manuscript under preparation)

9. Tunable blue emission from ZnGa₂O₄ nanoparticles by In³⁺ doping

B. S. Naidu, P.V Satyam, V. Sudarsan, R. K. Vatsa

(Manuscript under preparation)

10. Room temperature synthesis of multicolour emitting dispersible CaWO₄:Ln³⁺ (Ln = Eu, Tb, Sm, Dy) nanoparticles

B. S. Naidu, B. Vishwanadh, V. Sudarsan, R. K. Vatsa

(Manuscript under preparation)

Publications in Conferences proceedings

Poster presentations:

1. Surface modifications on the extent of energy transfer between Ce³⁺ and Tb³⁺ ions in SbPO₄:Ln³⁺ (Ln = Ce, Tb) nanoparticles and nanoribbons

B. S. Naidu, V. Sudarsan, R. K. Vatsa

2nd DAE-BRNS International symposium on material chemistry (ISMC-2008),

December 2-6, 2008, BARC, Mumbai, pp.192.

2. In³⁺ doped ZnGa₂O₄ nanoparticles with bright blue light emission

B. S. Naidu, V. Sudarsan, R. K. Vatsa

2nd DAE-BRNS International symposium on material chemistry (ISMC-2008),

December 2-6, 2008, BARC, Mumbai, pp.191.

3. Luminescence studies on GaPO₄: Ln (Ln = Eu³⁺, Dy³⁺, Tb³⁺ and Ce³⁺) nanoparticles
B. S. Naidu, V. Sudarsan, R. K. Vatsa and R. Tewari
53rd DAE solid state physics symposium, BARC, Mumbai, 53(2008) 491.
4. Blue light emitting In³⁺ doped ZnGa₂O₄ nanoparticles
B. S. Naidu, V. Sudarsan, R. K. Vatsa
National Conference on Advances in Nanomaterials, Devices and Technologies (NCANDT-2009), S. V. Degree college, Kadapa, July 11-12, 2009, pp. 54.
5. Microstructural studies on GaOOH and Ga₂O₃ nanorods
B. S. Naidu, J. Nuwad, V. Sudarsan, R. K. Vatsa, C. G. S. Pillai
Two Day Seminar on Microtexture and Microstructure (Microstructure-2009), BARC, Mumbai, November 27-28, 2009, pp. 87.
6. Lanthanide ions (Ce³⁺, Tb³⁺) doped nanoribbons/nanoparticles of SbPO₄
B. S. Naidu, V. Sudarsan, J. Ghattak, R. K. Vatsa
International Conference on Advances in Electron microscopy and Related Techniques (EMSI-2010), BARC, Mumbai, March 8-10, 2010, pp 433-434.
7. Room temperature synthesis and characterization of lanthanide ions doped MWO₄ (M = Ca, Sr, Ba) nanoparticles
B. S. Naidu, B. Vishwanadh, V. Sudarsan, R. K. Vatsa
3rd DAE-BRNS International symposium on material chemistry (ISMC-2010), BARC, Mumbai, December 7-11, 2010, pp.180

Oral presentations:

8. Synthesis and Luminescence studies of lanthanide ion doped BiPO₄ nanomaterials
B. S. Naidu, V. Sudarsan, R. K. Vatsa
Indo-Russian Workshop on Nanotechnology and Laser Induced Plasma (IRNANO-2009), Delhi University, Delhi, November 24-26, 2009, pp. 39.

9. Room temperature synthesis of multi colour light emitting CaWO_4 nanoparticles

B. S. Naidu, B. Vishwanadh, V. Sudarsan, R. K. Vatsa

International Conference on Recent Trends in Materials Science and Technology

(ICMST-2010), Indian Institute of Space science and Technology,

Thiruvananthapuram, October 29-31, 2010, pp. 6.16 - 6.18.

10. Synthesis and characterization of lanthanide ions doped nanomaterials

B. S. Naidu, V. Sudarsan, V. K. Jain

23rd Research Scholars Meet (RSM-2010), Indian Chemical Society (Mumbai branch)

and N. G. Acharya and D. K. Marathe College, Mumbai, February 25-26, 2011, pp. 2.